INTENSIFICATION OF HEAT TRANSFER IN THERMAL ENERGY STORAGE SYSTEMS WITH PHASE CHANGE MATERIALS

Mohammad Ismail

Ph.D.

2019

INTENSIFICATION OF HEAT TRANSFER IN THERMAL ENERGY STORAGE SYSTEMS WITH PHASE CHANGE MATERIALS

Mohammad Ismail

A thesis submitted in partial fulfilment of the requirements of the University of Northumbria at Newcastle for the degree of Doctor of Philosophy

Research undertaken in the Faculty of Engineering and Environment

October 2019

Abstract

This research work aims to develop low- and medium-temperature thermal energy storage (TES) systems using metallic alloys and solar salt as phase change materials (PCMs) for accumulating thermal energy in the temperature ranges between 120 and 140 °C and 215 and 250 °C, respectively. The low purity metallic alloy Bi 58%-Sn 42% was selected as the PCM for low-temperature applications because it is non-hazardous, relatively inexpensive, and it has a suitable melting temperature range. Commercially available high-purity metallic alloys (99.99%) are expensive, whereas lower purity alloys can be a cost-competitive alternative for PCM applications. The sample of a low purity metal alloy, namely Bi 58%-Sn 42% with a purity of 97% was sintered in the laboratory, and its thermal properties were characterized for application as a PCM. Experimental investigations demonstrated that deterioration of the thermal properties of the low purity metal alloy is not substantial in comparison to the pure metallic alloy and that it can be efficiently used as a PCM. Solar salt ($NaNO_3$ 60% - KNO_3 40%), selected as the PCM for medium-temperature applications due to its high latent heat value, has a relatively low thermal conductivity. Therefore, two techniques were adopted to improve the heat transfer in TES: deploying metallic fins and using graphite as an additive. The experimental tests demonstrate that both methods considerably improve heat transfer and data obtained was used to quantify these effects. In addition, the computational fluid dynamics (CFD) simulations were carried out to evaluate the thermal performance of the metallic alloy and solar salt TES systems with different concentrations of additives and number of fins in terms of the evolution of the liquid fraction and amount of energy stored

and released during charging and discharging processes as a function of time. The comparison of numerical and experimental results demonstrated the acceptable accuracy of the developed CFD models. Both experimental and numerical results were used to derive dimensionless correlations for estimation of the heat transfer intensity and time required for charging and discharging of the studied TES systems. These generated dimensionless correlations can be successfully used in engineering practice to design TES systems.

Publications

1. COSTA, S.-C., MAHKAMOV, K., KENISARIN, M., ISMAIL, M., LYNN, K., HALIMIC, E., & MULLEN, D., "*SOLAR SALT LATENT HEAT THERMAL STORAGE FOR A SMALL SOLAR ORGANIC RANKINE CYCLE PLANT*," Journal of Energy Resources Technology, March, vol. 142, no. 3, 2020.
2. COSTA, S.-C., M., ISMAIL, KENISARIN, M., MAHKAMOV, K., MULLEN, D., HALIMIC, E., & LYNN, K., "COMPARATIVE *STUDY OF TWO TYPES OF MEDIUM TEMPERATURE PHASE CHANGE MATERIALS,* " WIT Transactions on Ecology and the Environment 237: 37-49, 2019.
3. COSTA, S.-C., MAHKAMOV, K., KENISARIN, M., ISMAIL, M., HALIMIC, E., MULLEN, D., LYNN, K. & WERNER, T. "*EXPERIMENTAL AND NUMERICAL STUDY ON MELTING OF SOLAR SALT IN A FINNED METALLIC CONTAINER*," Proceedings of the 14th International Mechanical Engineering IMECE14, November, 9-15, 2018, Pittsburgh, PA, USA.

Table of Contents

List of Figures

List of Tables

Acknowledgment

First and foremost, I must thank Almighty Allah for giving me the courage, determination, and guidance in conducting this work.

My special thanks go to my supervision team Prof. Khamid Mahkamov and Dr. Murat Kenisarin and Dr. C. Costa for their invaluable guidance, encouragement, and support over the duration of this work.

I deeply appreciate the moral support of my brother Mahmoud who was always willing to help and give me his best suggestions, for what he had done to me over three years.

I am indebted to all members of my family who contributed in one way or another to drive me to succeed in my academic pursuit at Northumbria University.

Mohammad Ismail
Northumbria University
October 2019

Declaration

I declare that the work contained in this thesis has not been submitted for any other award and that is all my own work. I also confirm that this work fully acknowledges opinions, ideas, and contributions from the work of others.

I declare that the Word Count of this Thesis, excluding bibliography and appendices, is 30781 words.

I declare that this project has been through ethical clearance.

Name: Mohammad Ismail

Signature:

Date: October 2019

Nomenclature

A	Surface area (m^2)
C	Constant
C_p	Heat capacity (J/kg K)
$\|v\|$	Absolute velocity
E	Volumetric heat sources
E_f	Fluid total energy
E_s	Solid region total energy
F	External force (N)
Fo	Fourier number, $(\alpha t/N^2)$
g	Gravitational force (m/s^2)
G	Generation of energy
G_ω	Generation of specific dissipation rate
H	Heat of fusion (kJ/ kg)
h	Sensible enthalpy (kJ/ kg)
HTC	Heat transfer coefficient (W/m^2 °C)
I	Unit tensor
$\vec{J}$	Diffusion flux
k	Thermal conductivity (W/m· K)
L	Length of heat source (m)
M	Mass (kg)
N	Half of the height
$\overline{\mathrm{Nu}}$	Average Nusselt number
n	Thickness of porous media
O	Inertial resistance factor
P	Pressure (Pa)
Pr	Prandtl number
P_γ, E_γ	Transition sources
Q	Power (W)
$Q_{cooling}$	Heat transfer during cooling of liquid PCM (W)
$Q_{heating}$	Heat transfer during heating of solid PCM (W)
Ra	Rayleigh number
S_h	Heat of chemical reaction
S_k, S_ε	User-defined source terms
ST	Storage capacity (kJ)
Ste	Stefan number ($C_p\,\Delta T/H$)

T	Temperature (K, °C)
U	X-velocity (m/s)
V	Y-velocity (m/s)
W	Z-velocity (m/s)
X	Direction in x
Y	Direction in y
Z	Direction in z
Y_M	Contribution of the fluctuating dilatation
Y_k	Dissipation rate of k
Y_ω	Dissipation rate of ω

Greek symbols

α	Thermal diffusivity (m^2/s)
β	Coefficient of volumetric expansion (1/K)
μ	Dynamic viscosity (N/m^2 s)
v	Kinematics viscosity (m^2/s)
ρ	Density (kg/m^3)
λ	Liquid fraction
Ω	Permeability
Γ_k	Effective diffusivities of k
Γ_ω	Effective diffusivities of ω
σ_k	Turbulent Prandtl numbers for k
σ_ε	Turbulent Prandtl numbers for ε
τ	Dimensionless time number (Fo* Ste)
ς	Stress tensor
ξ	Medium porosity
Y	Mass fraction

Subscripts

b	Kinetic energy generation from buoyancy effects
eff	Effective
j	Specie
tke	Turbulent kinetic energy
l	Liquid
m	Melting
o	Reference value
w	Wall
t	Time
Exp	Experimental
Num	Numerical

Acronyms

TES	Thermal energy storage
SHS	Sensible heat storage
LHS	Latent heat storage
LTES	Latent thermal energy system
CHS	Chemical heat storage
CESS	Chemical energy storage system
LHTESS	Latent heat thermal energy storage system
PCMs	Phase change materials
Paraffin	PA
OPCMs	Organic phase change materials
IOPCM	Inorganic phase change materials
NEPCM	Nano-enhanced phase change material
NF	Number of fins
MPCMs	Microencapsulated Phase change materials
CS-PCMs	Core-shell phase change materials
SS-PCMs	Shape-stabilized phase change materials
ENG	Expanded natural graphite
EG	Expanded graphite
HTF	Heat transfer fluid
CSP	Concertation solar power
DSC	Differential scanning calorimetry
STA	Synchronous Thermal Analyser
TG	Thermogravimetric
AHFM	Algebraic Heat Flux Model
PMLH	Prediction Model of Latent Heat
FT-IR	Fourier transformation infrared spectroscopy
XRD	X-ray diffraction
SEM-EDX	Scanning Electron Microscopy
RE	Regulator
PA	Power analyser
PMLH	Prediction Model of Latent Heat
DL	Data Logger
PT	Thermocouple position
NS	Navier-Stokes
ES	Eddy Simulation
LF	Liquid fraction
EVM	Eddy Viscosity Models
DNS	Direct Numerical Simulation

SST	Shear-Stress Transport

Chapter 1 Introduction

1.1 Motivation

Since the industrial revolution, the growing demand for energy production has led to increased carbon dioxide emissions released into the atmosphere. As a result of this, there are higher levels of greenhouse gases, affecting the climate. Thus, finding alternative methods to satisfy the daily demand for energy has become imperative [1]. The focus has, therefore, shifted towards renewable energy sources, such as wind, solar, geothermal and hydropower. Among those resources, solar energy is prominent because it cannot be depleted, it is cost-effective to harness and has a low carbon footprint. Various methods have been developed to utilize solar energy, involving thermal energy storage (TES) systems [2].

The use of TES systems is an efficient technique for storing thermal energy by altering the temperature of the storage medium in a narrow temperature range. The stored energy can be utilized later to balance between supply and demand, as heat and/or power production [3].

TES systems can be classified into three main categories; sensible heat storage (SHS), latent heat storage (LHS) and chemical heat storage (CHS) systems.

In SHS systems energy is stored or released by increasing or decreasing the temperature of the storage medium whether it is solid or liquid, for instance, water-rock beds and molten salt. The SHS system depends mainly on the specific heat of the medium, the

temperature difference and the quantity of storage material. However, it requires a large space since the specific heat values are relatively low [2, 4].

In chemical energy storage systems (CES) the thermal energy can be absorbed or released during chemical reactions taking place between various materials [5].

In LHS systems energy is stored or released by increasing or decreasing the temperature of the medium, which changes its phase at a constant or nearly constant temperature. During the phase change, the state of the material usually changes from solid to liquid, or liquid to vapour. Using phase change materials (PCMs) is considered to be an efficient technique of storing the thermal energy due to high values of latent heat of the materials [2].

Among the above three types of TES systems, using LHS systems is considered to be an efficient and feasible method to store a large amount of thermal energy in small spaces. For example, LHS systems can deliver 5-10 times more heat than SHS systems of the same size, due to a large amount of energy released during melting and solidification processes [6, 7].

PCMs undergo solid-solid, solid-liquid or liquid-gas transitions depending on the temperature ranges. The phase change materials with solid-liquid transition are the most commonly used for various applications. Such PCMs are categorized into three main groups: organic PCMs, which include paraffin and non-paraffin; non-organic PCMs, which include salt hydrates and metallic and eutectic PCMs; and compound PCMs consisting of two or more substances [8, 9]. One of the main disadvantages of PCMs is their low thermal conductivity, which reduces the system response in absorbing or releasing energy [10].

Hence, the Renewable Energy Group, led by Prof Mahkamov in Mechanical Engineering Department of Northumbria University has been working on building efficient TES systems with the use of PCMs with enhanced thermal conductivity. This research was also conducted as a part of Horizon 2020 research and innovation project "INNOVA MICRO-SOLAR" and Marie Sklodowska-Curie Action project "Thermostall", funded by the European Commission. One of the main problems in building TES systems with non-metallic PCMs is their low thermal conductivity. The main disadvantages of metallic PCMs are their relatively high cost and density. Therefore, the motivation for this research was to improve the thermal conductivity of non-metallic PCMs through the use of extended surfaces or deployment of graphite additives in TES systems for application in solar power plants operating at the temperature range of 215-250 °C and to investigate the thermal performance of the TES system with low purity metal alloy PCM for low-temperature applications in the temperature range of 120-140 °C. Finally, the research was intended to develop the engineering method to evaluate the thermal performance of TES systems. It was planned to generate correlations to calculate the variations in the LF of PCMs as a function of time, depending on the design parameters and operating conditions in TES systems during charging and discharging processes.

1.2 Research Aims and Objective

This research focuses on intensification of the heat transfer in the latent heat thermal energy storage system (LHTESS) to accelerate the charging and discharging processes and on the evaluation of the potential for using metal alloys as PCMs. The study is confined to the detailed investigation of a single Bi-Sn metal alloy sample and solar salt to determine their applicability for low- and medium-temperature applications. The

influence of using extended surfaces and additives on the thermal performance of the TES system with solar salt was studied both experimentally and numerically (using computational fluid dynamics - CFD). Also, the thermal performance of the thermal storage with the metal alloy is addressed (both experimentally and numerically). Dimensionless correlations to describe the operation of thermal storage systems were derived using obtained data, which then can be deployed for designing purposes.

The aim of the work is to investigate the heat transfer in thermal energy storage systems with PCMs and evaluate methods of its intensification for systems with a PCM with low thermal conductivity.

The research objectives are as follows:

i. To investigate the thermo-physical properties of PCMs, namely solar salt, and the Bi-Sn metallic alloy

ii. To develop the experimental rig to investigate the performance of the TES system with PCMs.

iii. To evaluate experimentally the intensification of heat transfer using extended surfaces and additives in the TES systems with solar salt.

iv. To assess the potential applicability of using the low purity Bi-Sn metallic alloy as a PCM using the test rig.

v. Validate the deployed CFD model against obtained experimental results and refine the theoretical model if required.

vi. To use the CFD model of the TES system to compare different intensification techniques.

vii. To derive dimensionless correlations for describing the operation of TES systems to assist in their design process.

1.3 Methodology

The research will be conducted using both experimental and numerical investigations of the thermal performance of the TES system.

1.3.1 Experimental Investigations

Experimental investigations will be carried out to study the thermo-physical properties of metallic alloys and metallic hydrates as PCMs for the use in TES systems for low and medium temperature ranges, respectively.

Aavid Thermacore Ltd. provided some materials and supported with the experimental setup. The experimental work was conducted to investigate the thermal performance of the TES systems for various rates of energy input.

1.3.2 Numerical Investigations

Numerical investigations are conducted to investigate the performance of the TES system with PCMs (the metallic alloy and salts). A 3-D CFD model of the TES systems was developed in ANSYS/Fluent software. The validation of the numerical results was carried out using experimental results to refine the numerical model. Finally, the numerical model is used to generate data for the derivation of dimensionless correlations to describe the operation of TES systems, which could be used during the designing stage.

1.4 Originality and Contribution to Knowledge

The performed literature review demonstrated that the data obtained in previous studies are not applicable for evaluation of the thermal performance of TES systems. Therefore, a study of TES systems with solar salt and low purity metal alloy was carried out to develop engineering methods for the evaluation thermal characteristics of TES system such as PCM melting and solidification times as well as accumulated and released energy during charging and discharging processes.

1.5 Thesis structure

This thesis consists of the following chapters:

- Chapter 1, Introduction: This chapter, providing motivation for this research and introduction to the work undertaken in this study.
- Chapter 2, Literature Review: This chapter provides a comprehensive review of existing research related to the TES system using PCMs. The review highlights the various techniques to intensify the heat transfer and information on different PCMs and container materials and their design.
- Chapter 3, Experimental Set-up: The equipment, instrumentation, experimental procedures and data handling processes are described.
- Chapter 4, Experimental Results: The experimental results for different intensifications techniques deployed in the TES system with solar salt, solar salt with 10 wt% graphite, 4-fin design with solar salt and the metal alloy are presented for charging and discharging processes.

- Chapter 5, Data Analysis: This chapter focuses on data analysis and generation of dimensionless correlations for the Nusselt, Fourier and Stephan, Prandtl and Rayleigh numbers to describe processes in TES systems.
- Chapter 6, Methodology of CFD Modelling: This chapter presents the governing equations of the CFD modelling to simulate TES system using PCM. In addition, the selection of the numerical model such as laminar and turbulent flows, the heat transfer processes during melting and solidification of PCMs was presented.
- Chapter 7, CFD Model Validation and Methodology: In this chapter, the numerical model is validated against experimental measurements. A refined new numerical model was proposed for a comparison between different intensification techniques. Finally, dimensionless correlations to describe the thermal performance of TES systems during charging and discharging processes were carried out.
- Chapter 8, Conclusion and Future Recommendations: This chapter describes the main findings of the present study and recommendations for further work.

Chapter 2 Literature Review

2.1 Introduction

The first practical application of PCMs was carried out in 1978 by Telkes [1] with the use of sodium sulphate dehydrate. The first heated solar house using PCM was investigated by storing thermal energy through recirculating air. During the daytime, the air temperature rises, causing a phase change (from solid to liquid) transition when the temperature exceeds the melting temperature. In contrast, during the night-time, the air temperature drops below the melting temperature due to heat losses to the environment; resulting in the release of the stored energy during the phase transitions from liquid to solid. The phase change typically occurs at the constant temperature and the phase transitions are referred to as endothermic and exothermic reactions for the solid to liquid and liquid to solid transitions, respectively [2, 3].

PCMs have different melting temperatures that can be categorized into low, medium and high. PCMs ideally should have high latent heat, density, specific heat, and thermal conductivity to store large amounts of energy and not to be prone to super-cooling. In addition, they should vary little in the volume during the phase transition. Finally, PCMs preferably should be non-corrosive, non-hazardous, with affordable cost [1].

2.2 Classification of PCMs

Generally, PCMs are classified into three main groups that depend on their composition. Figure 2-1 indicates the groups of PCMs that are summarised into Organic, Inorganic, and Eutectic PCMs [2].

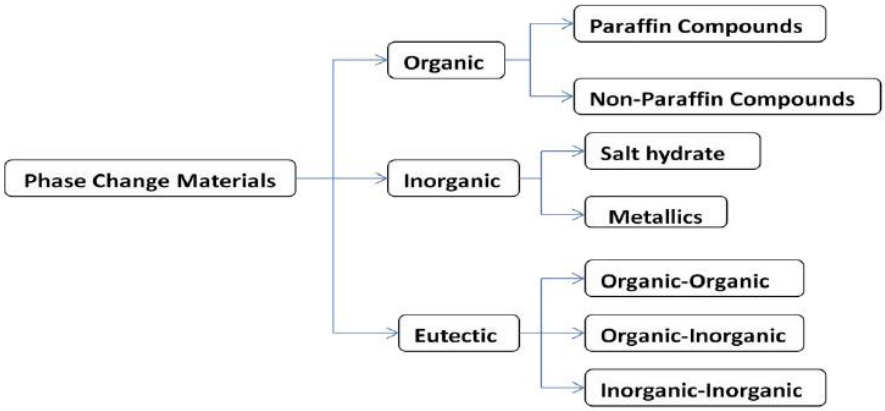

Figure 2-1: Classification of PCMs [2].

2.3 Organic phase change materials (OPCM)

Organic PCMs consists of paraffin (PA) and non-paraffin materials. The PA materials consist of saturated hydrocarbons (C_nH_{2n+2}) [3]. Non-paraffin materials include esters, glycols, fatty acids and alcohols [4]. Generally, the Organic phase change materials (OPCMs) have high latent heat of fusion, thermal and chemical stability and do not exhibit the super-cooling property. However, they have low thermal conductivity.

Numerous studies have been conducted to enhance the thermo-physical properties of OPCMs. Modern methods use various additives, which enhance the thermo-physical properties of the mixture. For example, graphene nano-platelets were used in [5] to

enhance the thermo-physical properties of organic alkane n-eicosane and n-eicosane were investigated numerically using the enthalpy-porosity model.

The melting process of paraffin wax with nanoparticles (Al_2O_3) in the LHS unit was carried out in [6]. The system with several identical vertical slabs of the nano-enhanced PCM, separated by rectangular channels with the heat transfer fluid, HTF (water), was explored numerically. The governing equations and the effect of natural convection were adopted in the numerical scheme and were solved using the finite volume method. The volumetric fraction of additives, type of the HTF and its inlet temperature were investigated to determine their influence on the thermal performance of the system.

The melting of nano-enhanced PCM was investigated numerically in [7]. The RT50 material with copper particles was used inside the shell and tube heat exchanger. Various dispersion ratios ($\emptyset = 0, 0.03, 0.05$) were used and the melting time, liquid fraction and penetration length were measured. The enthalpy porosity model, pure conduction and natural convection were all considered. The results showed that the rate of heat transfer in the heat exchanger was mainly affected by the inlet temperature of the HTF. On the other hand, it was shown that the mass flow rate has an insignificant influence.

The latent thermal energy system (LTES) containing PA and the copper foam was studied in [8]. A 3D numerical model, based on the enthalpy porosity model and the melting/solidification models, was used to evaluate the performance of LTES during the charging and discharging. The results of this numerical study were compared with experimental data and yielded a good agreement, which is shown in Figure 2-2.

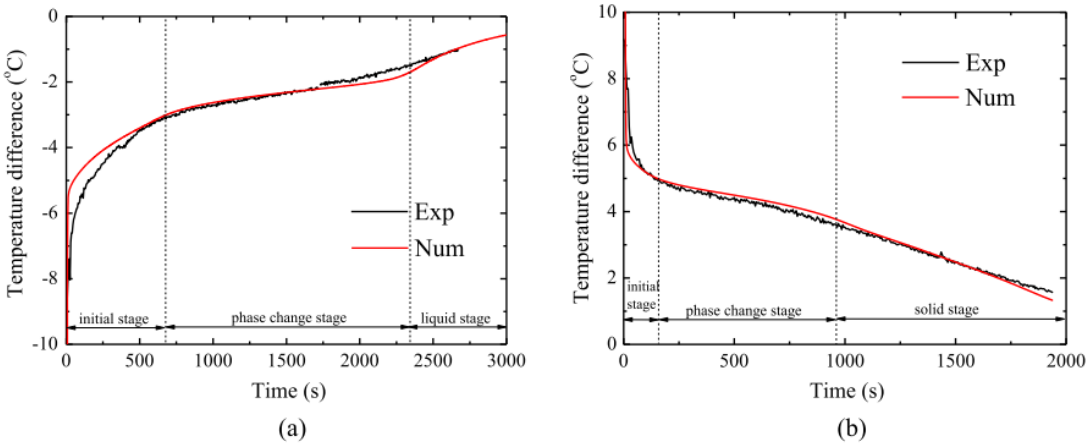

Figure 2-2: Comparison of the experimental and numerical results of the temperature difference of the HTF between (a) the inlet; (b) the outlet [8].

The composite PCM was found to enhance the thermal performance of LTES and thermal energy utilization. In addition, the higher inlet flow velocity and the temperature difference between the HTF and the PCM could enhance the heat transfer.

The solidification process of a triplex-tube system was investigated in [9]. Water was used as the HTF. PA wax was deployed with a porous medium (copper foam) and with impregnation by aluminium nano-particles. It was found that the results for PA with copper foam and with aluminium nano-particles were close to each other because the heat conduction was dominant in the solidification process.

The results indicated that the solidification time decreased significantly when the porous copper was used and that it could be further reduced using aluminium nano-particles. The findings of the study are summarized in Table 2-1.

Table 2-1: Comparison of melting time for three enhancement approaches: nanoparticles only, porous foam only and compound (nanoparticles & porous foam) [9].

Ø	**Time to reach a complete melting in (minutes)**			**% Total time saving**		
	Non-porous	**ε =0.98**	**ε =0.95**	**Non-porous**	**ε =0.98**	**ε =0.95**
0.00	403	106	16	0.0	73.7	95.7
0.01	386	102	15	4.2	74.7	96.2
0.03	371	99	15	7.9	75.4	96.2
0.05	353	95	15	12.4	76.4	96.2
0.08	324	90	14	19.6	77.7	96.5

The vertical shell and tube LHTES system, fabricated using two concentric aluminium tubes, was studied in [10]. Water and aluminium metal foam with paraffin PCM were used in the experiments. The local thermal non-equilibrium and enthalpy porosity models were adopted to explore the temperature performance between the HTF and the PCM. Various porosities were used in the experiments, the results of which are depicted in Figure 2-3.

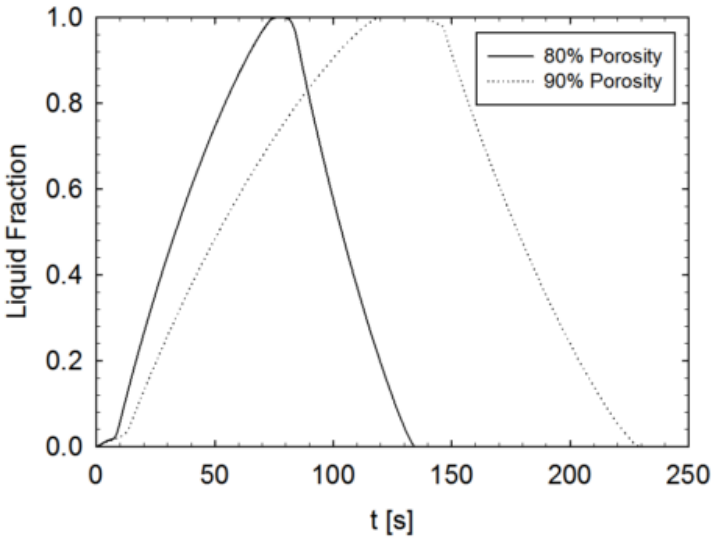

Figure 2-3: Comparison between experiments with two different porosities in terms of a liquid fraction [10].

The duration of the melting time of PA wax with Al_2O_3 nanoparticles, inside vertical channels of the LHS unit was determined numerically in [11]. The heat and flow characteristics were investigated using a 2D mathematical model and the enthalpy porosity model. A model, to take into account the effects of the additives volumetric fraction, Reynolds and Rayleigh numbers on flow and thermal performance, was developed to predict the melting time of nano-enhanced PCM (NEPCM) and was compared with data in the open literature. Figure 2-4 summarises the key findings of the study.

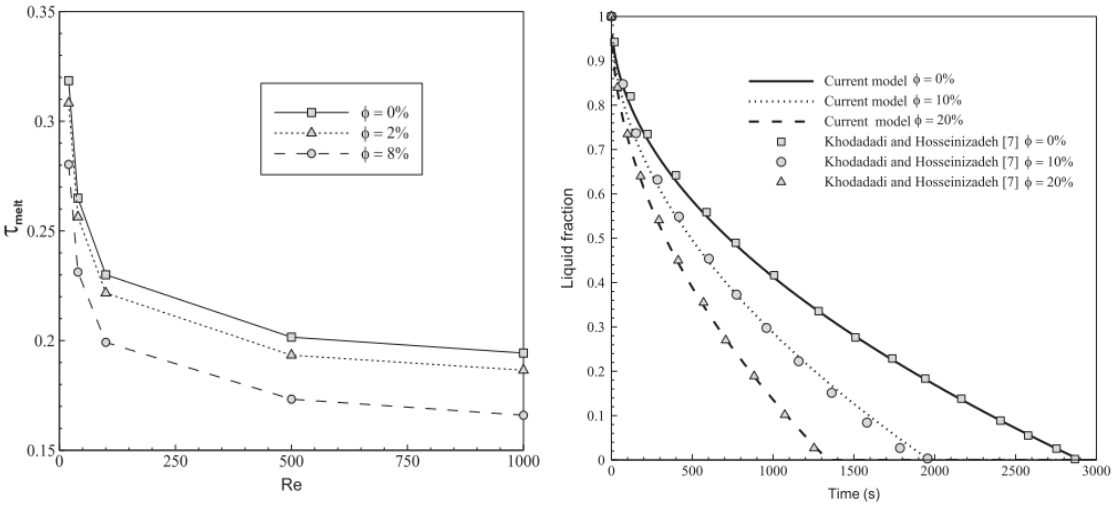

a) b)

Figure 2-4: Effect of the Reynolds number on the melting time for various volumetric fractions of nanoparticles (a) and instantaneous variation of the liquid fraction of NEPCM: comparison with the literature (b) [11].

The thermal behaviour of vertical and horizontal heat exchangers using combined models of conduction and convection heat transfer were investigated numerically in [12]. The results were compared to published experimental data. The study showed that the horizontal orientation had a better thermal performance than the case with vertical orientation and that the charging time was affected by the increase in the inlet temperature of HTF. The effects of orientation on the charging and discharging times and liquid fraction are shown in Figure 2-5 and Figure 2-6.

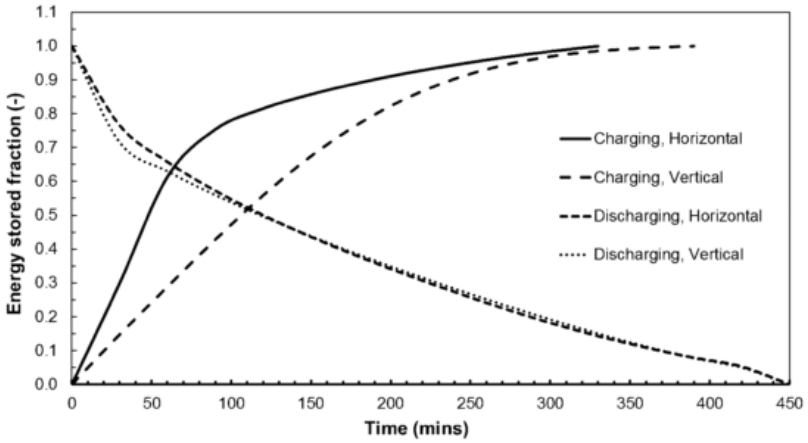

Figure 2-5: Comparison of the energy stored fraction in the horizontal and vertical systems during the charging and discharging processes [12].

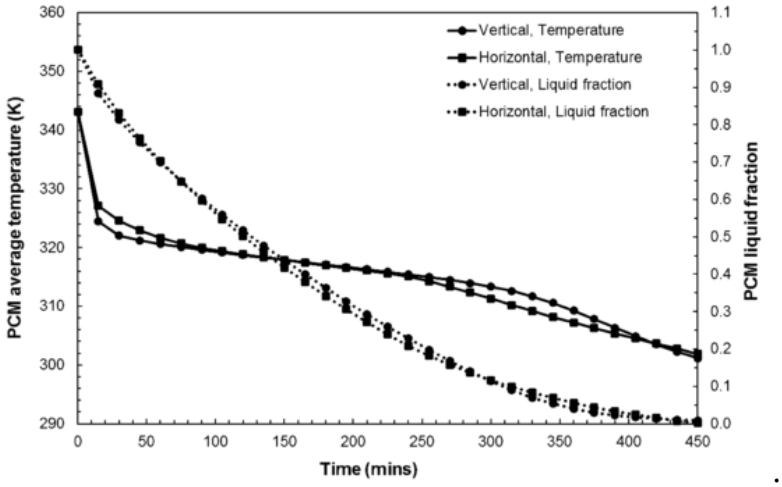

Figure 2-6: PCM average temperature and liquid fraction in the vertical and horizontal units during the discharging process [12].

2.4 Inorganic phase change materials (IOPCM)

Inorganic PCMs are divided into salts and metals and have high phase change enthalpy, wide melting temperature range with double heat storage capacity in comparison to the OPCM.

2.4.1 Salt and salt hydrate

The chemical compound of salt hydrates can be expressed as $A_xB_y.n\ (H_2O)$, where A_xB_y represents metal carbonate, phosphate, sulphite, acetate, nitrite or chloride, and n represents water molecules. Generally, salts and salt hydrates suffer from low thermal conductivity, and super-cooling during solidification process and cause corrosion [13].

Numerous research studies were performed to investigate the thermal properties of salts and salt hydrates to improve their thermal conductivity [13]. Investigation of the melting temperature of the salts and salt hydrates is also performed in the selection process.

Different techniques were investigated to enhance their thermal conductivity and control the melting and solidification processes. For instance, extended surface fins and additives were considered suitable techniques [14]. Table 2-2 tabulated some of the salts and salt hydrates with their melting temperature and heat of fusion.

Table 2-2 The prospective salt and salt hydrates with their thermal properties [15].

Compound	**Melting temperature (°C)**	**Heat of fusion (kJ/ kg)**	**Compound**	**Melting temperature (°C)**	**Heat of fusion (kJ/ kg)**
Salts			Salt Hydrates		
$AlCl_3$	192	280	$Na_2P_2O_7 \cdot 10H_2O$	70	184
$LiNO_3$	250	370	$Ba(OH)_2 \cdot 8H_2O$	78	266
$NaNO_3$	307	172	$(NH_4)Al(SO_4)_2 \cdot 12H_2O$	95	269
KNO_3	333	266	$MgCl_2 \cdot 6H_2O$	117	169
KOH	380	150	$Mg(NO_3)_2 \cdot 6H_2O$	89.9	150
$KClO_4$	527	1253			
LiH	699	2678			
$MgCl_2$	714	452			

A new composite material with enhanced thermo-physical properties, intended for solar thermal energy storage was investigated experimentally in [16]. The new composite material was prepared by mixing the salt ($LiNO_3$) with a different mass fraction of industrial graphite (graphite waste) from 0 to 20 wt% and the thermo-physical properties were measured and tabulated. The graphite has good resistance to corrosion and chemically stable and therefore it is considered to be a suitable material for PCMs applications.

In addition, the thermo-physical properties, such as thermal conductivity and thermal diffusivity were measured in [16] for the material with various graphite mass fractions, using transient hot wire apparatus and the flash method respectively, which the thermo-physical properties improved with increasing the mass fraction of graphite. Further

research was suggested to determine the melting temperature for different mass fractions of the composite material.

Various types of molten salts for concentrated solar power (CSP) applications were reported in [17]. For instance, pure molten lithium, sodium and potassium nitrates, solar salt ($NaNO_3$/KNO_3: 60/40) and HITEC (a ternary mixture of $NaNO_3$, KNO_3, and $NaNO_2$) were tested and had their properties such as melting point, density, viscosity, heat capacity, and thermal conductivity studied. Figure 2-7 shows the melting temperature of the pure alkali nitrates along with some other mixtures.

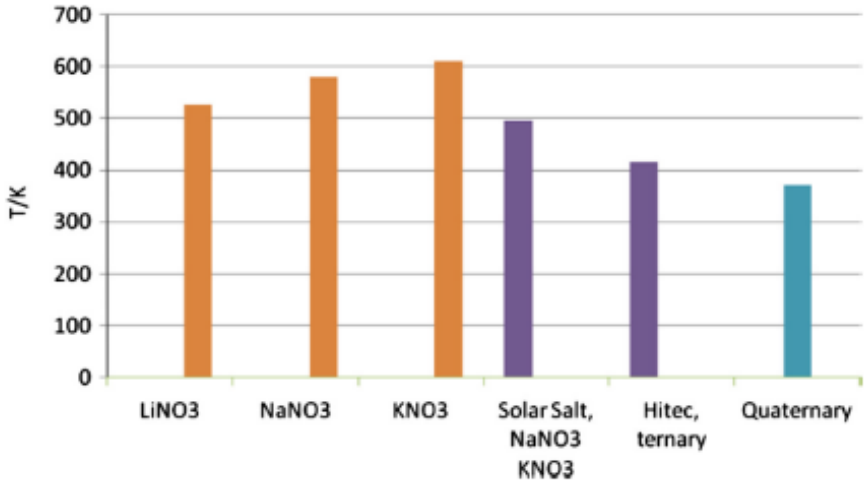

Figure 2-7: The melting temperature of some IOPCMs [17].

In addition, thermo-physical properties were also tabulated and reported. It was observed in the literature that molten salts were considered to be suitable as working fluids of TES systems. Furthermore, it was also found that there was a distinct lack of studies in the literature, regarding the thermal properties of multicomponent mixtures, compared to pure salts.

The melting temperature of various salts was studied in [18] with several cooling and heating rates. The sodium, potassium and rubidium nitrates were selected for investigation of the crystallization and melting points, using Differential scanning calorimetry (DSC). The melting and crystallization temperatures and enthalpy changes for various heating and cooling rates are shown in Figure 2-8.

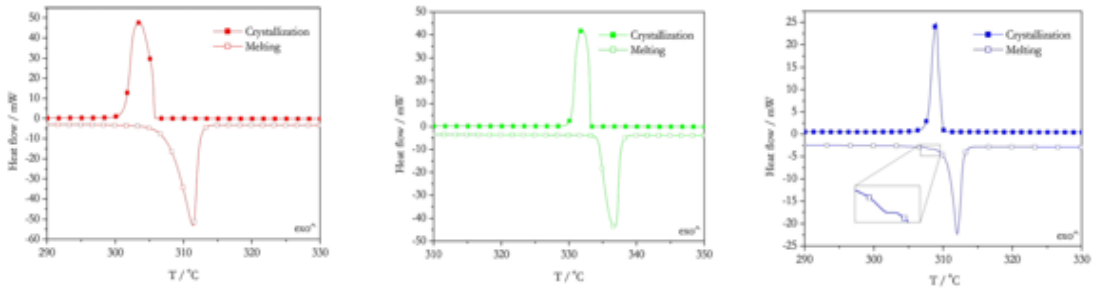

a) b) c)

Figure 2-8: Typical DSC curves of the crystallization and melting of sodium nitrates a) potassium nitrate b) and rubidium nitrate c) for heating and cooling rates of 5 °C/min [18].

A small super-cooling (< 0.5 °C) of sodium nitrates was demonstrated compared to the crystallization of indium (< 2.0 °C).

The heat capacities of $NaNO_3$ and KNO_3 were experimentally investigated in [19] for the temperature range of 350-800 K using DSC. The solid-solid transitions and melting temperatures were obtained at 550, 583 and 406, 612 K for $NaNO_3$ and KNO_3, respectively. Table 2-3 summarised the thermodynamic properties of transitions in $NaNO_3$ and KNO_3.

Table 2-3: Thermodynamic parameters of transitions in $NaNO_3$ and KNO_3 [19].

Compound	Tt (K)	ΔHt (kJ/ mole)	ΔSt (J/ k mole)
$NaNO_3$	500	4.42 ± 0.13	8.43±0.25
KNO_3	406	5.64±0.17	13. ±0.4

An open-cell polyurethane foam (PU foam) as a heterogeneous surface was introduced in [20] to mitigate the problems of salt hydrates, such as phase segregation, low thermal conductivity, density and voids that trap air. It was prepared by encapsulating the OPCM into PU foam. Sodium sulfate anhydrous and magnesium sulfate heptahydrate were used in the experiments which were performed in the temperature range of 6-24 ℃ for the cooling and heating cycles. The study found that the melting process occurred at 38 ℃. Figure 2-9 shows the results of the various experiments for different values of the foam thickness.

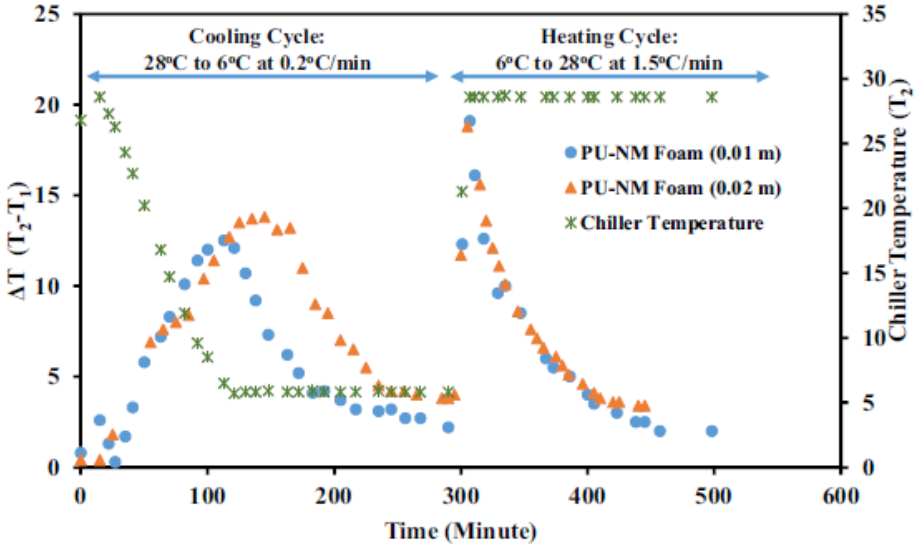

Figure 2-9: Heating and cooling cycles for various foams [20].

The dispersion of alumina nanoparticles was used in [21] in order to enhance the solidification in the triplex-tube where various volume fractions were used at constant charging temperature. Moreover, nanoparticles based on aluminium were used in [22] for developing a new type of eutectics based on salt hydrates using various volume mass ratio of the additives.

2.4.2 Eutectic salts

Eutectic salt is a combination of two or more different salts. Generally, the new compound's melting temperature is lower than that of the original salts [13].

A binary salt consisting of calcium nitrate and sodium nitrate with different mole fractions was explored in [23] to obtain an economically feasible PCM. It was found that the exothermic peaks for all binary mixtures were at 220 °C and that the enthalpy could be improved by increasing the ratio of $NaNO_3$. A summary of various kinds of molten salts applicable at temperatures under 300 °C is shown in Table 2-4.

Table 2-4: Summary of various molten salt [23].

Materials (mole %)	**Melting point (°C)**	**Heat of fusion (kJ/kg)**
$LiNO_3$	253	373
(28.5–28.9)LiCl–(43.5–44.5)CsCl–(13.7–14.1)KCl	256±2.5	375-380
(13.3–13.5) RbCl	270	167
59.15LiCl–40.85$Ca(NO_3)_2$	264	437
63LiOH–38LiCl	274	339
65.5LiOH–34.5LiCl	133	170
33$LiNO_3$–67KNO_3	105	110
29$LiNO_3$–17$NaNO_3$–49.4KNO_3–4.6$Sr(NO_3)_2$	166	272
58.1$LiNO_3$–41.9KCl	193	248
57$LiNO_3$–43$NaNO_3$	169–171	202–213
50NaOH–50KOH	210–216	278–329
30LiOH–70NaOH	230–232	206–252
20NaOH–80$NaNO_2$	237–238	249–295
73NaOH–27$NaNO_2$	291	283
87.3NaOH–6.1NaCl–6.6Na_2CO_3	208	369
87$LiNO_3$–13NaCl	287	177
86.3$NaNO_3$–8.4NaCl–5.3Na_2SO_4	142	80

Several samples were prepared using $Ca(NO_3)_2$ and $NaNO_3$ at various mass ratios, for which properties are presented in Table 2-5.

Table 2-5: Melting temperature and latent heat of fusion [23].

Molar ratio (Ca:Na)	Onset (°C)	Observed enthalpy (kJ/kg)
9-1	217.7	10.4
8-2	219.4	21.2
7-3	218.6	44.6
6-4	221.0	78.3
5-5	218.8	81.3
4-6	210.62	90.7
3-7	217.4	135.8
2-8	219.2	157.2
1-9	221.9	164.9

A ratio of 3-7 was investigated and found to form better compounds. The reason behind that is its low cost, high latent heat of fusion, thermal stability and lesser corrosion effect towards steel and aluminium alloys. Its thermal conductivity and the economic cost were estimated to be 0.496-0.516 W/m k and $ 409 per metric ton, respectively.

The binary salts, $NaNO_3$–$LiNO_3$ (46–54%) and $NaNO_3$–$LiNO_3$ (40–60%) were investigated in [24] to estimate their potential for medium temperature solar thermal storage applications. Figure 2-10 shows selected nitrate and chloride salts and their eutectics with their melting temperatures and latent heat of fusion.

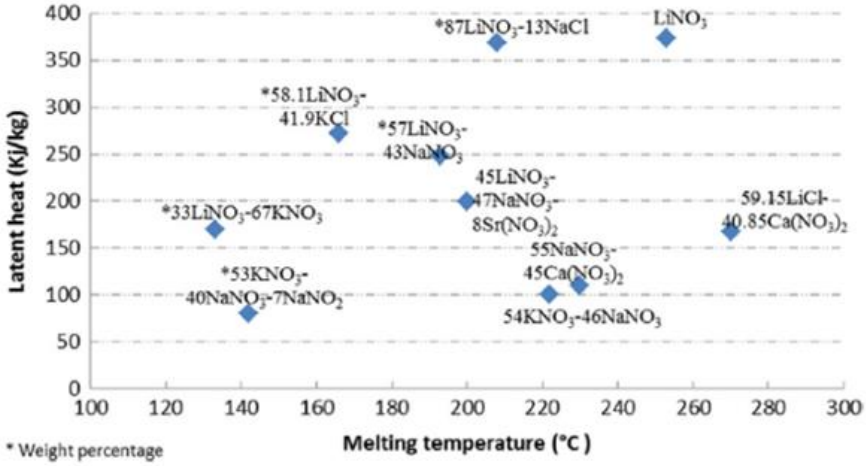

Figure 2-10: Latent heat and melting temperatures of IOPCMs [24].

The study found that the thermal repeatability of $NaNO_3$–$LiNO_3$ (46–54%) is superior to that of $NaNO_3$–$LiNO_3$ (40–60%) binary salt and that the melting temperatures were 193.87 °C and 193.27 °C, respectively. Furthermore, it was shown that both eutectics work well under 450 °C and that the mole fraction of $NaNO_3$ in the eutectic mixture controls the melting process.

The thermal behaviour of $LiNO_3$–NaCl (87–13%) for LHS in a medium temperature range was studied in [25]. DSC was used to evaluate the melting temperature and the latent heat of fusion. The eutectic mixture was made by heating it up to 150 ℃ for 30 minutes. To test its reliability, the sample was heated up and cooled down in the temperature range between 50-250 ºC.

In addition, the melting temperature and latent heat of fusion were measured to be 220 ℃ and > 290 kJ/kg, respectively. Furthermore, the thermal decomposition temperature of the eutectic salt was found to be in the range of 400-450 ℃ and therefore the substance was considered suitable for medium temperature latent heat storage systems. Finally, it was concluded that steel 316 was suitable for mitigating the corrosion phenomena.

Numerical and experimental investigations of the mixed convection heat transfer in molten salts inside horizontal square tubes under various side heating conditions were carried out in [26]. The mass flow rate, Nusselt and Reynolds numbers were enhanced with increasing the pump speed. The vortexes were created by a buoyancy force on two heated sides. Figure 2-11 shows the wall temperature distribution for different heat fluxes.

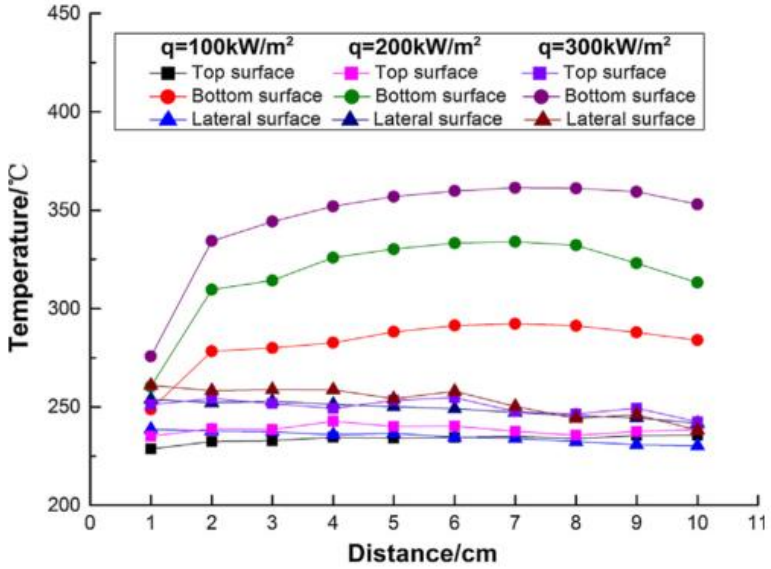

Figure 2-11: Wall temperature distribution for different heat fluxes [26].

The thermal energy performance of solar thermal power using a molten salt thermocline thermal storage system with a packed PCM was investigated in [27]. The transient 2-D model was used and simulation results revealed that the molten salt with packed PCM has a high heat storage density. The melting point, the effective discharging energy, and efficiency were all found to increase because of increasing the PCM content. Figure 2-12 shows the outlet temperature evolution of the thermocline system with PCMs of different melting points.

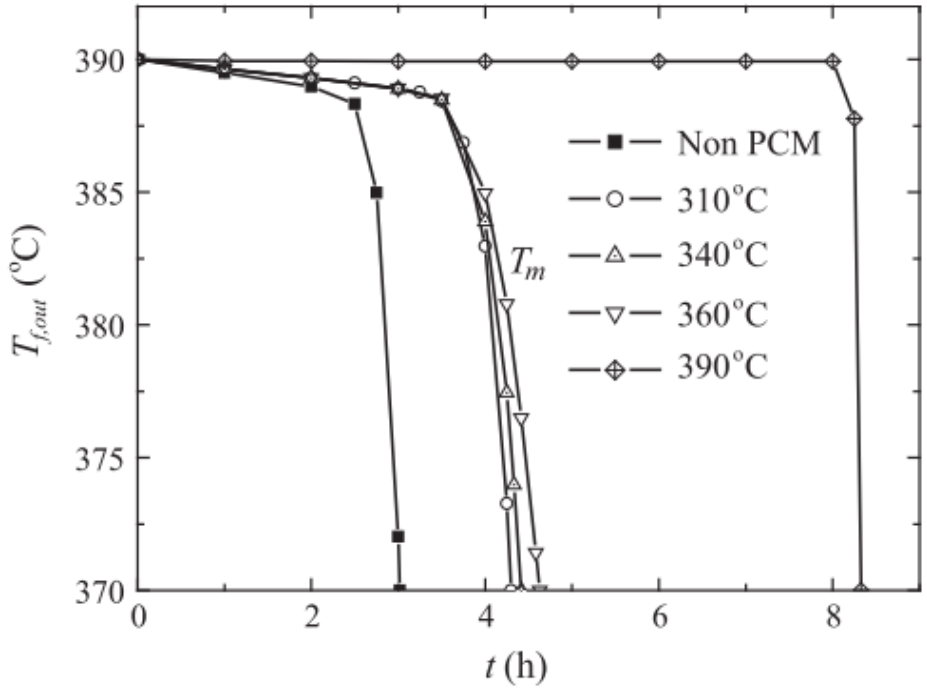

Figure 2-12: Outlet temperature evolution in the thermocline system with PCMs of different melting points [27].

A new binary mixed molten salt made of KNO_3-$Ca(NO_3)_2 \cdot 4H_2O$ with various mixing ratios was optimized in [28]. DSC, Synchronous Thermal Analyser (STA) and Thermo-gravimetric analysis (TGA) were used to experimentally measure the thermo-physical properties of the binary salt. Also, various mole fractions of calcium nitrate were investigated.

It was found that the mixture reaches the eutectic point and its melting temperature remained regular when the mole fraction of KNO_3 and $Ca(NO_3)_2 \cdot 4H_2O$ was 0.57:0.43. The thermo-physical properties, of the binary salt, were compared with solar salt and HITEC salt and presented in Table 2-6.

Table 2-6: Comparisons between different salts [28].

Salt mixture	Melting point (℃)	Decomposition temperature (℃)	Density at 500 (℃)	specific heat (J/g·K)	Thermal conductivity (W/m·K)	Storage cost ($·kW·h)
Solar salt	220	565	1.752	1.500	0.52	5.8
HITEC salt	142	535	1.723	1.400	0.35	10.7
binary salt	116.9	569.7	1.835	1.497	0.55	5.7

The results show that the new binary salt is competitive and promising for applications in concentrated solar power plants.

Thermo-physical properties of lithium-nitrate salt for TES systems as HTF were explored in [29]. It is considered a good candidate for enhancing the salt mixture's working temperature range for SHS systems. The study in [29] confirmed that the presence of oxides was found (corrosion) which reduced the heat capacity by 8-20%. In addition, the density was increased by 19 % by adding wt.10% of lithium and calcium nitrate. The thermo-physical properties were experimentally investigated and summarised as shown in Table 2-7.

Table 2-7: Thermo-physical properties of Chilean lithium nitrate [29].

Molten salt mixture (wt.%)	temperature range (°C)	Viscosity at 250 (°C)	Energy density (MJ/m^3)	Salt price (US$/Ton)	Cost/stored energy (US$/k Wh)
Solar Salt	221-589	5.51	550	893	11.67
20 $LiNO_3$ - 52 KNO_3 - 28 $NaNO_3$	128-600	6.3	513	1161	16.35
30 $LiNO_3$ - 10 $Ca(NO_3)_2$ - 60 KNO_3	134-567	5.72	607	1274	15.07
10 $LiNO_3$ - 10 $Ca(NO_3)_2$ - 60 KNO_3 -20 $NaNO_3$	131-580	5.78	680	1038	10.98

Ternary molten salts such as calcium, sodium and potassium nitrates with various weight ratios were experimentally investigated in [30]. The simultaneous thermal analyser was used to determine the heat of fusion, cycle stability, and the endothermic peak's property. In addition, DSC was used to evaluate the specific heat capacity of the salt. It was found that the optimum weight ratio in the mixture $Ca(NO_3)_2$, $NaNO_3$, and KNO_3 was 32:24:44 (wt.%) as such the mixture had superior thermo-physical properties compared to other weight ratios.

Furthermore, experimental measurements found that the melting temperature of the mixture was 80 °C, the latent heat was 67 J/g and its thermal conductivity was 1–3 W/m K in the temperature range of 80-200 °C with its cost being approximately $626 per metric ton. It was also concluded that the ternary salt could be used as a PCM as well as HTF in solar plants due to its suitable thermo-physical properties and low cost.

The viscosities of Hitec salt ($NaNO_3$-$NaNO_2$-KNO_3, 7–40–53 wt.%) and solar salt ($NaNO_3$-KNO_3, 60–40 wt.%) were measured experimentally in [31] using an optimized rotational coaxial cylinder. It was concluded that Hitec salt had a double thermal conductivity of OPCM, with a melting temperature of 415 K and a decomposition temperature of 773 K.

In addition, it exhibited no signs of corrosion effect on the stainless steel tube. The viscosity was measured and compared with literature, with the results showing a 2.5 % uncertainty in the temperature range of 420-695 K. On the other hand, the binary nitrate salt ($NaNO_3$-KNO_3, 60–40 wt. %) has a melting temperature of 511 K and was stable up to 873 K, and it is widely used due to its low cost. The viscosity of Hitec salt and solar salt were plotted in Figure 2-13.

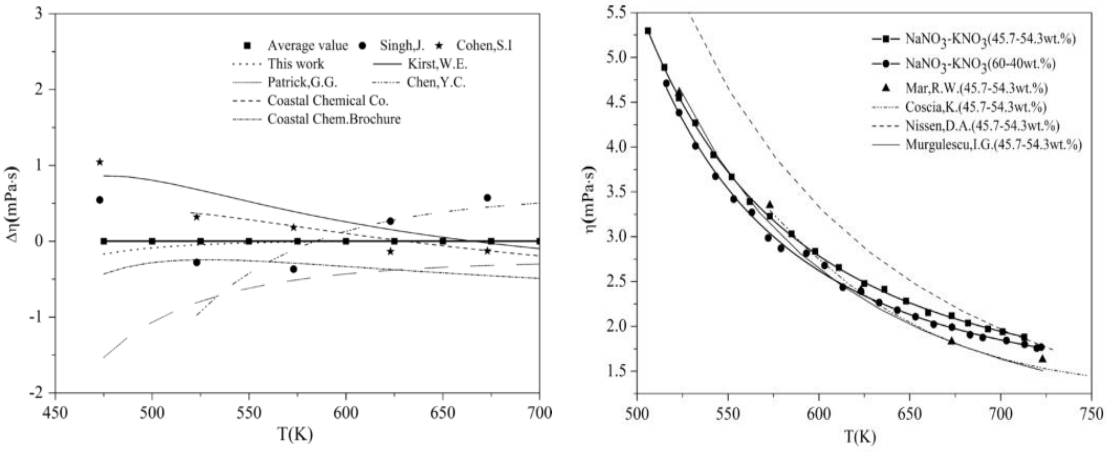

a) b)

Figure 2-13: Viscosity of Hitec salt (a) and solar salt (b) [31].

The study also found that the multi-component salts consisting of nitrates of sodium, potassium, lithium, and calcium with adding $LiNO_3$ increase their thermal stability. However, adding $Ca(NO_3)_2$ into the salts had a detrimental effect; decreasing both the

melting temperature from 413 K to 390 K and increasing the economic cost. The viscosity of the mixture with different components was tabulated and compared with their temperature range.

During the selection process of a suitable salt/salt hydrate and their eutectics for medium temperature applications, crucial parameters such as thermal properties and cost were considered. The solar salt KNO_3-$NaNO_3$ fitted both requirements and was used in this study.

2.4.3 Solar salt

In [32], research was performed to produce melting and solidification curves for a eutectic mixture of potassium nitrate and sodium nitrate. It was concluded, that the melting temperature of the solar salt depends on the concentration of the original salts, as seen in Figure 2-14.

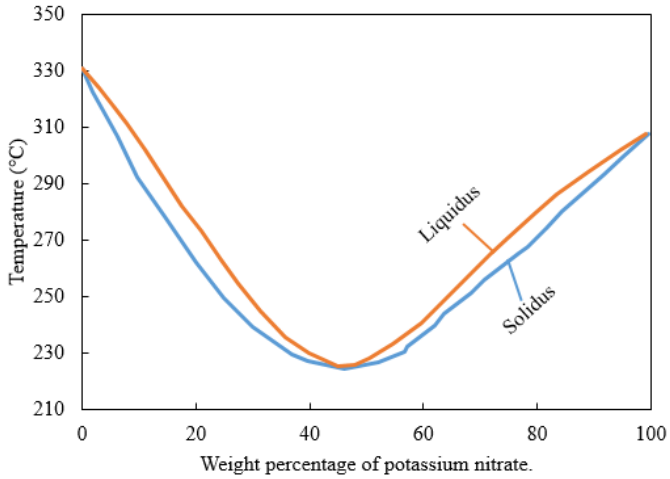

Figure 2-14: Composition of solid and liquid phases in equilibrium states in the mixture of potassium and sodium nitrates.

An investigation of a non-eutectic mixture of KNO_3-$NaNO_3$ was performed in [33] for a TES system. They concluded that a salt mixture is a promising option for solar thermal power generation due to its cyclic stability and low cost. However, it suffered from low thermal conductivity.

In addition, the long-term cyclic tests of a KNO_3-$NaNO_3$ sample which consisted of 30% KNO_3 and 70% $NaNO_3$ showed that the melting range, solid to melting range and melting to liquid phase range were 237-247 °C, 207-227 °C and 252-272 °C, respectively. DSC was used in the melting range of 223-262 °C and it was found that the sensible heat was 1.55 kJ/kg K and the value of sensible plus latent heat was 4.5 kJ/kg K.

The phase diagram of a binary mixture of KNO_3-$NaNO_3$ was explored in [34] using DSC. The various mole fractions of both salts were considered in the experiments, which are summarized in Table 2-8.

Table 2-8: DSC data for the $NaNO_3$-KNO_3 system [34].

Mole fraction $NaNO_3$	**Solidus temperature (K)**	**Liquidus temperature (K)**	**Mole fraction $NaNO_3$**	**Solidus temperature (K)**	**Liquidus temperature (K)**
0	608	608	0.55	494	505
0.03	562	608	0.60	494	514
0.05	522	605	0.65	494	520
0.10	500	592	0.70	494	529
0.15	499	578	0.75	494	545
0.20	495	564	0.80	495	550
0.25	495	552	0.85	497	558
0.30	494	535	0.90	499	568
0.35	495	528	0.95	539	577
0.40	494	510	0.97	549	580
0.45	493	505	1.00	580	580
0.50	494	500			

The investigation of using PCMs for potential cooking applications was carried out experimentally in [35]. Various mass fractions of $NaNO_3$-KNO_3 were used to identify the optimum thermal characteristics with DSC and determine the melting temperature, including the mass fraction of 60:40 wt %, results for which are shown in Figure 2-15.

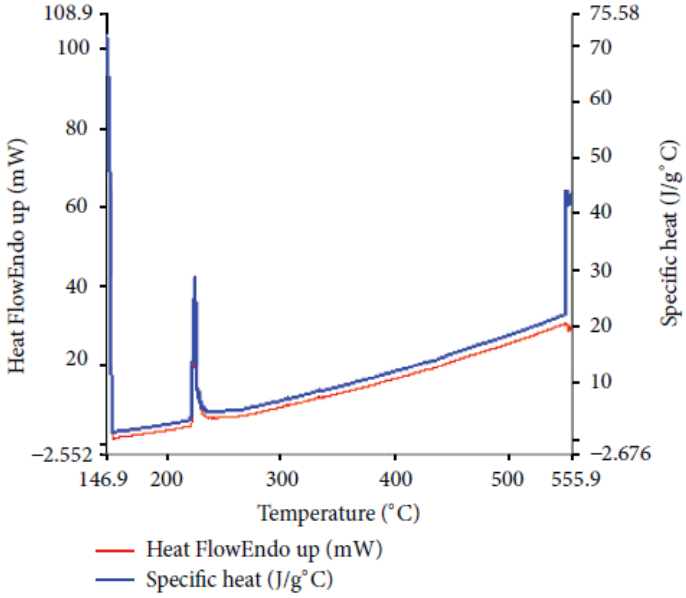

Figure 2-15: DSC result for sample ratio of $NaNO_3$ 60%-KNO_3 40% [35].

It can be seen in Figure 2-15 that the melting temperature is 225.38 °C, the enthalpy is 120.91 J/g °C, and the specific heat capacity at the melting temperature is around 10 J/g °C.

A review, presented in [36], summarises the thermo-physical properties of molten salts including the density [37], viscosity [38], thermal conductivity [39, 40], and heat capacity [41], which are essential parameters for HTF or heat storage subsistence. It is well known that fluid salts provide higher volumetric heat capacity than pressurized water, liquid sodium, lead, and lead-bismuth eutectic.

The correlation for density in the temperature range 573-873 K was presented as

$$\rho\left(\frac{kg}{m^3}\right) = 2263.628 - 0.636 \cdot T(K) \tag{2-1}$$

It was shown that there was no significant difference in density for various mass fractions in the $NaNO_3$- KNO_3.mixture (64-36% or 60-40%).

Most molten salts follow the Arrhenius behaviour, although there are exceptions especially at high temperature due to the decomposition of the compounds. The following relation describes the dynamic viscosity of solar salt in the temperature range of 573-873 K with a standard deviation of 2.33 %:

$$\eta(Pa \cdot s) = 0.075 - 2.77 \cdot 10^{-4} \cdot T + 3.49 \cdot 10^{-7} \cdot T^2 - 1.47 \cdot 10^{-10} \cdot T^3 \qquad (2\text{-}2)$$

The thermal conductivity for molten salts was studied by various researchers, especially at high temperature due to the uncertainties found in the heat transfer mode. For instance, values found are 0.45 W/m K and 0.48 W/m K with a deviation of 10.12 % and 4.36 % for solar salt and Hitec salt, respectively.

Another important thermal property is heat capacity. The following expression for nitrate and nitrite salts was presented to describe the general behaviour of heat capacity with a deviation of 2.36 %.

$$Cp\left(\frac{J}{kg\ K}\right) = 1396.044 + 0.172 \cdot T\ (K) \qquad (2\text{-}3)$$

The properties of the solar salt ($NaNO_3$-KNO_3 with a ratio of 46 - 54 wt%) were investigated in [42]. The thermal properties, such as density, heat capacity, thermal conductivity absolute viscosity as a function of temperature were determined as follows (for a temperature range of (300- 600 °C):

Density (kg/m^3):

$$\rho = 2090 - 0.636 \cdot T \qquad (2\text{-}4)$$

Heat Capacity (J/ kg K):

$$C_p = 1443 + 0.172 \cdot T \quad (2\text{-}5)$$

Thermal Conductivity (W/m K):

$$k = 0.443 + 1.9 \cdot 10^{-4} \cdot T \quad (2\text{-}6)$$

Absolute Viscosity (m Pa s):

$$\mu = 22.714 - 0.12 \cdot T + 2.281 \cdot 10^{-4} \cdot T^2 - 1.474 \cdot 10^{-7} \cdot T^3 \quad (2\text{-}7)$$

Here T is temperature in K.

The salt solidifies at 221 °C and starts to crystallize at 238 °C

The heat of fusion (based on the molecular average of the heat of fusion of each component) is H=161 (kJ/ kg).

Change in the density upon melting is

$$\Delta V / V_{solid} = 4.6\ \% \Rightarrow V_{liquid} = 1.046 \cdot V_{solid} \quad (2\text{-}8)$$

It was found that solar salt has a great potential for the TES system in the medium temperature applications. However, it suffers from low thermal conductivity, which limits the thermal energy charging process. Therefore, different methods are used to overcome the low thermal conductivity problem

2.4.3.1 Additives

Mass fractions between 0.1 and 3 % wt of CuO were used in [43] to enhance the thermo-physical properties of a binary salt ($NaNO_3$ 60 wt.% + KNO_3 40 wt.%). Noticeable improvement of specific heat was achieved in the solid and liquid phases, as illustrated in Figure 2-16. It was found that the optimal concentration of nano-particles was 0.5% wt.

in the temperature range from 160 to 300 °C, and the maximum specific heat improvement for solid and liquid phases were 7.96 % and 11.48 % respectively.

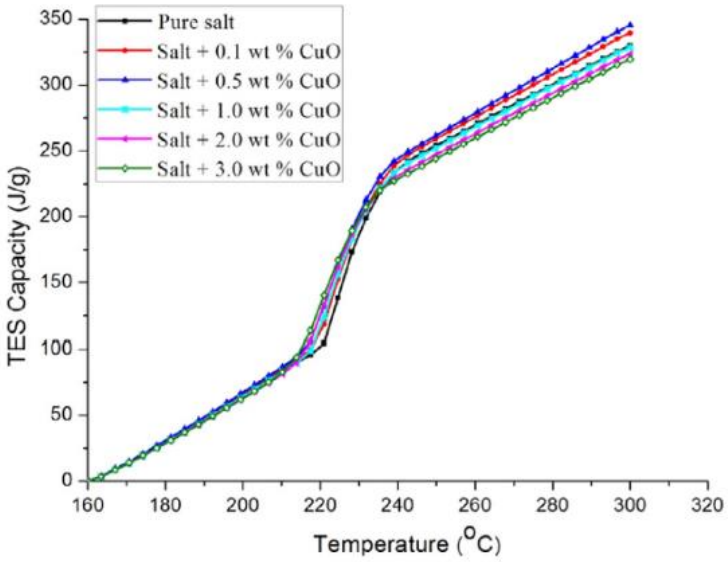

Figure 2-16: Specific heat vs. Temperature [43].

Cupric oxide(CuO) was used in [14] for improvements of the thermal conductivity in several types of nitrates salts, such as $NaNO_3$, KNO_3, and $NaNO_3$–KNO_3. Composites were prepared by mixing the salt with 2 wt% of cupric oxide at 20 °C above its melting temperature. Enhancements of thermo-physical properties of all the mixtures compared with the pure PCMs were observed by adding various types of additives up to certain amounts. Further research was recommended on the thermo-physical properties in the molten state and the dispersion of nanoparticles within the salt.

Improvement of solar salt (60 wt%$NaNO_3$+40 wt%KNO_3) by adding 14 different additives was studied in [44]. The samples were prepared and stored in a drying box at 200°C for 48 hours. The samples were expected to have a melting temperature under 200 °C at a constant point. Only five samples satisfied the above requirement.

In addition, the results of measurements of the melting point, the crystallization point, the decomposition point, and the specific heat were obtained in order to identify the general behaviour. It was found that the melting temperature for the samples 3, 7, 9, 10 were 92.3, 98.7, 101.8, 83.7, 128.9 °C, respectively. It was concluded that the average specific heats for these samples were 1.369, 1.725, 1.457 and 1.863 J/g K, respectively.

The thermo-physical properties of solar salt $NaNO_3$-KNO_3 (60–40 wt. %), with 1.0 wt.% of nano-particles, such as of SiO_2, Al_2O_3 and a mixture of SiO_2/Al_2O_3 were investigated in [45]. The results showed that the type of nanoparticle and the process parameters affect the thermo-physical properties. For instance, silica/alumina was mixed with base salt for 30 minutes at 200 rpm and was considered a key parameter for enhancement of the thermal properties of the salt.

Furthermore, it was found that the onset temperature was decreased and therefore, the phase change occurs at a lower temperature. Further research was recommended in order to understand the enhancement mechanism of the heat capacity.

The effect of adding Si_2O nano-particles to the eutectic salt ($NaNO_3$-KNO_3) was investigated in [46]. Three different mixtures, namely 49 %, 34 % and 64 % of $NaNO_3$ were used in the experiments. Various parameters such as latent heat of fusion and onset temperature have analysed as the effect of adding 1 wt% of Si_2O using the DSC technique. It was found that addition of SiO_2 decreased the latent heat as well as the onset melting temperature by 1.8 °C.

The melting range between solid/ liquid transition in eutectic and off eutectic mixtures for heating and cooling can be seen in Figure 2-17.

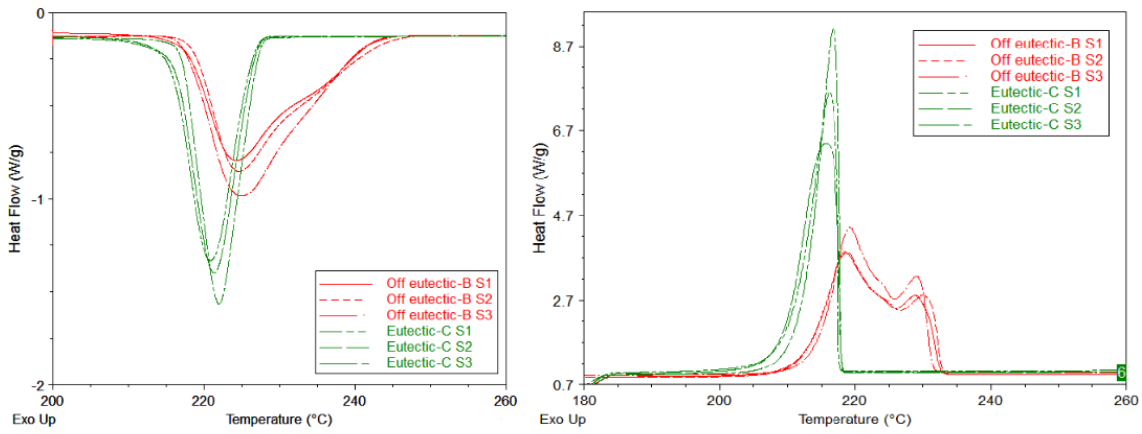

a) b)

Figure 2-17: Heat flow curves in heating (5°C/min) (a) and cooling (20°C/min) (b) for off-eutectic and eutectic compositions [46].

A mixture of graphite and salt was investigated in [47] for the TES system at a high temperature (>120 °C). A new mixing method was used, which is a cold compression of expanded natural graphite (ENG) with salt powder. The new method improved the thermal conductivity at a low cost because it can be performed at room temperature. Figure 2-18 shows the thermal conductivity of a composite with various mass fractions of ENG.

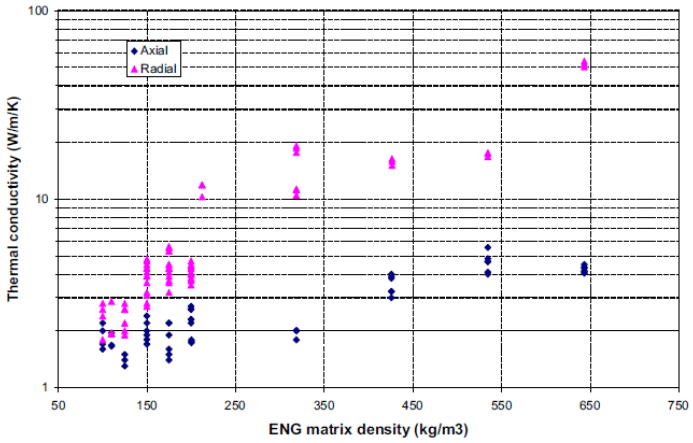

Figure 2-18: Axial and radial thermal conductivity vs. ENG matrix density [47].

It is shown in Figure 2-18 that the radial and axial thermal conductivities were improved with an increased amount of ENG. A difference between axial and radial thermal conductivity was within 2-3 W/m K when the ENG density is less than 1570 kg/ m^3. It was shown that cold-compression was an efficient and straightforward technique to improve the thermal conductivity of the eutectic mixture by a factor of 20 when ENG mass fraction was between 15-20 wt%.

The PCM which is the eutectic salt of $NaNO_3$ and KNO_3 (6:4) with various mass ratios of expanded graphite (EG) was developed and studied experimentally in [48]. The specific heat, thermal diffusivity, and thermal conductivity were measured and the results were summarised in Table 2-9. It was found that increase in the EG fraction improves the specific heat and thermal conductivity of the solar salt.

Table 2-9: The specific heat, thermal diffusivity and thermal conductivity coefficient of samples [48].

Expanded Graphite (Weight. %)	**Specific Heat (J/g K)**	**Thermal diffusivity (mm^2/s)**	**Thermal conductivity coefficient (W/m K)**
0	2.351	0.477	2.27201
0.5	2.485	0.573	2.876
1	2.586	0.639	3.338
1.5	2.593	0.791	4.143
2	2.6	0.93	4.884

It was found that increasing the percentage of EG into the eutectic salt also rises the melting temperature but decreases the latent heat as the amount of the eutectic salts decreases in the mixture, see Table 2-10.

Table 2-10: Phase change temperature and latent heat of samples [48].

Expanded Graphite	**Solid–solid phase change**		**Solid-liquid phase change**	
(Weight. %)	**Peak point (°C)**	**Latent heat (J/g)**	**Peak point (°C)**	**Latent heat (J/g)**
0	130.6	17.26	223.2	142.2
0.5	130.1	19.95	225.6	128.7
1	130.4	18.69	224.8	128.4
1.5	130.0	18.71	224.7	128.1
2	130.2	17.51	225.3	124.4

It was concluded that adding EG reduces the latent heat by 6.78-11 % and enhances the other thermal properties.

Composites made of EG and salt were investigated in [49] with the purpose to enhance the thermal conductivity of KNO_3-$NaNO_3$ (50 mol%) for TES systems operating at temperatures about 200 °C. EG has numerous advantages such as strong resistance to corrosion, chemical stability and has high thermal conductivity. The effect of adding EG to the salt hydrate is shown in Figure 2-19.

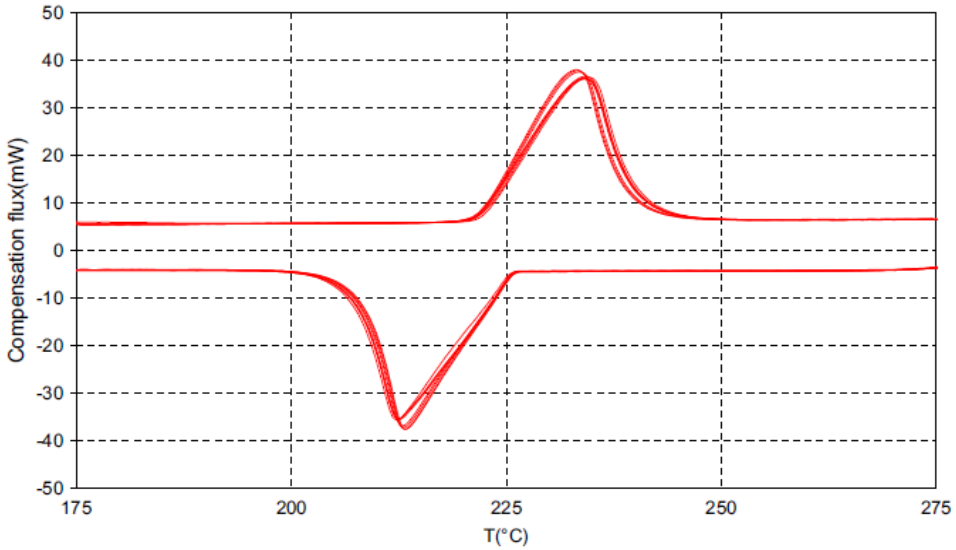

Figure 2-19: The measured compensation flux during the heating (positive values) or cooling (negative values) for a sample with 15% weight of EG (10 cycles at 5 ^{0}C/min) [49].

It was also shown that using EG and salt mixture reduces the investment cost by 20-45%. In addition, the mixture demonstrated very high thermal stability as shown in Figure 2-20.

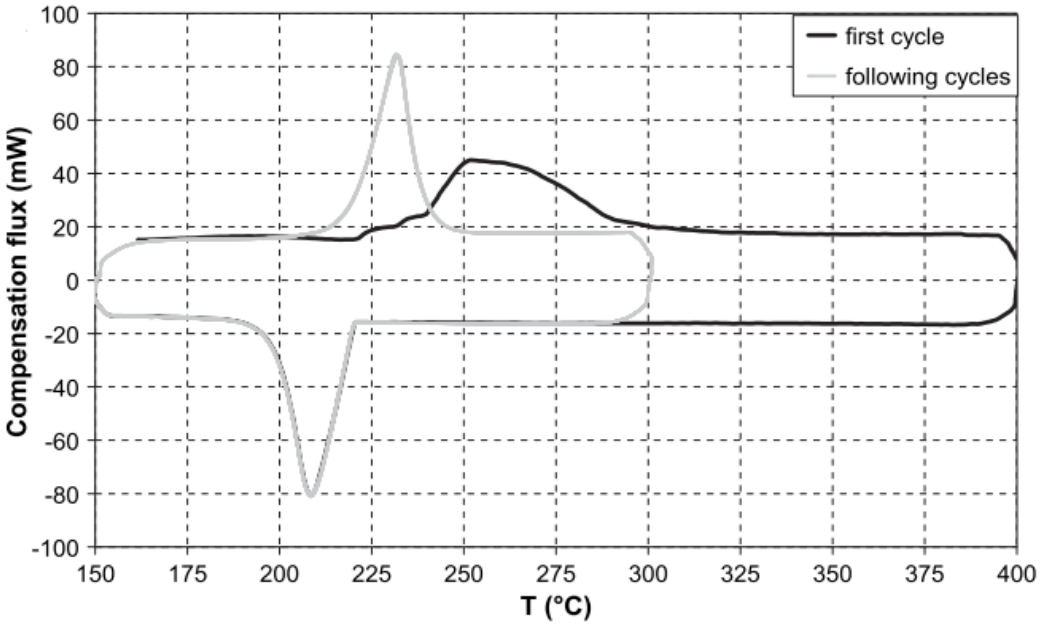

Figure 2-20: DSC results for one of the samples produced by the isostatic cold-compression method [49].

The thermal conductivity of the solar salt with different types of graphite powders was measured in [50, 51]. Natural graphite, ENG and EG powder were investigated. The thermal conductivities of mixtures with different graphites and for various mass fractions are shown in Figure 2-21.

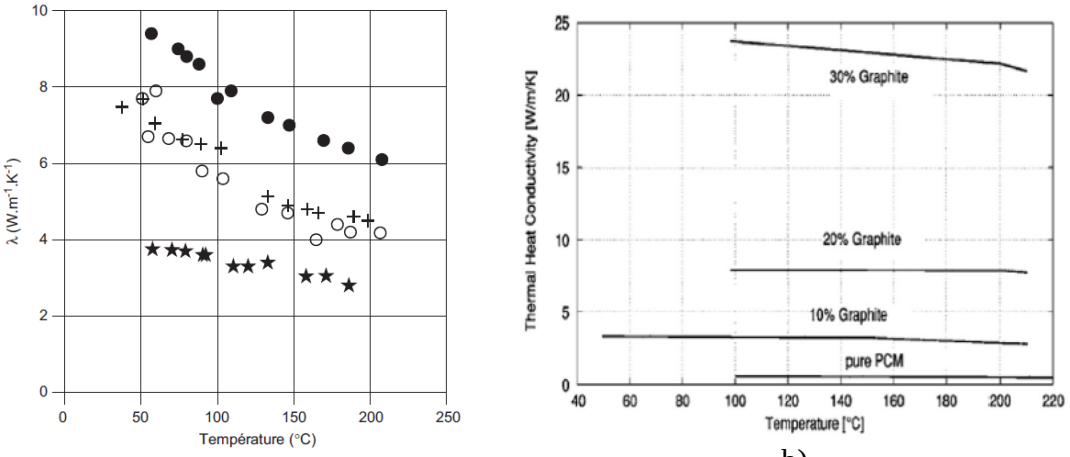

a) b)

Figure 2-21: Thermal conductivities of $NaNO_3$/KNO_3/graphite composites vs temperature: (a) depending on graphite type at 10 % wt - (*) graphite flakes I, (○) natural graphite, (+) graphite flakes II, (●) expanded graphite powder [50]; (b) thermal conductivity vs the graphite mass concentration [51].

It was found that the thermal conductivity of the solar salt with graphite decreases with increase in the temperature and that including graphite leads to decrease of the latent heat from 5% to 28% depending on the size and type of graphite.

In addition, an investigation of the high percentage of EG in a range of 10% -20% was carried out with and without 1 wt% of SiO_2 in [52]. It was found that the thermal conductivity was enhanced from 0.46 to 2.46, 3.36, 3.8 W/m K by adding 10, 15, and 20 wt % of EG, respectively. Moreover, it was found that using 1 wt% of SiO_2 with EG mixture enhances the thermal conductivity up to 3.7, 5.10 and 6 W/m K for 10, 15 and 20 wt% graphite, respectively in the temperature range of 250- 410 ° C, as shown in Figure 2-22.

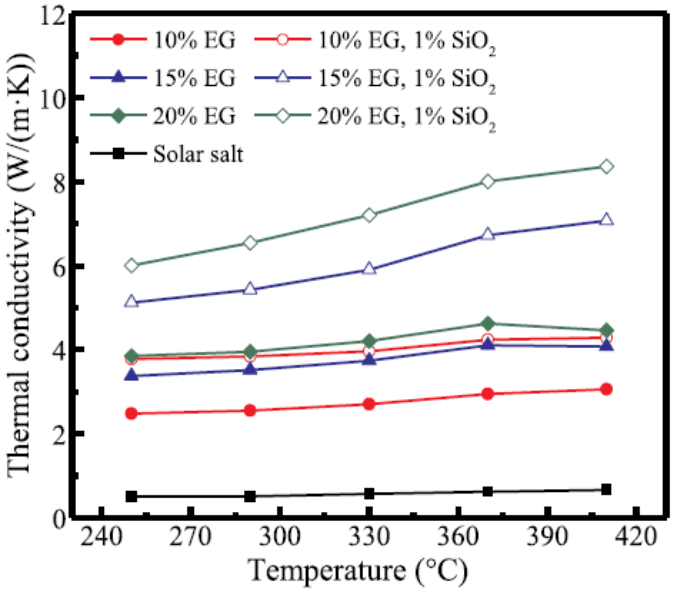

Figure 2-22: Thermal conductivity of binary nitrate and composites [52].

Graphite is an effective thermal conductivity enhancer due to its high thermal conductivity, low density, chemical stability and is suitable for high-temperature applications. However, it was tested only on small scale (laboratory research), with no research on the mixture at larger scales, especially with concentration more than 5 wt %. Therefore, in this study, the mixture of solar salt with graphite will be assessed with concentration of 10 wt%.

2.4.3.2 Extended surfaces (Fins)

Another method to intensify the heat transfer of PCMs is through the use of extended surfaces (fins).

A parabolic dish using solar salts was investigated using COMSOL multiphysics in [53]. The effects of aluminium fins, heat flux, and solar salt KNO_3- $NaNO_3$ (60: 40) were investigated. The effective heat capacity value was used in the numerical study, which can be expressed by:

$$C_{eff} = \frac{H}{T_1 - T_2} + C_p \tag{2-9}$$

Here H is the latent heat of fusion, T_1 is the onset temperature of phase transition and T_2 is the end temperature of phase change. The temperature profile of the solar salt during the charging process can be divided into three different regions which are the solid-state, phase change interface and liquid phase, shown in Figure 2-23.

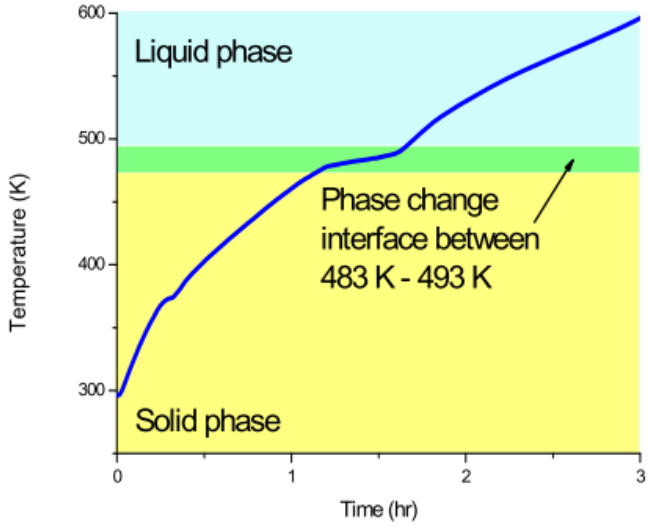

Figure 2-23: Temperature profile of the eutectic nitrate salt during the charging process [53].

It was found that increasing the number of fins increases the vertical temperature of the PCM except for the 1-fin case, see Figure 2-24.

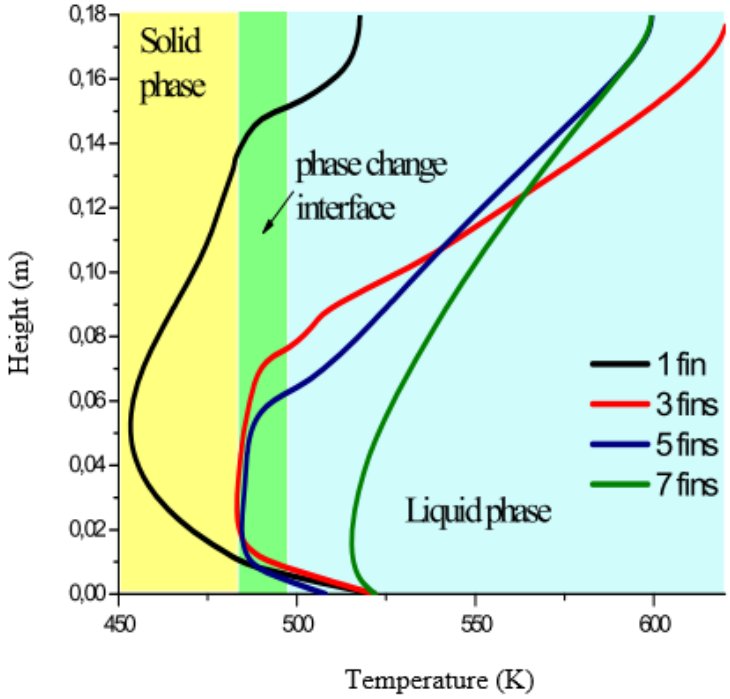

Figure 2-24: Vertical temperature profiles of the PCM with a heat flux of 20 kW/m^2 [53].

The performance of synthetic oil, as the HTF, was investigated in [54]. This HTF was used in the TES system of a solar power plant during the charging and discharging. ANSYS Fluent was used to model the charging and discharging processes and investigate the temperature variation in time. The sodium, potassium nitrate and eutectic mixture of potassium nitrate and chloride appeared to be suitable for the operating temperatures in the range of 300-400 °C. The results were validated with data from literature and a good agreement was observed.

In addition, different mesh topologies were adopted to determine the optimum size that gives accurate results with a minimum time cost. The results showed that the coefficient of heat transfer performance depends strongly on the flow rate of HTF and the PCM

properties. Furthermore, a comparison between finned and no-fin containers revealed an increase of up to 450 % in the heat flux, as seen in Figure 2-25.

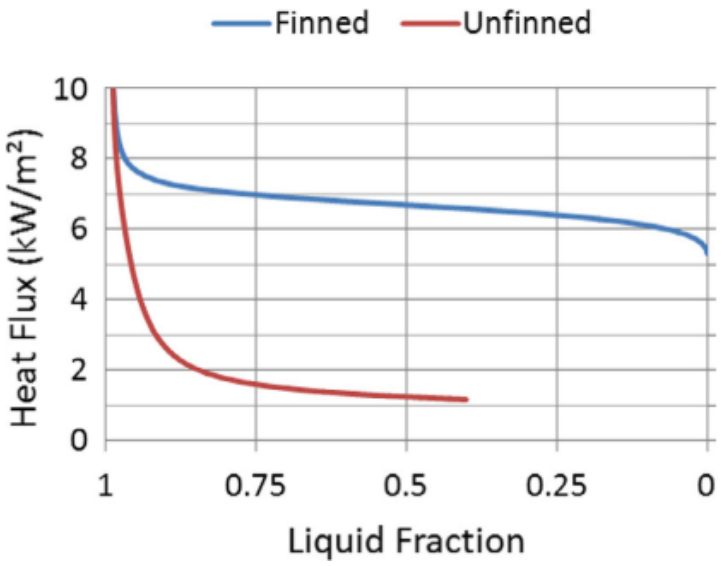

Figure 2-25: Comparison of the heat flux on the HTF-pipe wall during discharging for the finned storage element and that for no-fin storage element [54].

The effects of natural convection on the melting process in a flat-plate LHTES system was investigated both experimentally and numerically in [55]. The study focused on the effects of different system widths and heights on the melting process of KNO_3-$NaNO_3$ as a PCM. The charging process of the flat plate LHTES system is shown in Figure 2-26.

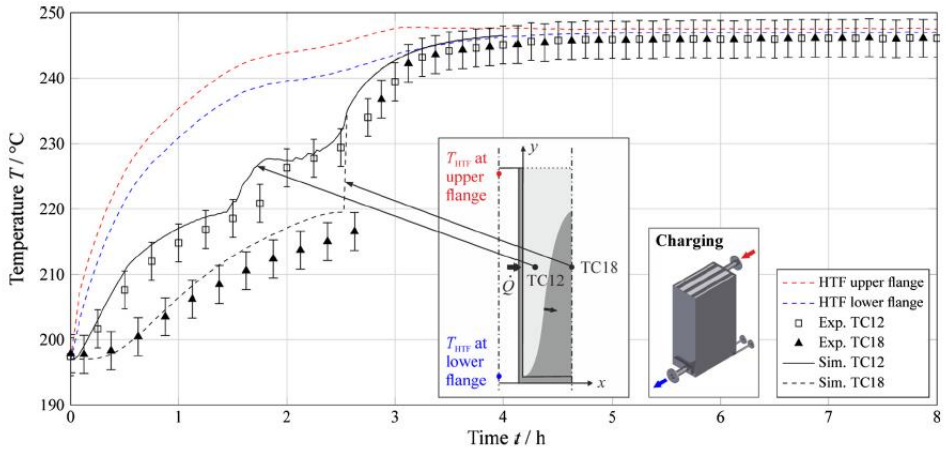

Figure 2-26: The simulated results against the experimental results of charging flat-plate LHTES system [55].

It was observed that the heat transfer was improved greater with the width than with the height due to the natural convection. Thus, small enclosures should be considered to improve the heat transfer during the charging process.

The effects of fins on the nitrate salt charging process was studied in [56]. Stainless steel fins, which were 1 and 4 mm in the thicknesses and the graphite fin of 1- mm thickness were used during the numerical study. The results for the charging process are shown in Figure 2-27.

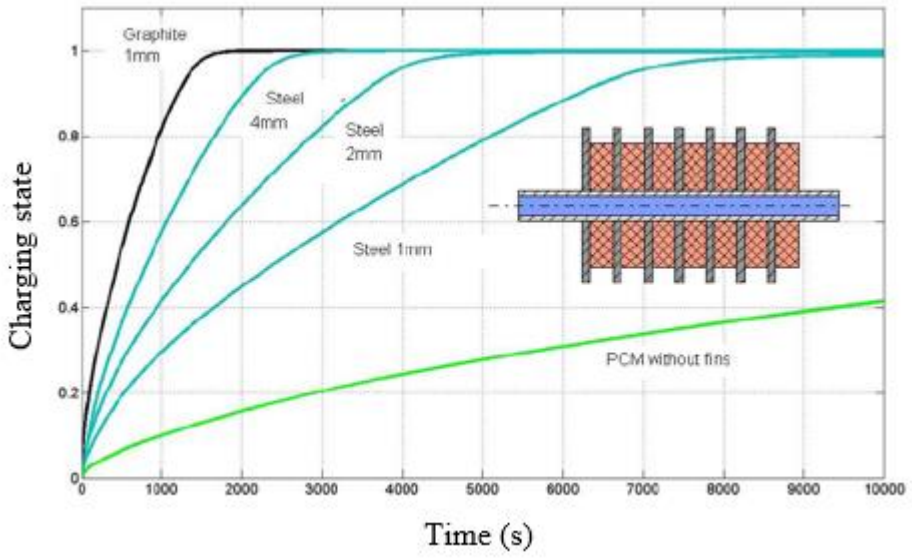

Figure 2-27: Investigation of the charging process of PCM with and without fins [56].

The graphite as a fin material provided the biggest increase in the speed of the charging process and showed suitability for melting temperatures up to 250 °C.

The effect of aluminium fins on the melting fraction was studied in [57] with the use of solar salt. The aluminium and solar salt were chosen due to their high thermal conductivity and melting temperature, respectively. Figure 2-28 shows the discharging process of PCM as captured at the instance of 3 hours and 50 minutes in the process.

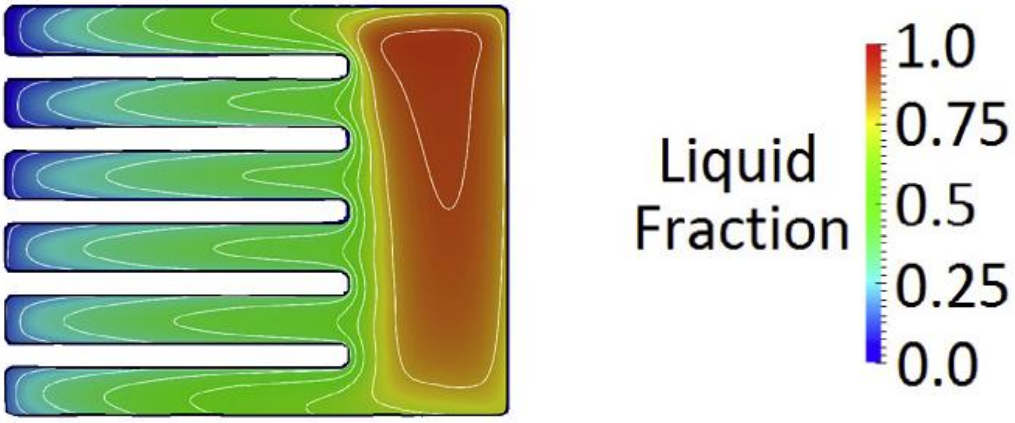

Figure 2-28: The discharging process of the PCM [57].

Furthermore, it was observed that the chamber aspect ratio has a higher impact on the performance of the TES system in comparison to the number, radius, and thicknesses of the fins [57].

Experimental and numerical investigations of a TES system using solar salt for cooking purposes were conducted in [58] during the charging and discharging processes. Welded aluminium fins were adopted and their influence on the thermal conductivity in the system was evaluated. A 40-mm gap between the fins was used in the experiment as shown in the 2D diagram of the system in Figure 2-29.

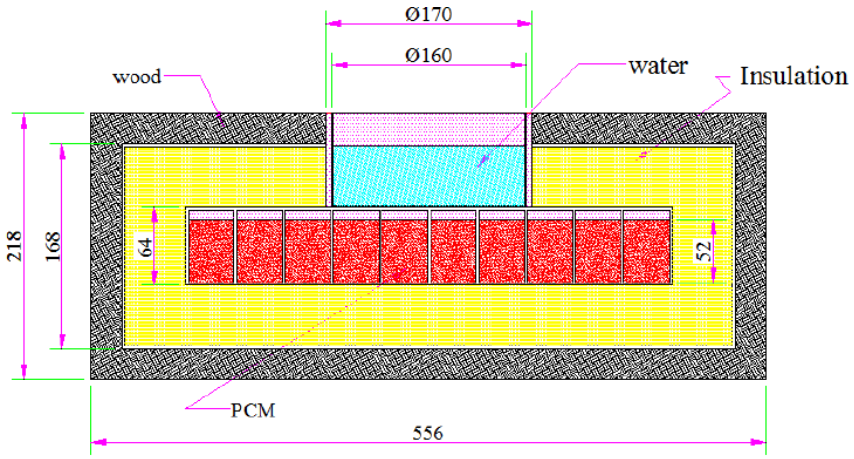

Figure 2-29: 2 D section of the TES system for cooking purposes [58].

It was concluded that a gap of 40 mm between the fins provided good performance. The PCM melts at a temperature of about 222 °C, which makes it suitable for cooking applications.

The eutectic mixture of KNO_3-$NaNO_3$ was numerically investigated in [59] for the effects of aluminium fins made of oil and tubes on the solidification process. Results for different thickness and radius parameters are shown in Figure 2-30.

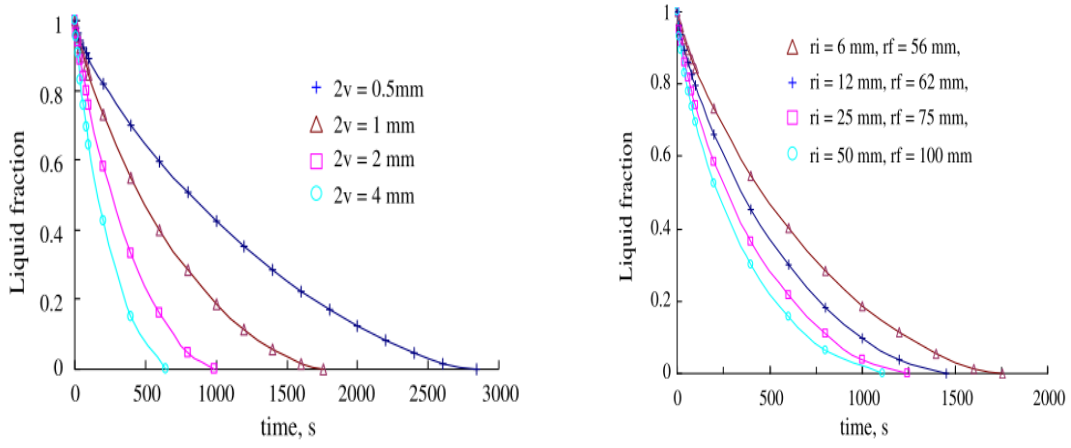

a) b)

Figure 2-30: Effect of (a) foil thickness and (b) tube radius on the liquid fraction formation [59].

The application of aluminium foils proved to accelerate the discharging process and was considered an efficient approach to increase the heat transfer inside the LHTES system.

In addition, the discharging process was found to be sensitive to the geometry and the radius of the tubes.

From the literature review, it is obvious that adopting extended surfaces intensifies the heat transfer in TES systems, although, though the only limited research has been carried out at medium and high temperatures. Despite providing certain advantages, fins increase the cost of manufacturing due to their complexity and decrease the packing of the PCM.

2.4.4 Metal PCM

Metal and metal alloys are considered as IOPCMs. They possess high thermal conductivity in comparison to salt and salt hydrates and are not prone to large volume changes during phase transition. Therefore, metals and metal alloys have received considerable attention for applications in TES systems. However, their drawback is the low latent heat of fusion per unit mass, and they are heavy [60]. Therefore, they have been studied to investigate their thermal properties, which helps to use them in different applications.

A numerical investigation of the low temperature melting alloy was carried out in [61]. The gallium metal and eicosane were used as a PCM. The gallium was adopted because of its low melting temperature, high thermal conductivity, and high volumetric latent heat. The numerical results of pure gallium in a rectangular cavity were validated against data in the open literature. The numerical study was performed for a rectangular cavity.

In addition, the laminar flow was adopted in the simulations. The time step of 0.01 s, as well as grid size of 60 × 60, were used in the numerical investigations. The melting fraction diagrams for gallium and eciosane are shown in Figure 2-31.

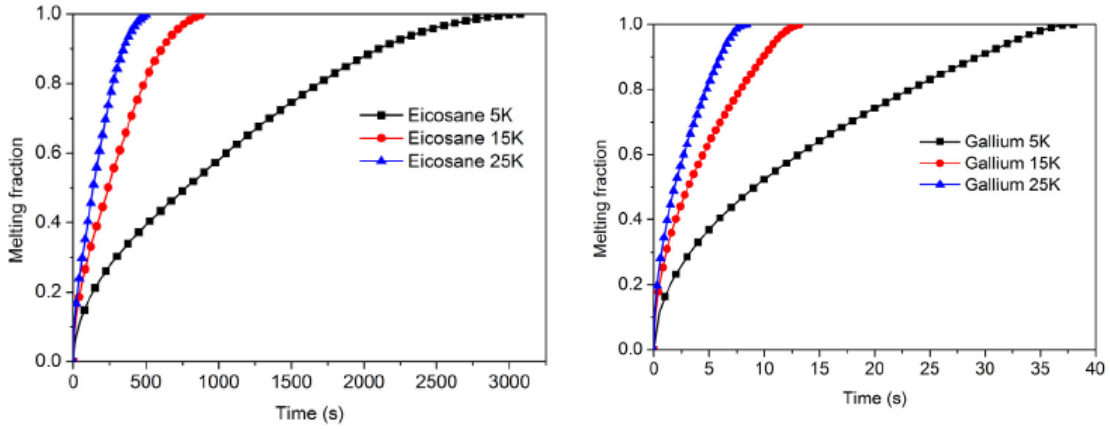

a) b)

Figure 2-31: Melting fraction versus time for eicosane and gallium under different overheating temperatures [61].

It was shown that the gallium metal melts in a short time compared to eicosane because the gallium has a higher thermal conductivity than eicosane.

The Al (25 wt%)/Si alloy has been investigated in [62] as a PCM for high-temperature energy storage. A three-dimensional model for the Al-Si alloy in the packed bed LHTES system was created, with air being used as a HTF. The air inlet velocity and temperature were considered constant for all cases.

Also, the adiabatic condition was applied to the walls of the system. The numerical model was validated using the experimental results from the literature and is shown in Figure 2-32. The performance of the system was evaluated in terms of the charging and discharging times, energy transfer efficiency and mean power.

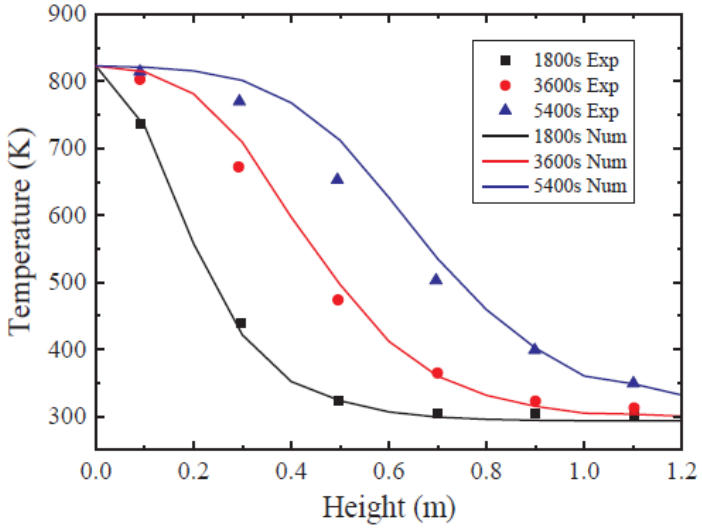

Figure 2-32: Comparison of the numerical and experimental temperature distributions in the storage tank [62].

The results show that the TES with such the PCM performs better than rock because of the latent heat value and high thermal conductivity of the PCM.

The melting process of gallium was numerically investigated in [63] using 2-D model. Two different configurations of heating were investigated to provide the improvement for the TES, which had a cylindrical heating source and four thin fins. It was found that integrating fins enhanced heat transfer and decreased the melting time. A comparison between the two configurations is shown in Figure 2-33.

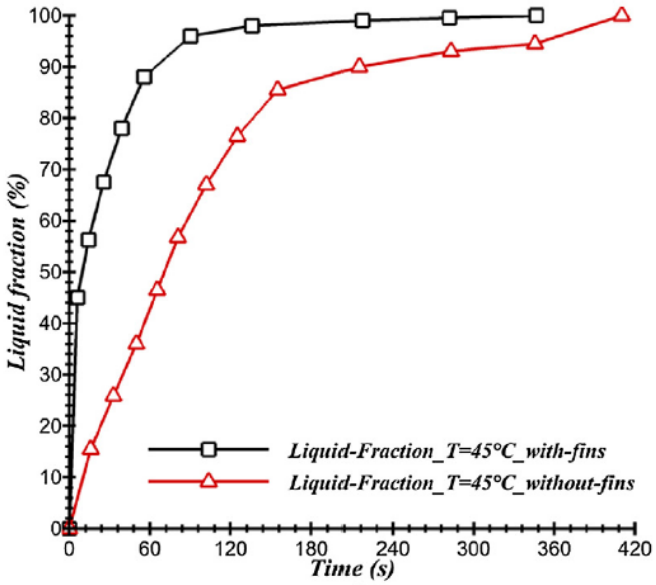

Figure 2-33: Evolution of the liquid fraction in the studied configurations for T = 45°C [63].

A low temperature melting metal was investigated in [64] for cooling electronic devices. An optimization of a gallium heat sink, using an internal copper fin, with heat sources of 100 W/cm^2 was performed. It was found that the thermal performance of the heat sink was affected by the geometry and dimensions of the fin structure. Figure 2-34 shows the effect of the fin width on the limiting value of temperature for various fin geometries.

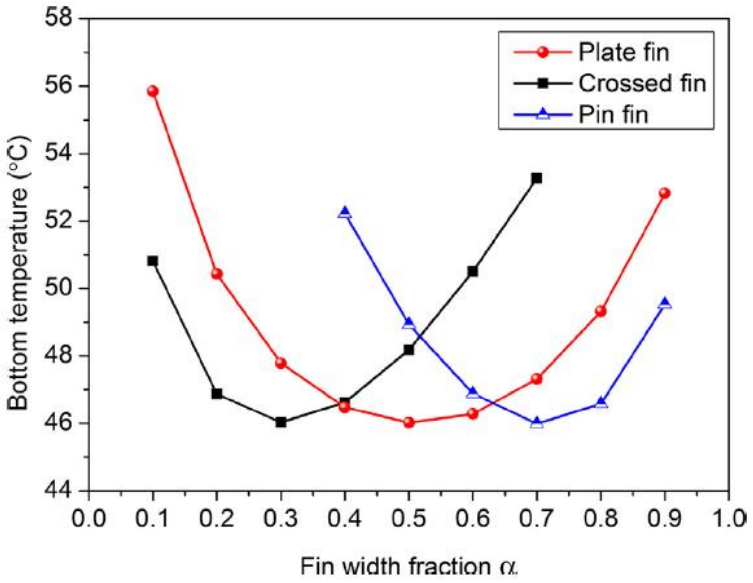

Figure 2-34: Limit temperature versus fin width fraction α for the three different types of fin geometries [64].

A magnesium and zinc eutectic metal alloy was investigated experimentally as a potential PCM for a low-temperature TES in [65]. The TES system consists of two concentric tubes. 67 kg of the metal alloy was used as a PCM and oil was used as HTF. The experimental results were used to validate the numerical model. It was found that the melting and solidification points were equal and at 34.2 °C. It was found that the limiting factor for heat transfer is not the thermal conductivity of the eutectic metal but the heat transfer on the liquid oil side in the pipe.

The performance of metallic PCMs, such as 32.5Bi/ 51In/16.5 Sn and 49Bi/ 18Pb/12Sn/ 21In were investigated in [66] for high heat fluxes at a short duration. The results were compared with other commercial PCMs and dielectric gel, such as PureTemp 29, PureTemp 58 and Sylgard 527 under high power, 19 ms pulses of maximum heat flux of 338 W/cm^2.

It was found that metallic PCMs can reduce the temperature rise during the pulse better than Organic PCMs, see Figure 2-35. That happens because of the high thermal conductivity of metallic alloy and low thermal resistance low. Also, it was shown that the metallic PCM enables thermal protection for high rate transient applications.

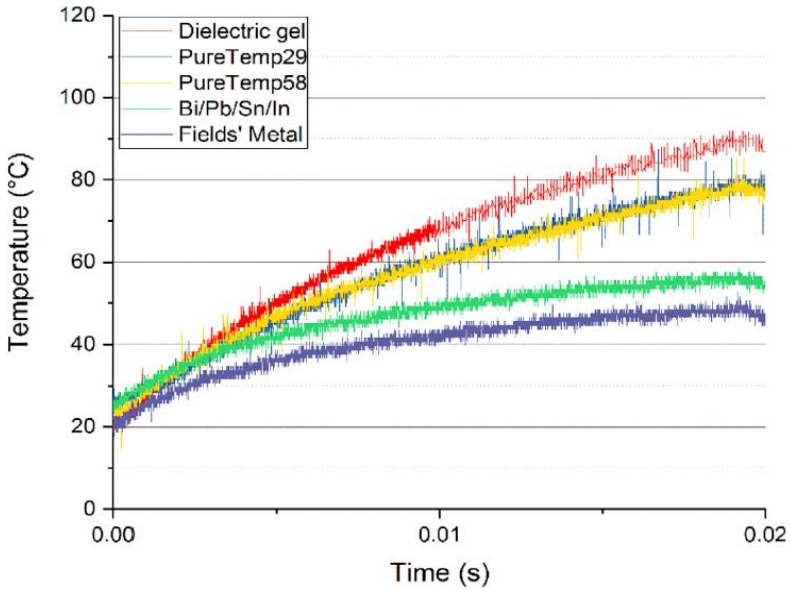

Figure 2-35: Results of PCM's performance under a pulse of 80 W power [66].

A eutectic alloy Bi31.6 In48.8 Sn19.6 was investigated in [67] for thermal management applications. The alloy was prepared and its thermal properties were measured. Then the thermal performance of the PCM was studied in a heat sink with internal crossed fins. Various heat fluxes as well as different numbers of fins were used and then results compared to the organic PCM, as shown in Figure 2-36.

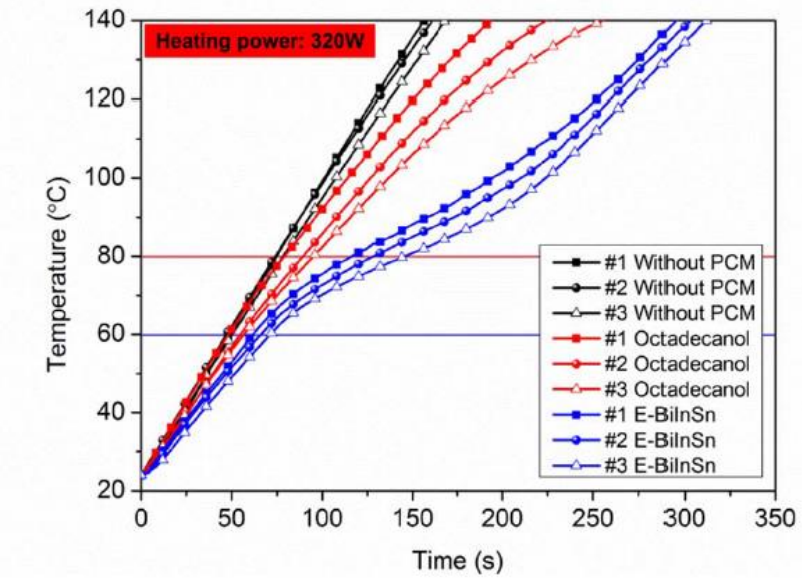

Figure 2-36: Transient thermal performances of the PCM heat sinks under the heating power of 320 W [67].

It was found that the metallic PCM has excellent heat extraction capability due to its high thermal conductivity. Hence it is considered a good candidate as a PCM for thermal management as well as thermal energy storage applications.

A metallic PCM, Bi_{49} Pb_{18} Sn $_{12}$ In $_{21}$, was used in [68] and placed on the top of a heat source to reduce the thermal resistance between the heat source and the device. The PCM was placed on a silicon nitride layer. Various pulsed powers of 40 – 160 W were applied with a 20 ms duration.

A 3-D numerical simulation of gallium in a rectangular cavity was performed in [69]. Various parameters were considered, such as thermal variations of properties and the presence of the mushy zone. 2-D and 3-D numerical models were built using COMSOL software to evaluate the characteristics of the melting and flow processes. The results were validated with the literature as well as the experimental work. It was shown that in 3-D the flow is less intensive than in the 2-D model.

The effect of the magnetic field on the melting process of gallium was studied numerically in [70]. The container was heated and cooled on its sides. Rotating hydrodynamic structure in clockwise and counter-clockwise directions was modelled using COMSOL software. It was found that the intensity of influence of magnetic field in the clockwise flow is higher. The reason behind that is the magnetic force enforces the natural flows in the same direction. The results were validated against experimental data obtained using ultrasonic Doppler velocimetry.

A low-temperature melting of Pb-Sn-In-Bi alloy was studied as a potential PCM in [71] and compared with 1-octadecanol. The organic PCM was selected because it has the same melting point of ~ 60 °C as well as the volumetric latent heat of fusion 215 MJ/m^3. The same volume of 80 ml was used in the TES system. Also, various heating fluxes up to 105.5 W/cm^2 were applied during the experiments, as shown in Figure 2-37.

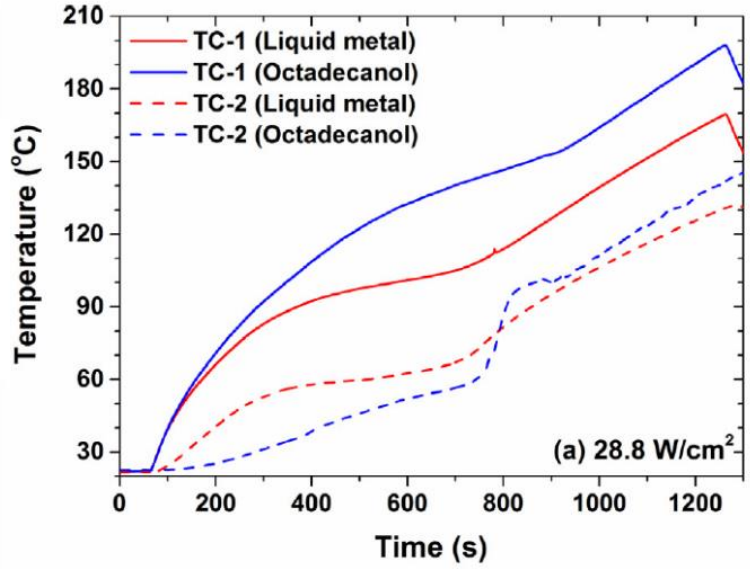

Figure 2-37: The temperature variations measured by thermocouples TC-1 and TC-2 during the heating period for the heat flux of 28.8 W/cm^2 [71].

It was found that liquid metal performs better than organic PCM by reducing the overheating temperature and doubles the effective protection time during the charging process while shortening the discharging process. Therefore, liquid metal is considered a promising PCM candidate for thermal energy storage.

A melting process around multiple cylinder heat sources in the presence of natural convection was investigated in [72]. The gallium was used as a PCM in the numerical instigation. The finite-volume method and enthalpy-porosity method were adopted. It was found that the melting shape was strongly affected by the natural convection as well as the heat source's arrangement.

Various liquid metals with their thermo-physical properties were reviewed and discussed in [73]. The liquid metals were classified into three main groups which are, Alkali, Heavy and Fusible metal groups. The groups consist of molten tin (Sn), gallium (Ga), lithium (Li), sodium (Na) and lead-bismuth (Pb-Bi). Liquid metals have a number of advantages such as wide operation temperature (usually > 1000 °C), lower and higher melting and boiling points, respectively, high thermal conductivity and high allowable heat fluxes.

On the other hand, liquid metals also have some drawbacks which include corrosion at high temperatures, high cost and safety issues especially for the Alkali metal group such as liquid sodium. Table 2-11 summarised their thermo-physical properties along with the cost of some liquid metals.

Table 2-11: Thermo-physical properties of liquid metals [69].

Liquid metal	**T_{fusion} (°C)**	**$T_{boiling}$ (°C)**	**Cp (kJ/kg K)**	**K (W/m K)**	**ρ (kg/m^3)**	**μ (mPa s)**	**Cost (USD/ kg)**
Molten Tin (Sn)	232	2687	0.24	33.8	6330	1.01	15.9
Gallium (Ga)	29.8	2403	3.75	59.5	5673	0.69	252
Sodium (Na)	98	883	1.26	57.5	761	0.16	2
Lithium (Li)	180	1347	4.16	63.3	436	0.20	11.82
Lead-bismuth (44.5Pb-5.5Biwt%)	125	1638	1.46	17.7	9710	1.33	13
Galinstan (66Ga-20.5 In-13.5Sn wt%)	-19	>1300	0.29	16.5	6440	2.4	450

Several liquid metals were modelled in CFD in order to predict the turbulent heat flux for natural, mixed and forced regimes of flow various models were suggested, such as the Algebraic Heat Flux Model (AHFM) and RANS coupled with the Kays.

A new metal alloy based on Cu-Bi was proposed in [74]. Various mass fractions of Bi were used ($\emptyset = 20, 40, 60$) for thermal surge protection and energy storage. The mixture had many advantages such as a limited solubility of Bi in the Cu, very good wettability between the liquid of Bi and the solid of Cu, manufacturing using a low-temperature processing technique and no formation of intermetallic compounds. DSC was used in order to measure the heat storage capacity of Cu-Bi alloy with 20 wt% of Bi during 8 cycles.

In addition, the latent heat of fusion was measured for all samples. It was shown that the heat storage capacity of the alloy did not change with the repeated heating-cooling cycles with various percentages of Bi, which can be seen in Figure 2-38.

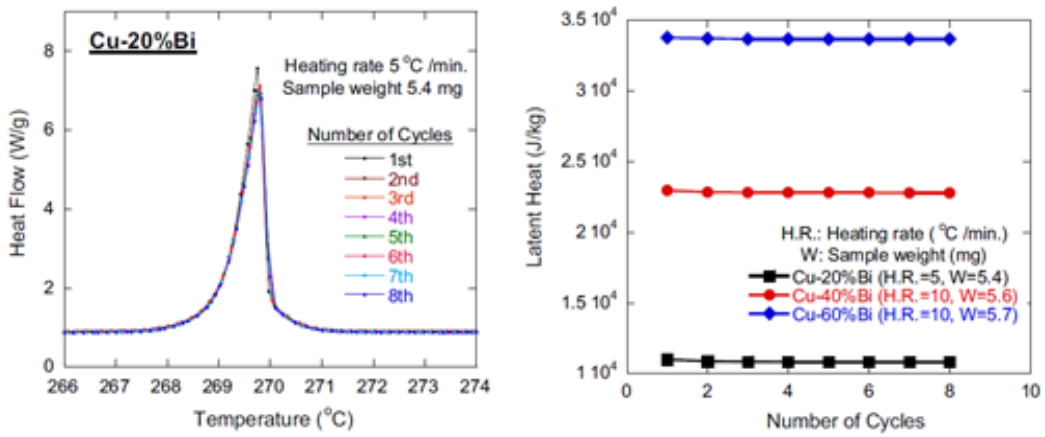

a) b)

Figure 2-38: Endothermic (a) and latent heat of fusion (b) for the Cu-Bi alloy [74].

A new model was developed in [75] to predict the melting temperature and the latent heat of fusion of low-melting alloys. The characteristic properties of entropy and enthalpy were considered. The models were developed for metals first and were then extended for their eutectic alloys. The experiments were performed on several Ga and Bi alloys in order to investigate the melting point and latent heat. The properties of some of the pure elements were tabulated and are shown in Table 2-12.

Table 2-12: Physical properties of the pure elements [75].

Element	**Melting point (K)**	**Latent heat (J/g)**	**Solid capacity (J/g K)**	**Liquid capacity (J/g K)**
Ga	302.9	80.22	0.372	0.343
In	429.7	28.47	0.238	0.273
Sn	505.1	60.29	0.243	0.255
Bi	544.5	60.29	0.127	0.151
Cd	594.2	54.00	0.239	0.291
Pb	600.6	24.28	0.126	0.142
Al	933.2	393.56	0.921	1.143

Furthermore, the thermo-physical properties of eutectics alloys, based on Ga and Bi, were measured and are shown in Table 2-13.

Table 2-13: Calculated and measured melting points and latent heats for selected binary, ternary and quaternary alloys [75].

Alloy	Melting point (K)		Latent heat (J/g)				
	Calculated	Measured	PMLH1		PMLH2		Measured
			Value1	Value2	Value1	Value2	
Ga-0.084Sn	291.4	293.0	73.37	74.12	75.17	75.17	78.29
Bi-0.782In	348.7	346.3	22.29	22.06	31.70	31.71	22.46
Ga-0.154In-0.111Sn	281.0	283.8	60.88	61.36	68.27	68.25	69.03
Bi-0.582In -0.188Sn	333.4	334.6	24.60	24.50	36.78	36.77	29.88
Bi-0.288Pb -0.244Sn	370.3	368.1	28.30	28.09	41.96	41.98	28.99
Bi-0.167Sn-0.144Pb-0.302In	356.4	331.5	26.24	23.83	37.73	38.00	28.98
Bi-0.194Sn-0.232Pb-0.158Cd	365.2	344.9	27.25	25.25	43.77	43.00	24.51
Ga-0.05Sn	296.0	293.1	76.38	75.71	74.40	75.71	79.22
Bi-0.645In	330.5	327.3	21.61	21.30	34.41	34.43	30.82
Ga-0.149In-0.067Sn	280.9	284.1	63.08	63.74	69.64	69.63	71.20
Bi-0.352In-0.223Sn	379.9	352.4	31.61	28.65	40.63	40.93	36.91

Here, PMLH is Prediction Model of Latent Heat; Value 1 is calculated using the calculated melting point; Value 2 is calculated using a measured melting point.
A good agreement was found between the calculated and measured values. PMLH1 was used for the exact values of the latent heat of fusion, which depends on the accuracy of the calculated melting temperature. Furthermore, PHLM2 was used for predicting the values of the latent heat of fusion which insignificantly depends on the melting point.

Additionally, liquid metals and their alloys were reviewed and summarized in [76]. The metals and their eutectics can be classified into three main categories. One of these categories is for a low-temperature range between 0–30 °C, where the suitable element was Ga-based metal alloy, and it is used for thermal management, building energy conservation and thermal comfort.

The medium temperature category ranges from 40-200 °C. The Bi-based metal alloy is considered suitable in that range and is used in waste heat recovery and solar energy applications. Finally, the high-temperature range of over 200 °C requires other metals and is used for solar energy applications.

Further research, into corrosion of metal containers with PCMs, was recommended along with a study into the super-cooling drawback of metals and metal alloys in order to improve the performance of phase change from liquid to solid. The thermo-physical properties of metals and their alloys were summarized in Table 2-14.

Table 2-14: Thermo-physical properties of typical metals and their alloys [76-79].

Liquid metals	**Melting point (°C)**	**Evaporation point (°C)**	**Specific heat (kJ/kg °C)**	**Density (kg/m^3)**	**Thermal conductivity (W/m °C)**	**Enthalpy of fusion (kJ/kg)**
Mercury	-38.87	356.65	0.139[a]	13 546[a]	8.34[a]	11.4[a]
Cesium	28.65	2023.84	0.236[d]	1796[d]	17.4[d]	16.4[d]
Gallium	29.8	2204.8	0.37[n]	5907[n]	29.4[n]	80.12[n]
Rubidium	38.85	685.73	0.363[m]	1470[m]	29.3[m]	25.74
Bi44.7Pb22.6In19.1Sn8.3Cd5.3	47	-	0.197	9160	15	36.8
Bi49In21Pb18Sn12	58	-	0.201	9010	10	28.9
Potassium	63.2	756.5	0.78[m]	664[m]	54.0[m]	59.59[d]
Bi50Pb26.7Sn13.3Cd10	70	-	0.184	9580	18	39.8
Bi52Pb30Sn18	96	-	0.167	9600	24	34.7
Sodium	97.83	881.4	1.38[d]	926.9[d]	86.9[d]	113.23[d]
Bi58Sn42	138	-	0.201	8560	19	44.8
Indium	156.8	2023.8	0.23	7030[c]	36.4[c]	28.59[m]
Indium	186	1342.3	4.389[b]	515[b]	41.3[b]	433.78[b]
Sn91Zn9	199	-	0.272	7270	61	32.5
Tin	232	2622.8	0.221	730[d]	15.08[b]	60.5[m]
Bismuth	271.4	1560	0.122	979	8.1	53.3

a - at 25 °C, b - at 200 °C, c - at 160 °C, d - at 100 °C, n- at 50 °C, m - at melting point.

Multi-component eutectic alloys consisting of Bi, Cd, Sn, Pb and In elements were investigated in [80]. Microstructure morphology, phase compositions, melting temperature and latent heat of fusion were studied. It was demonstrated that the current

work was more accurate than previous ones due to the use of modern instruments. The thermo-physical properties of thirteen specimens were measured and are presented in Table 2-15.

Table 2-15: Thermo-physical properties of eutectics alloys [80].

Alloy composition (weight %)	**Melting point (°C)**	**Latent heat (J/g)**	**Latent heat (J/cm^3)**	**Density (g/cm^3)**
In25.2Sn17.3Bi57.5	80.70	32.47	282.359	8.696
In51.34Sn15.56Bi33.1	60.42	24.34	195.986	8.052
In4Sn40Bi56	101.13	3.87	32.911	8.525
Sn22Bi50Pb28	97.06	17.55	165.619	9.437
Sn15.5Bi52.5Pb32	96.84	21.64	210.211	9.714
Sn16Bi52Pb32	96.91	22.02	210.643	9.566
Sn26Bi53Cd21	92.55	2.52	22.108	8.773
Bi51.6Cd8.2Pb40.2	92.97	26.66	277.717	10.417
Sn51.2Cd30.6Pb18.2	144.99	40.6	329.672	8.120
In10.5Sn19Bi53.5Pb17	60.66–76.18	16.91	154.879	9.159
In21Sn12Bi49Pb18	59.73	27.07	249.829	9.229
Sn13.3Bi50Cd10Pb26.7	72.14	30.35	290.814	9.582
In19.1Sn8.3Bi44.7Cd5.3Pb22.6	48.30	28.53	266.185	9.330

Liquid metals for room-temperature applications were reviewed in [81]. The suitable material should fulfil a number of requirements on superior chemical and physical properties. These also should be environmentally friendly, low cost and safe in exploitation. Liquid metals can be classified into single element liquids, which can be

combined with other metals and non-metals to create new alloys, and binary liquid alloys, which can be formed from alkali metals and have a high thermal conductivity.

Furthermore, liquid metals can also be classified as multicomponent alloys that mainly consist of Ga, In, Sn (liquid at room temperature). The final classification is the nano–liquid metals, which are formed by adding various nano-particles into liquid metals. However, metals and metal alloys suffer from the sub-cooling problem. Several types of liquid metals are summarised in Table 2-16.

Table 2-16: Melting points of metals and metal alloys under 60 °C [81].

Type	**Liquid metals**	**Melting point (°C)**	**Liquid metals**	**Melting point (°C)**
Single-element	Rubidium	38.89	Gallium	29.76
	Cesium	28.44	Mercury	– 38.83
	Francium	27		
Binary alloys	GaZn5	25	Na6.2Rb93.8	– 4.5
	GaSn8	20	K78Na22	– 11
	GaSn12	17	K76.7Na23.3	– 12.7
	Ga75In25	16	Cs77K23	– 37.5
Multicomponent alloys	GaIn12Zn16	17	GaIn60Sn10	12
	GaIn29Zn4	13	GaIn25Sn13Zn1	3
	GaIn25Sn13	5	Galinstan	– 19
	Ga62.5In21.5Sn16	10.7	Cs73.71K22.14 Na4.14	– 78.2

Further experimental and numerical investigations on the development of new liquid metals were recommended. The use of the CALPHAD method was suggested in future research.

Various methods of evaluating the thermo-physical properties of PCMs were critically evaluated in [82]. In addition, an economic study was performed concentrating on the cost of encapsulation, tank and storage material, the cost of storage material and the price of PCM and HTF. It was shown that there were disagreements in published results. It was found that the density of the eutectics can be predicted using the Artsdalan' model. Predicting the thermal conductivity proved to be difficult because of a large spread for thermal conductivity values.

The movement of the mushy zone inside various alloys such as (Bi–Cd–Sn–Pb) and (Pb–Sn) during the solidification process was investigated experimentally in [83]. Correlations were developed to predict their motion on the interface of liquid and solid zones. The correlations were for $0.93 \leq Bi \leq 13.7$, $0 \leq \Phi S \leq 0.24$ and $0 \leq \Phi L \leq 1.23$. It was observed that the development of the liquidus boundary was affected by the value of sensible heat in the liquid zone.

It was found that the development of the solidus boundary was affected by both sensible and latent heats as well as by the heat flux released from the mushy zone at the cooling interface. The study demonstrated a good agreement between the predicted and the experimental results. The properties of the investigated alloys are summarised in Table 2-17

Table 2-17: Thermo-physical properties of studied alloys [83].

Parameters	**Unit**	**Alloy (Bi–Cd–Sn–Pb)**	**Alloy (Pb–Sn)**
Density	(kg/m^3)	9760	8220
Heat capacity of solid	(J/kg·°C)	146	174
Heat capacity of liquid	(J/kg·°C)	184	193
Thermal conductivity	(W/m·K)	18	44.6
Latent heat	(J/kg)	32,900	36,700
Liquidus temperature	(°C)	70	183
Solidus temperature	(°C)	65	177
Initial temperature	(°C)	80	210
End temperature	(°C)	30	30
Stefan number	Ste	0.24	0.86
Thermal diffusivity of solid	(mm^2/s)	12.6	31.6
Equivalent thermal diffusivity in mushy zone	(mm^2/s)	0.27	0.72
Equivalent thermal diffusivity of liquid	(mm^2/s)	10	28.1

Newly developed alloys based on Mg and Zn were investigated in [84]. Various metals were used in the investigation such as Cu, Ni, and Sn which also could be used in TES systems. ThermoCalc software with the SSOL4 thermodynamic database was used in order to find alloys with a lower melting temperature than of Mg49Zn51. The simulations results were validated by existing data from the literature. For example, the simulation results of Mg-Zn alloys were 341.02 ºC and 170.69 J/g for the melting point and latent heat respectively, see Table 2-18.

Table 2-18: Comparison results between Thermocalc software and literature [84].

Composition	**Melting Temperature (T_m, °C)**		**Heat of Fusion (ΔH_f, J/g)**	
Thermocalc	**Thermocalc**	**Bibliography**	**Thermocalc**	**Bibliography**
Mg49Zn51	341.02	340-343	170.69	138, 180, 210
Mg49Zn47,02Al 3,97	338.08	340	158.47	132±25
Cu4.29Mg63.2 Al32.5	425.00	428	282.00	282.4

ThermoCalc software, in conjunction with the SSOL4 thermodynamic database, was used to predict the melting point and latent heat of alloys shown in Table 2-19.

Table 2-19: Calculated properties for some alloys [84].

Number	**Alloy**	**T_m (°C)**	**ΔH_f (J/g)**
1	Mg-Sn-Cu	200.6	65.2
2	Zn-Cu-Sn	215	80.2
3	Zn-Al-Sn	214.9	54.9
4	Mg-Sn-Li	134.35	58.34
5	Mg-Zn-Cu	285	168

A 3D numerical simulation of macro-segregation during the solidification of the Sn (3 wt%) Pb alloy in a rectangular cavity was carried out in [85]. The solidification model based on the Eulerian fluid-fluid model was used. The results of the model showed a good agreement with the experimental results on the thermal state during the solidification process, see Figure 2-39.

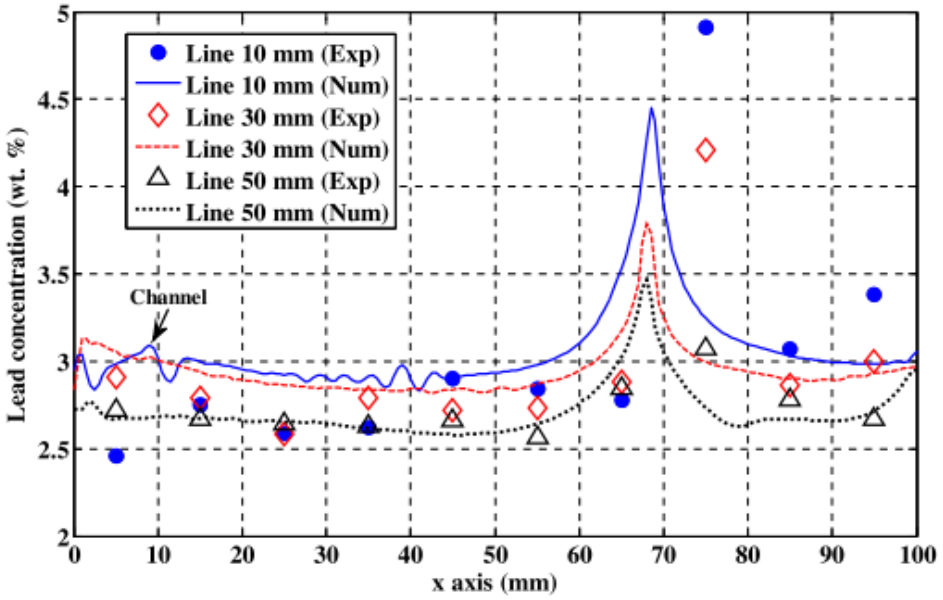

Figure 2-39: Lead concentrations obtained by Inductively Coupled Plasma analysis and numerical simulation at different heights of the storage [85].

Macro-segregation of the sample was captured using X-ray photography and the experimental results confirmed those predicted by simulations. It was shown that the melting temperature increased approximately from 232 °C to around 242 °C.

The effects of adding tin and indium to the liquid phase of Bi33.3-Ga66.7 immiscible alloy was investigated in [86]. The electrical resistivity measurement was used to study the liquid phase separation and the miscibility gap. It was shown that the electrical resistivity results were more accurate than that of DSC, see Figure 2-40.

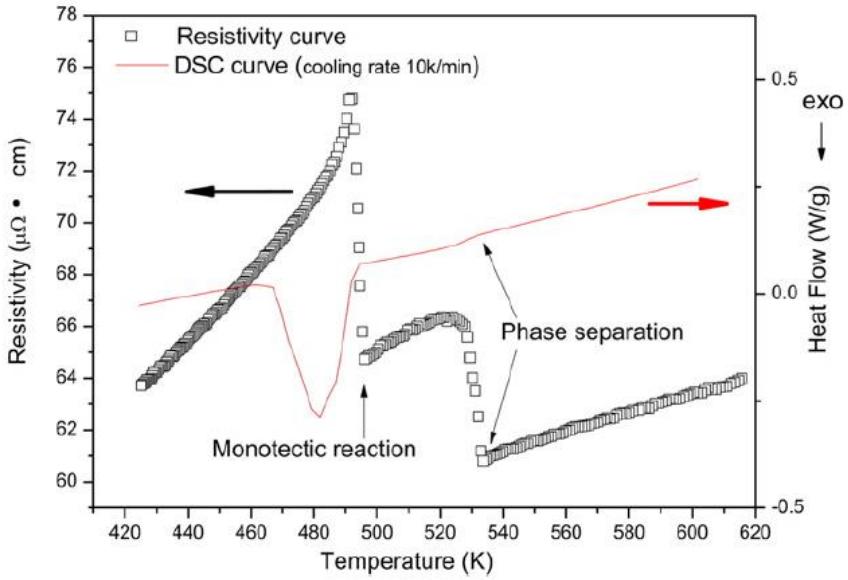

Figure 2-40: DSC and resistivity-temperature curves of Bi33.3-Ga66.7 alloy during the cooling process [86].

It was also shown that the phase separation occurred beyond the melting point which was around 493 K (Monotectic reaction). The phase separation tendency was found to be weakened by adding Tin but was strengthened by adding indium.

The influence of adding ceramic SiC into the SN-Cu-Ni solder alloy was studied in [87]. The powder metallurgy technique was utilized, with silicon carbide SiC used to enhance the properties of the composite solder Sn-0.7Cu-0.05Ni. DSC was carried out to investigate the melting temperature and melting range. It was shown that the melting temperature of Sn-Cu-Ni solder alloy was 226.5 °C and that adding SiC particles into the alloy insignificantly changed the melting point. Various mass fractions of ceramic were used in the experiments, see Table 2-20.

Table 2-20: Melting and solidification temperatures of the SN-Cu-Ni-xSiC composite solder [87].

Specimens	**SiC (wt %)**	**T_s (°C)**	**T_L (°C)**	**ΔT (°C)**
Sn-Cu-Ni	0	226.5	230.6	4.1
Sn-Cu-Ni-0.25SiC	0.25%	226.4	230.2	3.8
Sn-Cu-Ni-0.50SiC	0.50%	226.3	230.2	3.9
Sn-Cu-Ni-0.75SiC	0.75%	226.4	230.1	3.7
Sn-Cu-Ni-1.0SiC	1.0%	226.3	230.0	3.7

It was also found that the melting temperature did not change when adding SiC particles, but it reduced the melting range. Finally, it was observed that the hardness and the shear strength were enhanced by increasing the mass fraction of the SiC.

The properties of the Sn-Bi lead-free alloy were investigated in [88]. The DSC was carried out to measure the melting temperature. The alloy had a low melting point of about 141 °C, as seen in Figure 2-41, which is lower than the melting temperatures of Sn-Pb and Sn-Ag-Cu of 183 °C and 227 °C, respectively. The density of Sn-Bi was measured to be 8.56 g/cm^3. Furthermore, it was found that the alloy provided high hardness with average values of 11.8 and 3.87 for Vickers and Brinell hardness, respectively.

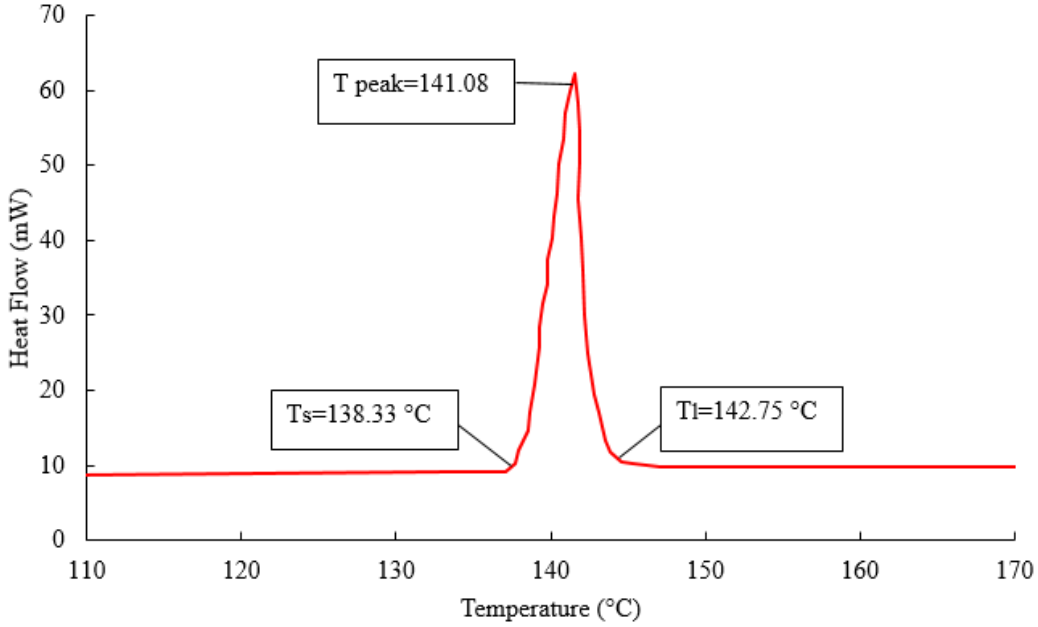

Figure 2-41: Melting temperature of Sn-Bi alloy [88].

The influence of adding Bi on the properties of a wrought Sn0.7Cu (SC) solder alloy was investigated in [89]. The mixture was prepared by using the directional solidification process. Moreover, the growth rate of solidification was investigated. The investigation of the melting point and undercooling of SC solder alloy was carried out using DSC. Table 2-21 summarises the influence of Bi addition on the SC alloy.

Table 2-21: Melting and solidus temperature of various contents of Bi in SC alloy [89].

Alloy	**T_m (°C)**	**T_s (°C)**	**Undercooling (T_m-T_s) (°C)**
Sn0.7Cu	220.3	191.8	28.5
Sn0.7Cu–0.7Bi	216.7	196.3	20.4
Sn0.7Cu–1.3Bi	214.7	200.8	13.9

It was found from the results that the melting and undercooling temperature were decreased by increasing the Bi content. Furthermore, it was concluded that the high content of Bi leads to the finer fibrous microstructure of Cu6Sn5.

The effects of adding Ti on the properties of Sn3.5Ag0.5Cu (SAC) solder was examined experimentally in [90]. The melting and solidus temperatures were calculated and are presented in Table 2-22.

Table 2-22: Melting and solidus points of SAC alloys with various percentages of Ti [90].

Specimens	**Ti (wt%)**	**T_S (°C)**	**T_L (°C)**	**ΔT (°C)**
SAC	Nil	216.92	221.58	4.66
SAC–0.25Ti	0.25	216.73	220.95	4.22
SAC–0.5Ti	0.5	216.75	220.86	4.11
SAC–1Ti	1	216.59	219.47	2.88

Increasing the amount of Ti content in the SAC alloy was found to decrease the melting temperature and the melting range. Furthermore, it was shown that the addition of Ti into the grains of the alloy made it finer and more uniform. It was also found that the maximum enhancement occurred when adding 1wt% of Ti.

The enhancement of thermo-physical properties of the SN-2Ag-0.5Cu (SAC 205) lead-free solder alloy using a various mass fraction of Ni and Zn was examined in [91]. The thermal reaction of adding Ni and Zn, during melting and solidification was carried out using DSC. The results showed little effect on the melting temperature, whereas the solidus temperature was shifted. The results on the melting and solidification processes are summarized in Table 2-23.

Table 2-23: Melting and solidification temperatures of Ni and Zn contents on SAC alloy [91].

Alloys	**T_{onset} (°C)**	**T_{end} (°C)**	**Melting temperature (°C)**	**Pasty range (T_{end}-T_{onset}) (°C)**	**T_{onset} cooling (°C)**	**Under cooling (T_h-T_c)**
SAC (205)	212.9	220.0	213.5	7.1	186.8	26.1
SAC (205) – 0.05Ni	212.7	221.6	214.1	8.9	194.7	18.0
SAC (205) – 0.5Zn	211.5	218.5	212.5	7.0	209.9	1.4

Various software suites, such as CES Edu-pack, were used for material selection and tabulation with their calculated properties. ThermoCalc, Pandat, Matcalc, and OpenCalphad are considered to be efficient software in predicting the general properties of binary and ternary compounds. These packages can be used to develop new compounds using various elements. The CALPHAD method was used to predict the properties of various alloys. The phase diagram of the Al-Ni alloy was plotted using Thermocalc and Pandat, see Figure 2-42.

a)

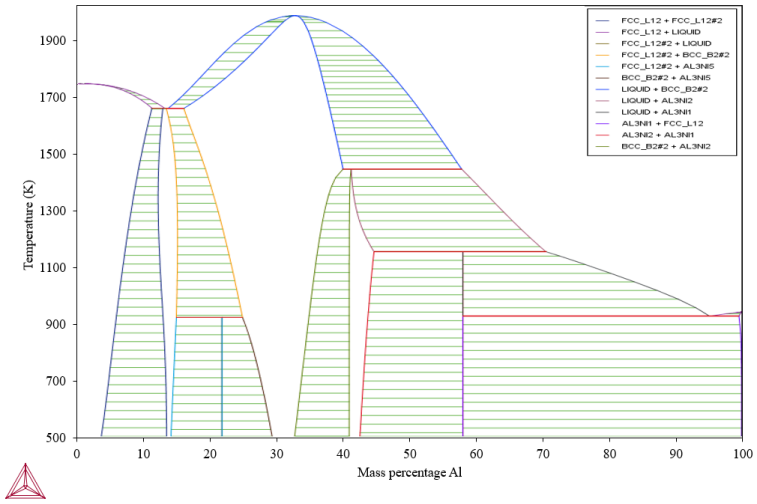

b)

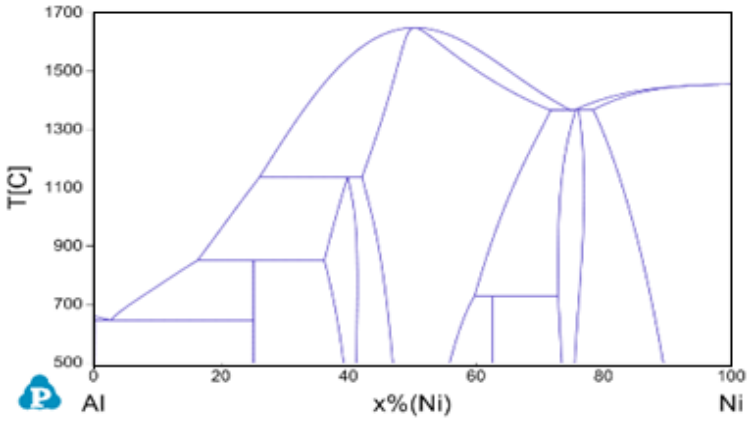

c)

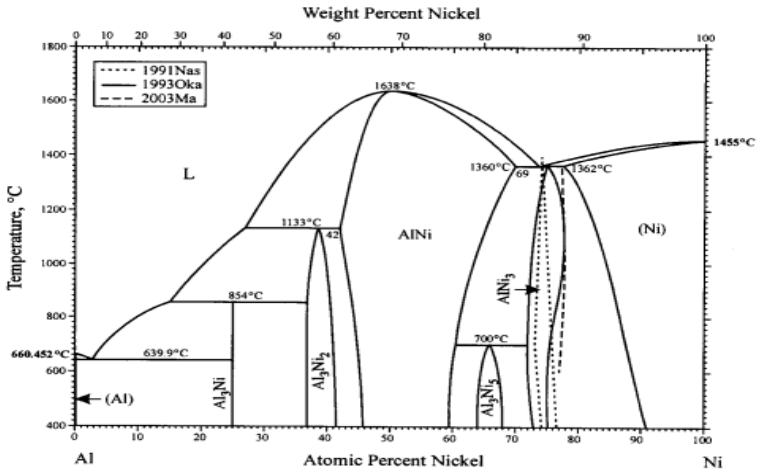

Figure 2-42: Comparison between a) Thermocalc b) Pandat and c) literature [92].

A list of low-temperature melting alloys was presented in [93] with various compositions of Sn, Pb, Bi, In in the temperature range between 50-183 °C. The melting and solidification points are summarised in Table 2-24.

Table 2-24: The Liquidus and Solidus Temperatures for various metal alloys [93].

Chemical composition (wt %)	Melting point (°C)	Solidus point (°C)	Chemical composition (wt %)	Melting point (°C)	Solidus point (°C)	Chemical composition (wt %)	Melting point (°C)	Solidus point (°C)
49Bi-21In-18Pb-12Sn	58	58	34Pb-34Sn-32Bi	133	96	45Bi-35Pb-20Sn	107	96
51In-32.5Bi-16.5Sn	60	60	56.84Bi-41.16Sn-2Pb	133	128	46Bi-34Pb-20Sn	108	95
49Bi-18Pb-18In-15Sn	69	58	38.4Bi-30.77Pb-30.77Sn-0.05Ag	135	96	54.5Bi-39.5Pb-6Sn	108	102
66.3In-33.7Bi	72	72	57.42Bi-41.58Sn-1Pb	135	135	67Bi-33In	109	109
57Bi-26In-17Sn	79	79	36Bi-32Pb-31Sn-1Ag	136	95	51.6Bi-41.4Pb-7Sn	112	98
54.02Bi-29.68In-16.3Sn	81	81	55.1Bi-39.9Sn-5Pb	136	121	52.95Bi-42.49Pb-4.53Sn	117	103
51.45Bi-31.35Pb-15.2Sn-2In	93	87	36.5Bi-31.75Pb-31.75Sn	137	95	52.98Bi-42.49Pb-4.53Sn	117	103
52Bi-31.7Pb-15.3Sn-1In	94	90	43Pb-28.5Bi-28.5Sn	137	96	52In-48Sn	118	118
52.5Bi-32Pb-15.5Sn	95	95	58Bi-42Sn	138	138	53.75Bi-43.1Pb-3.15Sn	119	108
52Bi-32Pb-16Sn	95.5	95	38.4Pb-30.8Bi-30.8Sn	139	96	55Bi-44Pb-1Sn	120	117
52Bi-30Pb-18Sn	96	96	33.33Bi-33.34Pb-33.33Sn	143	96	55Bi-44Pb-1Sn	121	120
50Bi-31Pb-19Sn	99	93	97In-3Ag	143	143	55.5Bi-44.5Pb	124	124
50Bi-28Pb-22Sn	100	100	58Sn-42In	145	118	50In-50Sn	125	118
46Bi-34Sn-20Pb	100	100	80In-15Pb-5Ag	149	142	58Bi-42Pb	126	124
50Bi-25Pb-25Sn	115	95	99.3In-0.7Ga	150	150	38Pb-37Bi-25Sn	127	93
56Bi-22Pb-22Sn	104	95	95In-5Bi	150	125	51.6Bi-37.4Sn-6In-5Pb	129	95
50Bi-30Pb-20Sn	104	95	42Pb-37Sn-21Bi	152	120	40In-40Sn-20Pb	130	121
52.2Bi-37.8Pb-10Sn	105	98	99.4In-0.6Ga	152	152	52Sn-48In	131	118

Many metals and metal alloys have a great potential for soldering purposes at high temperatures which limits their applicability for TES systems that operate at around 100 °C. Lead is considered as a hazardous and expensive material. Therefore, for this investigation, the study on the potential use of a cheaper metal alloy that is not hazardous and with low-melting temperature, such as Bi-Tin, is conducted.

2.4.4.1 Bi-Tin

The metal alloy Bi-Tin has a great potential for application in TES systems for the 100 °C temperature. Therefore, it was studied to determine its thermal properties, such as melting temperature and heat of fusion.

A comprehensive review of the low melting temperature of Pb-free solders was performed in [94]. Pb-free solder alloys fulfil various requirements such as having a low melting temperature and attractive thermal properties. Table 2-25 summarises the melting and solidification temperatures for Pb-free solder alloys.

Table 2-25: Pb-free solder alloys in the temperature range of 109-227 °C [94].

Alloy system	**Composition**	**Melting point (°C)**	**Alloy system**	**Composition**	**Melting point (°C)**
Bi-In	Bi-33In	109	Sn-Zn	Sn-9Zn	198.5
Sn-In	Sn-52In	118	Sn-Ag	Sn-3.5Ag	221
	Sn-50In	118-125		Sn-2Ag	221-226
Sn-Bi	Sn-58Bi	138	Sn-Ag-Cu	Sn-3.8Ag-0.7Cu	217
Sn-Bi-In	Sn-20Bi-10In	143-193		Sn-3.9Ag-0.6Cu	~217
Sn-Zn-Bi	Sn-8Zn-3Bi	189-199	Sn-Cu	Sn-0.7Cu	227

The melting temperature and density of different eutectic alloys were measured using the large drop method in [95]. It was found that there was a good agreement between experimental results and the literature review. Table 2-26 summaries information on the melting temperature and density for eutectic alloys.

Table 2-26: The melting temperature and density for binary and ternary liquid alloys of Bi-Pb-Sn [95].

Composition (wt %)			**Melting point (K)**	**Density at T_m (g/cm^3)**
Bi	**Pb**	**Sn**		
100	---	---	544	---
---	100	---	601	---
---	---	100	505	---
56	44	---	398	10.08
27.5	---	72.5	447	7.94
43	---	57	412	8.73
60	---	40	452	9.22
46	29	25	368	9.69

In [96] the effect of silver and indium addition on the physical properties of Bi-Sn alloys were investigated using a heating rate of 10 K/min. Under an argon atmosphere, it was found that the addition of Ag and In decreases the melting temperature and the enthalpy of the Bi-Sn alloy as shown in Table 2-27. Also, the specific heat of alloys was investigated, see Figure 2-43.

Table 2-27: The onset and peak points for some solders [96].

Solder	Onset Point (°C)	Peak top (°C)	Mushy zone (°C)	Enthalpy (µv.s/mg)
Sn-37Pb	183	187	0	12.13
Bi-42Sn	139.06	143.75	7.815	14.23
Bi-40Sn-2In	129.68	135.93	5.16	12.49
Bi-40Sn-2Ag	139.06	142.18	6.2525	13.01
Bi-38Sn-2In-2Ag	131.25	133.59	4.81	12.41

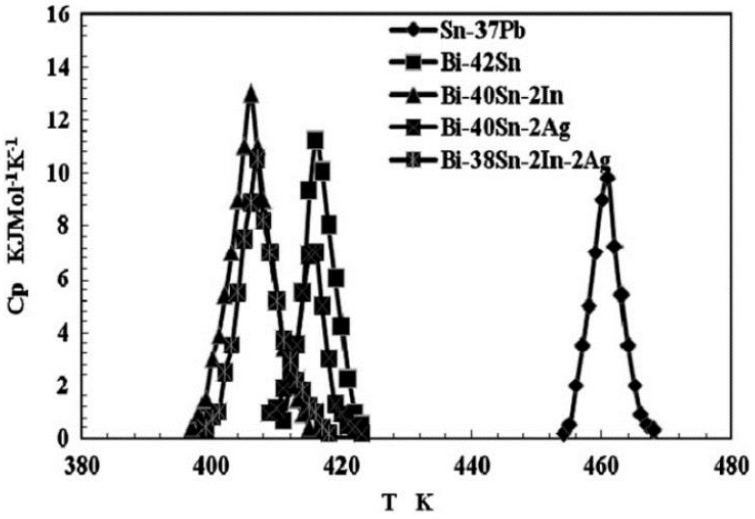

Figure 2-43: Temperature dependence of the specific heat for all melt-spun alloys [96].

The effect of adding various elements such as Al, Cu, Zn, Ga, Ag, In, Sn to the Sn-Bi eutectic on the melting temperature using a DSC was reviewed in [97]. It was found that these elements reduce the melting temperature of Sn-58Bi. However, the mushy zone temperature range of the new eutectic alloys increased from 2.7 °C to 3.9 °C. Both the melting and mushy zone temperatures are shown in Figure 2-44 and Table 2-28.

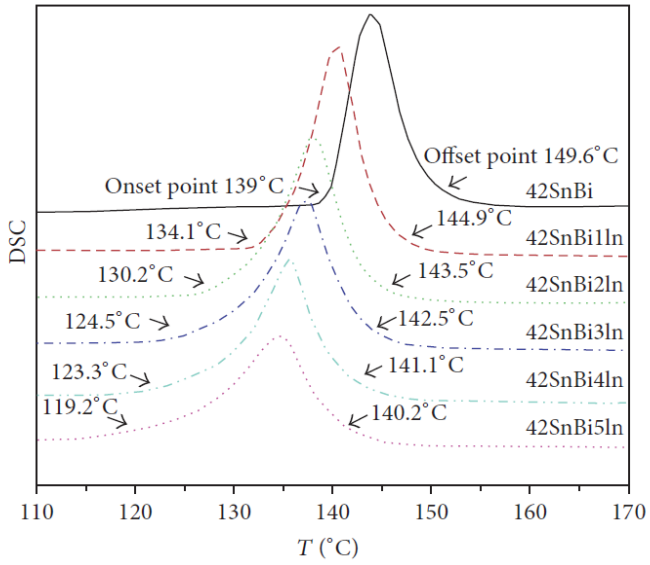

Figure 2-44: DSC curve of Sn-Bi-In alloys [97].

Table 2-28: Liquids and solidifying temperature of Sn-58Bi-based solder alloys (°C) [97].

Solder	**Sn-58Bi**	**Sn-58Bi-0.5Ag**	**Sn-58Bi-0.1Ag**
Solidus	136.1	135.7	136.2
Liquids	139.1	138.2	139.7
Mushy zone	3	2.5	3.5

Various metal alloys, based on Sn, Bi, Pb, were investigated in [98] using DSC to determine the onset temperature, enthalpy and thermal stability of the alloys at different heating and cooling rates. It was found that the heating rate affects both the reaction temperature and the enthalpy of fusion. The results are summarised in Table 2-29.

Table 2-29: Onset temperature and enthalpy for various metal alloys [98].

Composition (wt%)	**Scanning Rate (°C/min)**	**Reaction Temperature(s) (°C)**			**Enthalpy of Fusion (J/g)**
Sn-58 Bi	10	139	-	-	43.2
Sn-58 Bi	-10	123	-	-	-42.7
Sn-58 Bi	1.25	138	-	-	49.1
Sn-58 Bi	-1.25	131	-	-	-49.8
Sn-37 Pb	10	183	-	-	45.2
Sn-37 Pb	-10	172	-	-	-44
Sn-37 Pb	1.25	184	-	-	48.2
Sn-37 Pb	-1.25	172	-	-	-49.1
Sn-42 Pb-8 Bi	10	154	-	-	38.0
Sn-42 Pb-8 Bi	-10	171	162	128	-41.6
Sn-42 Pb-8 Bi	1.25	155	163	-	39.0
Sn-42 Pb-8 Bi	-1.25	179	171	-	-37.9
Sn-43 Pb-14 Bi	10	134	140	-	38.4
Sn-43 Pb-14 Bi	-10	160	151	128	-36.3
Sn-43 Pb-14 Bi	1.25	135	137	168	35.6
Sn-43 Pb-14 Bi	-1.25	166	159	134	-35.8
Sn-35 Pb-10 Bi	10	135	142	-	42.7
Sn-35 Pb-10 Bi	-10	147	142	128	-43.5
Sn-35 Pb-10 Bi	1.25	135	142	-	46
Sn-35 wt pct Pb-10 wt pct Bi	-1.25	164	134	-	-45.3

In [99] an experimental investigation on the thermo-physical properties of 58Bi-42Sn was performed to evaluate the thermo-physical properties at a heating and cooling rate of 40 °C/ min, which are presented in Figure 2-45, and Table 2-30.

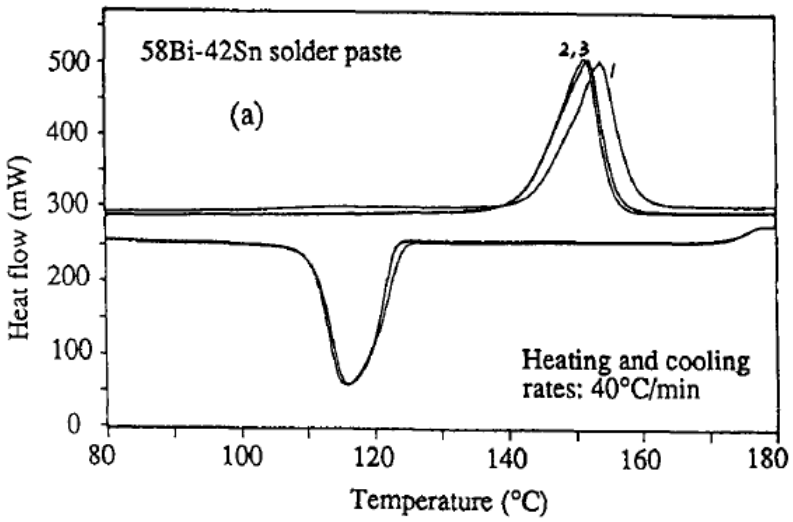

Figure 2-45: Differential Scanning Calorimeter results of 58Bi-42Sn [95].

Table 2-30: Thermo-physical properties of 58Bi-42Sn [99].

Melting temperature (°C)	**Density (kg/m^3)**	**Volume change Liquid to Solid**	**Specific Heat (cal/g/°C)**	**Thermal Expansion (1/°C)**
138	8700	+0.77%	0.045	0.000015

2.5 Application of PCMs in TES systems

TES systems using PCMs have been used in different industries. These include solar power plant, photovoltaic system, waste heat recovery, building heating and domestic hot water provision. PCMs store heat as the latent heat and release the energy when there is a shortage on the demand side [100].

Various kinds of materials and their eutectics that were used in heat storage systems were reviewed in [101]. A number of methods were used in order to enhance the thermal performance of the thermal storage systems. One such method is the use of a PCM in combination with another material that has higher thermal conductivity (such as graphite, carbon nanotubes, metal oxides, metallic nanoparticles).

In addition, different geometries and designs were deployed for LHTS systems such as cylindrical, rectangular, triplex with longitudinal and axial fins, cylindrical shell and tube LHTS.

The corrosion of the container due to PCM was also considered. It was observed that aluminium containers are prone to rapid corrosion when PCMs are salt and salt hydrates and that copper corrodes at a slower rate when used with fatty acid and can thus be used as a container.

Furthermore, it was noticed that the stainless steel has a strong resistance to the corrosion and was considered to be the best material for containers of PCM for high-temperature applications. On the other hand, polymers containers were found to be suitable for low-temperature applications.

A mathematical model for single-phase and encapsulated phase change materials based on the enthalpy model was developed in [102]. Temperature and interface profiles for both the charging and discharging processed showed a very good agreement with the experiment and the fluid temperature profile is shown in Figure 2-46. This method of characterization can be used for various initial conditions and any amount of filler and PCMs while providing highly accurate solutions.

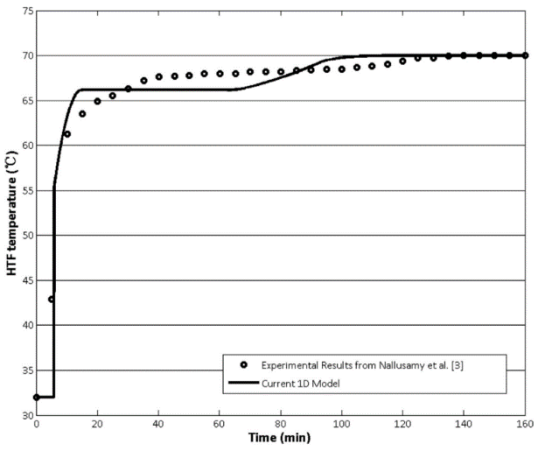

Figure 2-46: Comparison of fluid temperature in the middle of the tank [102].

The dynamic behaviour during charging and discharging cycles of encapsulated PCM for a TES system was experimentally investigated in [103]. Various design and operating parameters were considered during the experiments. Smaller capsules and higher capacitance ratios were found to increase the charging and discharging times. However, increasing the mass flow rate led to a decrease in both the charging and discharging times. The optimum design parameters were proposed and discussed for different working conditions.

Several physical models and empirical correlations for calculations of PCM TES systems were reviewed in [104]. These can be divided into single-phase, concentric dispersion,

and continuous solid phase models. The importance of convective heat transfer, natural convection, and effective thermal conductivity were highlighted, and these were investigated in [105]. Different models were deployed using the same initial and boundary conditions and air and water were used as an HTF. The influence of particle size, material, void fraction and working fluid temperature were all investigated numerically using the finite difference scheme.

A case study of a solar power plant with LHS technology was simulated in [106] using a combination of TRNSYS and EES software. The developed analytical transient model considers the phase change process inside encapsulated spheres placed in the cylindrical tank. The performance of the storage system was evaluated considering the storage and exergy efficiencies. Results show a satisfactory agreement with experimental results from literature data. The results of the comparative study are shown in Figure 2-47.

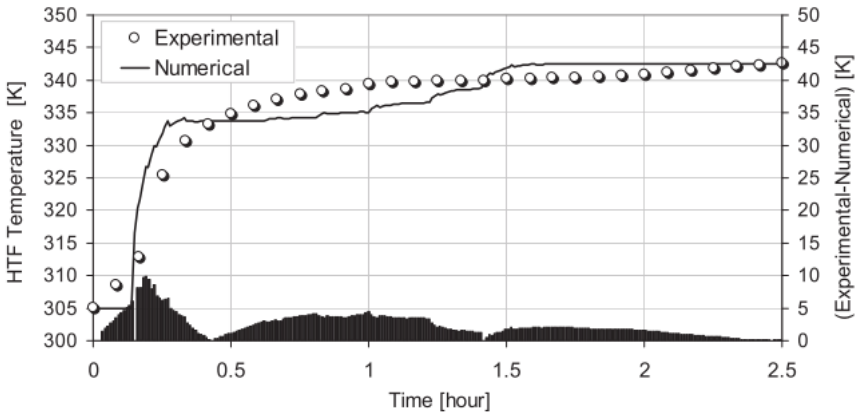

Figure 2-47: Comparison between the numerical simulation and experimental data [106].

The effects of super-cooling were highlighted in [107] with the developed a mathematical model. The system consists of a cylindrical tank filled with encapsulated PCM. The inlet

temperature and the flow rate of HTF were examined and plotted to observe the behaviour of the tank during both the charging and the discharging processes.

Moreover, the super-cooling and heat transfer phenomena were investigated numerically as well as experimentally in [108]. The solidification process was considered using the enthalpy model. The results were in agreement with that in the open literature.

One-dimensional moving boundary problem, known as the Stefan problem, was solved in [109] for the PCM melting process. The results of the Hopscotch method were compared with the exact solution of the Neumann type boundary condition and a good agreement was achieved. The enthalpy method was demonstrated to be efficient for simulating the moving boundary during the PCM melting process.

A literature review of the cooling of photovoltaic power systems was presented in [110]. PCMs can be used to delay the increase of the panel's temperature. It was found that PCMs increase the efficiency of a solar panel at the peak load and that the increase in efficiency occurs in high solar radiation areas.

Furthermore, it was also noticed that a combination of PCM with natural ventilation or heat sink, improves the overall efficiency of the panel. The OPCMs can be used at the desired operating temperature of around 25 °C. However, they are ineffective at the peak load.

On the other hand, high melting temperatures of around 30 °C are ineffective during the day. It is thus recommended to select the PCM melting temperature and thickness based on the peak load. Salt hydrates and organic PCMs demonstrated in a number of studies to achieve the highest efficiency performance and the optimum economic outcome.

An insulated house with PCM/air system for four different climates of French cities was simulated in [111]. TRNSYS software was used in combination with MATLAB to count the variable number of air units in the simulation. The results revealed that partial solidification occurs during the night and hence the PCM does not work efficiently. It was also demonstrated that using the PCM improved the thermal comfort at four cities better than air ventilation system without PCM.

The melting process inside a cavity was studied in [112] to enhance the efficiency and life cycle of a power battery. The effects of heat generation and heating wall locations were studied to enhance the heat transfer performance of the PA-based system. It was shown that the location of the heating wall was a dominant factor in the melting process.

Passive heating using PCMs was reviewed in [113]. Different PCMs such as PA, fatty acids, as well as esters were considered in the study. Various applications of PCMs in passive heating were discussed, such as gypsum wallboard, floors, ceilings, concrete blocks, roofs, and bricks. Impregnation of porous materials by PCMs, integration of microencapsulation and using macro encapsulated PCMs in buildings are considered the main incorporation methods of PCMs into buildings.

The study recommended further investigations on large-scale buildings. It was found that adding up to 3-5 wt% of PCM does not deteriorate the mechanical properties of concrete.

In addition, further work on mathematical models that predict the performance of building under various climates was also proposed along with investigations on the optimization of PCM-integrated buildings. It was suggested that further development and enhancement technologies were required to reduce the costs of microencapsulated PCMs for building applications.

Synthesis technologies, applications, and characterization of micro-encapsulated PCMs (MPCMs) were summarized in [114]. The MPCMs are popular in various applications such as in the pharmaceutical industry, food industry, agriculture, and TES systems. MPCM requires different materials in the synthesis process. For example, the core materials that are used in MPCMs are OPCMs because their melting temperature provides the thermal comfort range for humans, which is about 20 °C.

On the other hand, various materials are used to form the shell of capsules including organic, inorganic and organic-inorganic materials. Shell materials should prevent leakage and reacting with the core PCM as well as provide thermal stability. Various agent materials are required for MPCM such as an initiator which is used as an external heating agent or ionizing radiation in radical polymerization techniques.

It was found that cross-linking that links two different polymer chains through chemical bonds requires nucleating agent because the OPCM is super-cooled in a short period of time when it is encapsulated in the microcapsules.

Consequently, a wide range of shell materials was tabulated and summarized together with the required agents and operating conditions. The shell of MPCM is formed through physical synthesis methods, such as spray drying, chemical synthesis methods which include suspension polymerization, emulsion polymerization, interfacial polymerization, and condensation polymerization and physical-chemical synthesis methods which include complex coacervation, and the Sol-gel process.

It was found that the selection of MPCMs depends on physical properties such as its efficiency, which is the ratio of undissolved capsules to the original sample, microcapsule size distribution, encapsulation ratio, which is the ratio of PCM to the shell material

volumes, shell characteristics, and density. Chemical properties that measure the chemical composition of the material are characterized using various methods like Fourier transformation infrared spectroscopy (FT-IR) analysis.

In addition, thermal properties including thermal stability, which is measured by differential scanning calorimetry (DSC) analysis, thermo-gravimetric analysis (TGA), flammability, thermal reliability, and conductivity are also properties that influence the selection of MPCMs.

Therefore, MPCMs have been used in diverse applications in passive and active systems such as in buildings to maintain stability of thermal fluctuations, textiles to protect from a cold weather, slurry in which they are used in active systems by mixing HTF with the PCM to enhance its properties and in composite foam to improve the heat-insulating properties of polyurethane materials by embedding them with PCM.

Moreover, there is a significant potential for further research related to the performance of MPCMs in various other building applications and materials.

Various comprehensive reviews presented several types of PCMs in a wide range of applications. For example, a review on OPCMs highlighting their resistance to segregation, supercoiling and non-corrosion were presented in [115]. The encapsulation method was utilized to enhance the thermal conductivity, which is divided into using micro and macro MPCM. OPCMs were used in the extreme cooling/heating of buildings, cooling of electronic devices, solar energy storage, automobile applications, and food industries.

Future studies should consider the nano-organic or bio-organic PCMs as they provide higher thermal conductivity, appropriate thermo-physical properties, and have a higher

melting temperature. In addition, nano-capsules should be explored more because of their mixing properties with other materials.

The encapsulation techniques were reviewed and summarized in [116] along with the influence of synthesis parameters for IOPCMs. Encapsulation methods can be classified into core-shell phase change materials (CS-PCMs), in which PCMs are covered by another material like a shell, and shape-stabilized PCMs (SS-PCMs), in which the PCMs are compound with other materials such as porous media.

Consequently, encapsulation methods were summarized and tabulated for IOPCMs such as Emulsion, in situ and the sol-gel process. Thermal properties of various inorganic encapsulation methods of PCMs were also tabulated and summarized for a wide temperature range. It was shown that an enhancement in the thermo-physical properties by controlling the encapsulation factors, such as the solvent, stirring rate, and mass ratio can be achieved.

A comprehensive review of IOPCMs was presented in [77]. The work highlighted several factors for selection of IOPCMs, such as the thermal, physical, kinetic, chemical and economic factors. Generally, IOPCMs consist mainly of salt hydrates, metals, and alloys. They have double the heat storage capacity per unit volume, higher thermal conductivity, higher operating temperature, and lower cost compared to OPCM. The chemical formula of salt hydrate is AxBy.n(H_2O) which consists of metal carbonate, sulfite, phosphate, nitrite, acetate or chloride, and water.

In addition, numerous solutions have been developed to overcome the various disadvantages of salt hydrates. For instance, the change in volume at phase transition is considered a serious problem on which there is a lack of studies. Furthermore, the use of

various materials that have higher thermal conductivity or the use of fins and the encapsulation method to enhance the low thermal conductivity were demonstrated.

Furthermore, mixing nucleation seeds or using a cold finger technology were reported for tackling super cooling problems. Similarly, various kinds of nucleating materials were used in order to prohibit the corrosion phenomenon.

In addition, the cost of IOPCMs and environmental concerns were also considered as problems. Finally, salt hydrates have different melting temperatures due to the attached water not being enough to dissolve anhydrous salts. While this problem can be solved by increasing the amount of water in solute, the mixture would not be in equilibrium at the melting point.

A new classification of operating PCM systems was introduced by [117]. Continuous operation systems, in which the generation and absorption process takes place simultaneously, use an electrical power pump circulation. The intermittent systems utilise the generated pressure by isochronic heating and the absence of separate absorber.

The main design parameters that improve the performance and thermal reliability of the system such as thermal, kinematic, chemical and physical properties and economic factors were summarized and tabulated in [117]. For instance, organic and inorganic materials were considered the most important elements in latent energy storage, and as such their properties were studied and tabulated.

Consequently, the latent heat process is used in various applications as it stores more energy than the sensible heat process, such as the case in a solar collector, which depends on the operating and fluid temperatures.

Moreover, several types of heat exchangers including generators, evaporators, and condensers have seen their efficiency improved and power consumption decreased by utilizing PCMs.

Finally, the main challenging points in the selection of PCMs are the higher heat of fusion and temperature for the melting and solidification process without sub-cooling. Shell and tube heat and multi-tube exchangers are efficient designs of a storage tank where the thermal behaviour should be studied for the charging and discharging processes that depend on the heat transfer rate in the PCM.

It was found that the microencapsulation method increases the heat transfer area and overcomes the segregation problem in salt hydrates and that the sub-cooling phenomena could be solved by using the nucleating agents. Phase segregation and high thermal cycling problems require further research.

Using PCMs in different applications considering the method of integration and other selection criteria was summarized in [118]. The study considered the enhancement methods and highlighted the challenges and potential solutions for the low-temperature range of a solar absorption system. The use of microencapsulation to enhance heat transfer area, thermal conductivity and to decrease the segregation issue was highlighted.

Furthermore, nano-fluids were studied extensively due to their ability to decrease the melting time and enhance thermal conductivity. The optimum selection of PCMs depends on the amount of heat fusion and the precise melting temperature. Further research into nano-scale, high-temperature LHS, phase-segregation, sub-cooling and reliability of the products was recommended.

A review of TES systems for the buildings sector based on PCMs was presented in [119]. The authors studied the thermo-physical and chemical properties of PCMs and their potential applications. Selecting PCMs is considered a key factor in achieving the required performance. TES systems can be classified into passive, active and passive-active systems.

A literature review of the PCMs in the range of 0-250 °C was carried out in [120]. Organic and salt hydrates are suitable for applications under 100 °C, whereas the eutectic compounds are suitable for the temperature range of 100-250 °C. Most PCM containers are classified into compact containers, in which water is generally used as HTF and is surrounded by the PCM, and the encapsulated container, in which the PCM occupies small containers such as capsules with a diameter between 1-1000 μm.

It was found that the compact LHSS has higher volumetric ratios than the encapsulated LHSS, while, the encapsulated LHSS has higher heat transfer area per system volume. Various methods of enhancing heat transfer were analysed such as the use of extended metal surfaces, using carbon, metal matrices, conductive powders, and direct heat transfer techniques.

State-of-the-art PCMs for passive heating systems were summarised in [121], The PCMs were classified into organic, inorganic and eutectics. The cases in which PCMs were used in building applications for free cooling, peak load shifting to decrease temperature fluctuations and increase the thermal comfort, were considered.

In [10], increasing the insulation material as well as using PCM were the main strategies to mitigate heat transfer through building's walls. A lack of studies regarding the

performance of PCMs in construction applications for various weather conditions was stressed in [122].

Cooling systems were investigated in [121] and it was found that the power consumption in systems with PCMs and the emission of CO_2 were reduced compared to the ice system and the payback period was approximately four years. It was found that OPCMs are suitable for use in cooling systems in construction applications.

Heat transfer inside TES systems filled with PCMs for construction applications was inspected in [123]. Free-form and microencapsulated PCMs were used and the natural convection and sub-cooling phenomena were considered during the experiments.

It was found that the natural convection is dominant in the melting process of free-form PCMs and causes thermal stratification in the TES but can be neglected during the melting of MPCMs.

However, while it can be also neglected during the discharging process, the effect of sub-cooling must be considered for free-form PCMs. It was also found that increasing the number of fins increases the heat transfer up to a certain amount, however, this increase also results in a heavier system.

A comprehensive study of state-of-the-art technologies for construction architecture in hot and dry applications was reported in [124]. Fatty acids were used as an OPCM. The macro-encapsulation method was described which is the process of adding the PCMs directly into the construction material such as concrete and plaster during construction.

Drawbacks of that method include PCM leakage and in some cases incompatibility with the construction materials. The immersion method is also used which is the construction

materials, such as concrete, gypsum, and brick, being immersed into the melted PCMs. Applications of PCMs such as their use in Trombe-wall, shutters, floors, ceilings, and wallboards were discussed in [124].

Recent advances in using PCM in LHSS over 100 °C were reported in [125]. LHS systems were classified into three main categories: Indirect-passive which includes shell and tube heat exchanger and packed bed, Indirect-active such as a Fluidized bed and Direct-active. Common PCMs candidates were used in the LHSS such as sugar alcohol, molten salt, and alloys.

It was found that each type has its own melting temperature and involves a specific temperature range. Generally, the melting temperature of sugar alcohol, molten salt and alloys are in the temperature range of 100-200 °C, over 300 °C and over 500 °C, respectively.

Sugar alcohol provides many advantages, such as high storage density, non-toxicity, non-flammability and non-corrosion with the metal container. However, its drawback is its low thermal conductivity.

On the other hand, molten salts such as nitrates, carbonates, and chlorides were considered effective PCMs to be used in TES systems. However, molten salts have three main drawbacks which are: low thermal conductivity, high-volume expansion ratio, and corrosion.

Finally, metal alloys provide many advantages and therefore have become popular in various applications. Their advantages include high heat storage capacity, high latent heat per unit volume, low thermal expansion ratio and high thermal conductivity, while their

drawbacks included corrosion. The correlation between the energy level and the exergy based on the melting temperature and latent heat of PCMs is shown Figure 2-48.

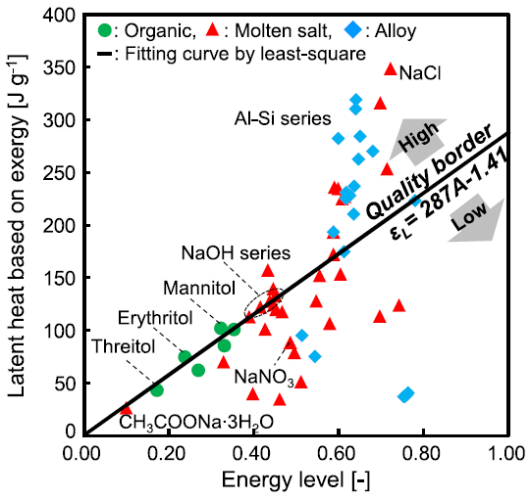

Figure 2-48: The correlation between the energy level vs. the Latent heat [125].

Figure 2-48 shows the various types of PCMs divided into high and low-quality materials. The material under the line such as $NaNO_3$ or $NaNO_3$–KNO_3 are considered as low-quality material and should not be selected for use in LHTES systems. It was recommended that the principle of exergy should be used in order to select high-quality PCMs candidates. Furthermore, it was shown that MPCM and catalyst PCMs have good potential for high-temperature applications in LHS systems.

A new TES system for a solar collector that works at the temperature up to 440 °C using encapsulated PCM was designed and built-in [126]. A mathematical model was developed and validated using the experimental investigations of the charging and discharging rates. PCM capsules were filled with $NaNO_3$.

In addition, experimental and numerical investigations showed that the system demonstrated good energy performance in both the charging and the discharging cycles.

The system demonstrated its ability to successfully transfer the thermal energy between the transport fluid and capsules which is illustrated in Figure 2-49.

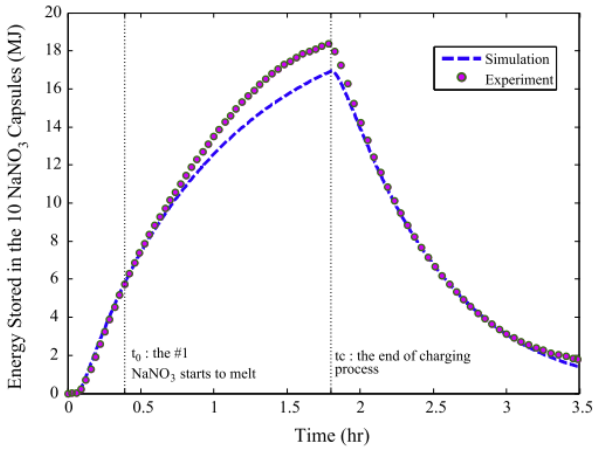

Figure 2-49: The energy stored in the 10 $NaNO_3$ capsules in a thermal cycle [126].

A shell and tube LHTS system was investigated numerically and analytically in [127]. H_2O/LiBr was used as HTF. It was found that the natural convection was dominant in the solidification process and as such cannot be neglected. It was also shown that this type of absorption system provided 100 -kW peak cooling demands without external energy input.

A concentrated solar power tower working in the temperature range of 286-565 °C was modelled in [128]. In the optimization work, a fixed amount of PCM was deployed while varying the geometric parameters. The results revealed that there was an optimum heat transfer surface for each PCM.

The addition of a TES system into a Dish-Stirling system was reported in [129]. Various PCMs were identified as candidates based on their melting temperature, cost, and performance. A metallic alloy of CaSi and CuMgSi was considered as a PCM for dish

Stirling application. It was found that the CuMgSi as PCM had a high heat of melting and the cost was reasonable for this particular application.

Numerical modelling of packed bed LHTES filled with spherical PCMs was proposed in [130]. The system was considered as porous media immersed in a heat transfer fluid. Energy equations accounting for the thermal energy transport between the PCM and HTF were introduced. The non-equilibrium models with two different temperatures and the enthalpy method were applied to simulate the phase change process.

In addition, different parameters were investigated such as the HTF's mass flow rate, the inlet-charging temperature, and the storage system dimensions. The mass flow rate and inlet-charging temperature were found to increase thermal performance during storing and retrieving energy. The overall effectiveness of the system was not impacted by the porosity and the storage system dimensions.

Another model for packed bed catalytic reactors was proposed in [131]. The developed model considered the effect of heat conduction through a solid phase. It was modified by considering a lager coefficient of fluid dispersion at low flow rates.

The behaviour of a packed bed using molten salt as HTF with capsules of PCM as a filler was investigated in [132]. The concentric-dispersion model and the enthalpy model were used which were based on using a finite difference approach. The capsule diameter, fluid inlet velocity, storage tank, and charge efficiency were studied and plotted and are shown in Figure 2-50. It was found that the small particle diameter leads to a higher charge efficiency.

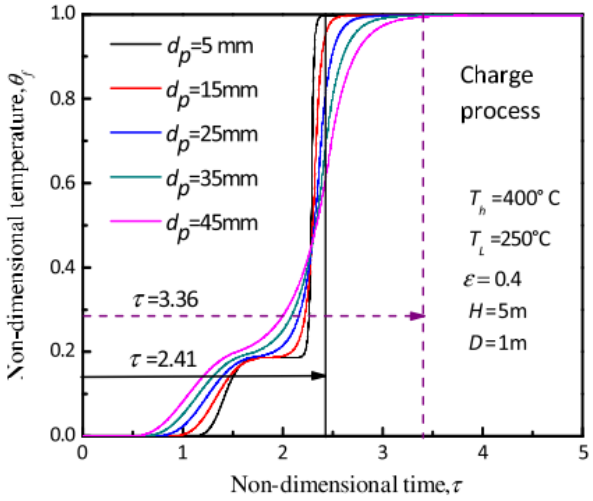

Figure 2-50: Temperature profiles of molten salt at Y = 0.5 for different particle diameters [132].

2.6 Corrosion and thermal stability problems in the application of PCMs

The PCM container's operational life and the thermal stability of PCM ensure long term working period of TES systems.

The corrosion issue occurs between the PCM and the container material. This issue was studied in [118] to provide suitable combinations of PCM and containers. The findings of the study are shown in Table 2-31.

Table 2-31: A list of compatible PCMs and container materials [118].

PCM	**Melting Point** (°C)	**reference**	**Brass**	**Copper**	**Aluminum**	**Stainless steel**	**Carbon steel**
$Zn(NO_3)_2 \cdot 6H_2O$	36	[133]	No	No	No	Yes	No
		[134]	No	No	No	Yes	No
$Na_2HPO_4 \cdot 12H_2O$	35	[133]	Yes	Yes	No	Yes	No
		[134]	Yes	Caution	No	Yes	Caution
$CaCl_2 \cdot 6H_2O$	32	[133]	Yes	Yes	No	Caution	No
		[134]	Yes	Yes	Caution	Yes	Caution
$NaOAc \cdot 3H_2O$	58	[135]	Caution	Caution	Yes	Yes	Yes
$Na_2S_2O_3 \cdot 5H_2O$	48	[135]	No	No	Yes	Yes	Yes
$Mg(NO_3)_2 \cdot 6H_2O$	89	[136]	No	No	Yes	-----	-----
S46 ($Na_2S_2O_3 \cdot 5H_2O$ + sepiolite + fumed silica)	46	[137]	-----	No	Caution	Yes	No
C48 ($CH_3OONa + H_2O$ + additives)	48	[137]	-----	No	Yes	Yes	Yes
$MgSO_4 \cdot 7H_2O$	48.5	[137]	-----	No	Yes	Yes	No
$Zn(NO_3)_2 \cdot 4H_2O$	45.5	[137]	-----	No	No	Yes	No
$K_3PO_4 \cdot 7H_2O$	45	[137]	-----	No	No	Yes	Yes

While salts hydrates were used in various applications, they cause the corrosion of container materials. The corrosion studies were performed in numerous works because it causes serious damage to containers. Various container materials were investigated in [138] in order to find out the most appropriate ones for salt hydrates.

Table 2-32 below summarises all the trials that were conducted in order to investigate the corrosion effect.

Table 2-32: Summary of the suitability of PCMs with stainless steel container materials [8].

Containers materials	**The recommended type of PCM**	**The recommended type of PCM**
Stainless steel	$MgCl_2$ [139]	Na_2SO_4·½ NaCl·$10H_2O$ [140]
	$Ca(OH)_2$ [139]	PCM-A ((C−18): $NaNO_3$ + H_2O + additives
	Na_2S [139]	Climator) [141]
	$CaCl_2$ ·$6H_2O$ [139, 140, 142]	PCM-B ((E−21): NaCl + H_2Oa Cristopia) [141]
	$Zn(NO_3)_2$ ·$6H_2O$ [134, 142]	PCM-C (NaCl + H_2Oa Cristopia + 1% CMC
	Na_2HPO_4 ·$12H_2O$ [134, 142]	Modified from Cristopia) [141]
	NaOAc·$3H_2O$ [135]	PCM-D (19% NH_4Cl + H_2O Own formulation) [141]
	Na_2SO_4·$5H_2O$ [135]	PCM-E (19% NH_4Cl + H_2O Own formulation +
	S10 [137]	1% CMC Own formulation)[141]
	C10 [137]	PCM-F (19% NH_4Cl + H_2O Own formulation +
	$ZnCl_2$·$3H_2O$ [120]	3% AlF_3 Own formulation) [141]
	NaOH·$5H_2O$ [137, 140]	S46 [137]
	K2HPO_4·$6H_2O$ [137]	C48 [137]

The corrosion behaviour of copper and carbon steel in nitrate hydrates was studied in [143, 144]. Several PCMs were used in the experiments, such as magnesium nitrate hexahydrate, calcium nitrate tetra-hydrate and a mixture of them. The results of the effect on container materials used can be summarised in Table 2-33.

Table 2-33: Corrosion rate of the carbon steel material in contact with salt hydrates [109, 110].

PCM	**Corrosion 1/(mg cm^{-2} year^{-1})**	
	Copper	**Carbon steel**
$Mg(NO_3)_2 \cdot 6H_2O$	8.6	11.9
$Mg(NO_3)_2 \cdot 6H_2O$ + 0.5 wt. % $Mg(OH)_2$	8.9	14.7
$Mg(NO_3)_2 \cdot 6H_2O$ + 0.5 wt. % $Sr(OH)_2$	5.4	33.3
$Mg(NO_3)_2 \cdot 6H_2O$ + $Ca(NO_3)_2 \cdot 4H_2O$ (1:1)	1.5	4.6
$Ca(NO_3)_2 \cdot 4H_2O$	5.4	24.7

It was found that the lowest corrosion rates in copper and carbon steel were when the mixture of $Mg(NO_3)_2 \cdot 6H_2O$—$Ca(NO_3)_2 \cdot 4H_2O$ (1:1) was used.

In addition, the corrosion effect of salt hydrates $MgCl_2 \cdot 6H_2O$ and bischofite were studied in [145]. The corrosion tests were performed on various metal sheets at a temperature of 120 °C during 1500 h. Scanning Electron Microscopy (SEM-EDX) and X-ray Diffraction (XRD) techniques were used in order to determine the corrosion, during which cuprite (Cu_2O) and hematite (Fe_2O_3) were formed on the copper and stainless steel samples respectively.

It was found that a little corrosion occurred in the immersed part of the different materials, while very severe corrosion was noticed at the salt-air interface due to the presence of air

enhancing the corrosion rate. The results of all the experiments are summarised in Table 2-34.

Table 2-34: Corrosion test results for studied PCMs [111].

PCMs	Metal Sample	recommended	Reference	PCMs	Metal Sample	recommended	Reference
Eutectic mixture $Mg(NO_3)_2 \cdot 6H_2O$ + $MgCl_2 \cdot 6H_2O$	1% Carbon steel	No	[146, 147]	Mixture $Mg(NO_3)_2 \cdot 6H_2O$ + 10% $MgCl_2 \cdot 6H_2O$	Aluminium	Yes	[148]
	Copper AISI-403	No			Copper	No	
		Yes			Brass	No	
Mixture 2:1 TH29 ($CaCl_2 \cdot 2H_2O$) and $MgCl_2 \cdot 6H_2O$	Aluminium	No	[149]		Carbon Steel	No	
	Copper	Yes			SUS304	No	
	Brass	Yes			SUS 316	Yes	
	Steel	No		$MgCl_2 \cdot 6H_2O$	Aluminium	No	[145]
	Stainless steel	Yes			Copper	No	
$MgCl_2 \cdot 6H_2O$	Aluminium	No	[150]		Stainless steel	No	
	Stainless steel	No					

Thermo-physical properties, including thermal stability of PCMs, were highlighted in various studies. For instance, the thermal stability of organic and inorganic materials in repetitive thermal cycles (to determine the change in melting temperature) and latent heat (to provide long-term performance and economic feasibility) were studied in [151].

The experiments were carried out using 200g of the PCM in the temperature range of 20-200 °C. The DSC was used to measure the latent heat and 1000 thermal cycles were performed. It was shown that the organic material was suitable for LHTE storage purposes. PA wax (A, B, C) and erythritol have shown good thermal reliability, with PA-C proving to be the most suitable PCMs. While, erythritol was found to be suitable for higher temperatures, on the contrary, IOPCMs did not demonstrate good thermal stability.

Two different organic materials, benzamide, and sebacic acid were investigated in [152]. The tested materials demonstrated good thermal reliability of their thermo-physical properties. It was also observed that studied materials were suitable for solar thermal applications in the temperature range of 120-135 °C.

A numerical model (CP-T based) for the different heating/cooling rates was developed in [153]. The charging/discharging time of PCM and the air temperature were simulated using Fluent and compared with the experimental results where a good agreement was demonstrated by selecting the correct thermo-physical properties of PCM and the proper solution method.

The use of PCMs crucially depends on their thermal stability in order to maintain the efficiency of LHS systems. As such, this issue has been explored to ensure the long lifetime and economic feasibility of the system. The thermal stability of various PCMs was summarised in [154]. DSC was used to measure the thermal stability as a function of

repeated thermal cycles. The thermal stability for various PCMs including paraffin, salt hydrates, and inorganic eutectics are listed in Table 2-35, Table 2-36 and Table 2-37.

Table 2-35: Thermo-physical properties of thermally stable PAs [116].

PCMs	**Melting Point (°C)**	**Latent heat (J/g)**	**Thermal cycles**	**reference**
Paraffin (70wt%) +Polypropylene (30 wt%)	44.77	136.16	3000	[155]
Paraffin (C22.2H44.1), technical grade	47.1	166	900	[156]
Paraffin (C23.2H48.4), technical grade	57.1	220	900	[156]
Paraffin wax 53 (commercial grade)	53 53	184 184	300 1500	[157, 158]
Paraffin wax 54	53.32	184.48	1500	[151]
Paraffin wax 58–60	58.27	129.8	600	[151]
Paraffin wax 60–62	57.78	129.7	600	[151]
n-Heptadecane/polymethyl methacrylate (C17H36) 44.77	18.8	84.7	5000	[151]

Table 2-36: Thermo-physical properties with thermal instability for some salt hydrates [116].

PCMs	Melting point (°C)	Latent heat (J/g)	Thermal cycles	References
Calcium chloride hexahydrate ($CaCl_2 \cdot 6H_2O$)	29.8	190.8	1000	[159]
	28	86	1000	[160]
	27	-	5650	[140]
	23.26	125.4	1000	[151]
Glauber's salt ($Na_2SO_4 \cdot 10H_2O$)	32.4	238	320	[161]
	32	-	5650	[140]
Magnesium chloride hexahydrate ($MgCl_2 \cdot 6H_2O$)	111.5	155.11	500	[162]
	110.8	138	1000	[163]
$Na_2SO_4 \cdot nH_2O$	-	-	1000	[164]
$Na_2SO_4 \cdot 1/2NaCl \cdot 10H_2O$	20	-	5650	[140]
$NaOH_3 \cdot 5H_2O$	15	-	5650	[140]
Sodium acetate tri-hydrate ($NaCH_3COO \cdot 3H_2O$)	58	230	500	[165]
	58	252	100	[166]
Tri-chloro fluoro methane hepta-deca hydrate ($CCl_3F \cdot 17H_2O$)	8.5	210	100	[167]

Table 2-37: Thermal stability of selected salt hydrates [2].

Type of PCM Ref.	Melting point (°C)	Latent heat of fusion (kJ/kg)	Thermal cycles	References
$CCl_3F \cdot 17H_2O$	8.5	210	100	[167]
$K2HPO_4 \cdot 6H_2O$	14	109		[168]
$NaOH_3 \cdot 5H_2O$	15	----	5650	[140]
$Na2SO_4 \cdot 1/2NaCl \cdot 10H_2O$	20	-----	5650	[140]
Calcium chloride hexa-hydrate ($CaCl_2 \cdot 6H_2O$)	29.8	190.8	1000	[159, 169]
	23.26	125.4	1000	[161]
	27	-----	5650	[140]
	28	86	1000	[160]
Glauber's salt ($Na_2SO_4 \cdot 10H_2O$)	32.4	238	320	[170]
	32	254	5650	[140, 171]
Sodium acetate tri-hydrate ($NaCH_3COO \cdot 3H_2O$)	58	230	500	[165]
	58	252	100	[166]
Magnesium chloride hexa-hydrate ($MgCl_2 \cdot 6H_2O$)	111.5	155.11	500	[162, 172]
	110.8	138	1000	[163]

A number of companies commercially supply various PCMs of any required quantity and Table 2-38 summarises various companies.

Table 2-38: Companies that provide PCMs.

Company	Reference
PCM Energy P.Ltd	[173]
RUBITHERM	[174]
Climator	[175]
PlusICE	[176]
Microtek	[177]
PureTemp	[178]

The thermo-physical properties of 18 salt hydrates were analysed in [179]. It was found that the working temperature of those salt hydrates is in the range of -50 to 120 °C. Salt hydrates can be classified into several main groups, such as lithium chlorate trihydrate and potassium fluoride tetrahydrate.

Further investigations on the thermo-physical properties of pure salt hydrate as well as commercial PCM products using modern instruments and software were recommended. It was also proposed to develop international standards for methods and apparatus being used in measurements of the thermo-physical properties

Results of investigations and developments of various PCMs for TES systems in solar energy applications in the temperature range of 120 to 1000 °C were presented in [180]. A number of PCMs were discussed such as fluorides, chlorides, hydroxides, nitrates, carbonates, vanadates, molybdates as well as other salts and metal alloys and their thermo-physical properties were listed. Table 2-39 shows the properties of PCMs based on nitrate and nitrites.

Table 2-39: Melting and solidification temperatures and heat of fusion for some compounds and compositions based on nitrates and nitrites [147].

Salt composition mol.%	**Melting point (°C)**	**Solidus point (°C)**	**Latent heat of fusion (J/g)**
$NaNO_3$·NaOH	271	213	265
$NaNO_3$·2NaOH	270	218	295
$NaNO_3$(72)–28NaOH	247	213	237
$NaNO_3$(41)–59NaOH	266	221	278
$NaNO_3$(18.5)–81.5NaOH	257	254	292
$NaNO_2$·NaOH	265	228	313
$NaNO_2$(80)–20NaOH	232	232	252
$NaNO_2$(27)–73NaOH	237	227	294

It should be noted that a relatively small number of PCMs were studied and further investigations are required to develop new PCMs with required properties. The authors also highlighted the lack of studies on metallic PCMs for thermal storage systems. Limited attention was given to studying the thermal stability, chemical compatibility and low heat conductivity of salt hydrates. Finally, it should be also noted that cost studies were mostly absent in the open literature.

2.7 Conclusions

The literature has shown that salts and metal alloys have double the value of the heat storage capacity, thermal conductivity and operating temperature range at relatively low cost, compared to the organic PCMs.

The literature examined the corrosive effect of PCMs, which shortens the lifetime and diminishes the performance of TES systems. Therefore, the most compatible container materials and PCMs must be selected when building the TES system.

It has been seen that thermal stability analysis of PCMs should be conducted to ensure the long-life and economic feasibility of the TES system.

Natural convection in some cases has a significant effect and is dominant during the melting and solidification processes, and its intensity depends on the density, viscosity and thermal conductivity of the PCMs.

The literature review demonstrated that solar salt was suitable for medium-temperature applications due to its high latent heat and operating temperature range of 215-250 °C. However, it suffers from the low thermal conductivity, therefore different methods are used to enhance its thermal conductivity, such as the use of various additives and fins.

The use of grpahite additives is considered as an efficient technique to enhance the thermal conductivity of solar salt. The literature review indicates that the use of additives with concentration of less than 5% was investigated. However, that level of concentration of additives resulted in a small-scale enhancement, which does not satisfy industrial requirements. Therefore, it is recommended that higher concentrations are adopted to enhance the thermal conductivity of solar salt to meet industrial needs.

Also, one of the conclusions of the literature review is that no engineering methods were developed to predict the thermal performance of TES systems, which would take into account different concentrations of additives and determine the melting and solidification times as well as the amount of the accumulated or released heat.

The technique of using fins is considered as a promising way to enhance heat transfer through the PCM in TES systems. However, designing a TES system with fins requires determination of fin design parameters, such as the thickness and number of fins with estimation of the resultant impact on the melting and solidification processes and on the amount of accumulated and released energy. However, the literature review revealed that there were no simple engineering methods to predict the thermal performance of TES systems with fins.

The literature review also demonstrated that metal alloys were used for the thermal management or soldering in electronics but very limited information was found on using metal alloys as PCMs in TES systems, because of the cost of these alloys.

The lead-free metallic PCM (Bi-Sn) was considered to be a promising substance as a PCM for low-temperature applications, in the temperature range of 120-140 °C, because it is a non-hazardous material. However, the cost of metallic PCMs is considered to be the main challenge to its adoption in TES systems. Therefore, only low purity metallic alloys can be deployed to achieve a reduction in the cost of metallic PCMs. As in other above cases, the literature review demonstrated that there were no simple engineering methods to evaluate the thermal performance of TES systems with metallic PCMs including melting and solidification times and the amount of accumulated and released energy.

Chapter 3 Experimental methodology and instrumentation

3.1 Introduction

In this chapter, the experimental methodology and instrumentation used for studying TES systems with PCMs are described. The heat source used was in the form of an electrical heating cartridge placed in the centre of the container. The thermal performance of such a TES system was investigated at medium and low temperatures, namely 215-250 °C and 120-140 °C, respectively. The experimental apparatus and the properties of the PCMs used will be presented. The experimental results will be then used to develop a numerical model, which will be used for further investigations.

From a large number of PCMs used for medium- and low-temperature applications, solar salt and a metal alloy were selected for this study. Solar salt ($NaNO_3$ 60% - KNO_3 40%) was selected due to its high latent heat and operating temperature range of 215-250 °C. The low purity Bi 58%-Sn 42% metallic alloy was selected for investigations because it is non-hazardous, inexpensive and has an operating temperature range of 120-140 °C.

Solar salt has a low thermal conductivity, which prolongs the charging and discharging times [13] for TES systems. Therefore, two different methods were used to enhance heat transfer in the TES system, and these are the deployment of fins and the addition of graphite to the PCM.

The metallic alloy used in experiments has high thermal conductivity when it is high purity (around 99.99%), but it is considered expensive [181]. The price of metal alloys is reduced significantly if the purity level is reduced from 99.99 % to about 97%. Therefore, the lower purity metal alloy Bi58%-Sn 42% was used in the investigation for low-temperature applications.

3.2 Experimental setup

Figure 3-1 shows the experimental setup used in this work. It consists of a metallic container with an electrical heating cartridge, PCM, placed inside the container, insulation material covering the container and housing unit, in which the container with surrounding insulation is placed. An array of thermocouples with a data logger and a laptop are used to record temperatures in different locations on the heating cartridge and inside the container during PCM melting and solidification processes. The housing unit is made of pine wood to reduce heat losses from the TES system to the environment. Inside the housing unit, the insulation band material surrounds the metallic container. The melting process and melting time were captured using thermocouples at bottom corners, as described by Abhat in [182]. Power to the heating cartridge was provided using a regulator to control its magnitude. The value of the input power was monitored using the power analyser.

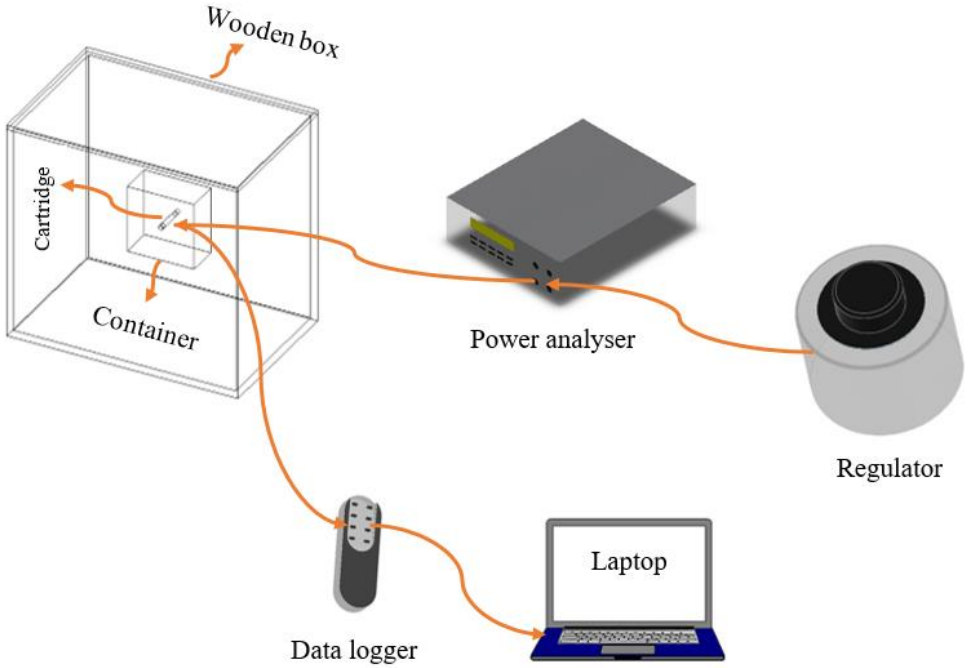

Figure 3-1: Schematic diagram of the experimental TES system.

3.2.1 PCM

3.2.1.1 Solar Salt

Solar salt (60 wt% $NaNO_3$ + 40 wt% KNO_3) was used in this investigation. Two different types of solar salt were analysed. The first one prepared by Aavid Thermacore Ltd using the nitrate salts KNO_3 and $NaNO_3$, which were separately supplied by ACS Material LLC [183] and then mixed at a proportion of 60 % of $NaNO_3$ and 40 % of KNO_3. The second solar salt was acquired from PCM Products in the form of H220 product [176], with a melting point of about 220 °C. Table 3-1 shows solar salts and composites used in each TES system.

Table 3-1: TES system with different types of containers.

PCM types	Description of PCM and composite used in TES containers
Solar salt type-I	• Solar salt alone. • Solar salt with 10 wt% graphite.
Solar salt type-II	• Solar salt used in the finned containers.

The $NaNO_3$ and KNO_3 were experimentally investigated separately using DSC Setaram EVO-131, which measures the amount of heat that is required to raise the temperature of a sample within a certain period of time to determine the latent heat and temperatures during melting and solidification processes as well as the specific heat. The measurements were carried out to measure their thermal properties, such as latent heat and melting and solidification temperatures, using 5 deg/min as heating and cooling rates. The thermal properties of the $NaNO_3$ and KNO_3 were evaluated to ensure their suitability for creating a mixture of solar salt. The DSC results for $NaNO_3$ and KNO_3 are shown in Figure 3-2, and Figure 3-3.

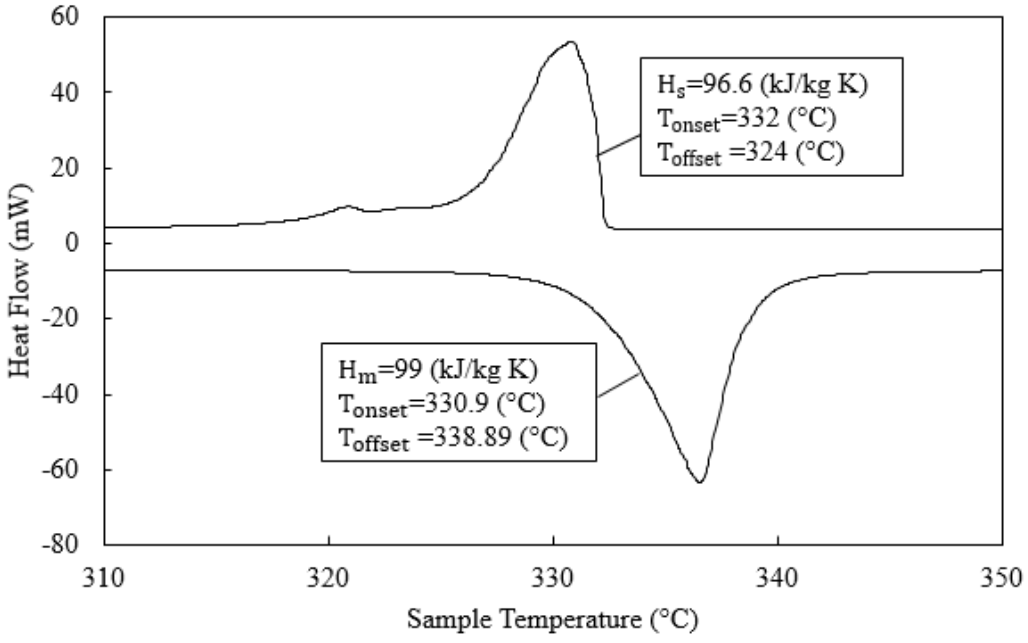

Figure 3-2: DSC curve for KNO_3.

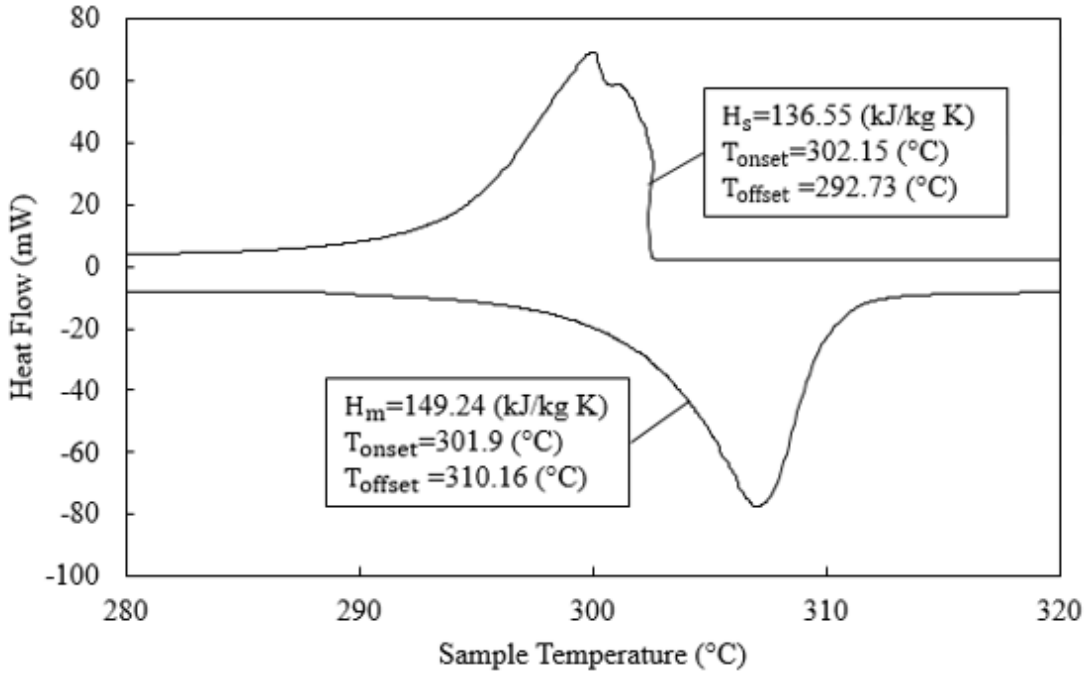

Figure 3-3: DSC curve for $NaNO_3$.

DSC results show that $NaNO_3$ and KNO_3 salts have high values of the latent heat during the melting and solidification processes: 149.24 and 136.55 kJ/K for $NaNO_3$, and 99 and 96.6 kJ/kg K for KNO_3. Also, the obtained DSC results indicate that the melting and solidification temperatures vary in the range less than 10 °C. Therefore, $NaNO_3$ and KNO_3 are used to create solar salt for the application as the PCM in TES systems.

The thermal properties of solar salts such as melting and solidification temperatures, latent heat, thermal conductivity, and heat capacity were also investigated experimentally using DSC. The thermal expansion coefficient and viscosity for this substance were obtained from the literature [31, 186, 187]. The thermal properties for solar salt of types I and II are shown in Figure 3-4 and Figure 3-5 and presented in Table 3-2 to Table 3-5.

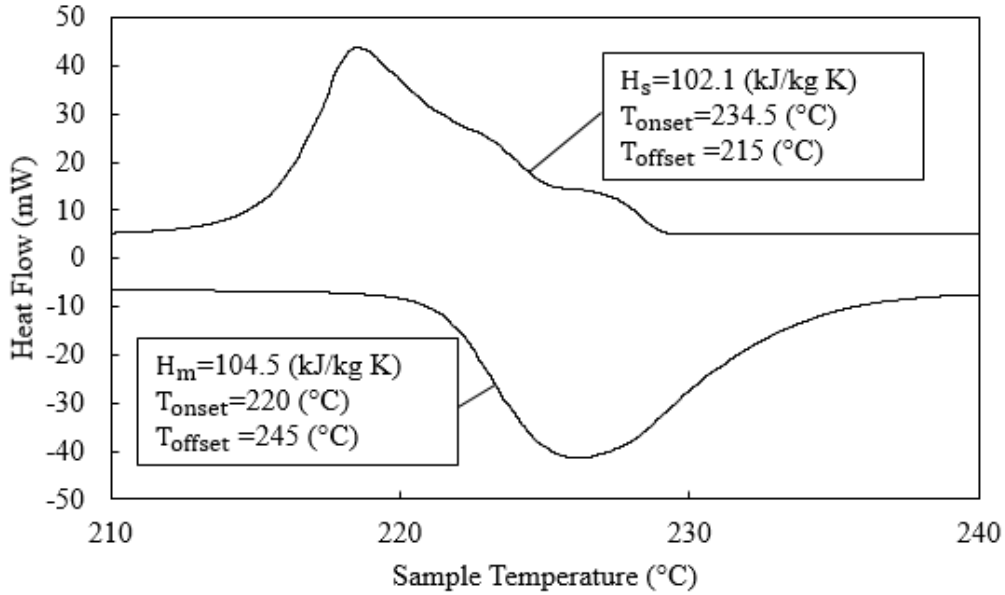

Figure 3-4: DSC curve for solar salt of type-I.

The DSC results show that solar salt, created by mixing $NaNO_3$ and KNO_3 at a certain proportion, has the high value of the latent heat, namely 104.5 and 102.1 kJ/kg K during melting and solidification processes, respectively. In addition, the melting and solidification temperature variation range is 25 °C and 15 °C, respectively. Therefore, the solar salt can be used as the PCM for medium-temperature applications.

DSC results on the specific heat (Cp) value for solar salt (type-I and type-II) showed that it is almost constant for solid and liquid phases during charging and discharging processes and the constant heat capacity value was used in the further analysis.

Table 3-2: Measured physical properties of solar salt of type-I.

	T_{onset} (°C)	**T_{offset} (°C)**	**ΔH (kJ/kg)**	**Density (kg/m^3)**	**Cp (J/kg °C)**	**λ (W/m°C)**
Melting	220	245	104.5	1958	1102	0.318
Solidification	234.5	215	102.1			

Table 3-3: Thermal properties of solar salt of type-I.

Properties	**value**
Thermal Expansion Coefficient. (1/K) [5]	*3.47 · E-04*
Viscosity in the liquid state (kg/m s) [10-11]	*1/(–0.263 + 0.002 · T (°C))/1000*

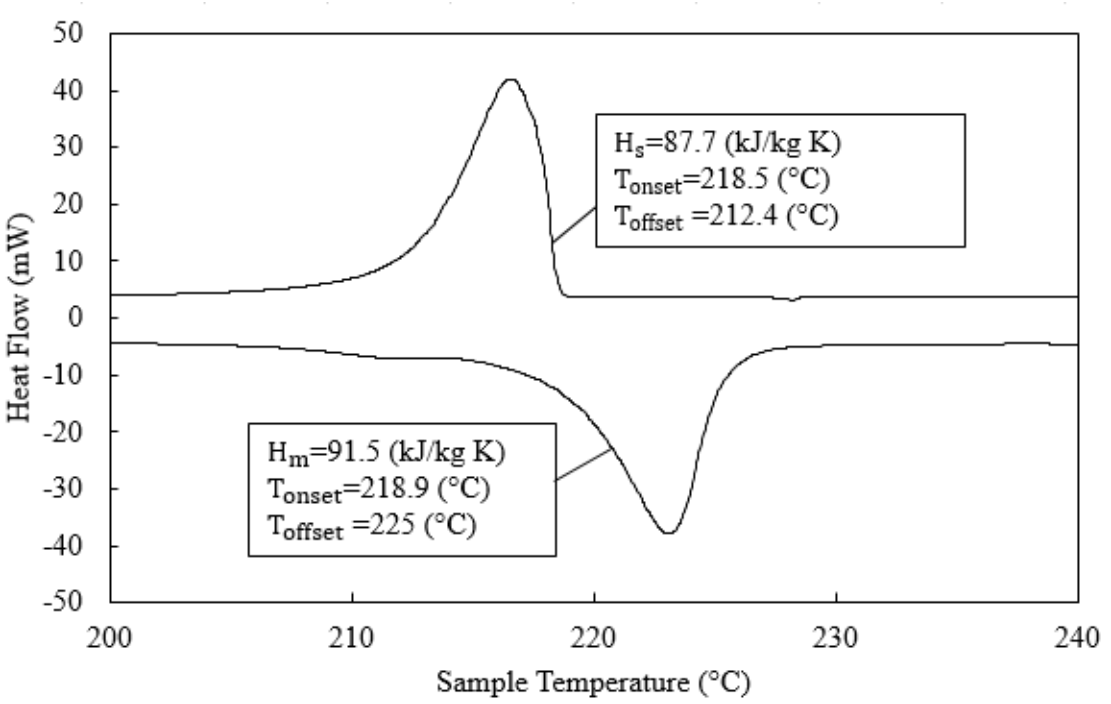

Figure 3-5: DSC curve for solar salt of type-II.

DSC results demonstrate that the latent heat of solar salt type-II is less than 100 kJ/kg K, namely 91.5 and 87.7 kJ/kg K during the melting and solidification process, respectively. The melting and solidification temperature variation ranges are 6.1 °C and 6 °C, respectively. However, it still can be used for the medium-temperature applications due to the narrow melting and solidification temperature ranges.

Table 3-4: Measured physical properties of solar salt of type-II.

	T_{onset} (°C)	T_{offset} (°C)	ΔH (J/kg)	C_p (J/kg °C)
Melting	218.9	225	91.5	1620
Solidification	218.5	212.4	87.7	

Table 3-5: Thermal properties of solar salt of type-II.

Properties	value
Density (kg/m^3) [5]	1958
Thermal Expansion Coefficient. (1/K) [5]	3.47·E-04
Thermal Conductivity (W/m K) [5]	$0.38+3.452\cdot10^{-4} \cdot T(°C)$
Viscosity in the liquid state (kg/m s) [10-11]	$1/(-0.263 + 0.002 \cdot T(°C))/1000$

3.2.1.2 Graphite

Graphite was adopted to improve the overall thermal conductivity of the solar salt due to its high thermal conductivity. It was provided by ACS Material LLC [183]. The thermal properties of graphite are shown in Table 3-6. The weight composition of graphite in the mixture with solar salt type-I by Aavid Thermacore Ltd is 10 wt%, see Figure 3-6. Normally, the thermal conductivity depends from the direction and is different in parallel or perpendicular directions to the plane of a single molecular. Therefore, two different thermal conductivities can be obtained depending on the bonds between the carbon molecules. However, in case of a mixture (solar salt with 10 wt% graphite) a bulk thermal conductivity value will be used.

Table 3-6: Thermal properties of graphite [183, 184].

Property	Value
Density (g/cm^3)	2-2.5
Particle size (μm)	<50
Thermal Conductivity (W/m K)	80 (perpendicular) 160-200 (parallel)
Thermal Expansion (μm/m °C)	20
Maximum operating temperature (°C)	2300

Figure 3-6: Solar salt mixture with graphite (10wt %).

The thermal properties of the compound mixture were determined experimentally and from the literature. The melting and solidification temperature, the heat of fusion and specific heat were investigated experimentally using DSC, as shown in Figure 3-7. Also, the bulk thermal conductivity and density of the PCM were measured by the National Physical Laboratory. On the other hand, the viscosity was calculated using the Einstein correlation [185], which can be expressed by:

$$\mu_{nf} = \mu_{bf}(1 + 2.5 \cdot \emptyset) \quad (3\text{-}1)$$

Here, $\mu_{nf}$is the viscosity of the base fluid, $\mu_{bf}$is the viscosity of the base fluid, and $\emptyset$ is the percentage of the additives.

The thermal properties for solar salt/graphite composition are presented in Table 3-7, and Table 3-8.

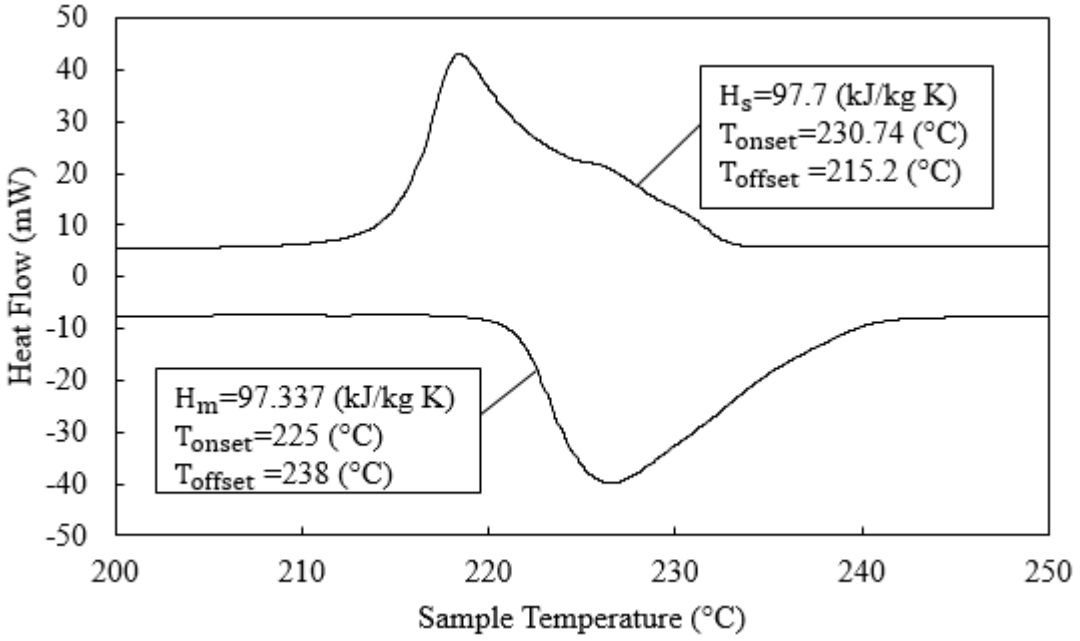

Figure 3-7: The DSC curve for solar salt type-I with 10 wt% graphite.

The investigations using DSC revealed that the amount of latent heat during melting and solidification processes was reduced by 6.7% because of the addition of graphite. It was shown that the melting and solidification temperature ranges were reduced due to addition of graphite. Despite the reduction of the thermo-physical properties, such as the latent and specific heats and melting and solidification temperature ranges, an increase in the thermal conductivity of solar salt with 10 wt% of graphite from 0.318 to 1.455 W/m °C was obtained. Therefore, the mixture of solar salt and 10 wt% of graphite is considered sufficient for medium-temperature applications.

In addition, it was obtained that the specific heat (Cp) value was almost constant for solid and liquid phases during charging and discharging processes. This is why the constant value of the heat capacity was used in further investigations.

Table 3-7: Measured thermal properties of solar salt type-I with 10 w% graphite.

	T_{onset} (°C)	T_{offset} (°C)	ΔH (kJ/kg)	Density (kg/m^3)	C_p (J/kg °C)	λ (W/m°C)
Melting	225	238	97.377	1958	1033	1.455
Solidification	230.741	215.2	97.4			

Table 3-8: Viscosity of the solar salt type-I with 10 wt% graphite.

Properties	value
Viscosity (kg/m s) [185]	$\mu_{bf}(1 + 2.5 \cdot \emptyset)$

3.2.1.3 The Metal Alloy used as a PCM

Bi 58%-Sn 42% alloy was used as a potential PCM in experiments for low-temperature applications, such as domestic hot water supply, due to its low melting point and high thermal conductivity. Low purity Bi and Sn, which were bought from Magnametals Company [181], were used to reduce the cost of PCM materials in real applications. The DSC analysis was performed of low purity Bi and Sn to evaluate their thermal properties (the latent heat, melting and solidification temperatures) in comparison to pure Bi and Sn. Figure 3-8 to Figure 3-11 show the DSC results for pure and low purity Bi and Sn, respectively.

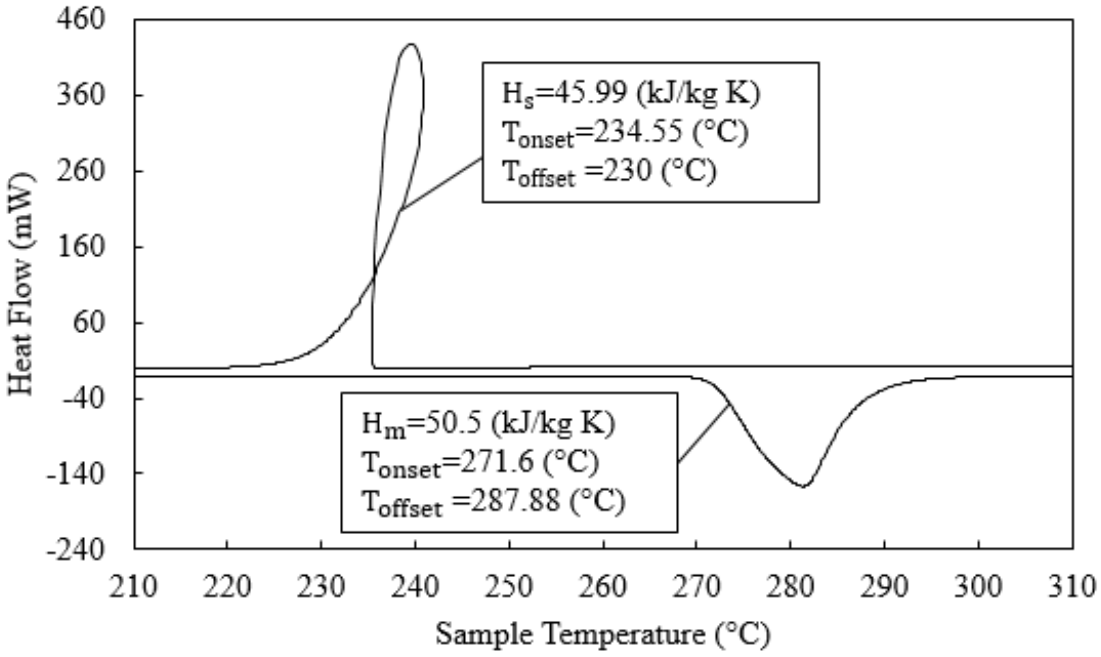

Figure 3-8: The DSC curve for pure Bi.

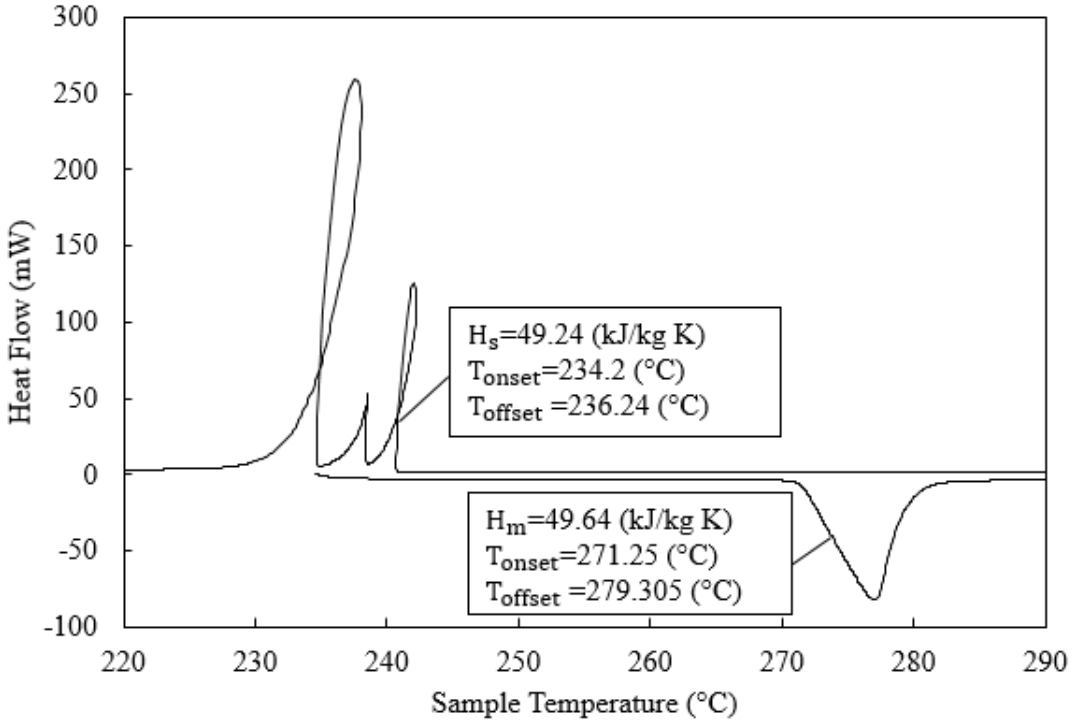

Figure 3-9: The DSC curve for low purity Bi.

It was determined that the values of the latent heat during the melting and solidification processes for low purity and pure Bi are very close. In addition, the melting temperature range for low purity Bi is the half of that for pure Bi. However, it was found that the low purity Bi has a wider solidification temperature range than pure Bi by 2 °C. Despite of this, low purity Bi is considered to be competitive in comparison to pure Bi.

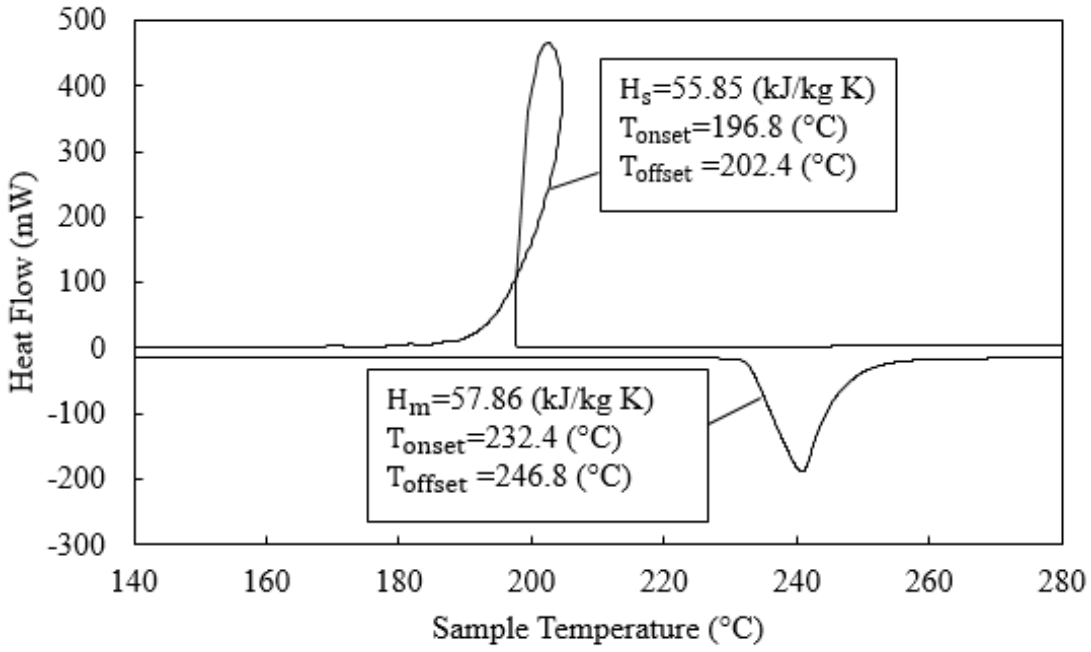

Figure 3-10: The DSC curve for pure Sn.

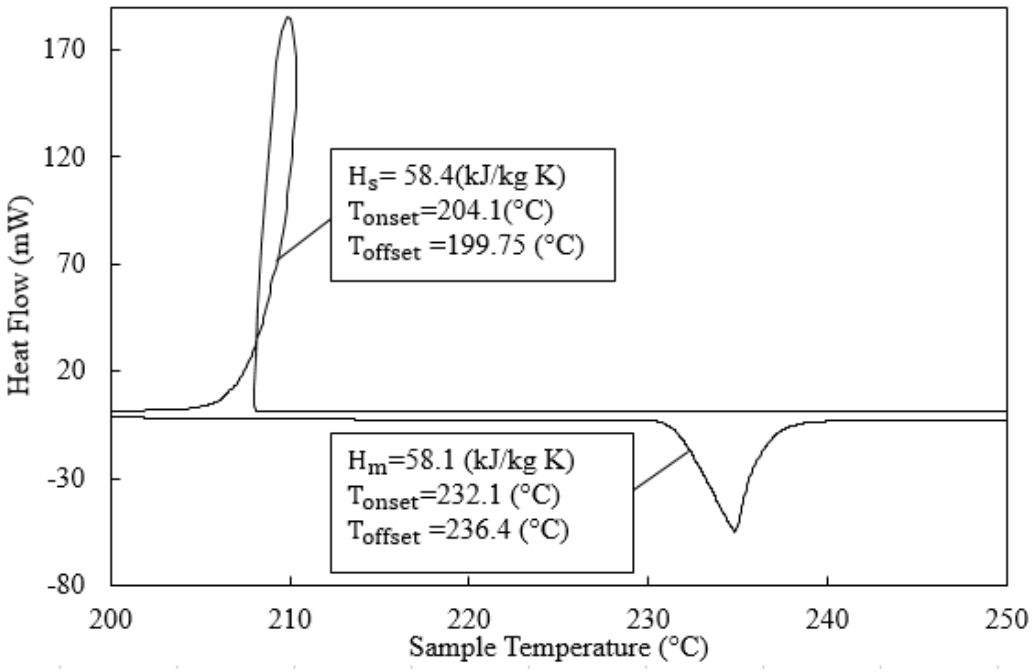

Figure 3-11: The DSC for low purity Sn.

It was demonstrated that low purity Sn has approximately the same values of the latent heat during the melting and solidification processes, whilst the temperature ranges during the melting and solidification were reduced for low purity Sn in comparison to pure Sn. However, low purity Sn can be used as a PCM instead of pure Sn.

The DSC results show that the low purity metals have almost the same thermal properties in terms of latent heat as well as melting and solidification temperatures. Therefore, the metal alloy using low purity metals was created to investigate its thermal properties in comparison to the pure metal alloy. The DSC results for the pure and low purity metal alloys are shown in Figure 3-12, and Figure 3-13, respectively.

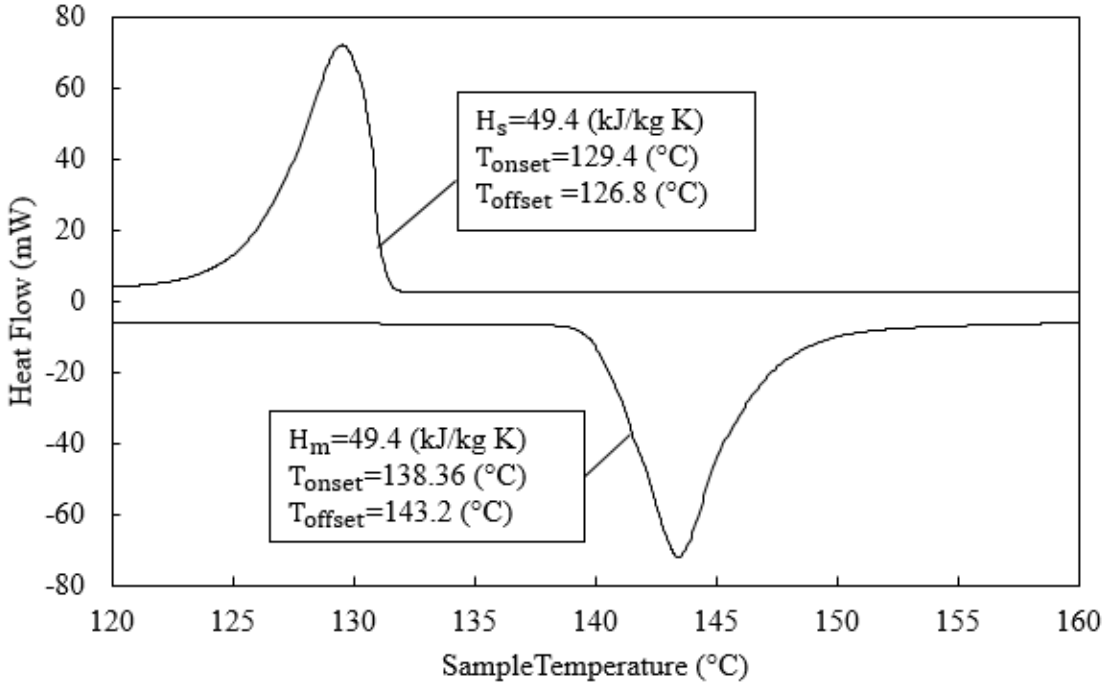

Figure 3-12: The DSC curve for the pure metal alloy.

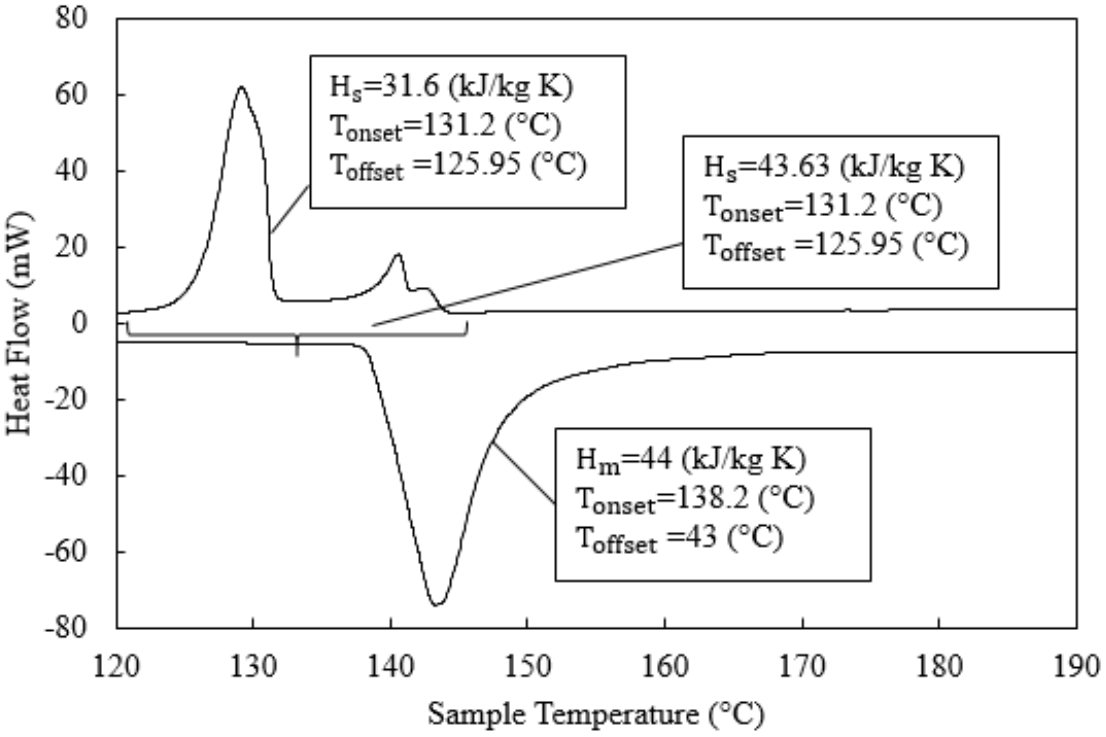

Figure 3-13: The DSC curve for the low purity metal alloy.

It was found that for the low purity metal alloy the melting and solidification temperature ranges widen compared to the pure metal alloy. It was shown that during the solidification process two peaks were formed at the temperatures of 140 °C and 130 °C, respectively. These peaks represent the liquid-liquid transition of Bi-Sn alloy and this is attributed to the change in the crystalline structure from one lattice configuration to another.

The thermal properties of the low purity metal alloy are shown in Table 3-9, and Table 3-10**.**

Table 3-9: Measured thermal properties of the low purity metal alloy.

	T_{onset} (°C)	T_{offset} (°C)	ΔH (kJ/kg)	C_p (J/kg °C)
Melting	138.2	143	44	160
Solidification	131.2	125.95	43.63	

Besides, the properties, such as density, thermal conductivity, and viscosity were obtained from the literature and tabulated in Table 3-10.

Table 3-10: Thermal properties of the low purity metal alloy.

Properties	value
Density (kg/m^3) [95, 186, 187]	8500
Thermal Conductivity (W/m K) [186, 188]	23
Viscosity (kg/m s) [95, 186, 187]	0.002
Thermal expansion coefficient (1/K) [189]	$(1.01\text{-}1.25) \cdot 10^{-4}$

3.2.2 Containers used for housing PCMs

Two types of containers were manufactured by Aavid Thermacore Ltd to assess the thermal performance of the TES system in different configurations. The first type includes two finned containers, one made of the aluminium material and the second one made of stainless steel. Fins are used to intensify heat transfer through solar salt. The other three containers in the second group were manufactured without fins and made of stainless steel. The finned containers and two conventional containers were used to evaluate the

thermal performance of TES system using pure solar salt, and solar salt with graphite. Only the third conventional container was used to investigate the performance of the TES system with the metal alloys.

3.2.2.1 The design of the finned containers

As described above, the first finned container was made of stainless steel and the other was made of the aluminium material to study the effects of different materials on the thermal performance of TES system. Each container was manufactured with dimensions of 150 × mm × 150 mm × 64 mm (width, height, and length, respectively). They were designed with four fins to intensify the heat transfer through the TES system with 10.4-mm space between fins. The fins were placed vertically into the container and fixed inside by welding to walls. The fins have 1.5 mm in the thickness and the thickness of the external walls of containers was 3 mm, see Figure 3-14. A pipe made of stainless steel with 12.5 mm and 70 mm in the diameter and length, respectively, was located at the centre of the container to house the electrical heating cartridge during the charging process. The total mass of stainless steel finned container and aluminium finned container were 0.734 kg and 0.251 kg, respectively.

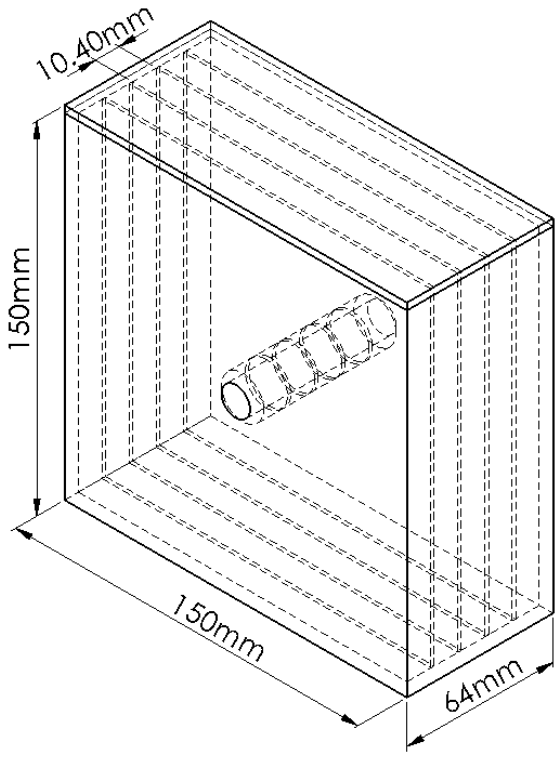

Figure 3-14: Schematic diagram of finned container.

3.2.2.2 Conventional containers (without fins)

Three stainless steel containers were built without fins to investigate the thermal performance of the TES system using PCMs for medium and low-temperature applications. The dimensions of the containers are the same as for the finned ones (150 mm × 150 mm × 64 mm) with the thickness of the external walls of 3 mm. The mass of the containers is 0.69 kg. The pipe in the container was fixed in its middle section to hold the electrical heating cartridge. A plate, made of stainless steel, was used to fix the thermocouples inside the container. The dimensions of the pipe were the same: 12.5 mm as internal diameter and 70 mm in length. An external plate of aluminium was also used to hold the thermocouples in their positions. The stainless steel finned container and aluminium plate are shown in Figure 3-15.

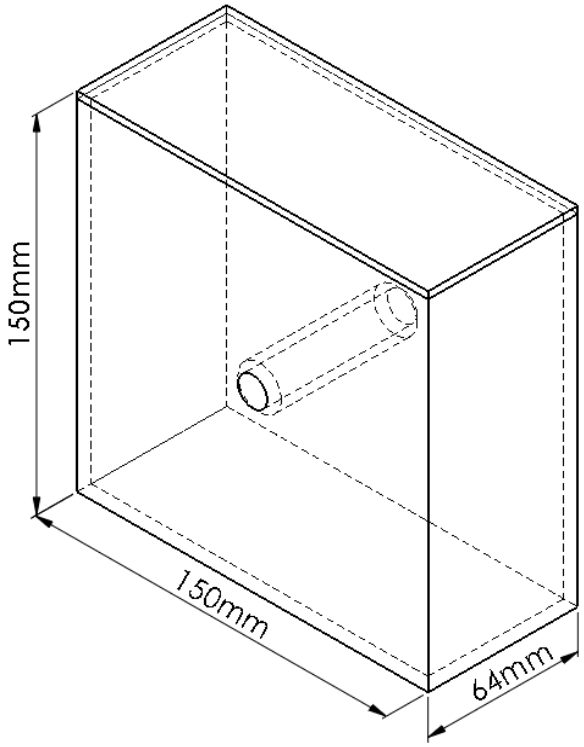

Figure 3-15: Stainless steel container.

The thermo-physical properties of aluminium and stainless steel, used in simulations are summarised in Table 3-11.

Table 3-11: Thermal Properties of Stainless Steel and Aluminium [190, 191].

Properties	**Aluminium**	**Stainless steel**
Density (kg/m^3)	2719	8030
Thermal Conductivity (W/m K)	202	18
Specific Heat (J/kg K)	871	502

3.2.2.3 Filing the containers with PCMs

To fill the containers the solar salt needs to be melted at a temperature exceeding the melting point of the original compounds, such as KNO_3 $NaNO_3$, that is about 350 °C. This was performed using an electric furnace. The filling process was performed by placing the PCM in the form of powder into the container and put the container into the furnace several times. The volume occupied by the powder PCM is reduced as a result of

the melting process, so the container was topped up with powder and the process was repeated until the container is full of molten salt. The filling process of the TES system using finned containers was carried out at Aavid Thermacore Ltd. The total mass of solar salt and the solar salt with graphite in the filled stainless steel containers was about 3 kg. while the total amount of solar salt that filled the stainless steel and aluminium finned containers was 2.9 Kg. The process of filling the containers with different PCMs can be seen in Figure 3-16 to Figure 3-18.

Figure 3-16: Filling a conventional stainless steel container with pure solar salt.

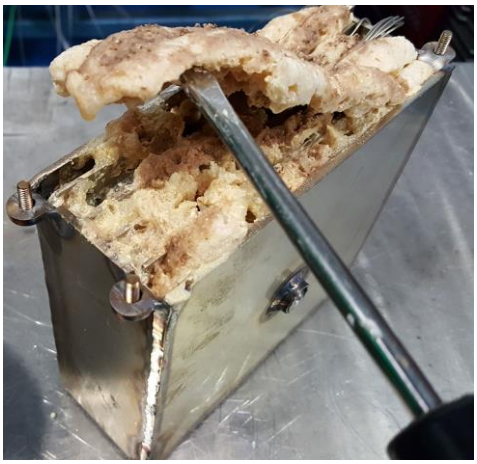

Figure 3-17: Filling the stainless steel finned container with solar salt.

Figure 3-18: Filling the container with solar salt and graphite (10wt%).

When filling the container with the metals the electronic balance scale was used to place Bi and Sn in the container in 58% - 42% mass proportion. Then, the stainless steel container was put in the furnace with a temperature of 280 °C to melt Bi and Sn and form a homogenous mixture. The process was continued until the mixture filled the stainless steel container. The total amount of the mixture was 11 kg, see Figure 3-19.

Figure 3-19: Filling the stainless steel container with Bi and Sn to form the PCM.

3.2.3 Electronic Balance Scale

A Fisher-brand Portable Balance Scale model PSS123 shown in Figure 3-20, was used to measure the weight of solid Bi and Sn to create a metal alloy. It has an accuracy of ± 0.003 g.

Figure 3-20: Electronic balance scale.

3.2.4 Heaters

Two electrical cartridge heaters with the specifications are shown in Table 3-12 were used in the containers. They were placed into the stainless steel pipe, fixed in the middle of the container which is also used to protect the cartridge from the melting PCM. These cartridges were used to provide power inputs at 100, 70 and 50 W to rapidly reach the initial temperature in the experiment prior to providing the required level of power in the experiment. In each experiment, various power inputs were used, such as 18, 25, 35 and 50 W to investigate the influence of power input on the PCM melting process.

Table 3-12: The specifications of electrical cartridge heaters.

	Diameter (mm)	**Length (mm)**	**Power (W)**	**Voltage (V)**	**Containers**
Cartridge I	6.2	25	200	220 ac	Normal container
Cartridge II	9.5	50.8	150	220	Finned containers

The cartridge heaters are shown in Figure 3-21. The position of the cartridges in the containers is shown in Figure 3-22.

a) b)

Figure 3-21: Cartridge heater a) type I b) type II

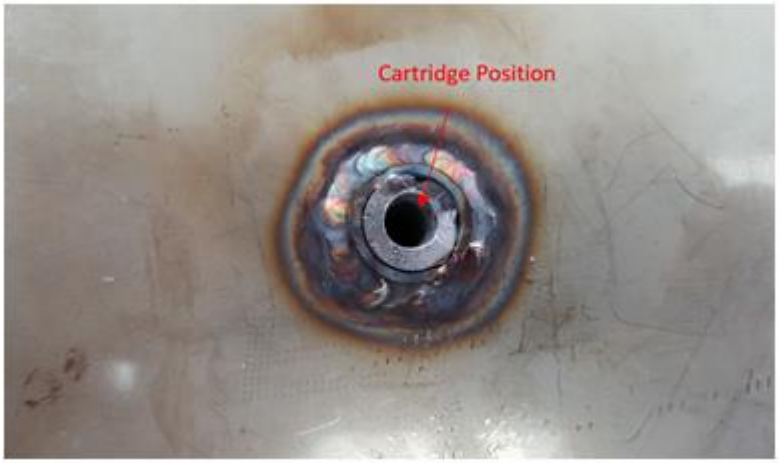

Figure 3-22: Cartridge heater position in the container.

3.2.5 Thermocouples used to record temperatures inside the container

The transient processes in the TES system during the melting and solidification processes were monitored using K-type thermocouples. Two types of K-type thermocouples with the specifications shown in Table 3-13 were used in tests with an accuracy of about ± 2.5 °C. The 1.5 mm thermocouples were attached to the fins prior filling with the PCM. The 4.5-mm thermocouples were inserted into the container from the top. The thermocouples were supplied by RS Components Ltd [192]. The K-type thermocouples used are shown in Figure 3-23.

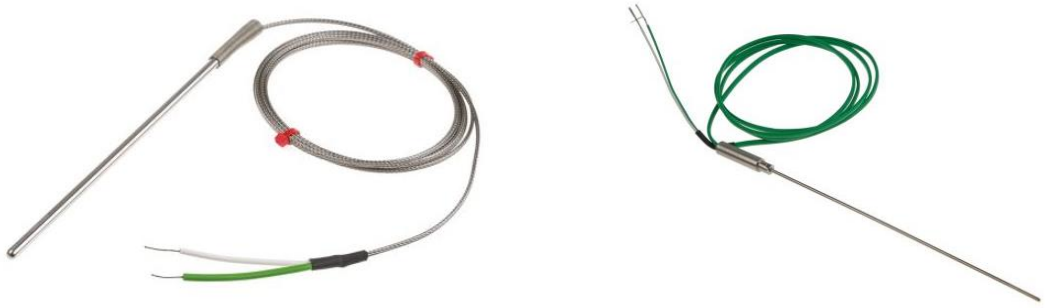

a) b)

Figure 3-23: K-Type thermocouple a) 4.5 mm, b) 1.5 mm.

Table 3-13: The specifications of the used thermocouples.

Thermocouples	**Diameter (mm)**	**Length (mm)**	**Probe material**	**Maximum operating temperature (°C)**	**containers**
type I	1.5	150	Stainless Steel	0 to +1100	Finned container
type II	4.5	150	Stainless Steel	0 to +350	Conventional containers

The thermocouples were placed at certain points across the entire containers to assess the thermal performance of TES systems and investigate the phase change process, starting in the vicinity of the heat source. Thermocouples were also placed in the lower part of the container to more accurately record the melting time.

However, it was not possible to set all thermocouples at the same locations for solar salt TES systems with different configurations (with fins or graphite) due to the design features of containers with fins. The TES system with the metal PCM was also considered as a separate case from the TES system with solar salt.

The positions of thermocouples in each TES system are graphically shown in Figure 3-24 to Figure 3-27. Also, thermocouple positions are presented in Table 3-14 to Table 3-17 (with an accuracy of ± 3mm).

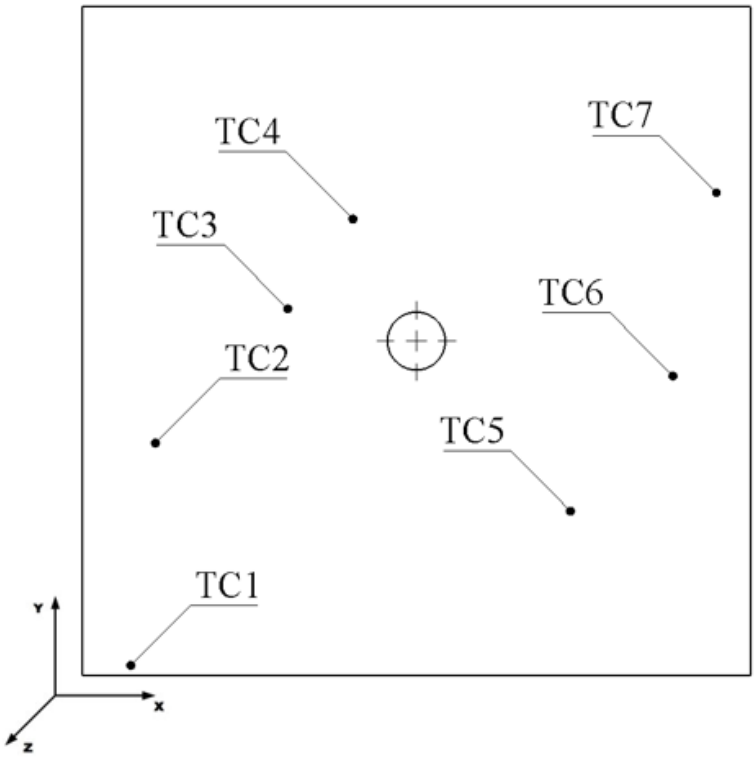

Figure 3-24: Positions of thermocouples in the TES system with solar salt.

Table 3-14: Positions of thermocouples in the TES system with solar salt.

Points	**X- Position (mm)**	**Y- Position (mm)**	**Z-Position (mm)**
TC1	12	5	-10
TC2	16	52	-32
TC3	46	82	-32
TC4	61	102	-32
TC5	110	37	-32
TC6	130	70	-32
TC7	140	107	-53

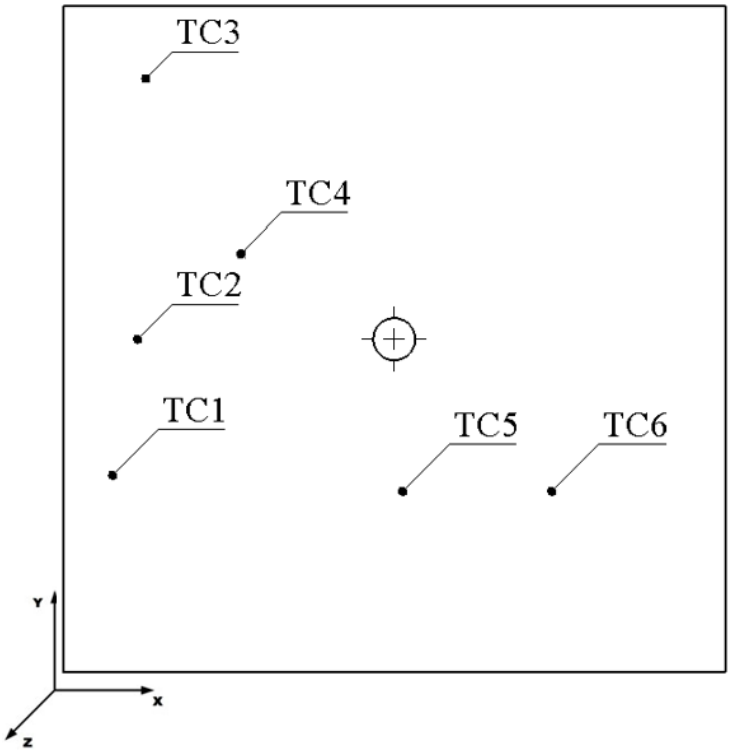

Figure 3-25: Positions of thermocouples in the TES system with finned containers.

Table 3-15: Positions of the thermocouples in the TES system with finned containers.

Points	**X- Position (mm)**	**Y- Position (mm)**	**Z-Position (mm)**
TC1	11.25	43	-32
TC2	16.87	75	-32
TC3	18.75	133.75	-32
TC4	40.3	94.22	-32
TC5	76.87	40.7	-32
TC6	110.62	40.7	-32

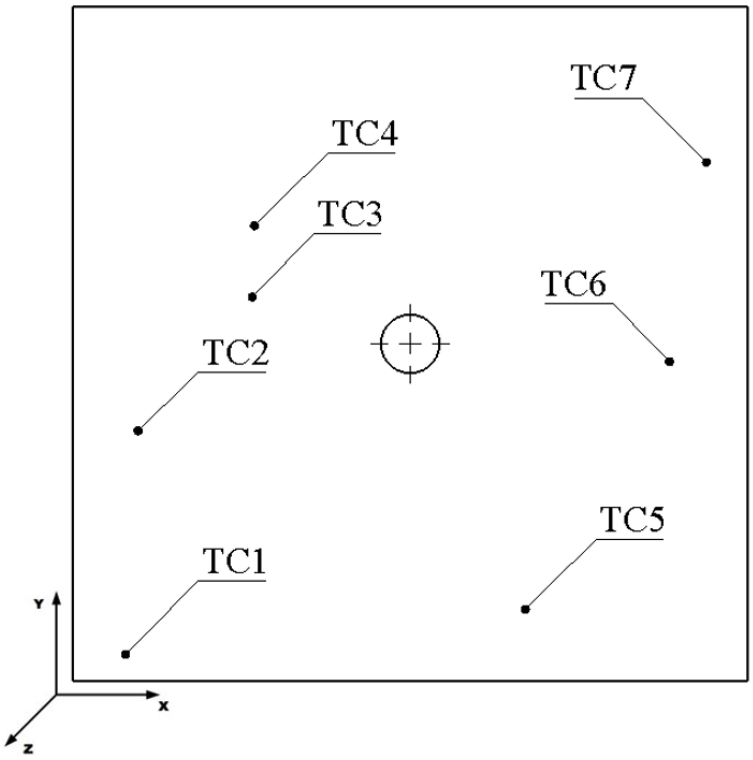

Figure 3-26: Position of the thermocouples in the TES system with solar salt and graphite.

Table 3-16: Position of thermocouples in the TES system with solar salt and graphite.

Points	**X- Position (mm)**	**Y- Position (mm)**	**Z-Position (mm)**
TC1	11	7	-17.5
TC2	14	48	-32
TC3	40	85	-32
TC4	60	100	-32
TC5	100	10	-32
TC6	132	70	-32
TC7	140	115	-17.5

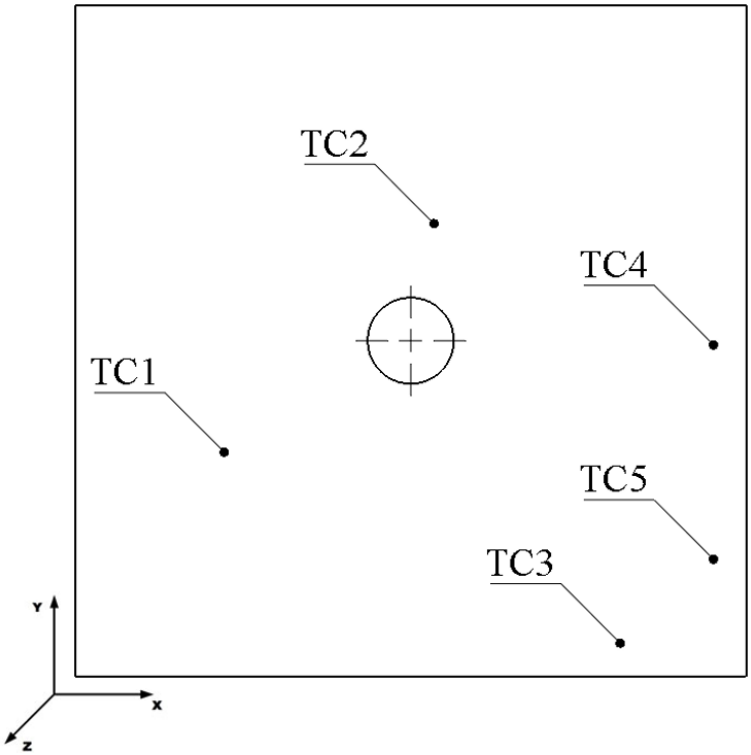

Figure 3-27: Positions of thermocouples in the TES system with metal alloy PCM.

Table 3-17: Positions of thermocouples in the TES system with metal alloy PCM.

Number	X position (mm)	Y- Position (mm)	Z-Position (mm)
TC1	35	51	-32
TC2	80	100	-32
TC3	120	14	-32
TC4	140	74	-32
TC5	140	28	-10

3.2.6 Description of Insulation Material used around containers

To reduce the heat losses from the containers, high-temperature strip insulation was used around all surfaces of the container, as shown in Figure 3-28. Super-wool 607 HT with the specifications presented in Table 3-18 was chosen due to its low thermal conductivity

and stability at high temperatures. One sheet of this insulation material with a length of 5 m and 6-mm thickness was used to cover the whole container.

Figure 3-28: Insulation material.

Table 3-18: The specification of the insulation material [6].

Material	Calcium-Magnesium Silicate
Maximum Operating Temperature (°C)	+1150
Density (kg/m³)	96
Thickness (mm)	6
Thermal Conductivity (W/m K)	0.05
Specific heat (J/kg-K)	2100
Length (m)	5
Width (m)	0.61

3.2.7 Housing unit

A wooden box, manufactured by Aavid Thermacore Ltd., see Figure 3-29, was used to house the containers with its insulation. The dimensions of the wooden box are 52 cm × 33 cm ×48 cm (length, width, and height), and the thickness of the walls is 10 mm.

Figure 3-29: Housing unit.

3.2.8 Power regulator and analyser

A Carroll and Meynell 4.8KVA, type 436-8912 power regulator with capacity up to 250 W was used to control input power to the heating cartridge, see in Figure 3-30. Its accuracy is 0.2 W.

In addition, an AC power analyser (PA) PM 1000, shown in Figure 3-31, with an accuracy of ± 0.02 % was used to measure input power value.

Figure 3-30: The electrical power input regulator.

Figure 3-31: Power Analyser.

3.2.9 Data acquisition system used in tests

The transient thermocouple signal readings were recorded using thermocouple Data Logger (DL) TC-08, as shown in Figure 3-32. The sampling frequency of the Data Logger was set to 0.16 Hz (i.e. a sample per minute) to provide continuous recordings of

temperature values during the experiments. A PICO log software designed by Pico Technology was used to record these values. The data logger used is suitable to record temperatures between -270 to + 1820 °C, with high resolution and accuracy of up to 10 measurements per second.

Figure 3-32: Data Logger used with thermocouples.

3.3 Experimental procedure in running tests on TES systems with sample results

The experimental work was carried out to investigate the thermal performance of TES systems during melting and solidification processes. Therefore, a heating process was carried out to achieve the appropriate the initial temperature to start the experiments, which is below the melting temperature and is 210 °C for TES systems of different configurations with solar salt (fins or graphite) and 133 °C for the TES system with the metal alloy. Consequently, a comparison can be carried out between different configurations and computational costs can be reduced during the numerical investigation.

3.3.1 Sample result for solar salt in the conventional container

The melting temperature of solar salt is approximately between 220-250 °C and due to its low thermal conductivity, the heating process for given dimensions of the TES system has to be carried out over two days as demonstrated in Figure 3-33. On the first day, a constant power input of about 60 W was applied to increase the temperature of solar salt from 25 °C to the level exceeding 240 °C, which takes around 6 hours. A mechanical timer was used to switch off the power supply when the required temperature level is achieved to allow solar salt to cool down overnight to a certain temperature. The following day, the process is repeated using 40 W power input but starting temperature is higher (approximately 100 °C to 240 °C) which also takes around 6 hours to complete. The timer switches off the power supply again, and the cooling process begins. Finally, the temperature of about 210 ± 4 °C was obtained.

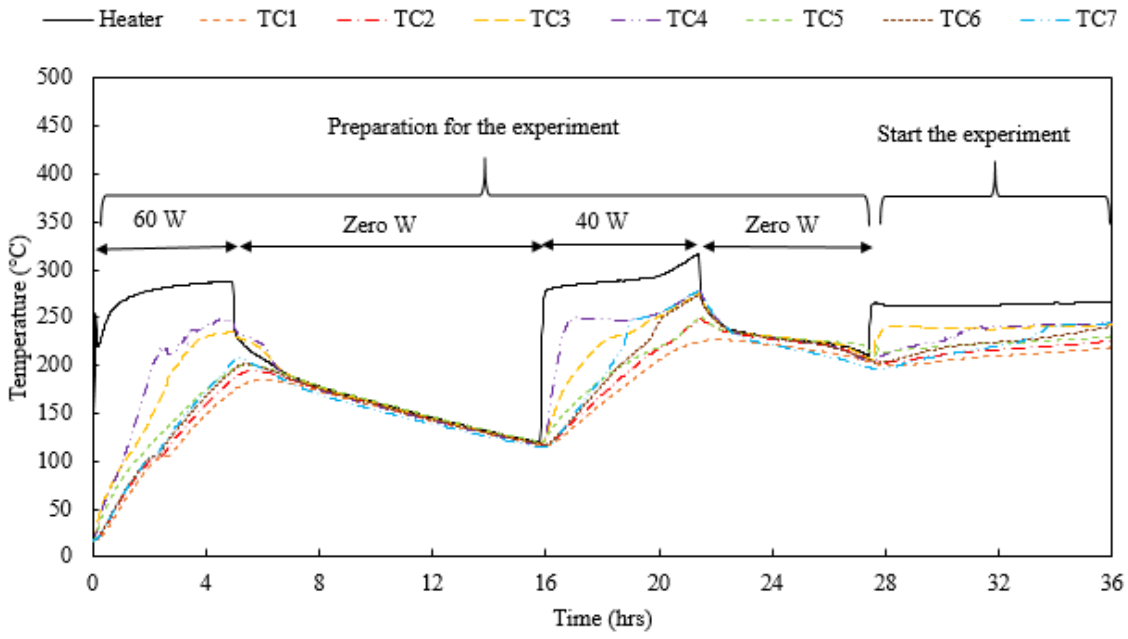

Figure 3-33: The heating process of solar salt.

3.3.2 Sample result for solar salt in the finned containers

A heating process of solar salt is necessary to achieve an initial temperature of 210 ± 4 °C. Power inputs of different magnitudes were used to increase the temperature of solar salt from 25 °C to 210 °C, as shown in Figure 3-34. Initially, a power input of 100 W was used to accelerate the heating process with a gradual power reduction to zero in order to avoid large discrepancies in the temperature across the container.

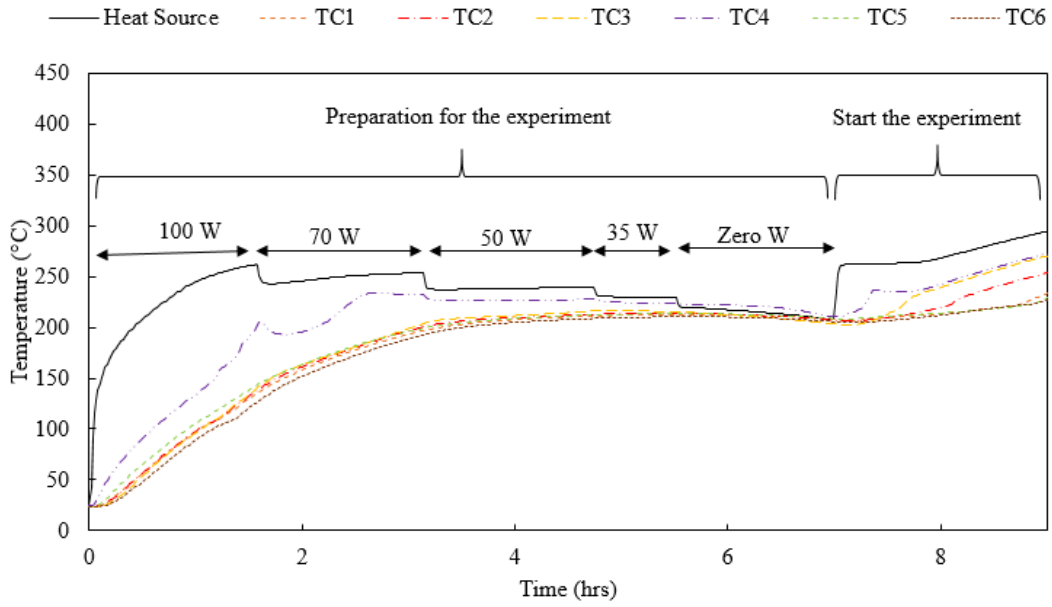

Figure 3-34: The process of increasing the temperature of solar salt using stainless steel finned container.

3.3.3 Sample result for solar salt with graphite

The TES system with solar salt and graphite was heated up from room temperature to 210 ± 4 °C as the initial temperature in the test, see Figure 3-35. The initial power input of 100 W was used to increase the temperature from 25 °C to around 210 °C, followed by 50 W input to avoid large temperature differences through solar salt with graphite.

Finally, the power input was switched off to bring down the temperature closer to 210 ± 4 °C. The heating process needs about 6 hours to complete.

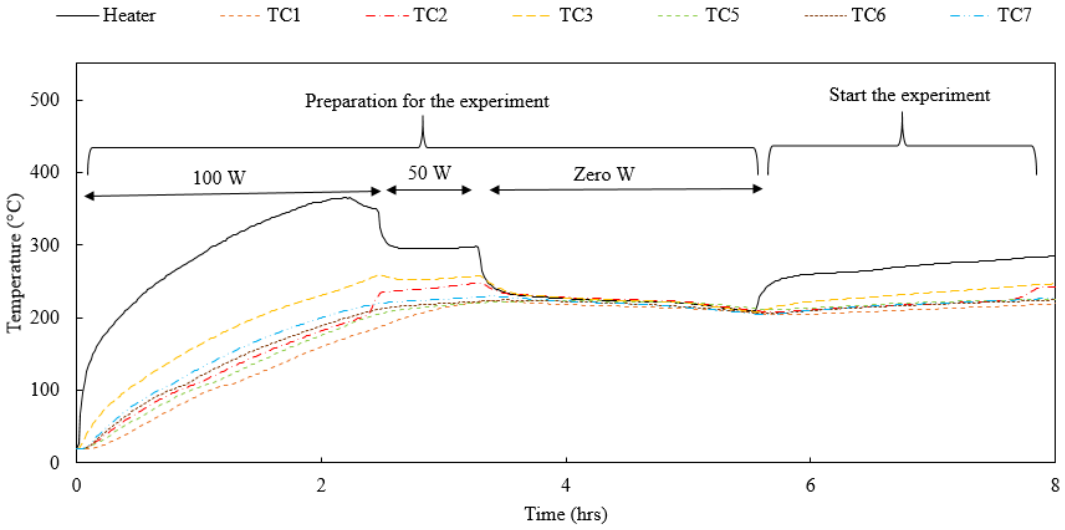

Figure 3-35: The process of heating solar salt with graphite in the container.

3.3.4 Sample result for the metal alloy PCM

The TES system with the metal alloy was investigated for low-temperature applications (with a temperature around 100 °C). The heating process was carried out from room temperature of about 25 °C to 133 ± 3 °C. The power input of 50 W was used initially to speed up the heating process. Then a 20-W power input was used to raise the temperature slowly in the process. In this way, a large temperature difference inside the container can be avoided. Finally, the power input was switched off to bring down the PCM temperature to about 133 °C. The heating process takes only about 160 minutes due to the high thermal conductivity of the PCM. The raise of the PCM temperature in the process of heating is shown in Figure 3-36.

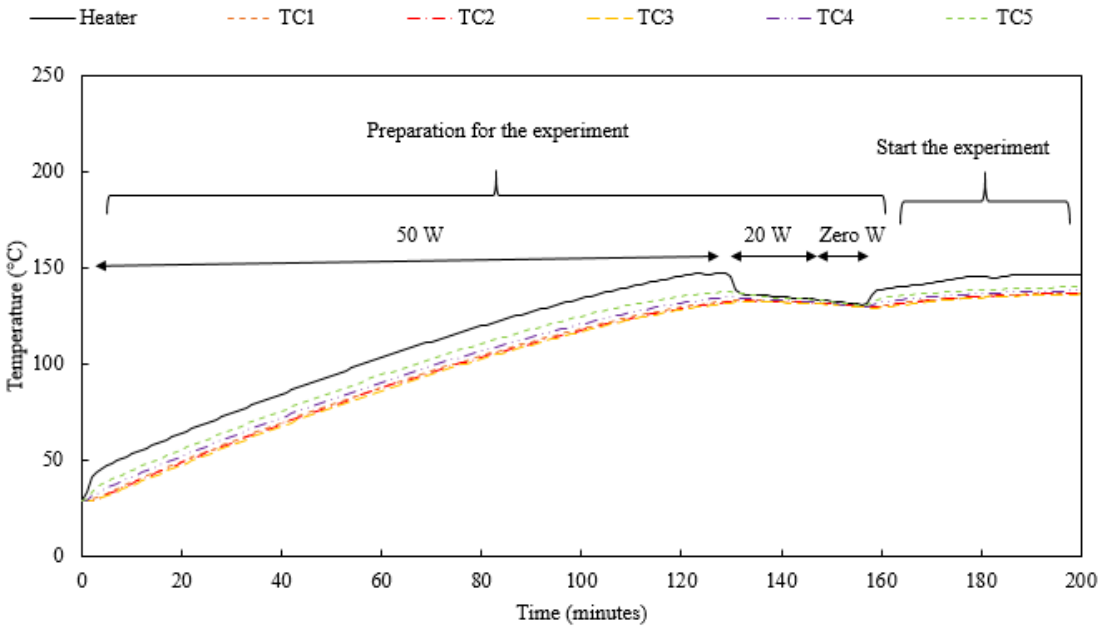

Figure 3-36: Raising the temperature of the metal alloy during tests.

3.4 Experimental uncertainty

It is necessary to determine the accuracy of measurements in the experimental work to experimentally validate the numerical results. The systematic and random uncertainty can be determined in accordance with Kline and Mcclintock [193]. The systematic uncertainty is due to the technical specifications of the measurement instruments or because of the experimental procedure. The random uncertainty is caused by unpredictable variations, such as the precision in the conducted measurements.

The experimental data recorded during the experiments were the power input, the position of thermocouples and the temperature of the PCM.

In this experimental work the uncertainty related to the registration of signals from K-type thermocouples is ± 2.5 °C (1.2%), the uncertainty in reading off indicators of the power regulator is ±0.2 W, power analyser is ± 0.02%, data logger ±0.025 °C, and in positioning of the thermocouples is ±3 mm.

The uncertainty was evaluated using Equation (3-2), as follows:

$$\sigma = \sqrt{(\frac{\delta T}{T})^2 + (\frac{\delta RE}{RE})^2 + (\frac{\delta PA}{PA})^2 + (\frac{\delta\, DL}{DL})^2 + (\frac{\delta\, PT}{PT})^2} \qquad (3\text{-}2)$$

Here, σ is the total uncertainty of the experimental system, $\delta T\ and$ T are the accuracy and temperature value in the measuring procedure, δRE and RE are the accuracy and the measured value in the power measuring procedure, $\delta\, PA\ and$ PA are the accuracy and measured value by the power analyser, $\delta\, DL,$ and DL are the accuracy and measured values for the data logger, $\delta\, PT$ and PT are the accuracy and measured value of coordinates of the thermocouple positions. The overall uncertainty in the experimental results is calculated to be less than 8%.

Chapter 4 Experimental results

4.1 Solar salt

4.1.1 The thermal energy charging process in the conventional container

Figure 4-1 shows the results obtained for the case with 18 W power input, indicating that this power level was not sufficient to melt solar salt within available time for the experiment (18 hours) due to the solar salt's low thermal conductivity and heat losses.

The results for the cases with 25, 35, and 50 W power inputs are shown in Figure 4-2, Figure 4-3, and Figure 4-4, respectively. TC1, placed in the lower corner of the container, indicates the overall melting time of solar salt. The lower section of the container melts at the end of the process for all power inputs, and this is due to flows caused by natural convection.

The thermocouples TC2, TC5, and TC6 record the temperature profiles in solar salt also in the lower part of the container. Here temperatures increase in time due to their positions being closer to the heat source.

TC3 indicates a rapid rise in the temperature due to its position being above the heat source, showing an increase from 210 °C to 240 °C in a short time. Similarly, TC4 was placed above the heat source, however in much closer proximity to it; thus it demonstrates a quicker response.

Fluctuations were observed in the temperature measured with TC4 during the temperature increase due to the effect of natural convection in molten solar salt.

Finally, TC7 was located at the top section of the container and next to the wall. The temperature in this region increases gradually and affected by natural convection due to the melting of solar salt.

The temperatures measured by thermocouples TC3, TC4, and TC7 increase from 210 °C up to about 240 °C and become almost constant, as the melting process of solar salt being completed. For the temperature to increase further, it requires more time. The temperatures increase due to the accumulation of heat in the form of sensible heat (heating of the liquid).

In general, the melting time shortens with the power input increased. It was found that the melting time was reduced from 20 hours to 5.5 hours by increasing the power input from 25 W to 50 W.

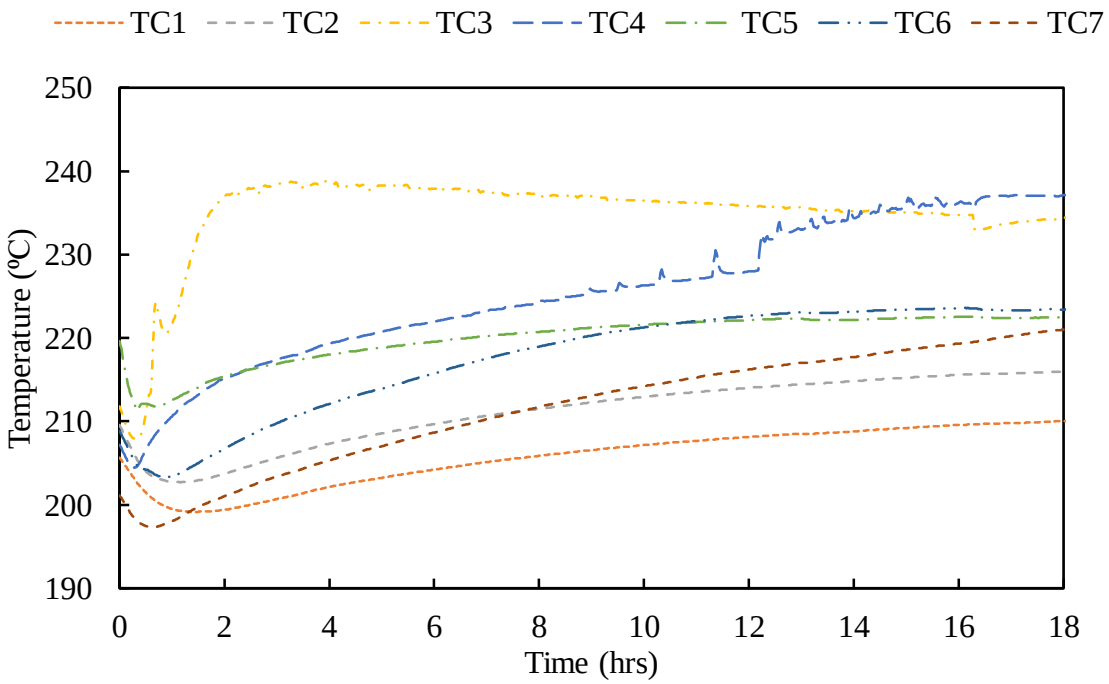

Figure 4-1: Experimental temperature variation in the TES with solar salt when using the 18 W power input.

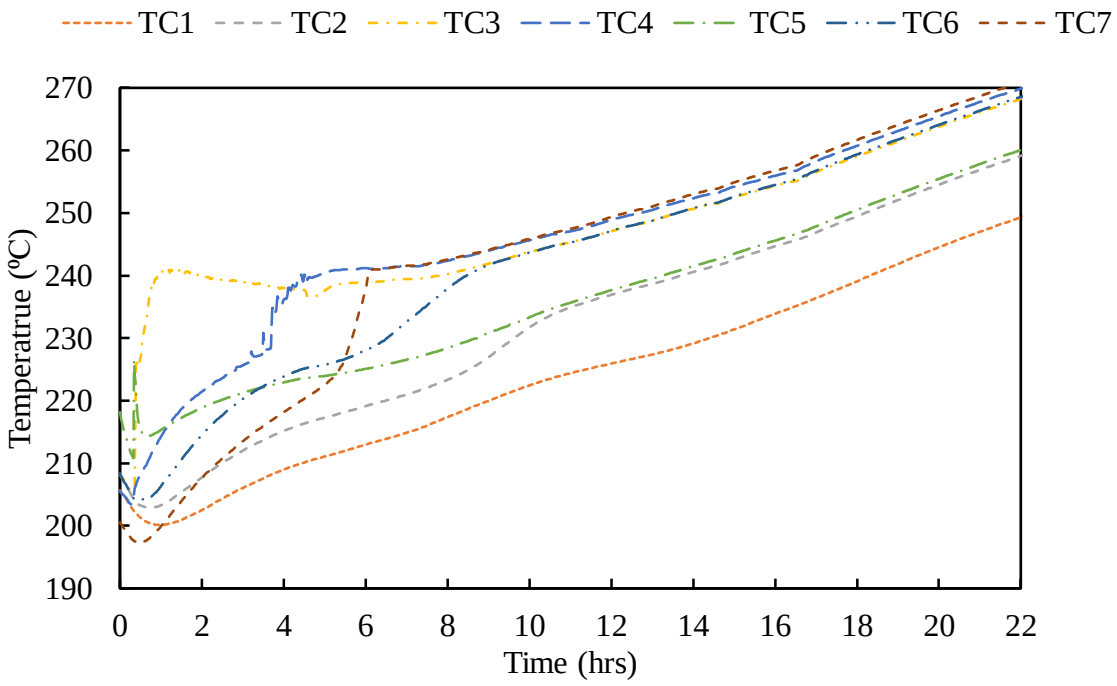

Figure 4-2: Experimental temperature variation in the TES with solar salt when using the 25 W power input.

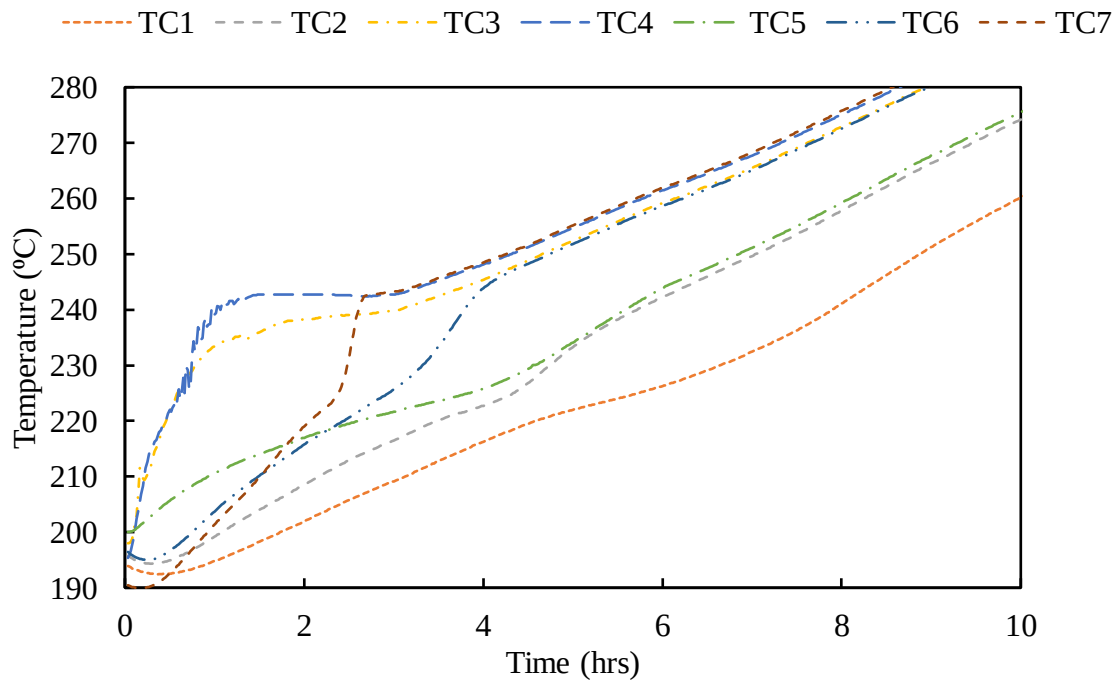

Figure 4-3: Experimental temperature variation in the TES with solar salt when using the 35 W power input.

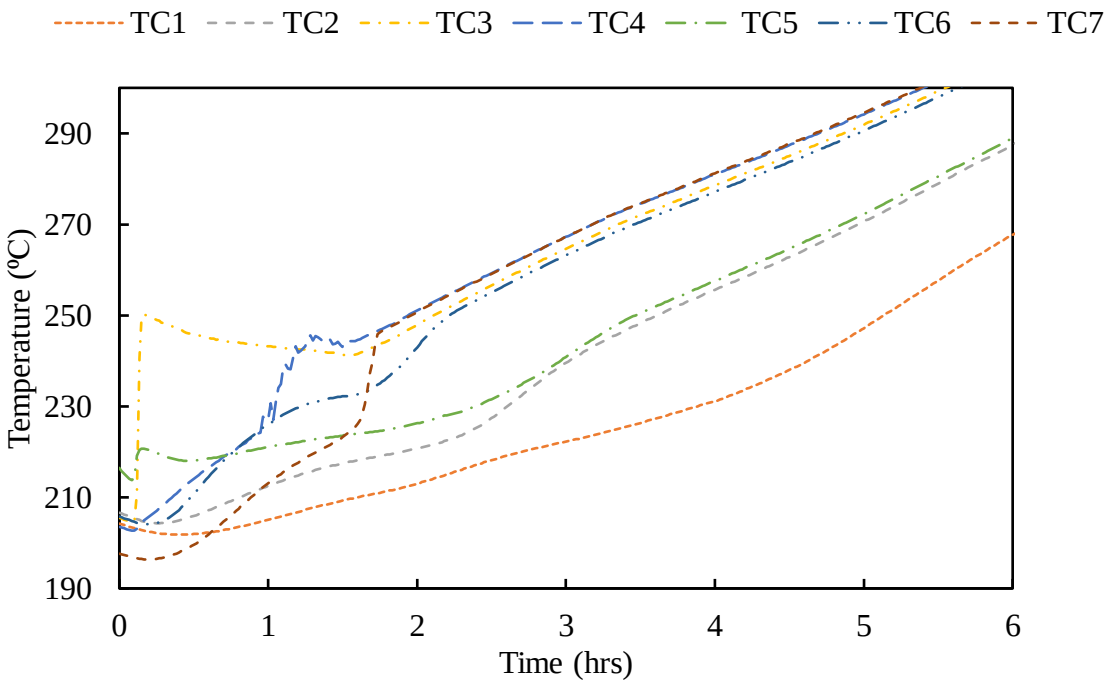

Figure 4-4: Experimental temperature variation in the TES with solar salt when using the 50 W power input.

4.1.2 The thermal energy discharging process in the conventional container

The discharging process in the TES system with solar salt is shown in Figure 4-5. The process of cooling occurs due to heat losses to the environment and results can be used to estimate the intensity of heat losses from the TES system. The process begins at a temperature of 247 ± 3 °C and ends at a temperature of about 200 °C. During this process, the power supply is switched off and heat losses through the boundaries of the TES system can be calculated.

The temperature of the solar salt decreases gradually from 247 °C to 234 °C for 60 minutes. Then the temperature decreases at a slower rate from 234 °C to 215 °C due to the phase change from the liquid to solid state (this takes about 5 hours). At about 215 °C the solar salt has completely transformed from the liquid to solid-state and the cooling

process occurs as a loss of sensible heat from the solid solar salt down to 200 °C (this takes around 60 minutes).

In total, the discharging process takes around 7 hours and solar salt is cooled down from liquid to solid-state with a cooling rate of about 15 °C/hr.

The heat losses from the TES system were calculated from the amount of heat transfer during the cooling process (liquid phase) and the amount of heat transfer during the heating process (solid phase) to be approximately 50%.

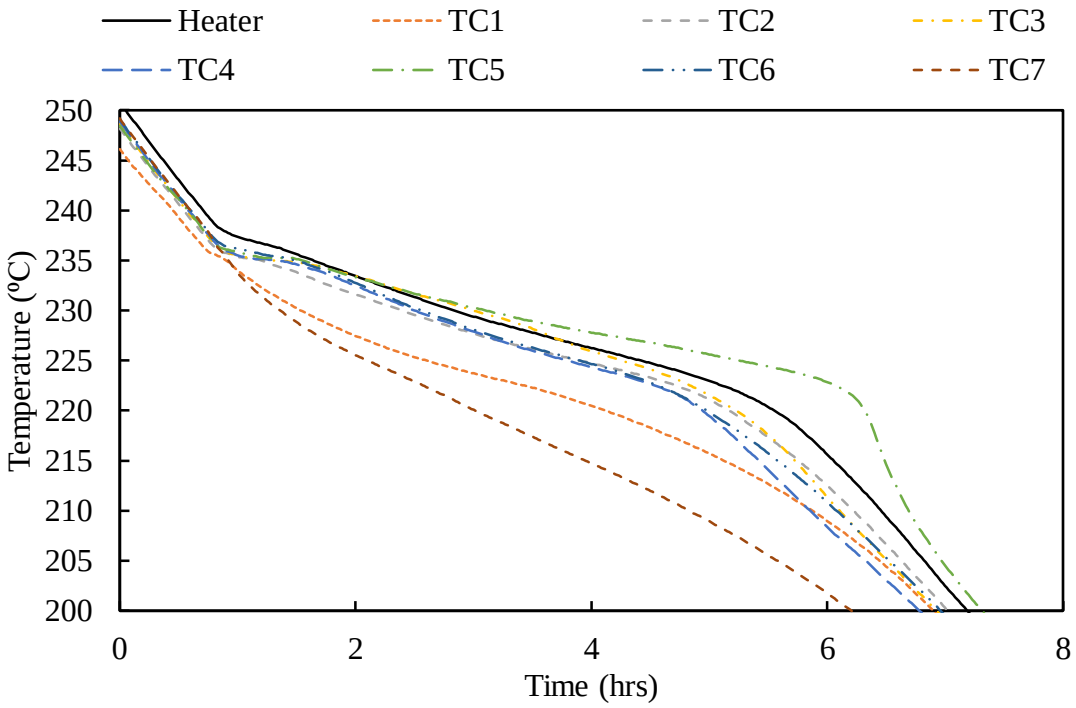

Figure 4-5: Discharging process in the TES with solar salt.

4.2 Finned containers

4.2.1 The thermal energy charging process

The temperature profiles in the finned TES system for various power inputs are presented in Figure 4-6 to Figure 4-11. Figure 4-6 and Figure 4-9 indicate that the PCM does not

melt when the constant power input is 18 W, regardless of the experiment duration in both stainless steel and aluminium finned containers, respectively. This happens because of the high heat losses from the TES system in comparison to the low power input.

For power inputs of 25 and 35 W, the solar salt melts as the temperature exceeded 225 °C. For the power input of 25 W to melt solar salt takes nearly 10 hours. This period halved for the power input of 35 W in the stainless steel finned container, as shown in Figure 4-7 and Figure 4-8. In the aluminium-finned container, the melting process of solar salt takes 8.3 and around 4 hours for the power inputs of 25 and 35 W respectively, as shown in Figure 4-10 and Figure 4-11.

The conduction heat transfer mechanism is dominant at the initial stages, during which the temperature increases linearly with time. The melting process begins when reaching the melting temperature of 218.9 °C and that causes the solid salt to melt around the heat source. As time elapses, the liquid region increases rapidly in the upward direction because of natural convection; this was confirmed by the sharp increase in temperature at TC2, TC3, and TC4 in the corner (these are in the proximity of the heat source). The volume of the molten solar salt expands nearly up to 10% compared to the solid solar salt [42], which also creates favourable conditions for the convection heat transfer to become dominant.

While heating continues, the temperature of the system increases and it is recorded by other surroundings thermocouples. However, the temperature of solar salt in the lower section of the container remains below the melting temperature as shown by thermocouple readings (TC1, TC5, and TC6). The melting of solar salt in this part of the container determines the complete melting time.

The temperature increases linearly with time for the TES system when using aluminium fins container. The reason behind that is aluminium has high thermal conductivity. The temperature in TC2 has a very rapid increase, which is also enhanced by the effects of natural convection.

The temperature increases rapidly to 225 °C and then becomes constant due to the phase change process from solid to liquid. At the end of the phase change process, the temperature starts to increase and heat accumulated as the sensible heat of the liquid. This is not visible in the lower points in which the phase change process takes significantly longer time.

It is observed that increasing the power input to the TES system decreases the melting time of solar salt. This occurs because of the increased temperature difference between the heat source and solar salt, which enhances the heat transfer process.

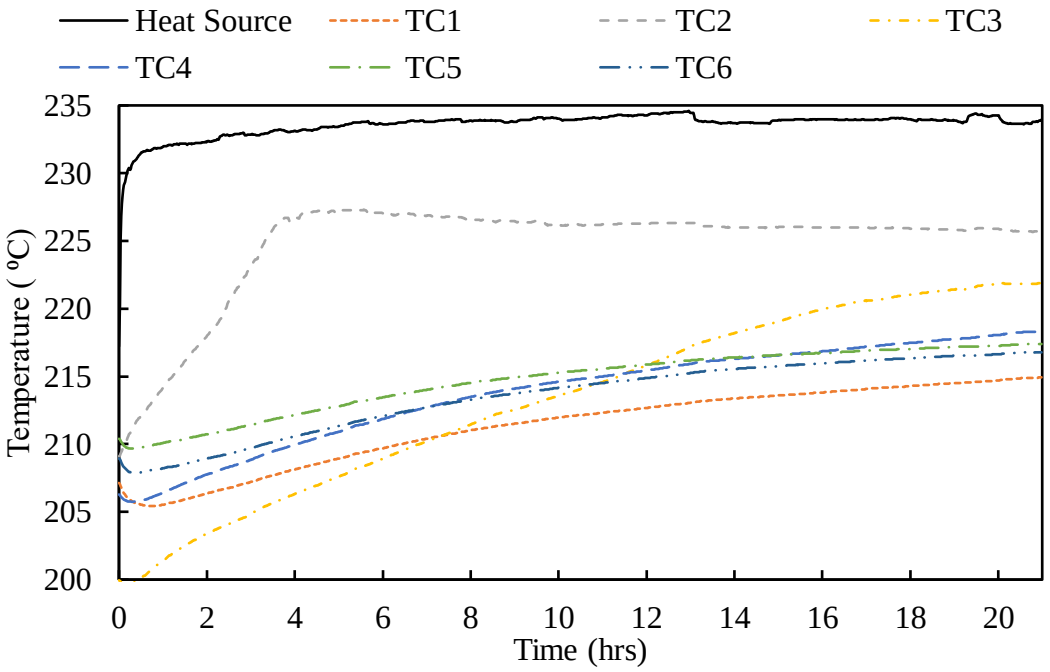

Figure 4-6: Experimental temperature variation in the solar salt during the melting process for the 18 W power input (stainless steel finned container).

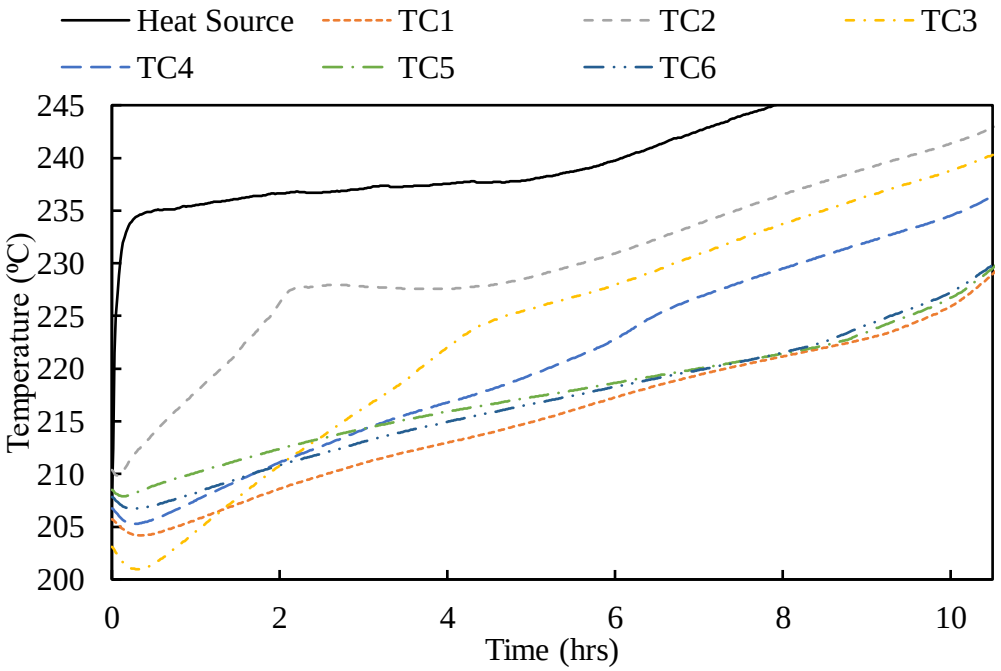

Figure 4-7: Experimental temperature variation in the solar salt during the melting process for the 25 W power input (stainless steel finned container).

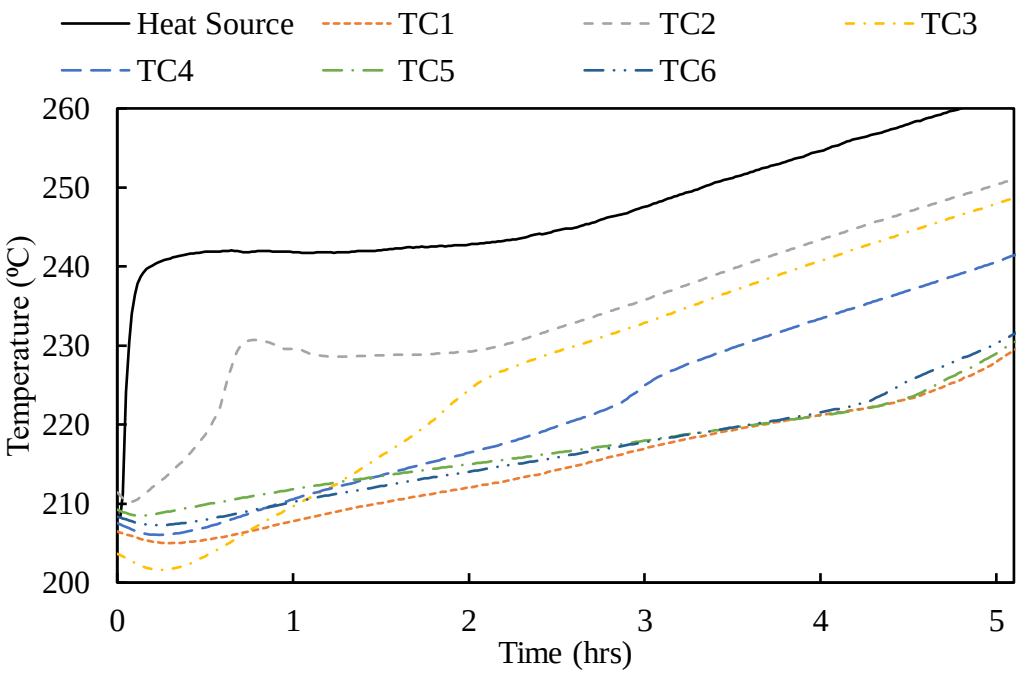

Figure 4-8 Experimental temperature variation in the solar salt during the melting process for the 35 W power input (stainless steel finned container).

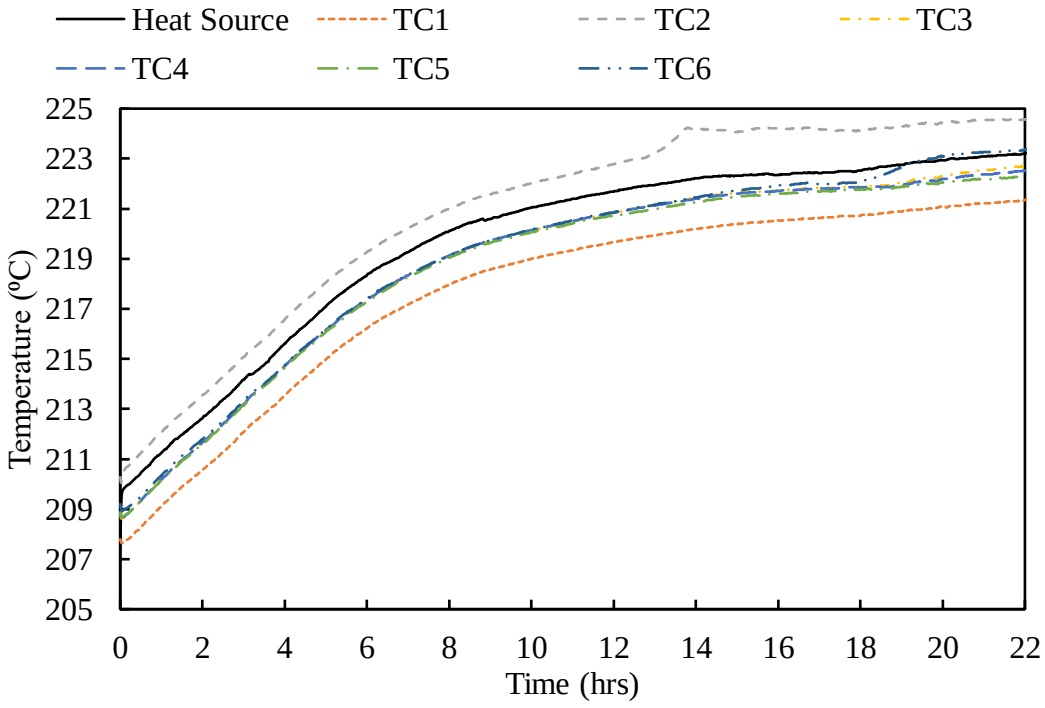

Figure 4-9: Experimental temperature variation in the solar salt during the melting process for the 18 W power input (aluminium finned container).

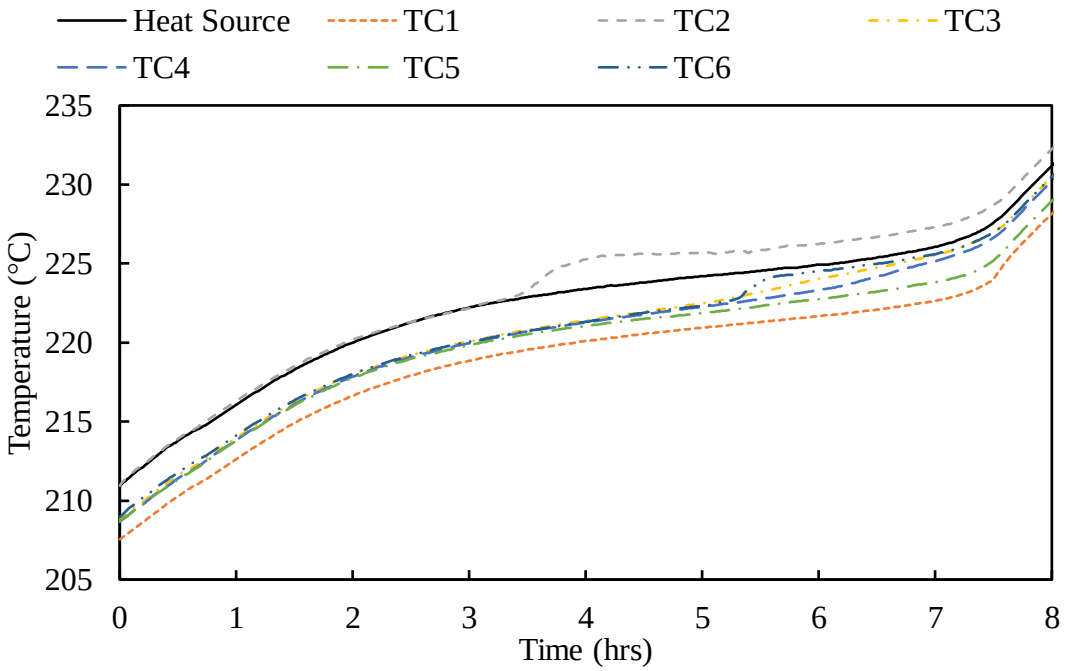

Figure 4-10: Experimental temperature variation in the solar salt during the melting process for the 25 W power input (aluminium finned container).

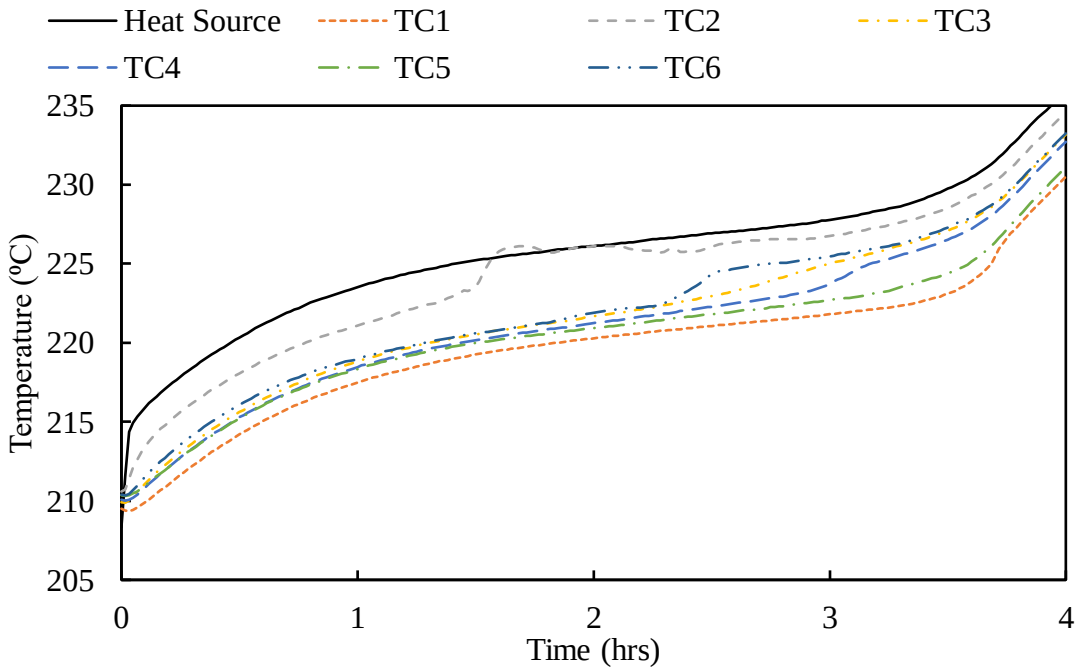

Figure 4-11: Experimental temperature variation in the solar salt during the melting process for the 35 W power input (aluminium finned container).

The time required to melt the PCM in the aluminium finned container is significantly shorter than in the stainless steel finned container mainly due to the higher thermal conductivity of the aluminium.

4.2.2 Thermal energy discharging process

Figure 4-12 and Figure 4-13 show the temperature variation in the finned containers during the cooling process of solar salt. The initial temperature from which the solidification process started was set to be 235 ± 3 °C, and the PCM was cooled down to 200 °C. The cooling process was carried out by switching the power supply to cartridge off and energy was removed from the TES due to heat losses to the environment.

As time elapses, the temperature decreases linearly, until the level of 222 °C is reached. At this temperature, the change in phase from liquid to solid results in a constant temperature as solar salt releases the stored heat energy through heat losses. The results show that the solidification time is about 6 hours. The temperature at the TC3 (the corner point) decreases significantly during the discharging process, which suggests that rapid heat losses occur particularly near this corner of the TES system together with shrinking of the volume of solid solar salt.

The heat losses of the system were calculated based on free cooling speed and to be 40 % during the charging time. The cooling rate of the discharging process was found to be around 13 °C /hr.

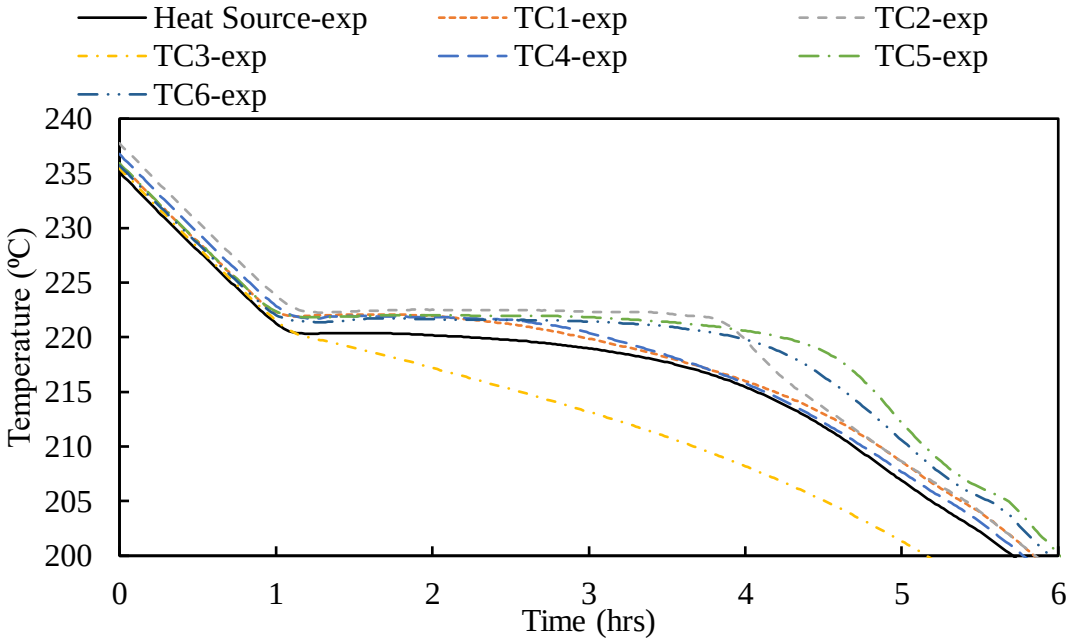

Figure 4-12: Experimental temperature variation of the solar salt during the solidification process in stainless steel finned container.

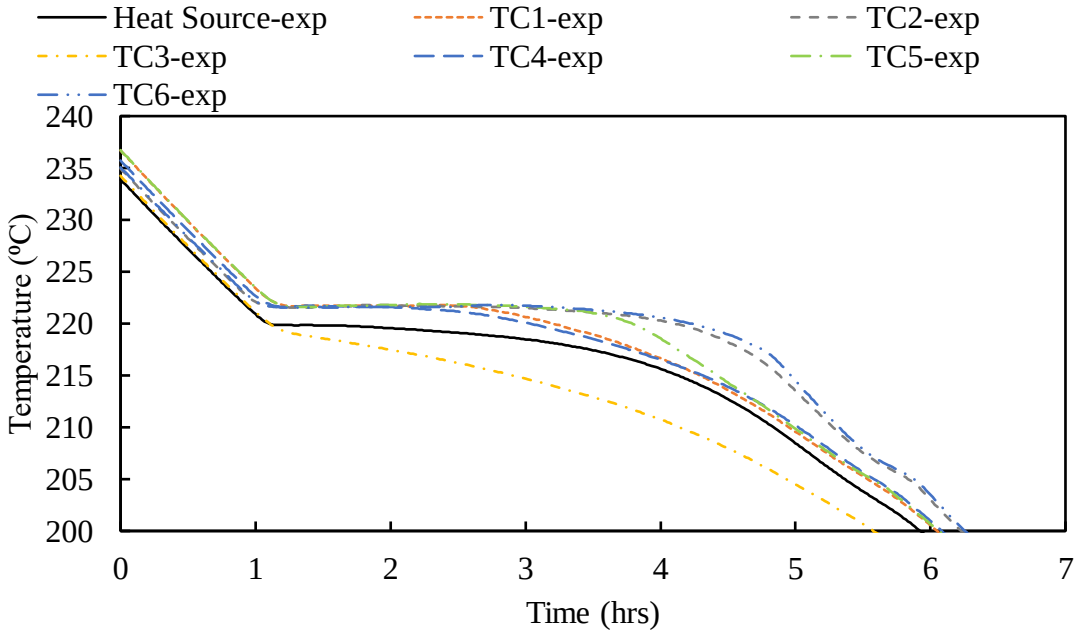

Figure 4-13: Experimental temperature variation of the solar salt during the solidification process in the aluminium finned container.

4.3 Solar salt and graphite

4.3.1 The thermal energy charging process

Figure 4-14 shows the thermal charging process when 18 W power input is applied to the TES system. This power input was not sufficient to melt solar salt and graphite due to the greater heat losses in the system. For the power inputs of 25, 35 and 50 W solar salt and graphite melt as shown in Figure 4-15 to Figure 4-17, respectively. The melting time for melting solar salt and graphite using 25, 35 and 50 W power inputs is 10, 5 and 2.8 hours, respectively.

The temperature first increases in the solid phase of solar salt with graphite due to thermal conduction heat transfer. When the temperature reaches the melting level of about 225 °C, the phase change process starts to take place. The melting process starts around the heat source due to the higher temperature and then spreads towards the sides of the container.

As time elapses solar salt with graphite melts around and above the heat source, affected by the natural convection flows. TC2 and TC3 show a linear increase in the temperatures from 225 °C to 245 °C due to their close proximity to the heat source.

TC1 at the lower point has a slower response. TC1 recordings are used to determine the complete melting time due to its position at the corner. It was shown that the temperature becomes constant at about 245 °C at TC3, TC6, indicating the phase change process taking place.

At the same time the temperatures in TC5, TC6, and TC7 lag behind in reaching the phase transition stage due to their positions (to the heat source). Then the temperatures at these

points start to increase again after the PCM is fully melted since heat accumulation occurs in the form of increasing sensible heat of the liquid.

However, the transformation from solid to liquid was not detected at the lower points due to the low melting rate. During the experimental work TC4 was damaged so data on the temperature at this location was lost.

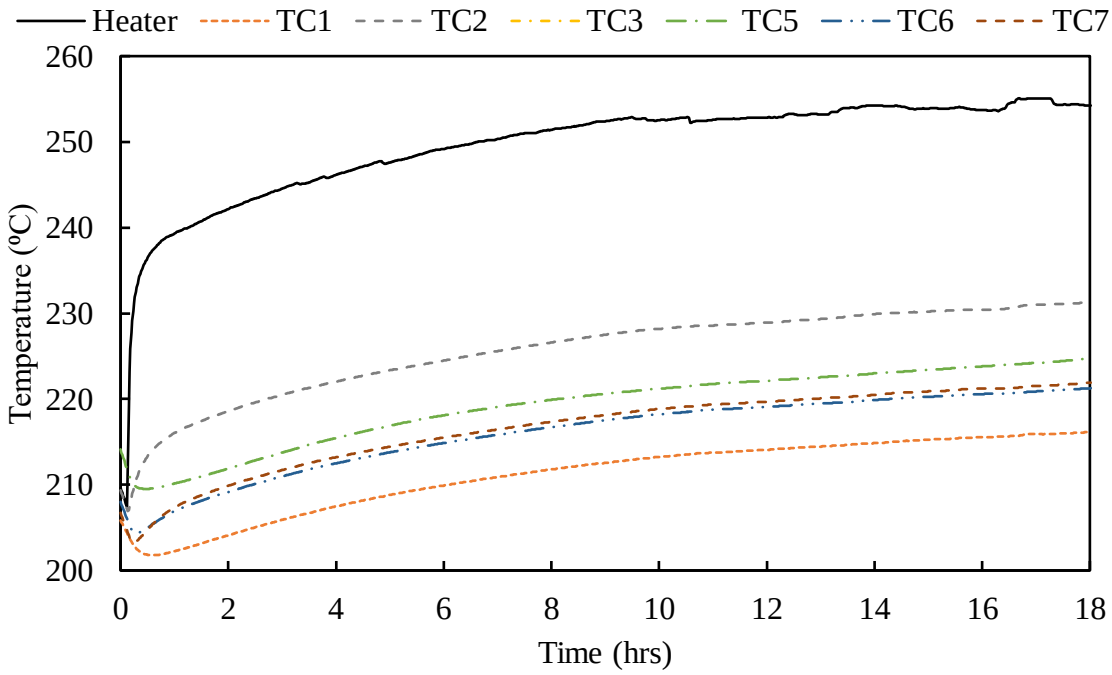

Figure 4-14: Experimental investigations of the temperature variation in the solar salt with 10 wt% of graphite for 18 W power input.

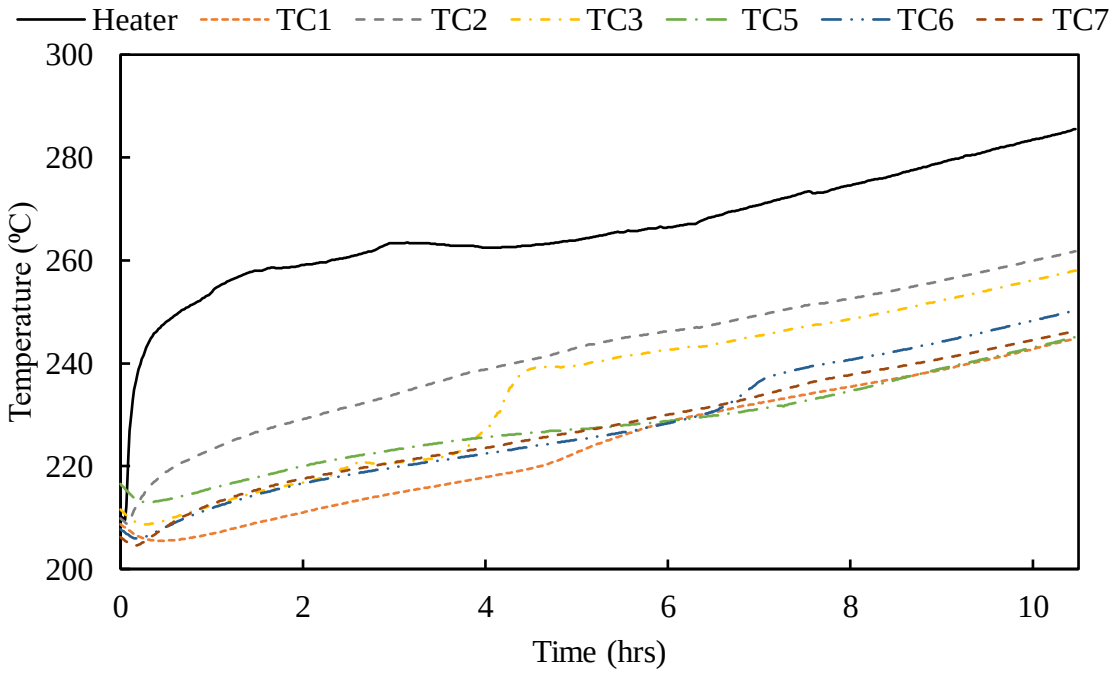

Figure 4-15: Experimental investigations of the temperature variation in the solar salt with 10 wt% of graphite for 25 W power input.

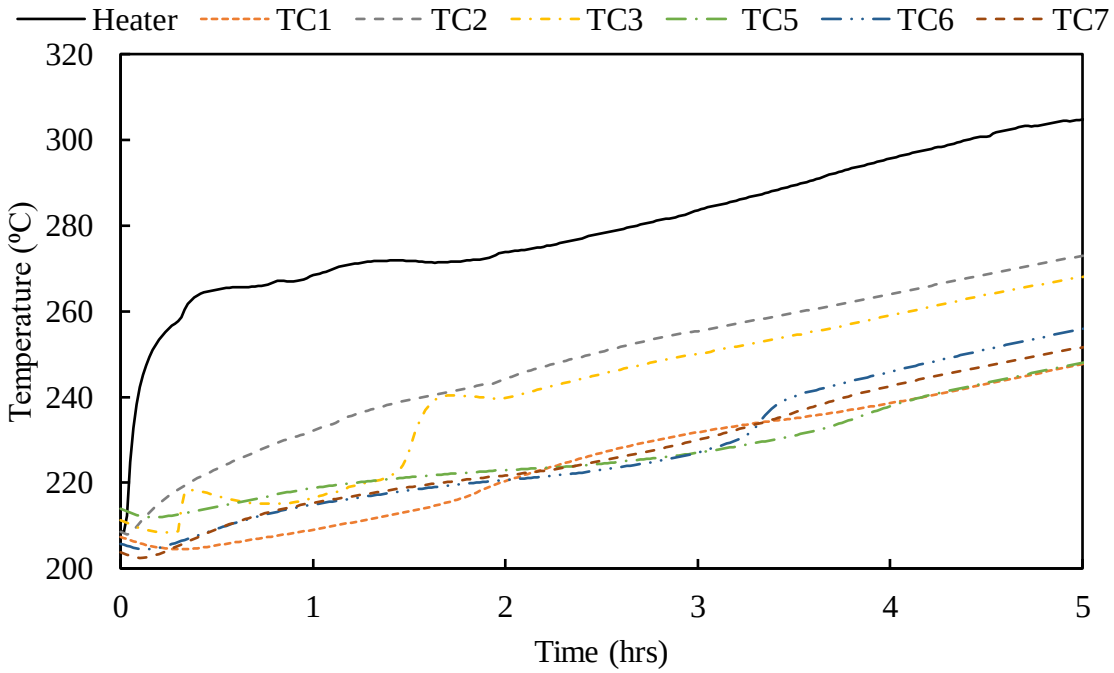

Figure 4-16: Experimental investigations of the temperature variation in the solar salt with 10 wt% of graphite for 35 W power input.

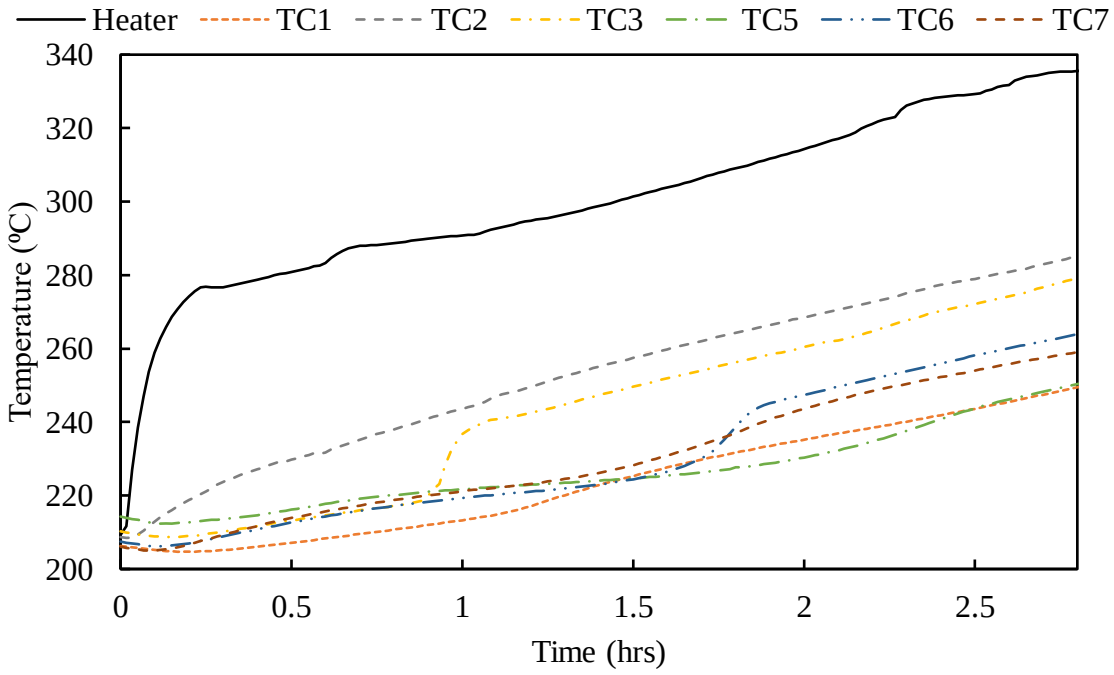

Figure 4-17: Experimental investigations of the temperature variation in the solar salt with 10 wt% of graphite for 50 W power input.

4.3.2 Thermal energy discharging process

Figure 4-18 shows the thermal energy discharging process that begins at the initial temperature of 245 ± 2 °C. This temperature initially decreases rapidly to 230.7 °C in 45 minutes in liquid's sensible heat loss mode due to the high thermal conductivity of solar salt with graphite.

The cooling rate varies from one location to another. For instance, TC1 and TC5 detect the lower cooling rate at about 13 °C/hr (compared to all other locations in which the cooling rate is around 28 °C/hr).

The temperature then decreases gradually due to phase change process from the liquid to solid-state, which is at 215.2 °C and this transition requires about 3 hours.

Finally, the temperature decreases as a loss of sensible heat of the solid phase to around 200 °C. The complete discharging process takes 6 hours to decrease the temperature from 245 °C to 200 °C with heat losses being approximately 30%. This translated to an average cooling rate of about 20 °C /hr.

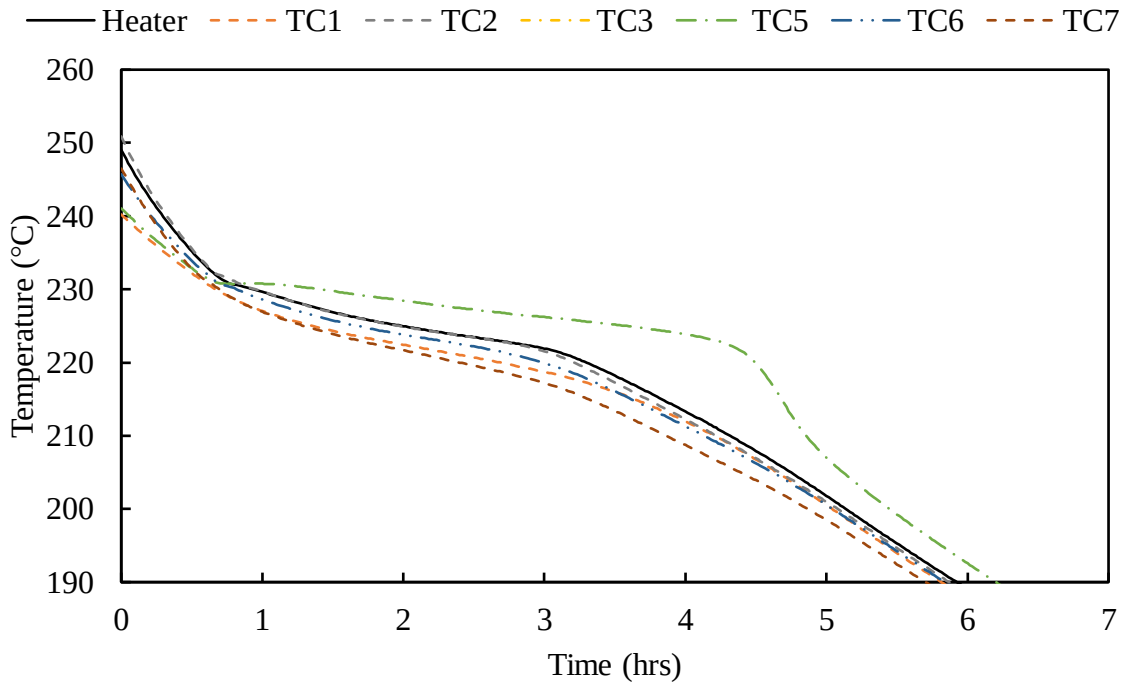

Figure 4-18: Experimental investigations of the temperature variation in the solar salt with 10 wt% of graphite during the discharging process.

4.4 The metal alloy

4.4.1 The thermal energy charging process

The thermal energy charging process in the TES with the metal alloy is shown in Figure 4-19 to Figure 4-22. The process starts at the initial temperature of 133 ±3 °C. It can be seen that the melting time in the case of using the metal alloy is decreased from 10 to 2.6 hours by increasing the power input from 18 to 50 W. The temperature increases in the

TES system first by thermal conduction heat transfer until the melting temperature of about 138 °C is reached. The melting process is observed as the constant temperature due to the change in metal alloy's phase from solid to liquid.

The input power of 18 W is sufficient to melt the metal alloy (unlike solar salt) due to the high thermal conductivity of the PCM.

As time elapses, the temperatures in TC1 and TC4 increase to reach the melting temperature range of about 138 – 143 °C. Then the temperature becomes constant due to the phase change process. Finally, the temperature starts to increase linearly due to heat accumulation in the form of sensible heat of the liquid.

The temperatures in TC3 and TC5 locations exhibit similar variation but at a slower rate, increasing from 133 °C to about 137 °C. This occurs due to their position being below the heat source and reduced effect of natural convection flows. The temperature becomes almost constant at about 138 °C due to the slow phase change transformation from solid to liquid. After completion of the phase change process, the temperature at the lower locations increases linearly to increase the sensible heat of the liquid alloy. The melting process is considered complete when the temperature the lowest point starts rising linearly beyond the melting range and this determines the complete melting time during the charging process.

In addition, it was shown that the temperature of TC2 is higher than the temperature of the heat source. The reason behind that is the position of the TC2 is above the heat source and the effects of convection heat transfer.

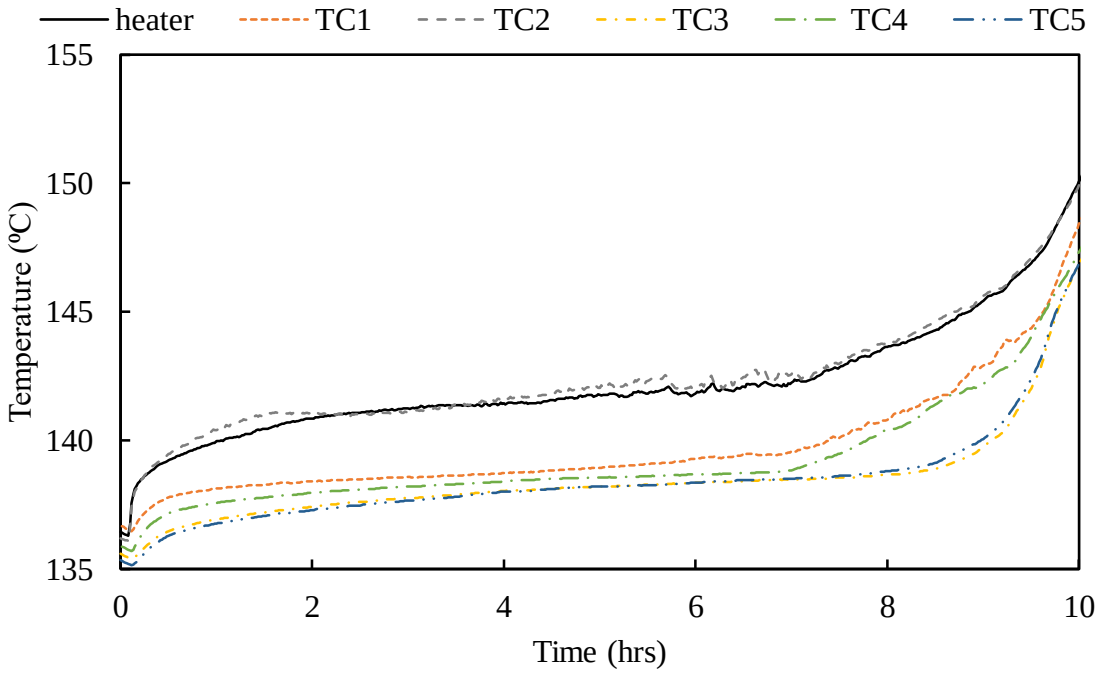

Figure 4-19: Experimental temperature variation in the metallic alloy during the melting process for 18 W power input.

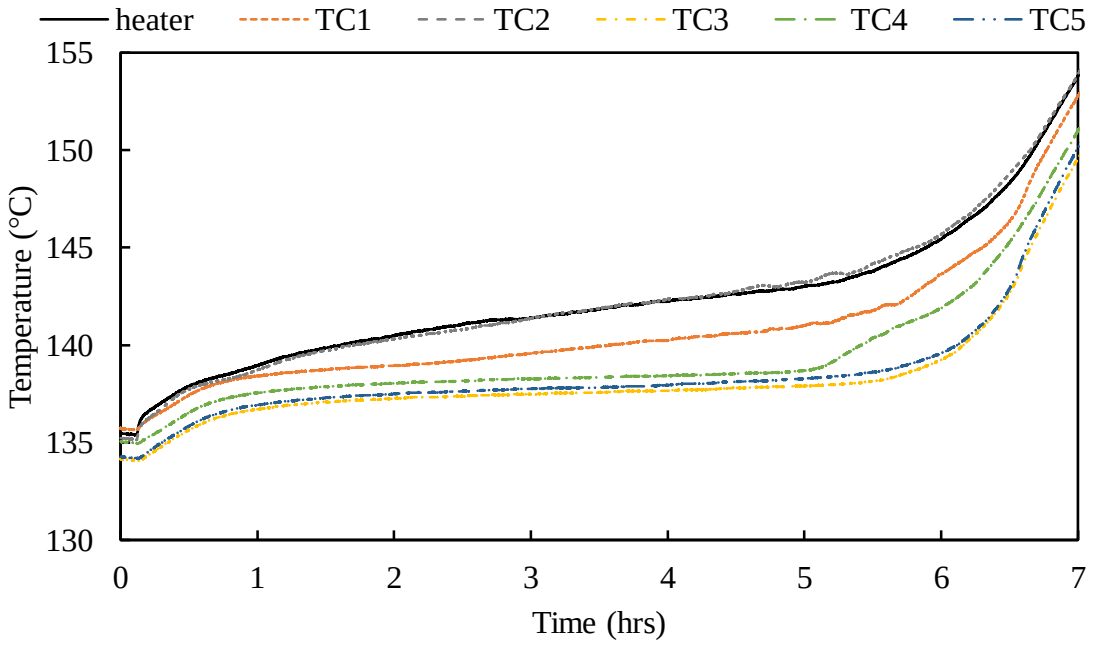

Figure 4-20: Experimental temperature variation in the metallic alloy during the melting process for 25 W power input.

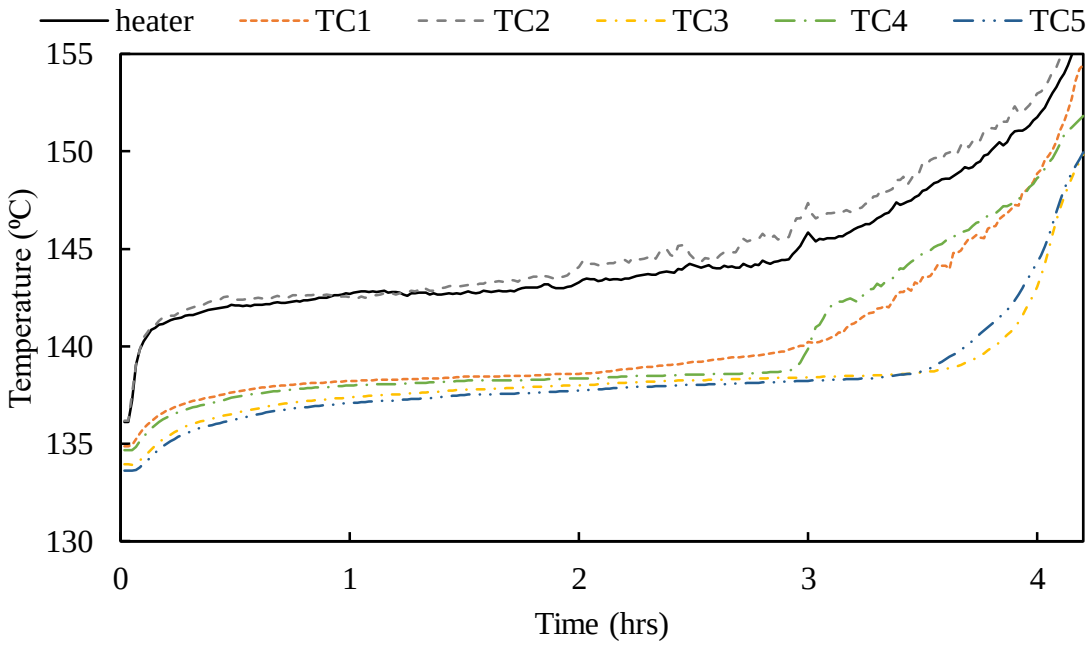

Figure 4-21: Experimental temperature variation in the metallic alloy during the melting process for 35 W power input.

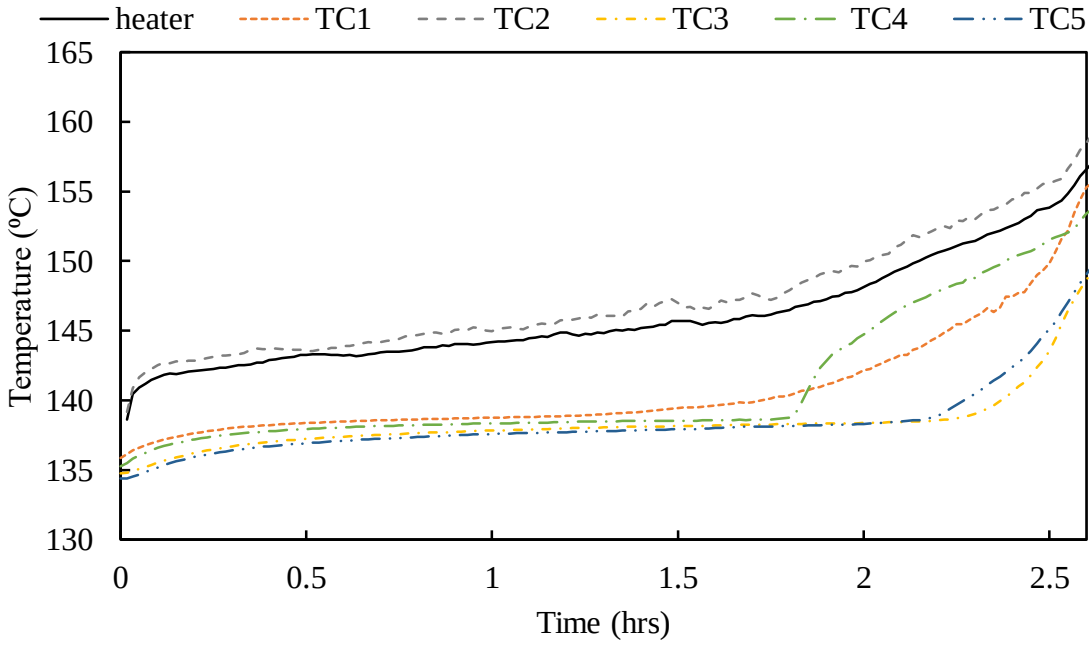

Figure 4-22: Experimental temperature variation in the metallic alloy during the melting process for 50 W power input.

4.4.2 The thermal energy discharging process

Figure 4-23 shows the solidification process of Bi58%-Tin 42%, which starts at the 153 ±3 °C level and ends at 120 °C. The solidification process due to heat losses to the environment, which takes around 15 hours. The solidification process starts with the metal alloy being entirely in the liquid phase.

Initially, the metal alloy temperature decreases linearly with time during the cooling of the liquid phase. The solidification process exhibits two different temperature dips that occur at 137 °C and 135 °C. This is due to the effect of undercooling, in which some of the molecules are not completely solidified due to additional new surfaces that contain liquid.

When the liquid solidifies, it releases energy. The phase change process begins at 136 °C and takes about 12 hours to complete the transformation to solid. The linear cooling process starts again after the phase change is completed and energy is lost as a reduction in the sensible heat of the solid alloy. The cooling rate was about 8 °C/hr for a sensible heat process with the heat losses being approximately 40%.

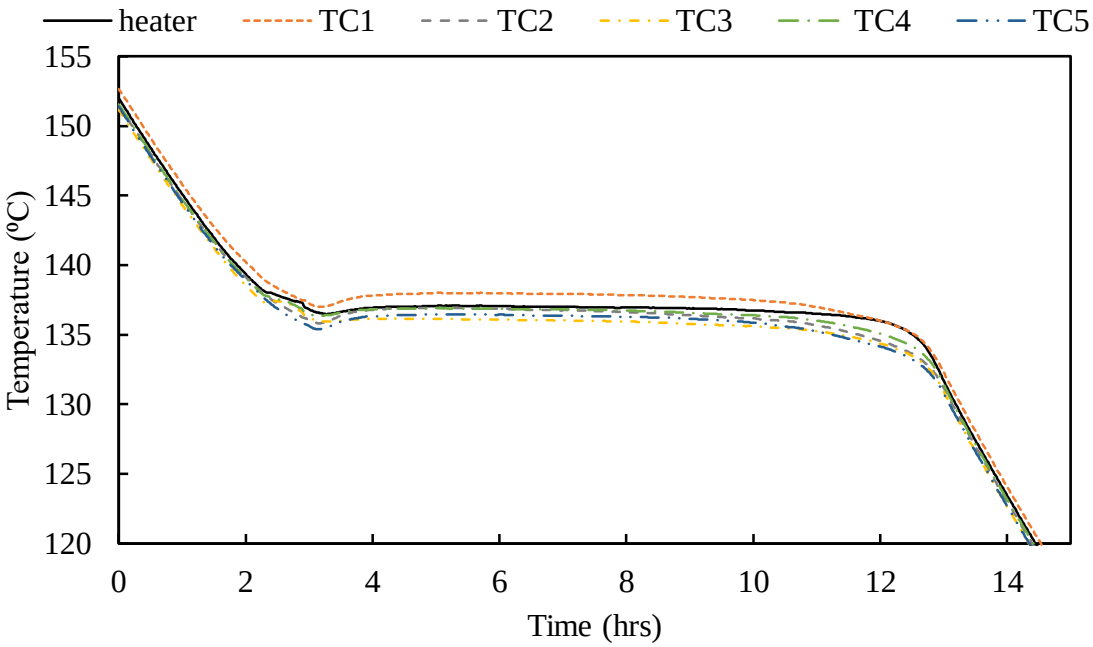

Figure 4-23: Experimental temperature variation in the metallic alloy during the thermal energy discharging process.

4.5 Conclusion

In this chapter, the results of experimental investigations carried out on the TES system using different PCMs were described. Solar salt (suitable for medium-temperature applications) exhibited significantly slower energy charging and discharging times in the conventional container compared to the case in which finned containers were used or in which its thermal conductivity was enhanced by adding 10 wt% of graphite.

The metal alloy PCM (suitable for low-temperature applications) was also investigated in the TES system using a conventional container. It was seen that this TES system can be charged and discharged significantly faster compared to the TES system using solar salt, or solar salt enhanced with graphite or using fins. This is due to the high thermal conductivity of the metal alloy.

Finally, the heat losses from the TES system were evaluated based on the heat transfer during discharging and charging processes, as defined by Equation (4-1).

$$heat\ losses\ = \frac{Q_{cooling}}{Q_{\ heating}} \times 100\% \tag{4-1}$$

Here, $Q_{\ cooling}$ is the heat transfer during the cooling process in the liquid phase, and $Q_{\ heating}$ is the heat transfer during the heating process in the solid phase. The heat transfer was calculated based on the change in the sensible heat of the liquid and solid phases as defined by Equation (4-2):

$$Q = m \cdot C_p \cdot \Delta T \tag{4-2}$$

Here, m is the mass of PCM (kg), $C_p$is the specific heat of the PCM (J/kg °C) and ΔT is the temperature difference during heating and cooling with respect to time (°C/Second).

The heat losses from solar salt TES systems with different configurations were calculated to be approximately 50%, 40% and 30% for solar salt TES, solar salt with the finned containers and TES with solar salt with graphite, respectively. The heat losses from the TES system with the metal alloy was calculated to be 40%. Improving the insulation of the system at high temperatures would improve the efficiency of the thermal performance of the TES system.

Chapter 5 Dimensionless and dimensional parameters used for evaluation of TES systems

This chapter describes the evaluation of the TES system performance based on the value of the accumulated energy. Also, this chapter presents the different parameters used to predict the nature of fluid flow (laminar or turbulent) in order to select the appropriate model in the numerical modelling process. In addition, this chapter describes dimensionless parameters, which are used to generate dimensionless correlations to describe the evolution of the PCM liquid fraction as well as the energy accumulated and released.

5.1 Dimensionless Parameters

To characterize the melting and solidification processes of PCMs under various operating conditions, two main dimensionless parameters are used. These are the melted fraction, which can be defined as a ratio of the melted mass over the total mass of the PCM, and the averaged Nusselt number, which is the ratio of convection heat transfer in comparison to the conduction heat transfer, and is defined by Equation (5-1).

$$\overline{Nu} = \frac{Q\ N}{k\ A\ (T_w - T_{ave})} \tag{5-1}$$

Here, Q is the power input, T_w is the wall temperature of the heat source, T_{ave} is the average temperature of the PCM, N is half the height of the PCM, A is the surface area of the heat source and k is the thermal conductivity of the PCM.

The Nusselt number can be used to calculate the heat transfer coefficient (HTC), which is the measure of convection heat transfer in the melted PCM:

$$HTC = \overline{Nu} \cdot {}^{k}/_{N} \tag{5-2}$$

Typically, the transient heat conduction process increases the temperature of the PCM up to the melting temperature which can be characterised using Fourier number:

$$Fo = \alpha t/N^2 \tag{5-3}$$

Here, α is the thermal diffusivity of the PCM, which is described by Equation (5-4):

$$\alpha = {}^{k}/_{C_p \cdot \rho} \tag{5-4}$$

where, C_p is the specific heat of PCM, ρ is the density of PCM, N is the half-height of the PCM and t is the elapsed time.

The Stefan number, which accounts for the phase change process from the solid phase to the liquid phase and vice versa is defined by Equation (5-5):

$$Ste = C_p \Delta T/H \tag{5-5}$$

Here, ΔT is the temperature difference between the heat source and the mean melting temperature of PCM and H is the latent heat of fusion.

The dimensionless time number τ is defined as a multiplication of Stefan and Fourier numbers:

$$\tau = {}^{C_p \Delta T}/_{H} \cdot {}^{\alpha t}/_{Y^2} = Ste \cdot Fo \tag{5-6}$$

Prandtl number defines the ratio between the momentum diffusivity and the thermal diffusivity, as expressed by Equation (5-7):

$$Pr = \frac{\nu}{\alpha} = \frac{\mu/\rho}{k/(C_p\rho)} \tag{5-7}$$

Here, μ is the dynamic viscosity.

Rayleigh number describes the behaviour of fluids, in particular whether the flow in the boundary layer is laminar or turbulent, as expressed by Equation (5-8):

$$Ra = \frac{g\beta\Delta T l^3}{\nu\alpha} \tag{5-8}$$

Here, ΔT is the temperature difference between the wall and the average temperature of the PCM, l is the length of the heat source, ν is the kinematic viscosity.

5.2 Thermal energy storage capacity

The heat storage of the LHTES system is defined as absorbed and released heat. Typically, PCMs can save more thermal energy (around 5-10 times) in the form of latent heat rather than sensible heat. The solid-liquid transition is considered the most suitable phase change for TES systems.

The storage capacity of the LHTES system is the sum of latent heat in the solid-liquid transition and the sensible heat of the metal:

$$ST = M_{PCM}\left[\int_{T_i}^{T_m} C_{p,s}\, dT + \lambda\, H + \int_{T_m}^{T_f} C_{p,l}\, dT\right] + M_{metal}\int_{T_i}^{T_f} C_{p\ metal}\, dT \qquad (5\text{-}9)$$

Here, ST is the storage capacity, $C_{p,l}$ is the specific heat in the liquid phase, $C_{p,s}$ solid-phase for PCM and metal of the container and λ is the liquid fraction.

Chapter 6 The Methodology of CFD Modelling

6.1 Introduction

This chapter describes the theoretical background and selection of the CFD model used for the analysis of the TES systems with PCMs. Numerical simulations were performed by using the commercial software package ANSYS/Fluent to provide data about the liquid fraction, the average temperature of the PCM and temperature of the heat source. ANSYS/Fluent is capable of modelling the phase change phenomena (melting and solidification) relevant to this work as well as heat and mass transfer processes which occur in the TES systems.

ANSYS/Fluent CFD software is based on numerical solution of the governing partial differential equations of conservation of mass, momentum and energy to describe the processes of melting and solidification during the simulation of TES system.

6.2 Governing differential equations of the fluid flow

To describe the velocity, pressure, temperature, and density variations in a moving fluid the conservation laws of physical parameters are used. The main conservations equations used are:

- Conservation of Mass (continuity equation).
- Conservation of Momentum.
- Conservation of Energy.

6.2.1 Continuity equation

The continuity equation is used by ANSYS/Fluent software to describe the conservation of mass in an infinitesimally small control volume of a PCM during simulation of the TES system. The form of the continuity equation can be expressed as:

$$\frac{\partial \rho}{\partial t} + \frac{\partial (\rho U)}{\partial x} + \frac{\partial (\rho V)}{\partial y} + \frac{\partial (\rho W)}{\partial z} = 0 \quad (6\text{-}1)$$

Here, ρ is the fluid density and U, V, W are the velocity of the fluid in *x*, *y z* directions, respectively.

The equation is valid for compressible flow. For incompressible flow the first term turns to zero, $\frac{\partial \rho}{\partial t} = 0$.

6.2.2 Momentum equations

The momentum equations (6-2 to 6-4) are derived from Newton's second law, which is used in ANSYS/Fluent software to describe the interaction and balance of the various forces applied to a fluid, passing through an infinitesimally small control volume during simulation of a PCM in the TES system.

$$\frac{\partial (\rho U)}{\partial t} + \frac{\partial (\rho U^2)}{\partial x} + \frac{\partial (\rho VU)}{\partial y} + \frac{\partial (\rho UW)}{\partial z} = -\frac{\partial P}{\partial x} - \frac{\partial \varsigma_{xx}}{\partial x} - \frac{\partial \varsigma_{yx}}{\partial y} - \frac{\partial \varsigma_{zx}}{\partial z} + \rho g_x + \rho F_x \quad (6\text{-}2)$$

$$\frac{\partial (\rho V)}{\partial t} + \frac{\partial (\rho UV)}{\partial x} + \frac{\partial (\rho V^2)}{\partial y} + \frac{\partial (\rho VW)}{\partial z} = -\frac{\partial P}{\partial y} - \frac{\partial \varsigma_{xy}}{\partial x} - \frac{\partial \varsigma_{yy}}{\partial y} - \frac{\partial \varsigma_{zy}}{\partial z} + \rho g_y + \rho F_y \quad (6\text{-}3)$$

$$\frac{\partial (\rho W)}{\partial t} + \frac{\partial (\rho UW)}{\partial x} + \frac{\partial (\rho VW)}{\partial y} + \frac{\partial (\rho W^2)}{\partial z} = -\frac{\partial P}{\partial z} - \frac{\partial \varsigma_{xz}}{\partial x} - \frac{\partial \varsigma_{yz}}{\partial y} - \frac{\partial \varsigma_{zz}}{\partial z} + \rho g_z + \rho F_z \quad (6\text{-}4)$$

Here, p is the static pressure, $\overrightarrow{g}$ is gravitational body force, $\overrightarrow{F}$ is the external body force and ς is the stress tensor on the body.

When the fluid flow is uniform through the computational domain it is called laminar flow. On the other hand, if the fluid flow is not uniform due to fluctuations in some properties through the computational domain the fluid flow is called turbulent flow.

6.2.3 Laminar flow

Laminar flow occurs when a fluid flows in parallel layers, with no disruption between the different layers of fluid. The Rayleigh number is used to provide an indication of fluid flow in solar salt simulation. Thus, the Ra number was calculated using Equations (5-8) to be 8×10^7, which suggests laminar flow [194]. Therefore, the laminar flow was adopted in ANSYS/Fluent software to simulate the different configurations of the TES systems with solar salt.

The momentum equations for the laminar fluid flow can be written as:

$$\frac{\partial(\rho U)}{\partial t} + \frac{\partial(\rho U^2)}{\partial x} + \frac{\partial(\rho VU)}{\partial y} + \frac{\partial(\rho UW)}{\partial z} = -\frac{\partial P}{\partial x} + \rho g_x + \rho F_x \quad (6\text{-}5)$$

$$\frac{\partial(\rho V)}{\partial t} + \frac{\partial(\rho UV)}{\partial x} + \frac{\partial(\rho V^2)}{\partial y} + \frac{\partial(\rho VW)}{\partial z} = -\frac{\partial P}{\partial y} + \rho g_y + \rho F_y \quad (6\text{-}6)$$

$$\frac{\partial(\rho W)}{\partial t} + \frac{\partial(\rho UW)}{\partial x} + \frac{\partial(\rho VW)}{\partial y} + \frac{\partial(\rho W^2)}{\partial z} = -\frac{\partial P}{\partial z} + \rho g_z + \rho F_z \quad (6\text{-}7)$$

6.2.4 Turbulence modelling

Generally, the dynamic boundary layer is similar to the thermal boundary layer that occurs in cases with Pr ~ 1. However, for the metal PCM Pr <<1, due to the high thermal conductivity, which makes the thermal boundary layer thicker than the dynamic boundary layer. That causes fluctuations in the velocity components of the fluid flow, which transport quantities of momentum and energy. These oscillations are characterized by a wide spectrum of energies with a wide range of spatial and temporal scales. The three-

dimensional unsteady form of the NS equations can describe the turbulence, although in practice they are too difficult to solve analytically and numerically without approximations. Some approximated versions of the NS equations for turbulent flows, such as large eddy simulation (LES), eddy viscosity models (EVM) and direct numerical simulation (DNS), have been shown to be reliable methods to be applied to turbulent flows [195]. The most feasible turbulent model for industrial flows is EVM. However, the DNS is considered to be the most accurate model but it is highly expensive in terms of computational time.

In this study, the choices of turbulent models were limited to the specific models of EVMs, which are presented together with a discussion of the boundary conditions to be used to simulate the TES systems with the metal PCM, since these models have an acceptable computational cost, compared to DNS and LES [196].

6.2.4.1 k-ε Model

The k-ε turbulence model is suitable for a wide range of applications at a low computational time and providing robustness, although at the expense of accuracy. The turbulent length and time scales are determined using two-equations that are for the kinetic energy (k) and dissipation rate (ε). In addition, this model predicts turbulent generation due to shear buoyancy, accounting for the effects of compressibility [197].

The transport equations for the standard k-ε model can be written as:

$$\frac{\partial}{\partial t}(\rho k) + \frac{\partial}{\partial x_i}(\rho k u_i) = \frac{\partial}{\partial x_j}\left\{\left(\mu + \frac{\mu_t}{\sigma_k}\right)\frac{\partial k}{\partial x_j}\right\} + G_{tke} + G_b - \rho\varepsilon - Y_M + S_{tke} \tag{6-8}$$

and,

$$\frac{\partial}{\partial t}(\rho\varepsilon) + \frac{\partial}{\partial x_i}(\rho\varepsilon u_i) = \frac{\partial}{\partial x_j}\left\{\left(\mu + \frac{\mu_t}{\sigma_\varepsilon}\right)\frac{\partial \varepsilon}{\partial x_j}\right\} + C_{1\varepsilon}\frac{\varepsilon}{k}(G_{tke} + C_{3\varepsilon}G_b) - C_{2\varepsilon}\rho\frac{\varepsilon^2}{k} + S_\varepsilon \quad (6\text{-}9)$$

Here, G_{tke} is the generation of turbulent kinetic energy because of the mean velocity gradients, G_b is the kinetic energy generation from buoyancy effects, Y_M is the contribution of the fluctuating dilatation incompressible turbulence to the overall dissipation rate; $C_{1\varepsilon}$, $C_{2\varepsilon}$, and $C_{3\varepsilon}$ are constants; $\sigma_\varepsilon$and σ_k are the turbulent Prandtl numbers for k and ε respectively; S_k and S_ε are user-defined source terms.

6.2.4.2 Standard and SST k-ω models

The standard k-ω model in ANSYS/Fluent is based on the k-ω model of Wilcox [198] which is sufficiently powerful to capture low-Reynolds number effects, compressibility, and shear flow spreading. However, the sensitivity of the solutions to the values of specific dissipation rate (ω) and kinematic energy (k) outside the shear layer is its weak point. The model was developed based on transport equations for the turbulence *k* and *ω*. The transport equations for the *k-ω* model can be formulated as [197]:

$$\frac{\partial}{\partial t}(\rho k) + \frac{\partial}{\partial x_i}(\rho k u_i) = \frac{\partial}{\partial x_j}\left\{\Gamma_k\frac{\partial k}{\partial x_j}\right\} + G_k - Y_k + S_k \quad (6\text{-}10)$$

and,

$$\frac{\partial}{\partial t}(\rho\omega) + \frac{\partial}{\partial x_i}(\rho\omega u_i) = \frac{\partial}{\partial x_j}\left\{\Gamma_\omega\frac{\partial \omega}{\partial x_j}\right\} + G_\omega - Y_\omega + S_\omega \quad (6\text{-}11)$$

Here, Γ_k and Γ_ω are the effective diffusivities of k and ω, G_k is the generation of the turbulence kinetic energy yields by velocity gradient, G_ω represents the generation of specific dissipation rate, Y_k *and* Y_ω express the dissipation rate of k and ω, S_k and S_ω are user-defined source terms.

The Shear-Stress Transport (SST) k-ω model was developed in [199]. The developed model combines the accurateness and robustness of the *k-ω* model near-wall regions, with the freestream independence in the regions far from the wall.

6.2.4.3 Transition-SST model

In ANSYS/Fluent, the transition SST model is based on combining the SST of the *k-ω* model with two other transport equations. The first equation is for intermittency and the second equation is for the transition onset criteria, which is expressed by the momentum-thickness Reynolds number. The transition-SST model covers the transition process from laminar to turbulent flow and flows in a low freestream turbulence environment, and such the model provides an accurate prediction of the boundary layer near the wall of the heat source. Consequently, this model was selected to simulate the TES system with the metal PCM.

The transport equations for the transition SST model [197] can be formulated as:

$$\frac{\partial(\rho\gamma)}{\partial t}\frac{\partial\left(\rho U_{j\gamma}\right)}{\partial x_j} = P_{\gamma 1} - E_{\gamma 1} + P_{\gamma 2} + E_{\gamma 2} + \frac{\partial}{\partial x_j}\left[\left(\mu + \frac{\mu_t}{\sigma_\gamma}\right)\frac{\partial\gamma}{\partial x_j}\right] \quad (6\text{-}12)$$

Here, $P_{\gamma 1}$ and $E_{\gamma 1}$ the transition sources which control the length of the transition area and $P_{\gamma 2}$ and $E_{\gamma 2}$ are the destruction/ relaminarization sources.

6.2.5 Energy equation

The first law of thermodynamics is used to derive the energy equation that is applied to the fluid passing through an infinitesimally small control volume. The ANSYS/Fluent software considers the energy transfer in the PCM of TES systems as heat transfer, which occurs by conduction and convection in the solid and fluid regions of computational domain. The energy equation in ANSYS/Fluent software can be expressed as [197]:

$$\frac{\partial}{\partial t}(\rho E) + \nabla.\left(\vec{u}(\rho E + p)\right) = -\nabla.\left[k_{eff}\nabla T - \sum_j h_j \vec{J}_j + \left(\bar{\bar{\varsigma}}_{eff}.\vec{u}\right)\right] + S_h \qquad (6\text{-}13)$$

Here,

∇ is defined as:

$$\nabla = \frac{\partial}{\partial x} + \frac{\partial}{\partial y} + \frac{\partial}{\partial z} \qquad (6\text{-}14)$$

$\bar{\bar{\varsigma}}$ is the stress tensor and is expressed as:

$$\bar{\bar{\tau}}_{eff} = \mu\left[(\nabla\vec{v} + \nabla\vec{v}^{T}) - \frac{2}{3}\nabla.\vec{v}\, I\right] \qquad (6\text{-}15)$$

Where, μ is the molecular viscosity, I is the unit tensor, and the second term on the right-hand side of Equation (6-13) is the effect of volume dilation. k_{eff} is the effective thermal conductivity, $\vec{J}_j$ is the species j diffusion flux and S_h includes the heat of chemical reaction, and any other user-defined volumetric heat sources.

E is defined as:

$$E = h - \frac{p}{\rho} - \frac{u^2}{2} \qquad (6\text{-}16)$$

Here, the term h is the sensible enthalpy and expressed by ideal gas law as:

$$h = \sum_j Y_j h_j \qquad (6\text{-}17)$$

For incompressible flow the sensible enthalpy is expressed as:

$$h_j = \int_{T_{ref}}^{T} C_{p,j}\, dT \qquad (6\text{-}18)$$

Here, T_{ref} is reference temperature, which is equal to 298.15 K, Y_j is the mass fraction of the species.

When the heat is added to a fluid, its density varies with temperature, resulting in fluid motion, which is defined as natural convection. ANSYS/Fluent can model the natural convection of liquid PCMs in TES systems with solar salt using two different schemes. The first scheme uses the piecewise model to define the fluid density as a function of temperature, whether it is a polynomial or a set of various values for various operating temperatures. The second scheme uses of constant density in the momentum equation. This is referred to as the Boussinesq model.

The Boussinesq model can be expressed by Equation (6-19):

$$(\rho - \rho_o)g \approx -\rho_o \beta (T - T_o)g \tag{6-19}$$

Here ρ_o is the reference fluid density, β is the thermal expansion coefficient of the fluid and T_o is the reference operating temperature. The Boussinesq approximation can be obtained by using the relation presented in Equation (6-20):

$$\rho = \rho_o(1 - \beta T_o) \tag{6-20}$$

The Equation (6-20) was used to re-define the density using temperature. The Boussinesq approximation assumption is only valid when there is a small variation for temperature and density.

6.3 General formulation of melting and solidification

When the heat is added to or released from a fluid passing through an infinitesimally small control volume at the certain temperature level, it changes the phase of the material from solid to liquid and vice versa - the phenomenon is known as the phase-change process, which includes melting and solidification. This is considered in ANSYS/Fluent software to simulate the TES systems with PCMs.

The main problem of phase transitions in matter lies within the interface that defines the solid and liquid phases, which is referred to as "Stephan problem". Typically, a sharp interface boundary separates the solid and liquid phases that are characterized by the non-linear, transient phenomenon. The mathematical formulation of the phase change process requires the heat transfer for the solid phase and liquid phase to be defined separately. In addition, a condition at the solid-liquid interface has to be defined [200] as follows:

-heat transfer in the solid phase, which is expressed by Equation (6-21):

$$\rho_s C_s \frac{\partial T_s}{\partial t} = \frac{\partial}{\partial x}\left(k_s \frac{\partial T_s}{\partial X}\right) \qquad 0<x<s(t) \tag{6-21}$$

-heat transfer in the liquid phase, which is expressed by Equation (6-22):

$$\rho_l C_l \frac{\partial T_l}{\partial t} = \frac{\partial}{\partial x}\left(k_l \frac{\partial T_l}{\partial X}\right) \qquad s(t)<x<\infty \tag{6-22}$$

Here, $T_l \; and \; T_s$ represent the temperature in liquid and solid phases, $k_l \; and \; k_s$ represent the thermal conductivity of liquid and solid phases, ρ_l and ρ_s represent the density in liquid and solid phases, $s(t)$ is the position of moving boundary, which is determined by Stephan's condition.

The Stefan condition was implemented to enforce the heat balance at the solid-liquid interface, expressed by Equation (6-23):

$$k_s \frac{\partial T_s}{\partial x} - k_l \frac{\partial T_l}{\partial x} = \rho_l H_m \frac{\partial s}{\partial t} \tag{6-23}$$

6.4 Numerical models of the phase change

Different numerical methods used to predict the liquid-solid interface during phase change phenomena can be categorized into moving and fixed grids. The moving grid

method solves the interface locations at each time step, which is a superior approach to capture the interface of phase change, although it is computationally expensive. The fixed grid method was adopted in ANSYS/Fluent to solve the governing equations to identify the interface between solid and liquid. In ANSYS/Fluent the fixed grid method is based on the enthalpy method which is used to predict the position of the solid-liquid interface during melting and solidification processes of PCMs in TES systems.

6.4.1 Enthalpy method

The enthalpy method is a simple and useful technique to describe the phase change process, and has been implemented in ANSYS/Fluent to compute the liquid fraction of the PCM during simulation of the TES system. It considers the effect of sensible heat along with latent heat during the phase change phenomena by introducing a mushy zone at the interface between solid and liquid [197]. The mushy zone is created when the solidified material melts and vice versa. This method can be expressed in terms of temperature and enthalpy as shown by Voller and Parakash [201] in Equation (6-24):

$$\partial(\rho H)/\partial t + \nabla \cdot (\rho u H) = \nabla \cdot (k \nabla T) \quad (6\text{-}24)$$

Here, H represents the enthalpy of material and k is the thermal conductivity.

The enthalpy of the material can be calculated in terms of latent heat and sensible heat, as demonstrated in Equation (6-25) :

$$H = h + \Delta H \quad (6\text{-}25)$$

Here, h and ΔH represent sensible heat and latent heat of the material, respectively.

The sensible heat can be calculated using Equation (6-26):

$$h = h_{ref} + \int_{T_{ref}}^{T} C_p \Delta T \tag{6-26}$$

Here, h_{ref}, C_p and T_{ref} represent the reference enthalpy, reference specific heat and reference temperature at a constant temperature, respectively.

Equation (6-27) calculates the latent heat based on the liquid fraction during the phase change:

$$\Delta H = \lambda L \tag{6-27}$$

Here, λ is the liquid fraction, and it can be evaluated based on temperature during the phase change process, as follow:

$$\gamma = \begin{cases} 0 & if \quad T < T_S \\ \dfrac{T - T_l}{T_l - T_s} & if \quad T_{Solid} < T < T_l \\ 1 & if \quad T > T_l \end{cases} \tag{6-28}$$

6.4.2 Modelling heat transfer through porous media

When the phase change process occurs, a thin layer with high viscosity forms between the solid and liquid regions, which is called the mushy zone. ANSYS/ Fluent defines the mushy zone region, in which the liquid fraction varies between 0 and 1, as a porous media to simulate the phase change process of a PCM in the TES system. This is considered through an additional source term, which is represented in the momentum equation by the $\overrightarrow{F}$ term. Two different losses, which are viscous and inertial, are associated with the source term. The inertia loss can be expressed by Equation (6-29):

$$S_i = -\left[\sum_{j=1}^{3} \mathcal{D}_{ij} \mu v_i + \sum_{j=1}^{3} \mathcal{C}_{ij} \frac{1}{2} \rho |v| v_i\right] \tag{6-29}$$

Here, $S_i, v_i, |v|, \mathcal{D}$ and $\mathcal{C}$ represent the porous media source term, the velocity, the absolute velocity, and the last two terms are prescribed matrices. Generally, the momentum is related to the pressure gradient through the porous zone resulting in pressure drop, which is proportional to the fluid velocity. However, for a homogeneous media, the source term can be formulated as Equation (6-30):

$$S_i = -\left(\frac{\mu}{\Omega} v_i + O\frac{1}{2}\rho|v|v_i\right) \tag{6-30}$$

Here Ω and O are the permeability and the inertial resistance factor, respectively.

When the fluid flow through the porous media is laminar, the second term on the right-hand side can be neglected. Therefore, the pressure drop can be evaluated in Cartesian coordinate by Equations (6-31) through to (6-33):

$$\Delta p_x = \sum_{j=1}^{3} \frac{\mu}{\Omega_{xj}} v_i \Delta n_x \tag{6-31}$$

$$\Delta p_y = \sum_{j=1}^{3} \frac{\mu}{\Omega_{yj}} v_i \Delta n_y \tag{6-32}$$

$$\Delta p_z = \sum_{j=1}^{3} \frac{\mu}{\Omega_{zj}} v_i \Delta n_z \tag{6-33}$$

Here, Δn_x, Δn_y, and Δn_z represent the thicknesses of the porous region in the Cartesian coordinate. Heat transfer through the porous media can be reformulated based on the conduction flux and transient terms only. Therefore, the standard energy equations can be expressed as Equation (6-34):

$$\frac{\partial}{\partial t}\left(\gamma\rho_f E_f + (1-\xi)\rho_s E_s\right) + \nabla.\left(V\left(\rho_f E_f + p\right)\right) = \nabla.\left[k_{eff}\nabla T - \left(\sum_i h_i j_i\right) + \left(\bar{\bar{\tau}}\vec{V}\right)\right] + S_f^h \tag{6-34}$$

Here, E_f,E_s, ξ and S_f^h represent the fluid total energy, the solid region total energy, the medium porosity and the enthalpy source term of the fluid, respectively.

The effective thermal conductivity k_{eff} is evaluated in ANSYS/Fluent based on the volume average conductivity of the fluid as well conductivity of the solid by Equation (6-35):

$$k_{eff} = \xi k_f + (1 - \xi) k_s \tag{6-35}$$

Here k_f and k_s represent the thermal conductivity of the fluid and the thermal conductivity of the solid medium.

Chapter 7 Numerical modelling and validation of TES systems

7.1 Introduction

A numerical model was created to investigate the thermal behaviour of the TES system with PCMs in ANSYS/Fluent environment. Solar salt and Bi-Tin alloy were used as PCMs for medium and low-temperature applications, respectively. Extended surfaces (fins) and additive (graphite) were used to intensify the heat transfer in the TES system. Numerical results were validated using experimental data. This chapter numerically assesses the influence of various parameters on the temperatures and the flow velocity profiles and velocities of thermal energy charging and discharging during the melting and solidification processes. Results are used to derive dimensionless equations to describe the performance of the TES systems which then can be used for the TES design purposes.

7.2 Modelling procedure

Numerical modelling consists of three main stages: in the first stage, the geometry of the TES systems (finned container and conventional container) was created. In the second stage, the computational mesh was generated. Finally, the appropriate mathematical model (laminar or turbulent flow) settings were selected with boundary and initial conditions to simulate cases with solar salt and metal alloy PCM to determine the charging and discharging times.

7.2.1 The geometry of TES system

Figure 7-1 shows the geometry of the TES systems used with the dimensions specified. The TES systems consist of a square container with a circular cylinder extruded along its centre. The outer boundary of the container was modelled as a solid, whilst internally it was filled with PCMs. A heat source was applied on the surface of the extruded circular cylinder and different thicknesses of insulation were used to simulate the heat losses from the container. The thickness of the container walls is 3 mm.

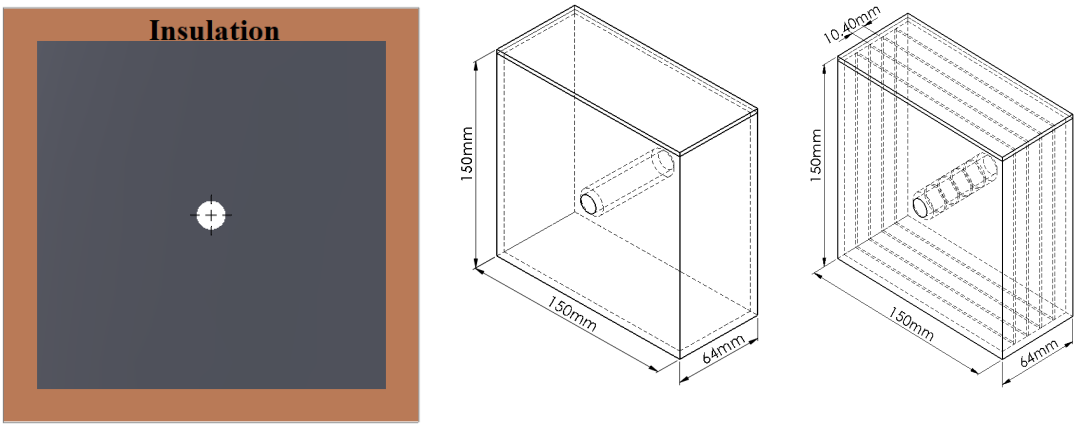

a) b) c)

Figure 7-1: Schematic diagram of TES system a) Front view of the container with insulation material. b) The stainless steel container. c) The container with fins.

7.2.2 Generation of the computational grid

The number of cells within a computational domain affects the calculation time and the solution accuracy, and therefore a mesh sensitivity study was performed to ensure the mesh independence of the obtained solutions. The domain was discretized using sweeping mesh to create the mesh with a hexahedral structure, as shown in Figure 7-2.

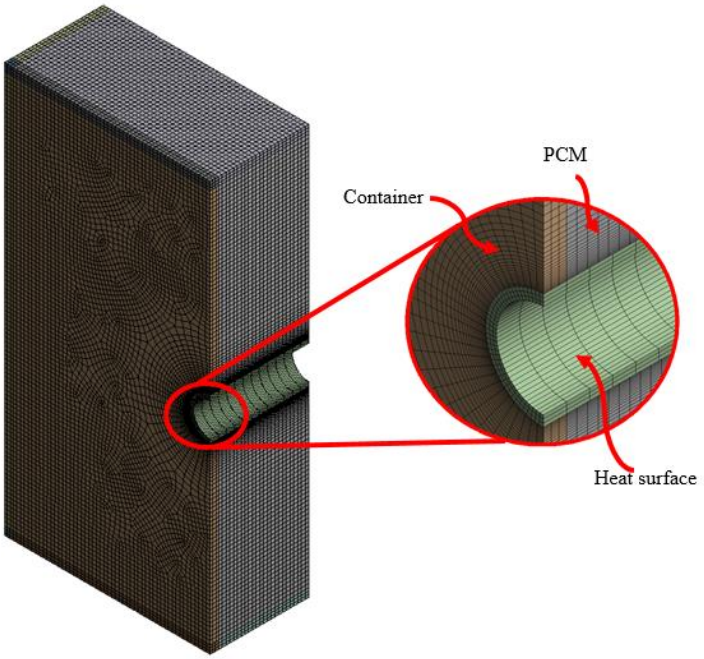

Figure 7-2: Generated mesh of the hexahedral type.

The finned and conventional containers were discretized using the sweeping mesh method that provides hexahedral volumetric cells with local refinement near the heat source to capture the sharp gradients between the solid-liquid interfaces. Two final mesh sizes examined are shown in Figure 7-3 that indicates no influence on the solution accuracy as the grid size is refined from 0.3 to 0.6 million cells with power input of 70 W.

In addition, the analysis of the influence of the time step was conducted as shown in Figure 7-4 that ranged from 0.1 s to 0.5 s using 70 W, as power input. It was found that the time step of 0.2 s was sufficient to capture the flow characteristics with increasing of simulations time of the melting process by 8 %. Therefore, the time step of 0.2 s and a computational grid of 0.3 million cells were used in numerical simulations in this work.

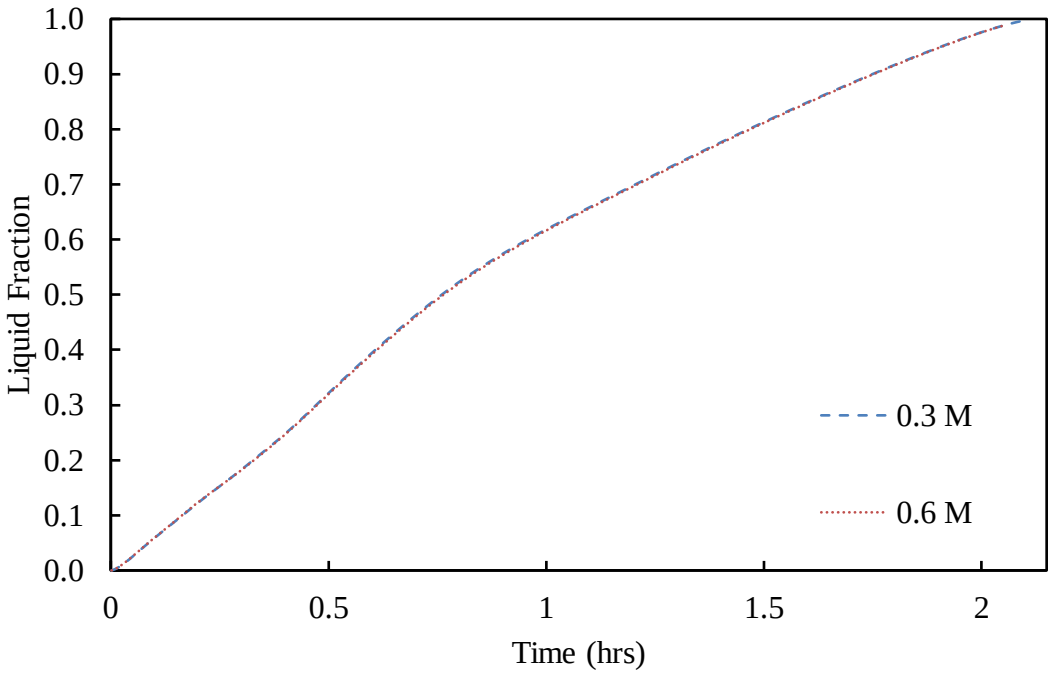

Figure 7-3: Mesh dependence study.

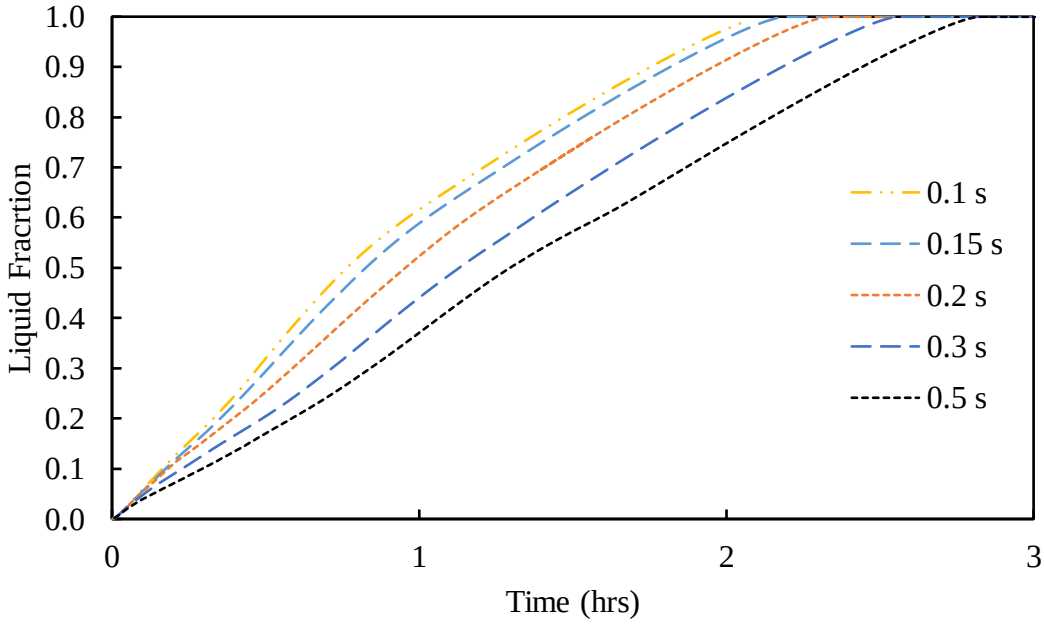

Figure 7-4: Time step dependence study.

7.2.3 Mathematical model description

A three-dimensional CFD model of the TES systems with PCMs was developed using the commercial software package ANSYS/Fluent 18.2. The enthalpy-porosity approach was implemented to simulate the melting and solidification processes of the TES system. The flow regime of solar salt within the TES system of different configurations (fins and additives) is likely to be laminar, due to the small value of the Rayleigh number, as explained in Section 6.2.3. Therefore, the natural convection flow was considered during numerical modelling to consider the effects of the expansion of the fluid during the melting and solidification processes by deploying the Boussinesq approximation, as suggested in [55, 202, 203].

A turbulent flow model was used in the TES system with the metal alloy due to the low Prandtl number, which means the thermal boundary layer is thicker than the dynamic boundary layer. Thus, the SST-turbulent model was found to be sufficient to simulate the transition from the laminar flow to turbulent flow, which occurs in a low freestream turbulence environment, as well as to provide an efficient resolution of the boundary layer near the wall of the heat source, as explained in Section 6.2.4.3.

The melting and solidification model was adopted to describe the phase change process. The simple Pressure-Velocity-coupling scheme was deployed using PRESTO algorithm with second-order upwind spatial discretization, as recommended by ANSYS. The default relaxation factors for pressure correction were used: these parameters for body forces, momentum, energy, and liquid fraction calculations were set to 0.3, 1, 0.7, 1 and 0.9, respectively.

A constant power input boundary condition was applied on the inner surface of the cylinder with prescribing the constant power input, to simulate the charging process of

the LHTES system. Free cooling caused by heat losses was adopted to simulate the discharging process by prescribing corresponding heat fluxes on the boundaries of the TES system. The boundary condition can be shown in Figure 7-5. Table 7-1 summarises information on the flow regimes and the thickness of the insulation used in the modelling of different TES systems.

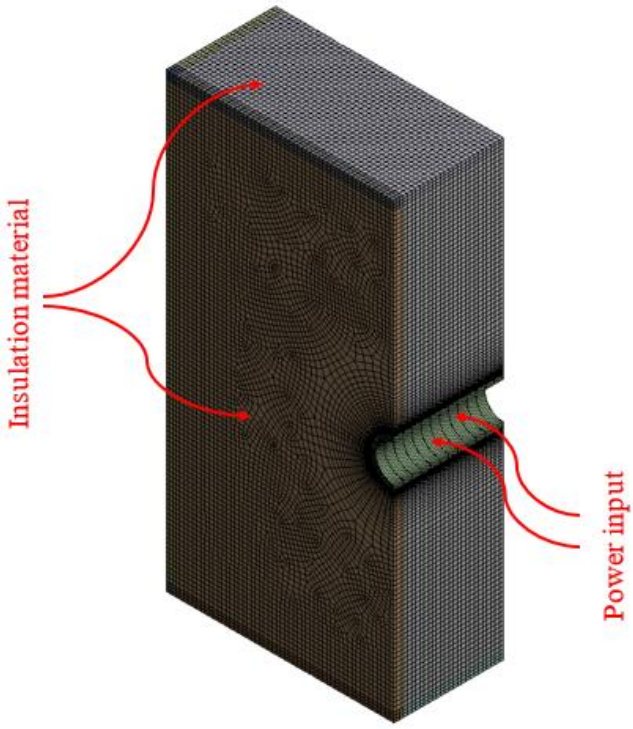

Figure 7-5: Boundary conditions of TES systems.

Table 7-1: The numerical model of TES systems.

TES type	Model	Insulation thickness
Solar salt	Laminar flow	30 mm
Finned container	Laminar flow	50 mm
Solar salt with 10 wt% graphite	Laminar flow	40 mm
Metal alloy	SST-Turbulent flow	50 mm

7.2.4 Initial conditions

The initial conditions applied to the TES systems during the melting and solidification processes are shown in Table 7-2.

Table 7-2: The initial conditions applied in the modelling of TES systems during charging and discharging processes.

TES type	Initial temperature for charging (°C)	Initial temperature for discharging (°C)	Power (W) during charging	Power (W) during discharging
Solar salt	210	265	35, 50	zero
Finned container	210	235	25, 35	zero
Solar salt with 10 wt% graphite	210	245	25,35,50	zero
Metal alloy	135	210	18, 25, 35, 50	zero

The natural convection was considered on the external walls of the TES system, with 5 W/m^2 K and 25 °C as heat transfer coefficient and ambient temperature, respectively.

7.3 Model validation

In order to examine the reliability of the numerical model, a validation procedure was conducted by comparing the numerical results to the experimental measurements discussed in Chapter 3. The comparison was confined to the PCM temperature range for certain design parameters and operating conditions such as the ambient temperature, insulation material thickness, power input and initial temperature of the TES system. In addition, different TES system types were simulated, including conventional and finned containers with pure solar salt, solar salt with graphite and metal alloys to evaluate the accuracy of the numerical models. A condition was set that the maximum relative deviation value (described in Equation 7-1) should not exceed 4% between the two measurement techniques.

$$Deviation = |(T_{Exp} - T_{Num})/(T_m)| \times 100\ \% \quad (7\text{-}1)$$

Here, T_{Exp} is the temperature of the experimental results, T_{Num} is the temperature of the numerical results and T_m is the melting temperature of the PCM.

The charging process of TES systems is shown in Figure 7-6, Figure 7-7, Figure 7-11, Figure 7-12, Figure 7-16, Figure 7-17, Figure 7-21 and Figure 7-22. Conduction heat transfer is initially dominant in transferring energy from the source to the PCM. As time elapses, the temperature of the PCM reaches the melting temperature near the heat source and then energy is transferred across the container because of natural convection. The points near the heat source have a sharp rise in the temperature due to their proximity to the heat source. Recirculation of the molten PCM occurs between the bottom and top regions of the container due to convection during the charging process. Furthermore, the temperature rises in the vicinity of points that start melting, as shown in the temperature and melting contours in Figure 7-8, Figure 7-13, Figure 7-18 and Figure 7-23. Also, figures show the velocity contours, in which it can be seen that the molten PCM ascends from the top surface of the heat source at the centre of the TES system. The convection is intensified as time elapses due to the increasing liquid fraction. In the case of solar salt container of different configurations, the velocity contours indicate the uniform laminar flow. On the other hand, the velocity contours in the metal PCM storage show fluctuations during the melting process due to the turbulent flow.

Whilst the temperature of the PCM in the bottom section remains lower than the melting temperature as a consequence of the effect of small intensity natural convection, it can be seen that the PCM temperatures reach the melting point at different times and locations because of the distance between the thermocouples and the heat source, as well as the effect of natural convection. The PCM within the container is fully melted when the locations at the bottom section reach a stable temperature above the melting temperature. The temperature of the PCM increases with time until it reaches the melting temperature.

It then plateaus during the phase change process and begins to rise again due to the sensible heat of the liquid PCM. The total charging time can be defined as the time between the instants at which the temperatures of all thermocouples at different locations reach a stable temperature during the charging time and sensible heating of the liquid begins.

The free cooling caused by heat losses through the container boundaries was used during the discharging process, see Figure 7-9, Figure 7-14, Figure 7-19 and Figure 7-24. Initially, the process of solidification of the PCM begins at a temperature higher than the melting temperature, i.e. 265 °C, 235 °C and 245 °C for solar salt using different configurations (fins or graphite) and 210 °C for the metal alloy. It was found that during the solidification of the metal alloy some of the latent heat represents the transition of the Bi-Sn alloy in the liquid-liquid mode. Therefore, the latent energy of 31.6 kJ/kg is used for validation of the numerical model for TES system using metal alloy.

When the solidification process begins, a thin layer of solid PCM forms next to the walls (due to the heat losses through the boundaries) and gradually thickens with time, as seen from melting and temperature contours, see Figure 7-10, Figure 7-15, Figure 7-20 and Figure 7-25. It can be noticed that the process begins with sensible heat reduction in the molten PCM followed by the phase change when the temperature reaches the solidification temperature.

The solidification process is mainly determined by the conduction heat transfer. Consequently, the velocity contours in Figure 7-10, Figure 7-15, Figure 7-20, and Figure 7-25 show that the velocity of the molten PCM for solar salt storage of different configurations as well as metal PCM decreases as time elapses because of the reduction in the temperature difference in the molten PCMs due to heat losses through the boundary.

Furthermore, the temperature becomes constant during the phase change as the heat is released and the PCM transforms into a solid. Finally, sensible heat reduction occurs again when the phase change is completed and the PCM becomes completely solid.

The difference between the experimental and numerical temperature of the heat source was shown in Figure 7-16 (part-1) and that may be due to the heat flux from the cartridge not being uniform or due to the position of the thermocouple, which had not been placed correctly during the experimental work.

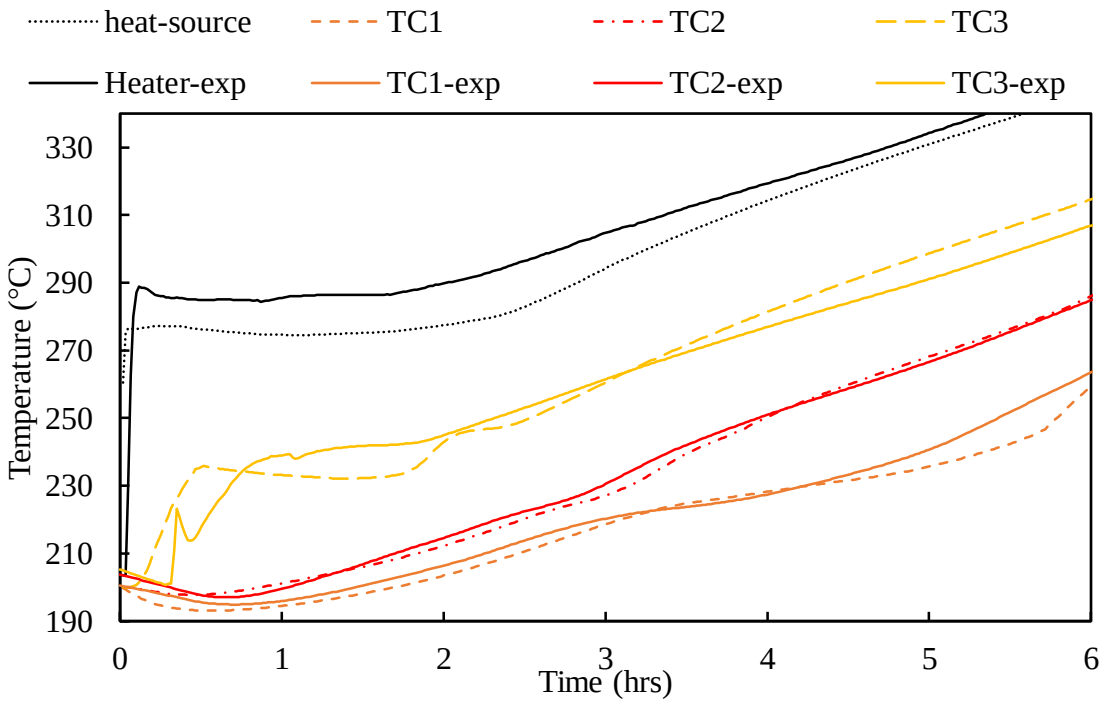

Figure 7-6: Temperature distribution and variation in the TES system with pure solar salt during the charging process with the power input of 50 W (part-1).

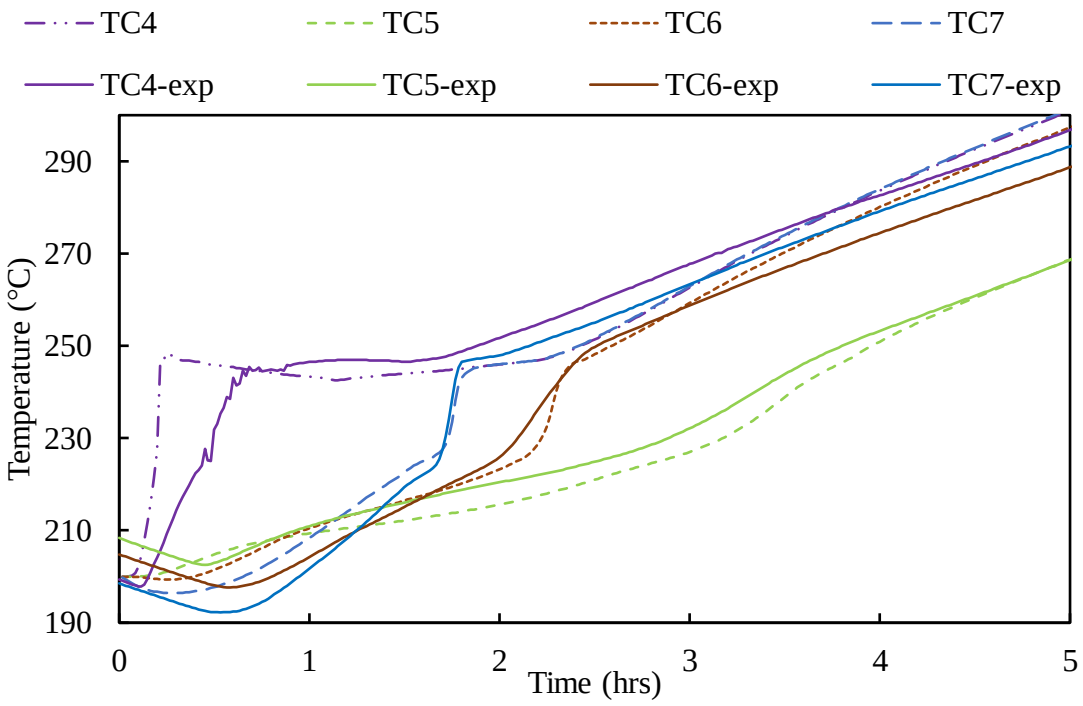

Figure 7-7: Temperature distribution and variation in the TES system with pure solar salt during the charging process with the power input of 50 W (part-2).

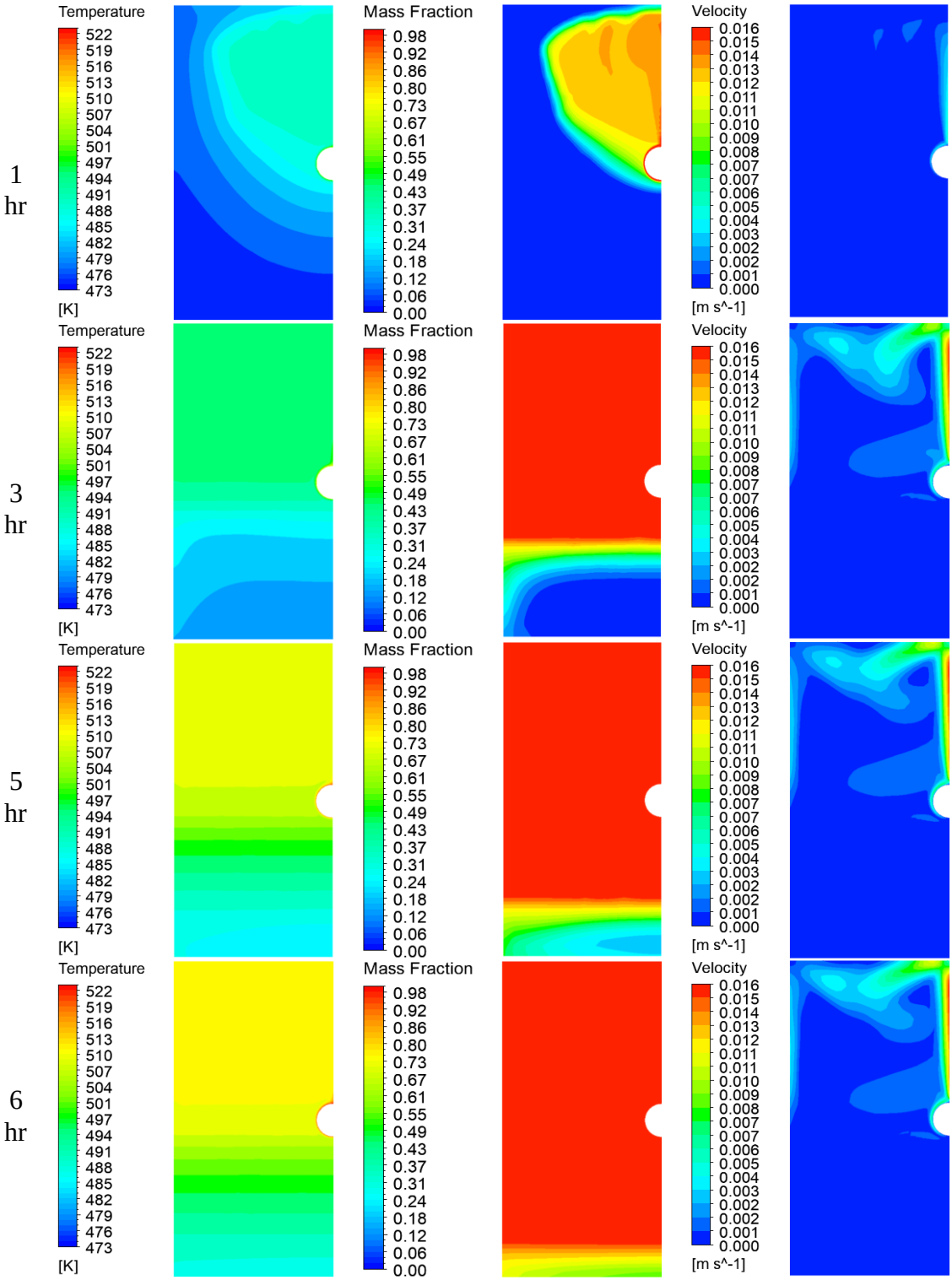

Figure 7-8: TES system with pure solar salt during the charging process with power input of 50 W (a) Temperature contours (b) Melting fraction (c) velocity contours.

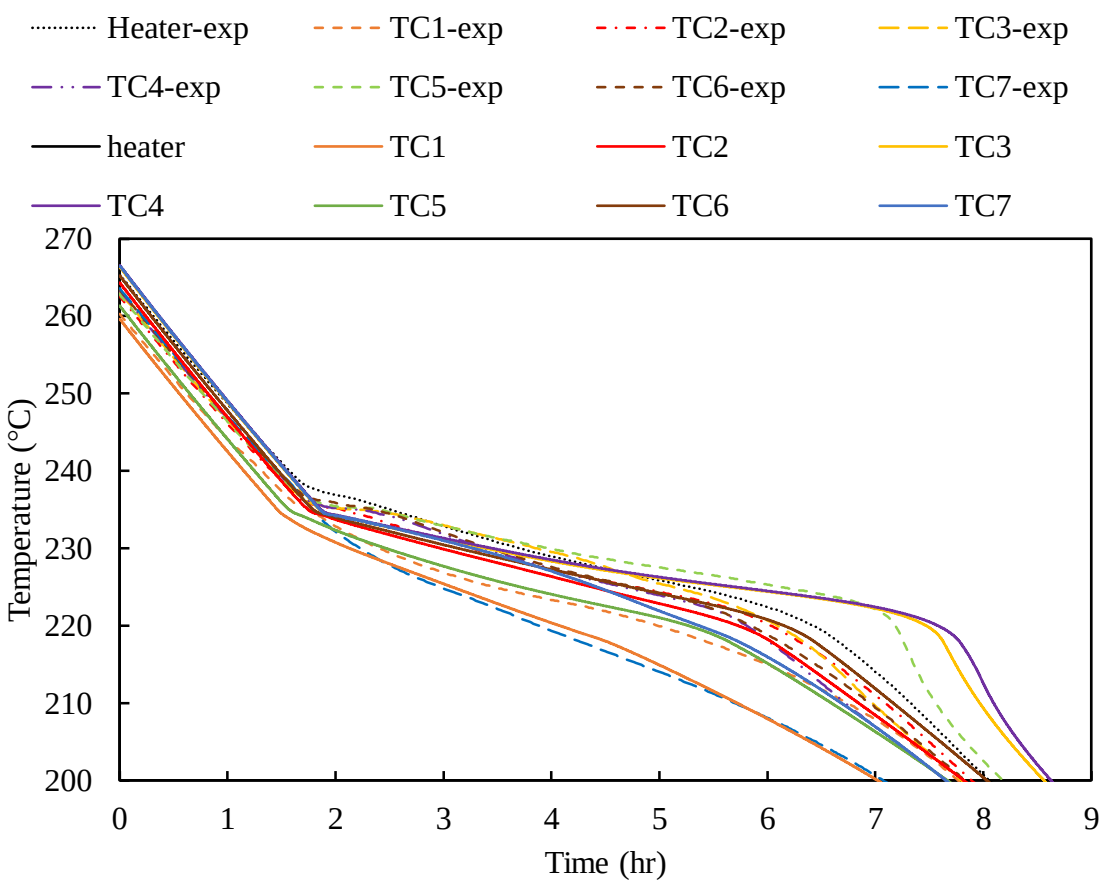

Figure 7-9: Temperature distribution in the TES system with pure solar salt during the discharging process.

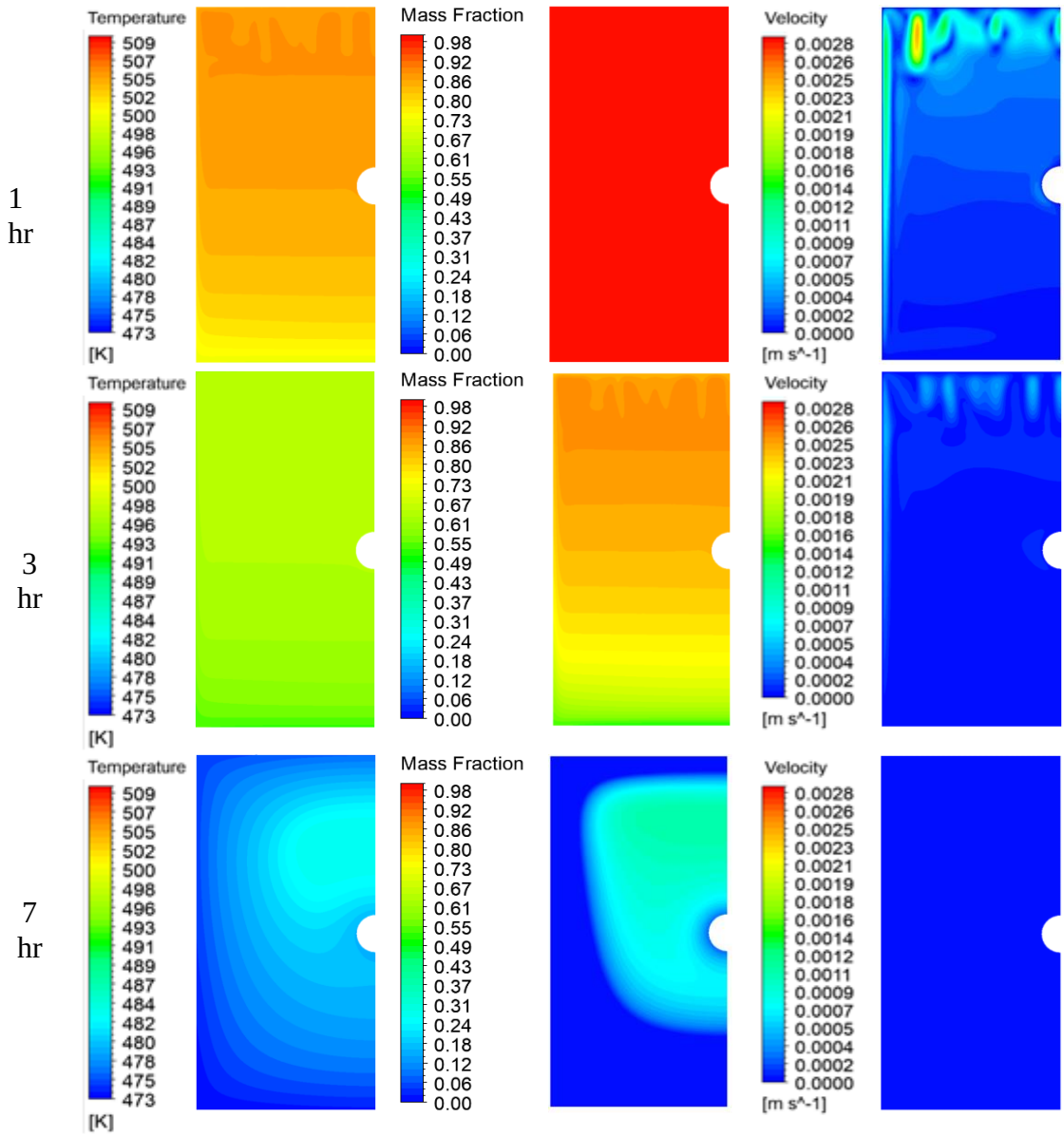

Figure 7-10: TES system with solar salt during the discharging process (a) Temperature contours (b) Melting fraction (c) velocity contours.

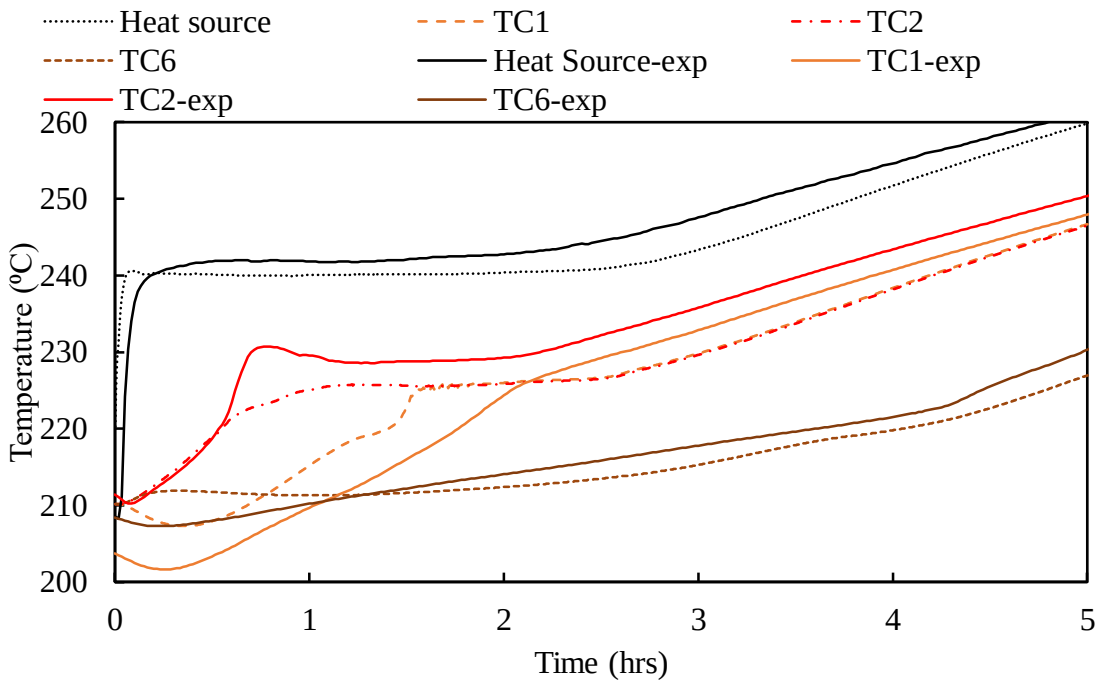

Figure 7-11: Temperature distribution in the TES system with solar salt stainless steel finned container during the charging process with the power input of 35 W (part-1).

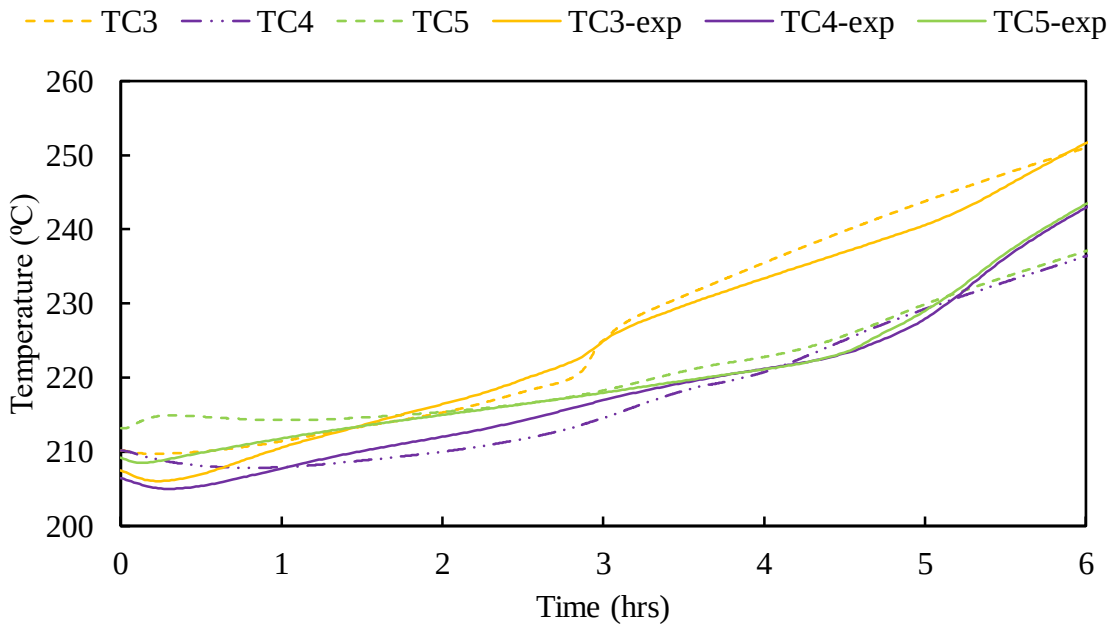

Figure 7-12: Temperature distribution in the TES system with solar salt and stainless steel finned container during the charging process with the power input of 35 W (part-2).

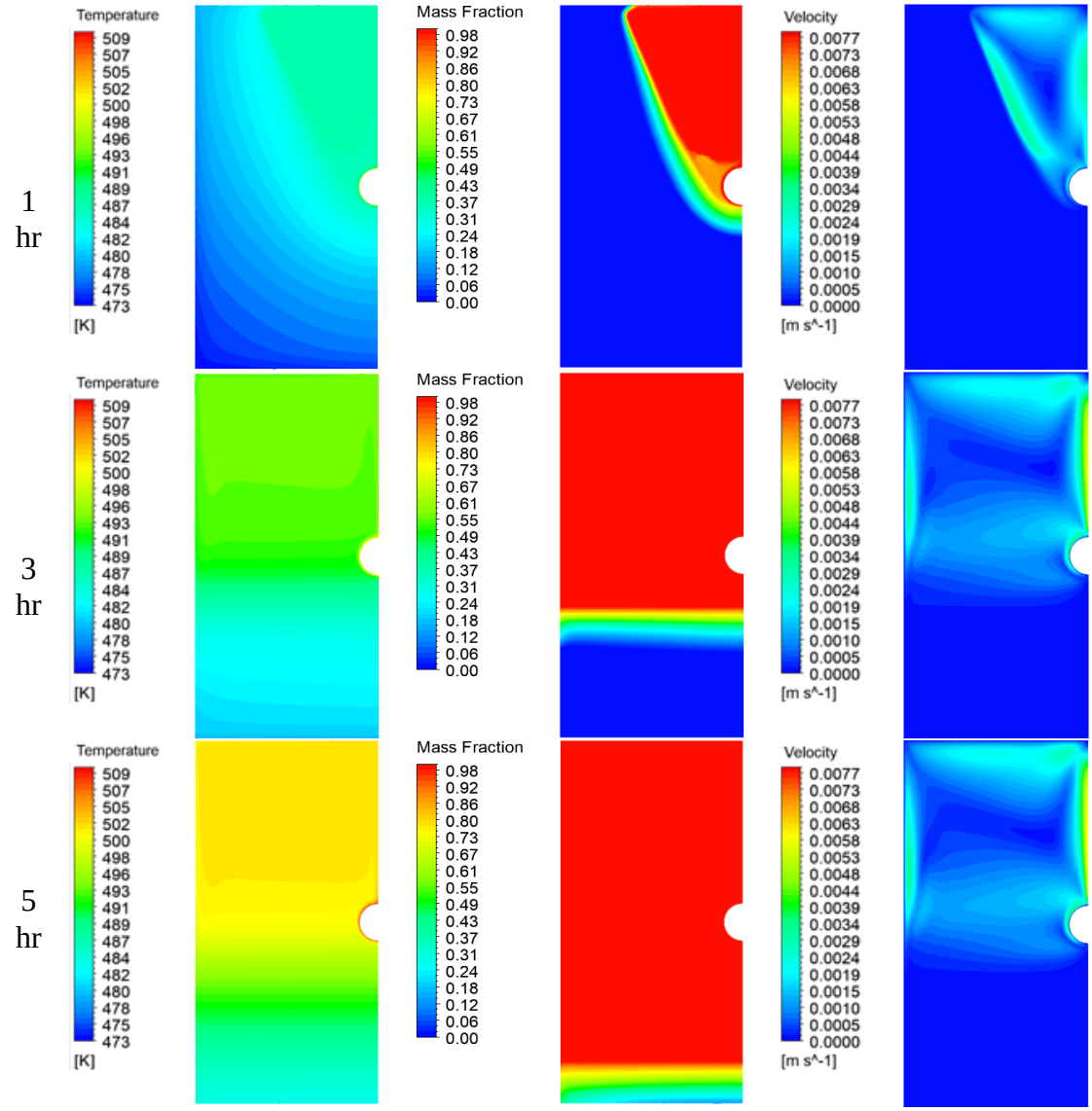

Figure 7-13: TES system with solar salt and stainless steel finned container during the charging process with the power input of 35 W (a) Temperature contours (b) Melting fraction (c) velocity contours.

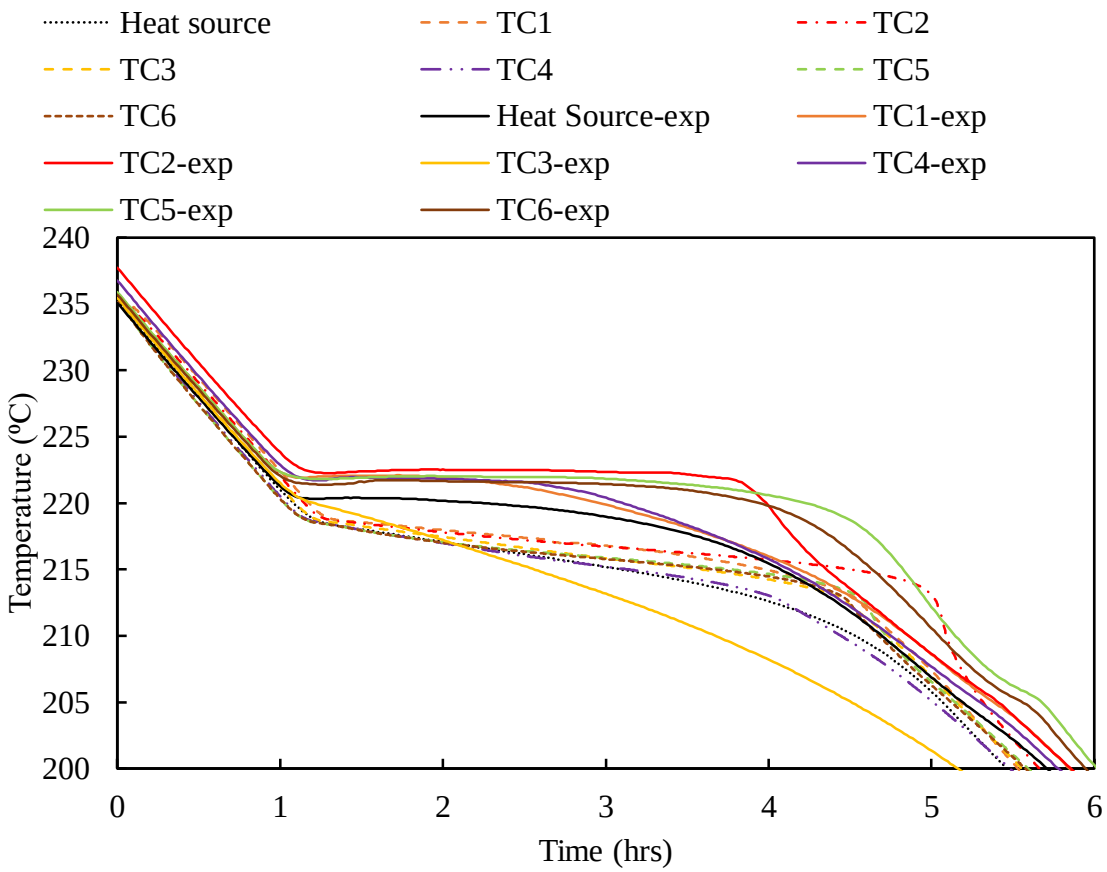

Figure 7-14: Temperature distribution and variation in the TES system with solar salt and stainless steel finned container during the discharging process.

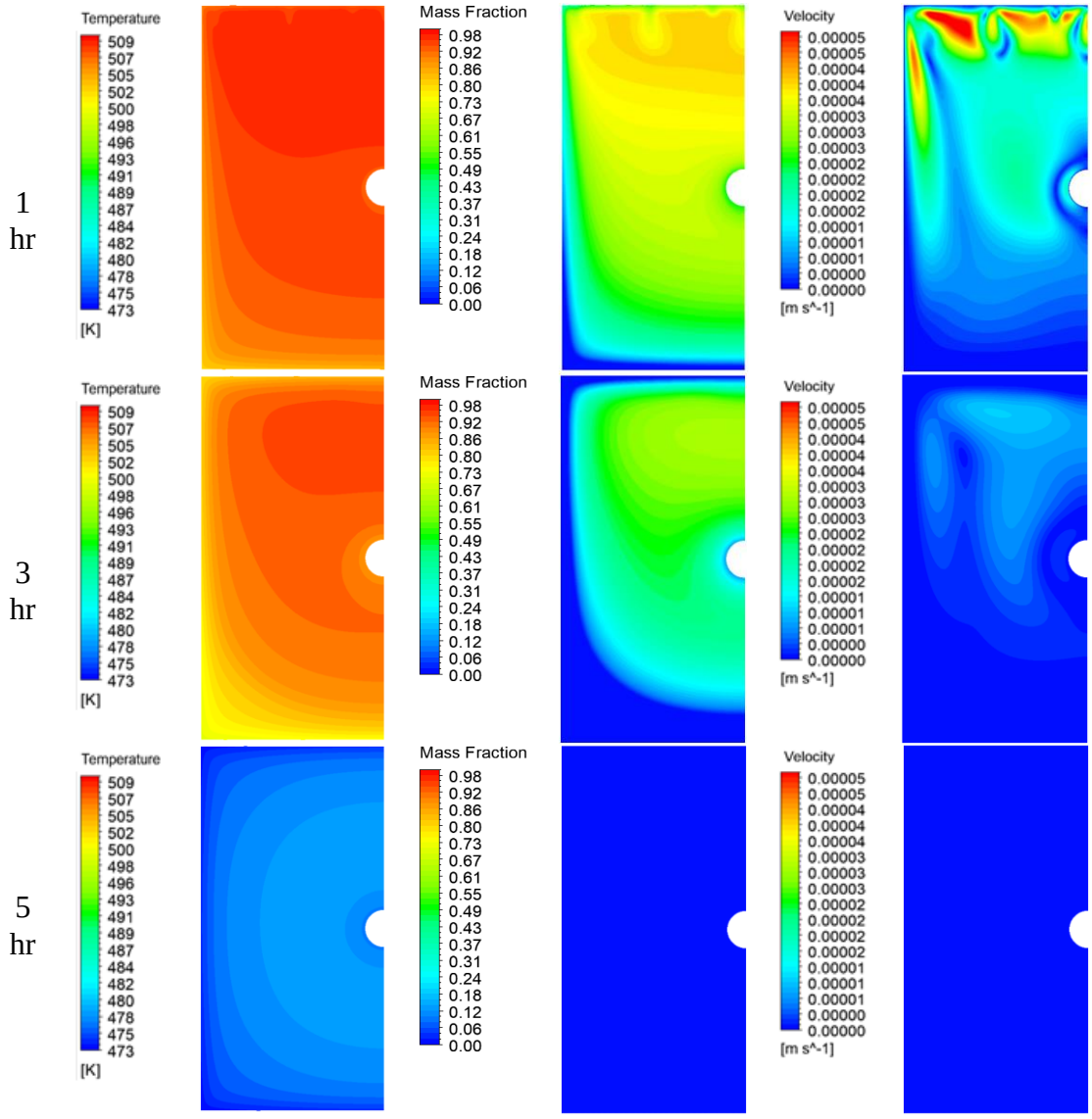

Figure 7-15: TES system with solar salt and stainless steel fins during the discharging process (a) Temperature contours (b) Melting fraction (c) velocity contours.

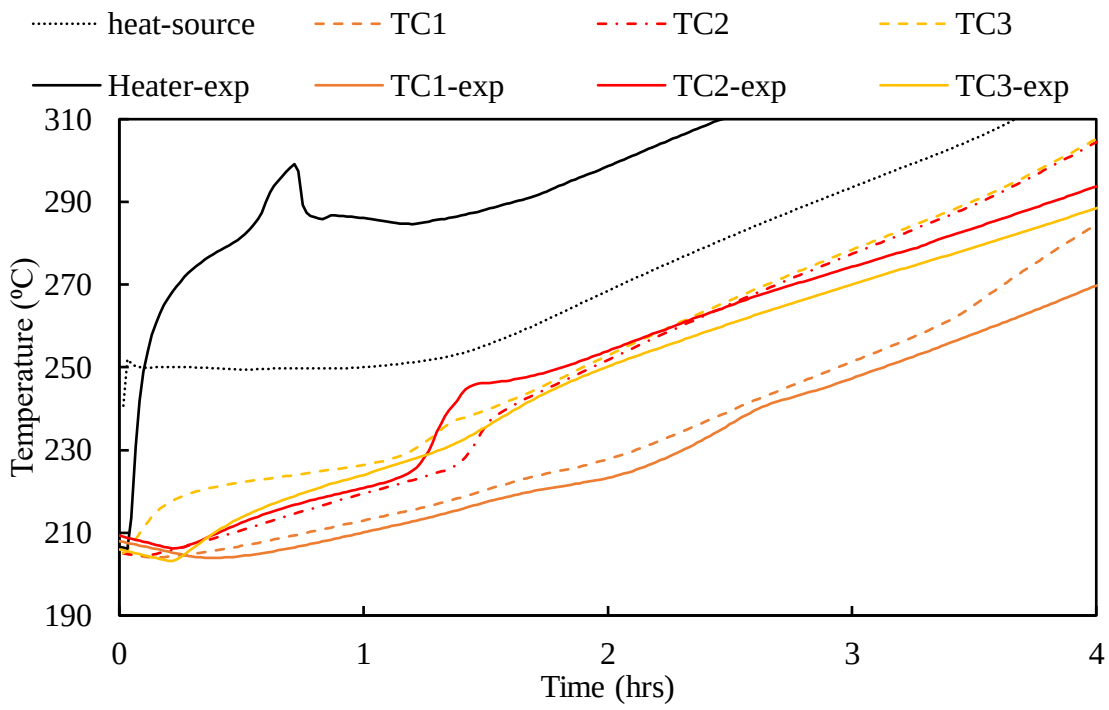

Figure 7-16: Temperature distribution and variation in the TES system with solar salt and 10 wt % graphite during the charging process with the power input of 50W (part-1).

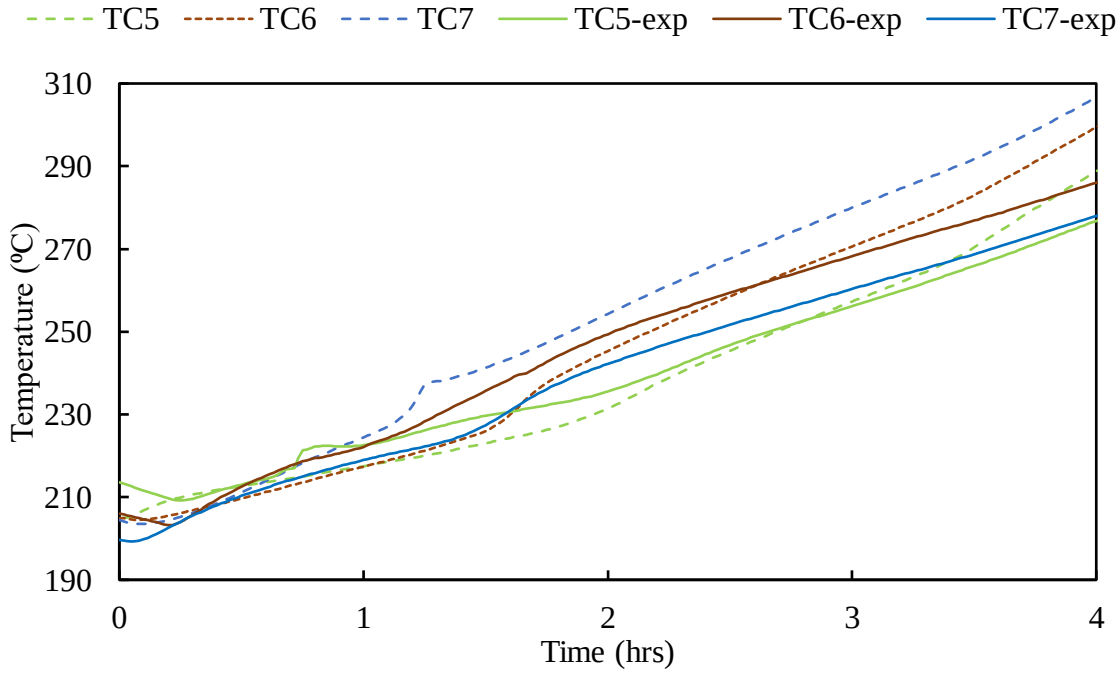

Figure 7-17: Temperature distribution and variation in the TES system with solar salt and 10 wt% graphite during the charging process with the power input of 50W (part-2).

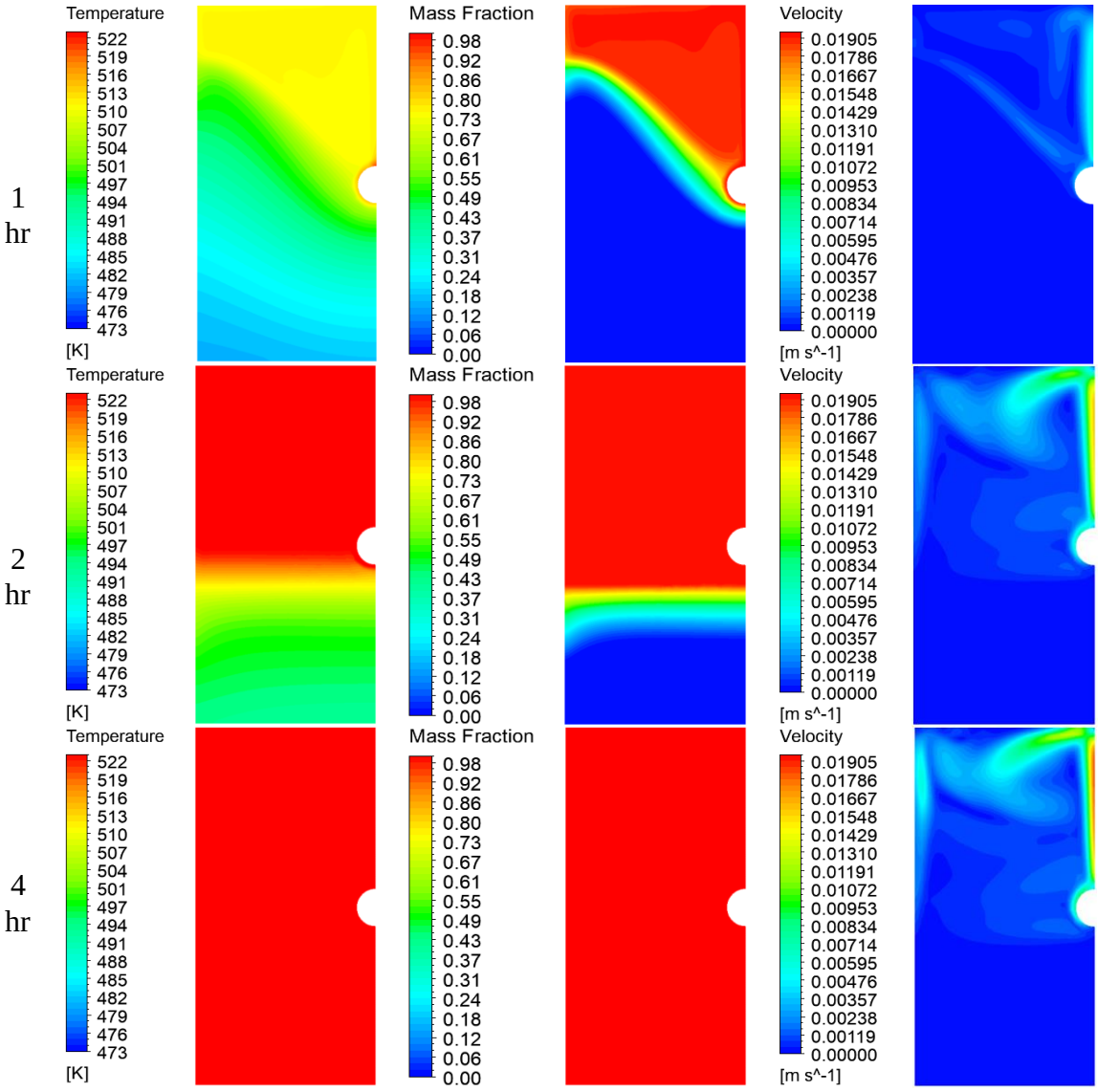

Figure 7-18: TES system with solar salt and 10 wt% graphite during the discharging process (a) Temperature contours (b) Melting fraction (c) velocity contours.

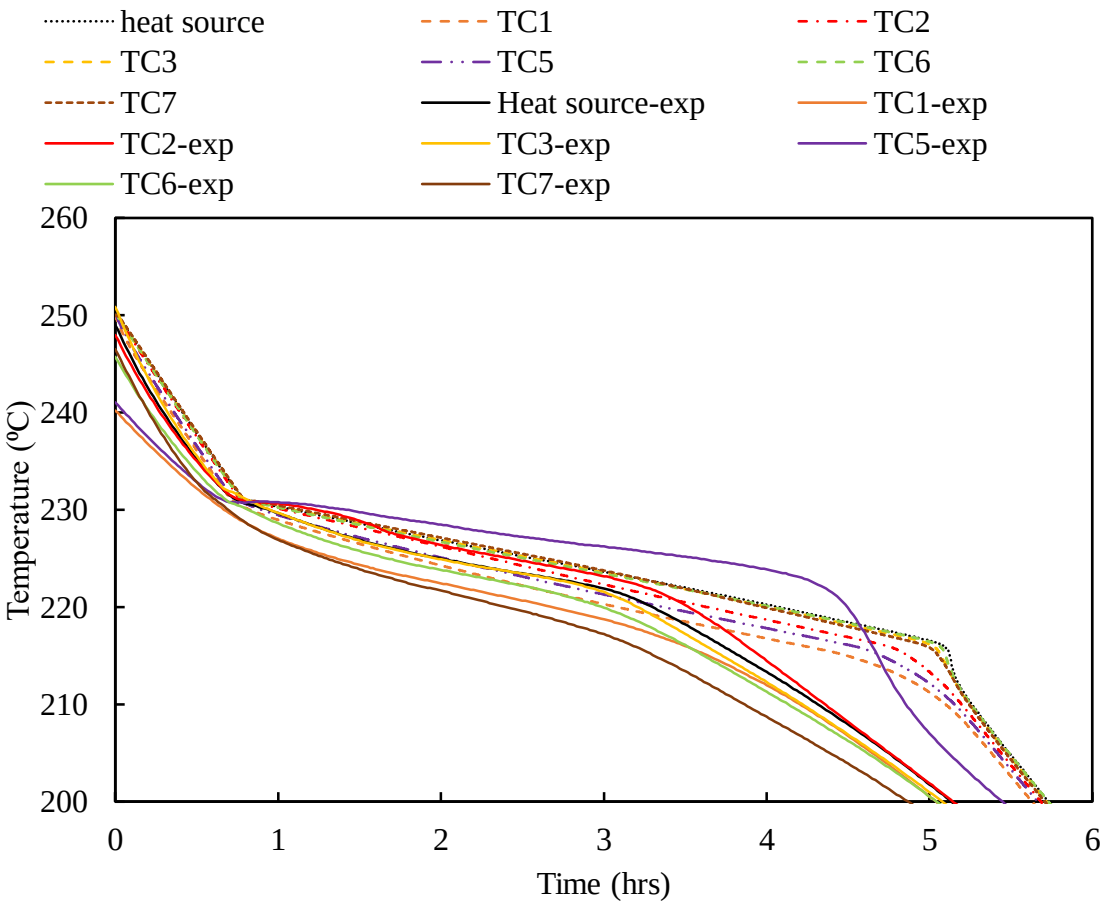

Figure 7-19: Temperature distribution and variation in the TES system with solar salt and 10 wt% graphite during the discharging process.

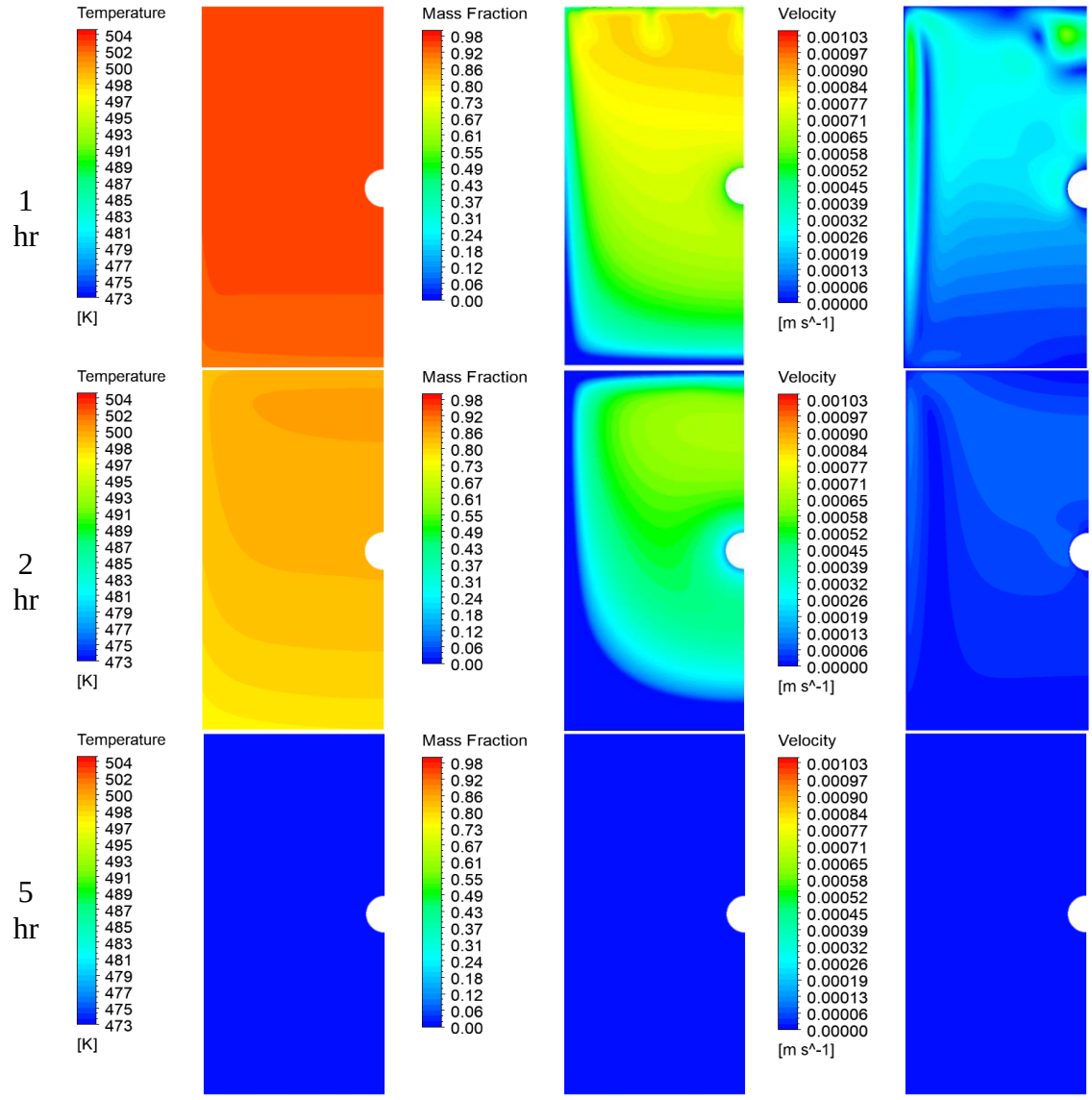

Figure 7-20: TES system with solar salt and 10 wt% graphite during the discharging process (a) Temperature contours (b) Melting fraction (c) velocity contours.

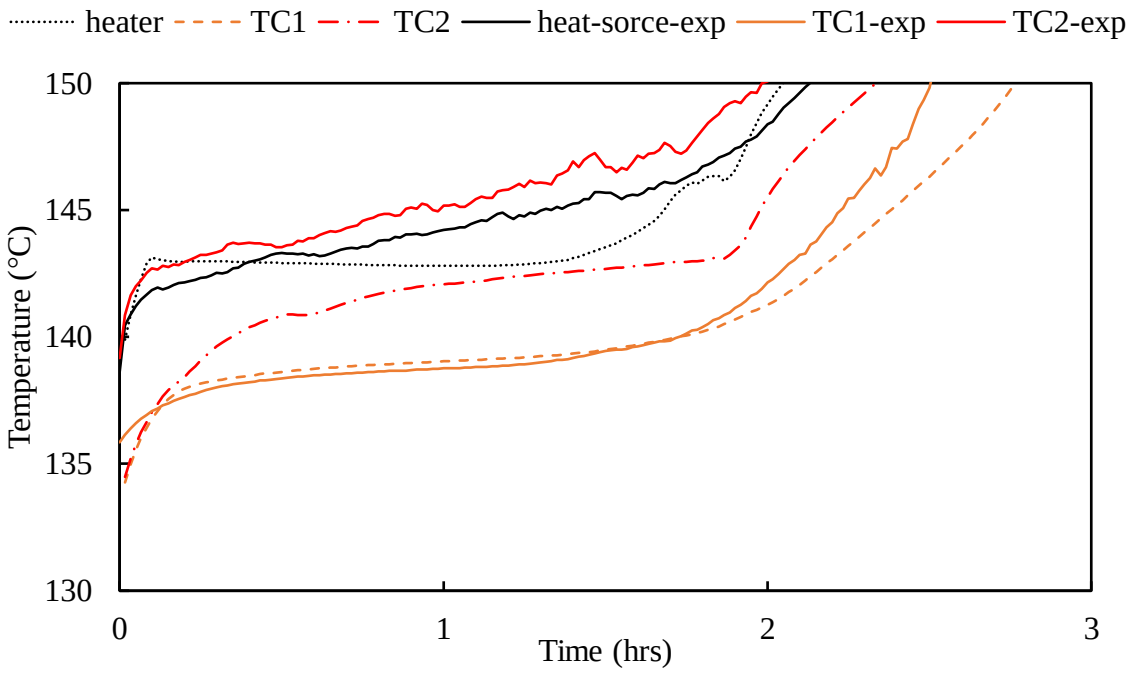

Figure 7-21: Temperature distribution and variation in the TES system with metal alloy during the charging process with the power input of 50 W (part-1).

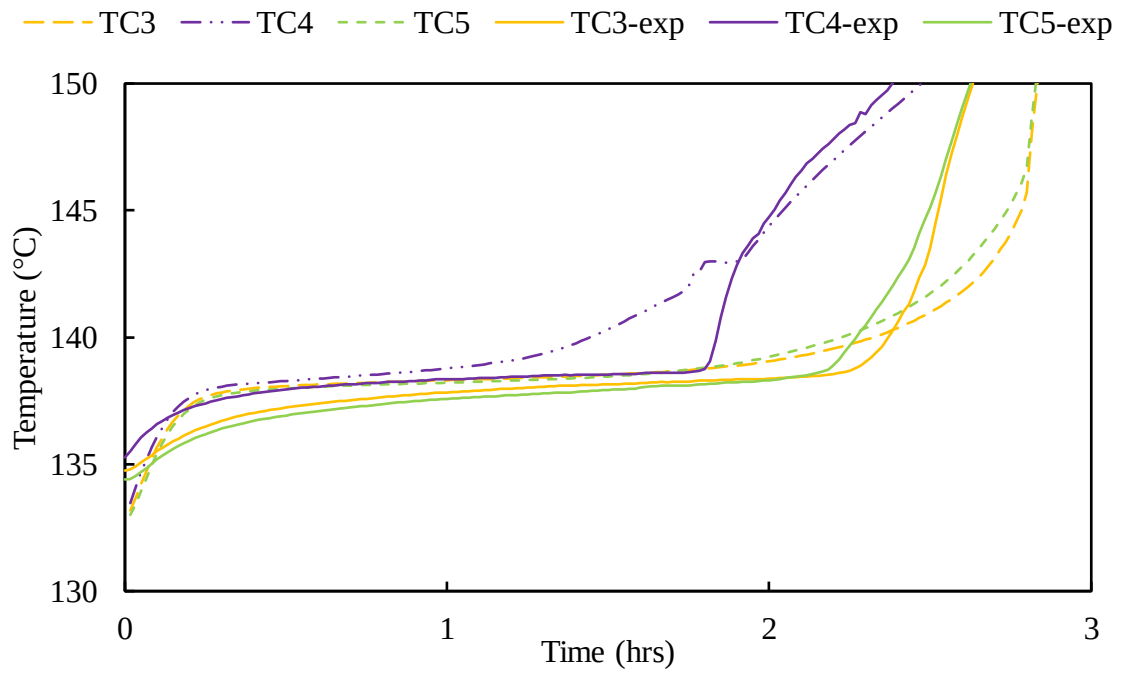

Figure 7-22: Temperature distribution and variation in the TES system with metal alloy during the charging process with the power input of 50 W (part-2).

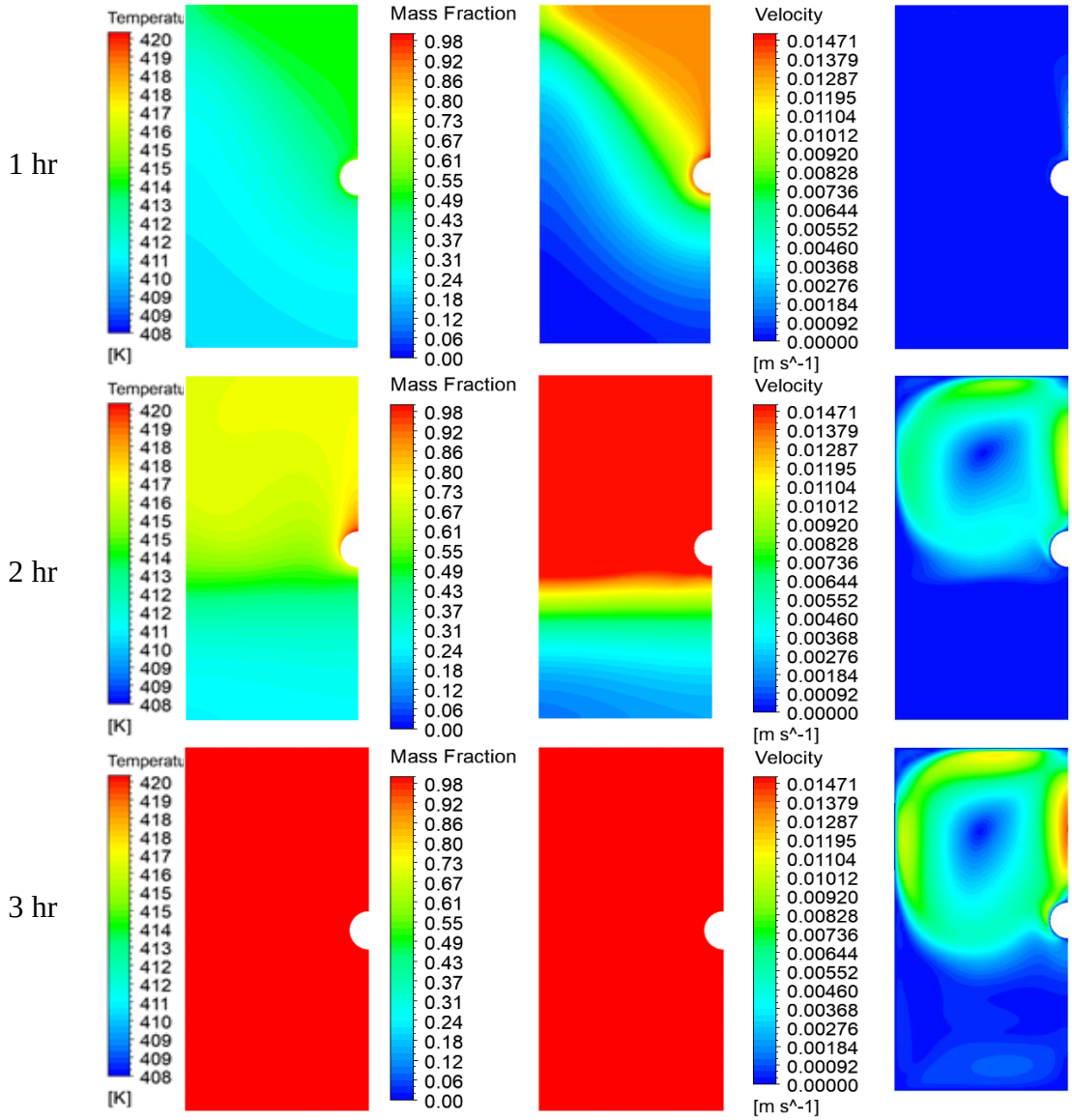

Figure 7-23: TES system with the metal alloy during the charging process with the power input of 50 W (a) Temperature contours (b) Melting fraction (c) velocity contours.

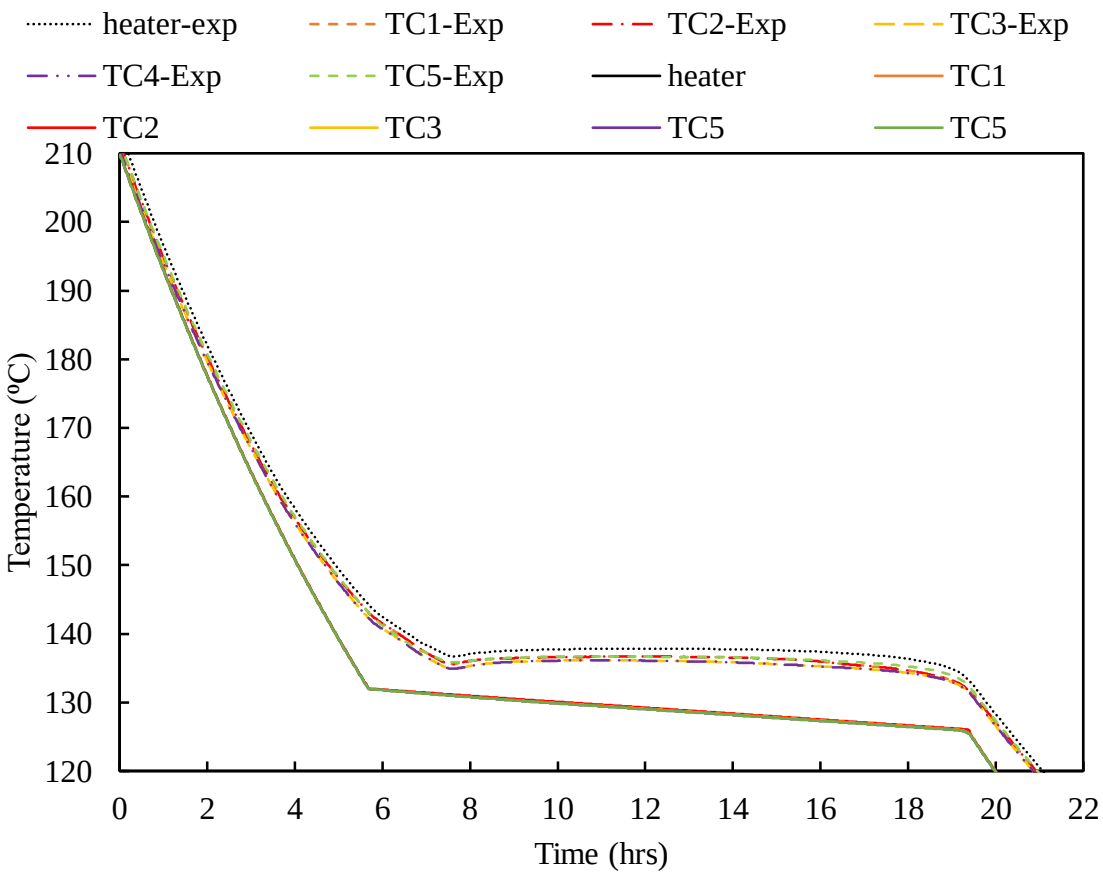

Figure 7-24: Temperature distribution and variation in the TES system with metal alloy during the discharging process.

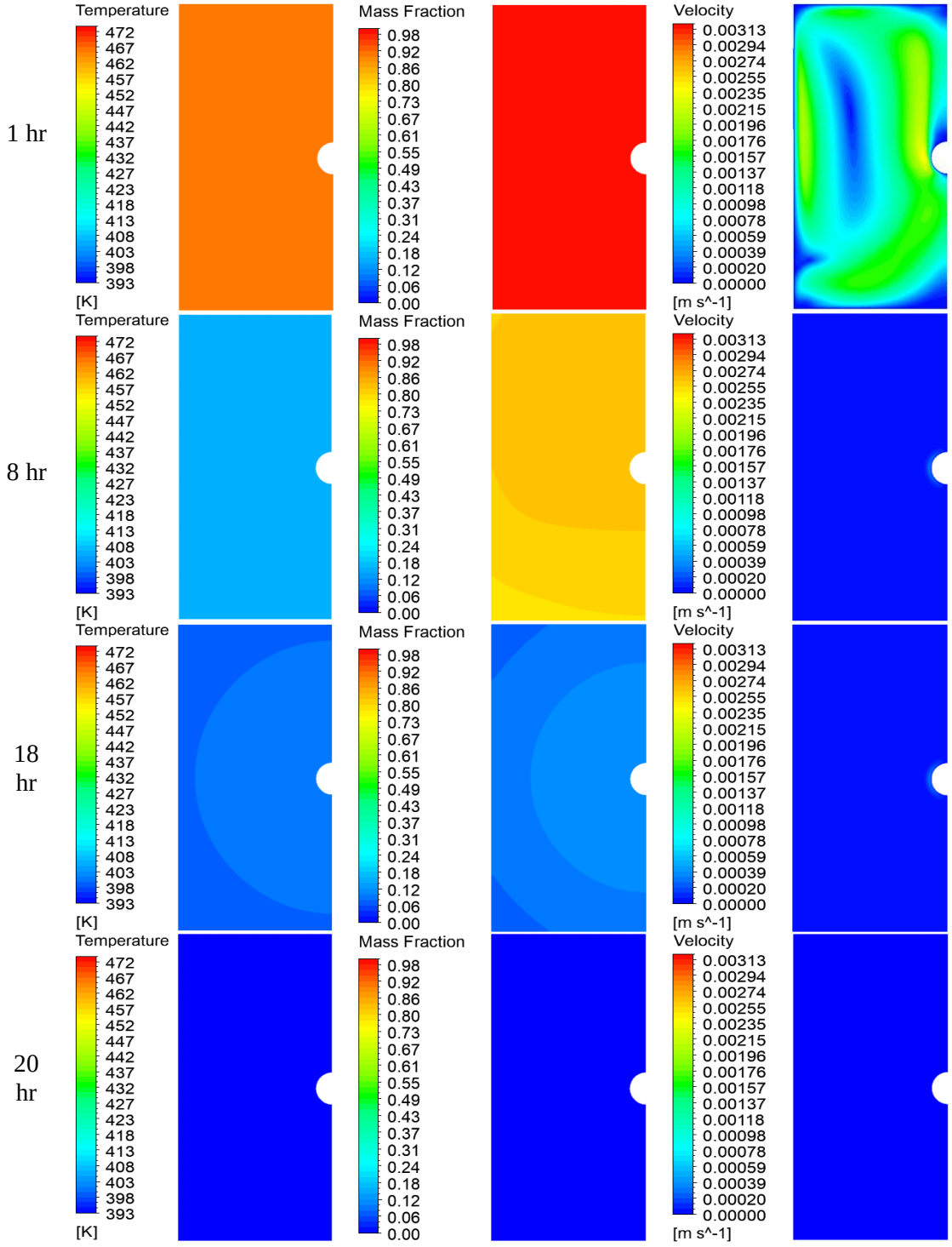

Figure 7-25: TES system with the metal alloy during the discharging process (a) Temperature contours (b) Melting fraction (c) velocity contours.

It can be clearly seen that the numerical results are in close agreement with the experimental measurements. Some differences can be observed in the measured and predicted temperature behaviour. That could be due to the numerical model considering the thermo-physical properties of PCM to be constant. In the case of metal alloy, the effects of the circulation of molten PCM are less intensive in the melting process in comparison to the experimental results.

Even though the validation procedure was found to be successful, it is difficult to compare the results directly to each other due to the different properties of the used salts (such as melting temperature) and different heat loss magnitudes in the TES systems. It is, therefore, necessary to conduct a numerical comparison where the parameters are similar.

7.4 Numerical investigation of the operation of TES systems using dimensional and dimensionless parameters

This section describes results of numerical investigations carried out for TES systems with two different PCMs, solar salt and metallic alloy, at different input powers during charging and discharging processes, namely 25, 35, 50 and 70 W, using adiabatic boundary condition.

1. Different heat transfer intensification methods in the TES systems were analysed using solar salt (type-I): using graphite as an additive to solar salt at 5 wt% and 10 wt% as well as using fins (4, 6 and 8 fins).
2. Numerical investigation of the TES system with the metal alloy PCM was undertaken to evaluate the thermal performance during charging and discharging processes.

3. Dimensionless correlations were derived to describe the liquid fraction as well as the amount of accumulated and released energy of the TES systems using solar salt and metal alloy during melting and solidification processes.

The numerical model and the initial conditions for TES systems using solar salt and the metal alloy are presented in Table 7-3.

Table 7-3: Numerical model for TES systems.

TES type	Model	Temperature range during charging (°C)	Temperature range during discharging (°C)
Pure salt	Laminar flow	200-270	270-160
Finned container	Laminar flow	200-270	270-160
Solar salt with 10 wt% graphite	Laminar flow	200-270	270-160
Metal alloy	SST-Turbulent flow	136-160	150-120

In addition, the thermo-physical properties of solar salt with 5wt% and 10wt% graphite were measured using DSC with the specific heat and thermal conductivity obtained values measured by the National Physical Laboratory, whilst the viscosity was evaluated by Equation (3-1). The thermal properties of solar salt with 5wt% and 10wt% graphite are presented in Table 7-4 and Table 7-5.

Table 7-4: Thermal properties of solar salt with different percentages of graphite

Graphite percentage	Process	T_{onset} (°C)	T_{offset} (°C)	ΔH (kJ/kg)
10 %	Charging	225	238	97.37
	Discharging	215.2	230.74	97.4
5%	Charging	225	247	101.6
	Discharging	215	234.5	100.1

Table 7-5: Thermal properties of solar salt with different percentages of graphite.

Graphite percentage	Process	ρ (kg/m^3)	Cp (J/kg °C)	μ (kg/m s)	λ (W/m˚C)
10 %	Charging	1958	1033	0.004864	1.455
	Discharging				
5%	Charging		964	0.004377432	1.062
	Discharging				

7.4.1 TES system with solar salt

The charging process of the TES system was performed between the starting temperature of 200 °C and ending temperature of 270 °C. The results are presented in this section for the 25 W power input. The similar behaviour was observed for other values of power inputs and the results for power inputs from 25 to 70 W are presented in Appendix A. The results for liquid fraction and Nusselt number using dimensionless parameters are also presented in Appendix B. Figure 7-26 and Figure 7-27 show the average temperatures in the TES systems with solar salt, and mixtures of solar salt and graphite, and different configurations using a 25 W power input. It is obvious that the average temperature of the PCM increases more rapidly in the different configurations compared to the basic case (pure solar salt) in the sensible heat mode due to intensification of the heat transfer through the PCM using fins or graphite as an additive. The temperature gradient appears to decline when the average temperature reaches the melting temperature at around 225 °C due to the beginning of the phase change. During the phase change, solar salt in the container with fins is exposed to a higher heating rate than in the case of the solar salt and graphite mixtures. This is due to the increased surface to volume ratio, which rises as the number of fins increases, and higher average conductivity in the system because of the thermal conductivity of the fins. After the PCM fully melts at about 247 °C the temperature starts rising sharply in the sensible heating mode. It was shown that the average temperature of solar salt with graphite reaches the temperature of 270 °C more rapidly as the percentage of graphite increases, and compared to the finned configurations, due to higher thermal conductivity and lower specific heat of the mixture, which heats up more quickly than pure salt.

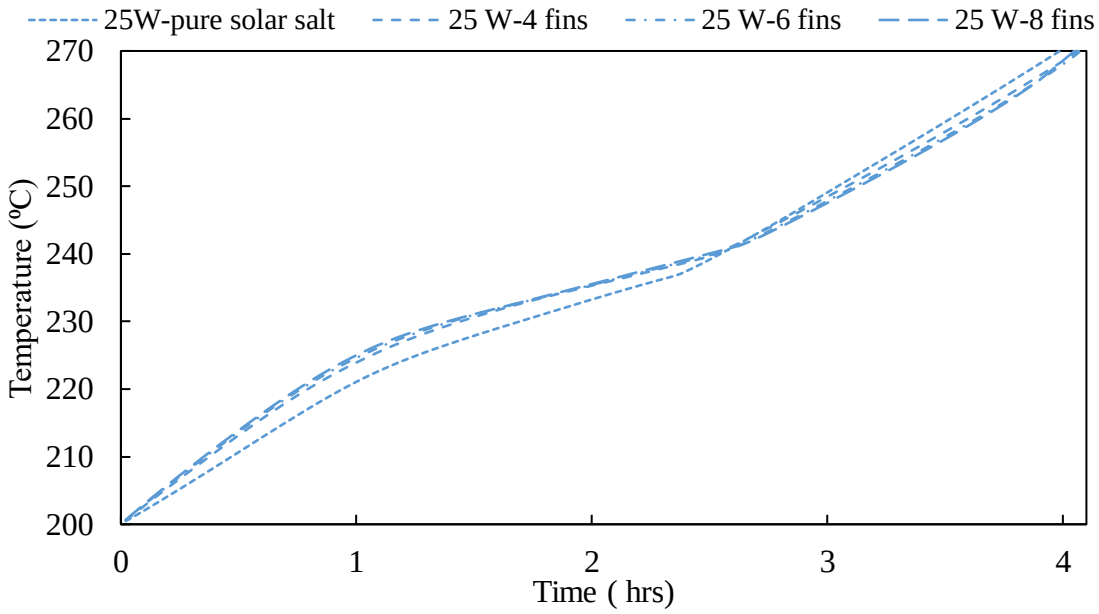

Figure 7-26: Average temperature of TES systems with pure solar salt and solar salt with fins during the charging process.

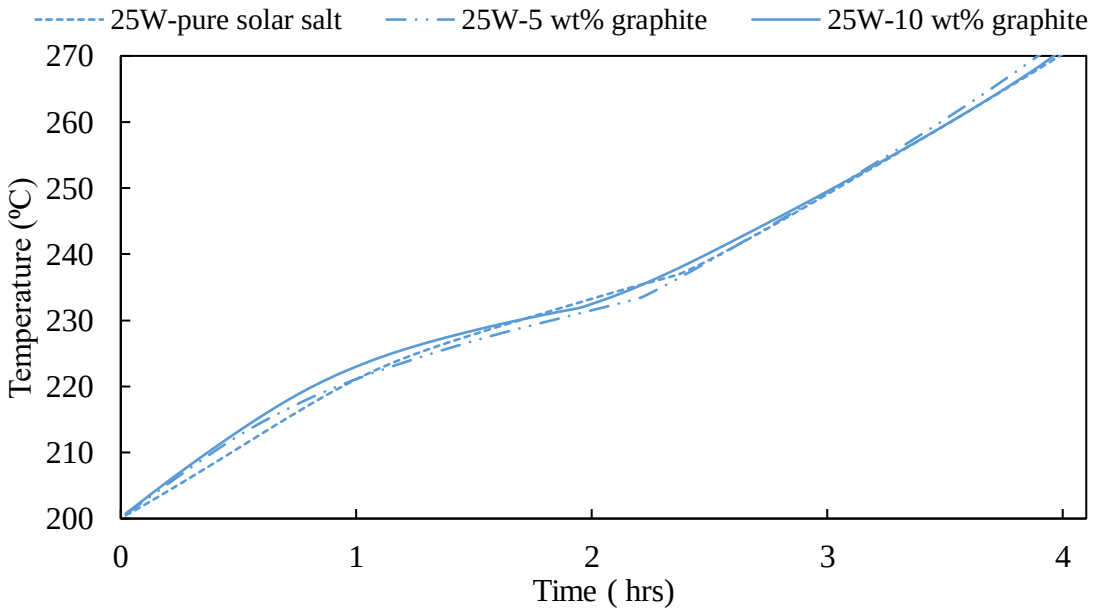

Figure 7-27: Average temperature of TES systems with pure solar salt and solar salt with 10 wt% graphite during the charging process.

Figure 7-28 shows the variation in the liquid fraction (LF) of the TES systems with PCMs and different configurations. It was found that the TES system with pure solar salt begins melting earlier than the graphite mixture and pure solar salt with fins. This occurs because the average thermal conductivity of solar salt with graphite and fins transfer is greater than that of pure salt.

It was found that the mixture with 5 wt% graphite initially melts faster than that with a 10 wt% mixture due to the lower specific heat of the mixture. As the process progresses in time, the melting process decreases in the speed in all configurations. The reason behind that is that the upper half of the PCM is melted, and with further progression, in time the lower half also melts but this process is dominated by the heat transfer conduction mechanism. However, with time the melting rate of the mixture with 10 wt% graphite becomes higher due to the increased thermal conductivity. It was found that some configurations decrease the melting time by more than 20 %. Using 8 fins in the TES system decreases the melting time greater than using the mixture with 10 wt% graphite, and 6 fins decrease the melting time greater than the mixture with 5 wt% graphite by 9% and 5%, respectively. The average temperature does not provide an accurate indication of the melting process. For example, pure solar salt reaches 270 ° C within 4 hours but the LF curve indicates that the melting process needs 5 hours to be fully completed.

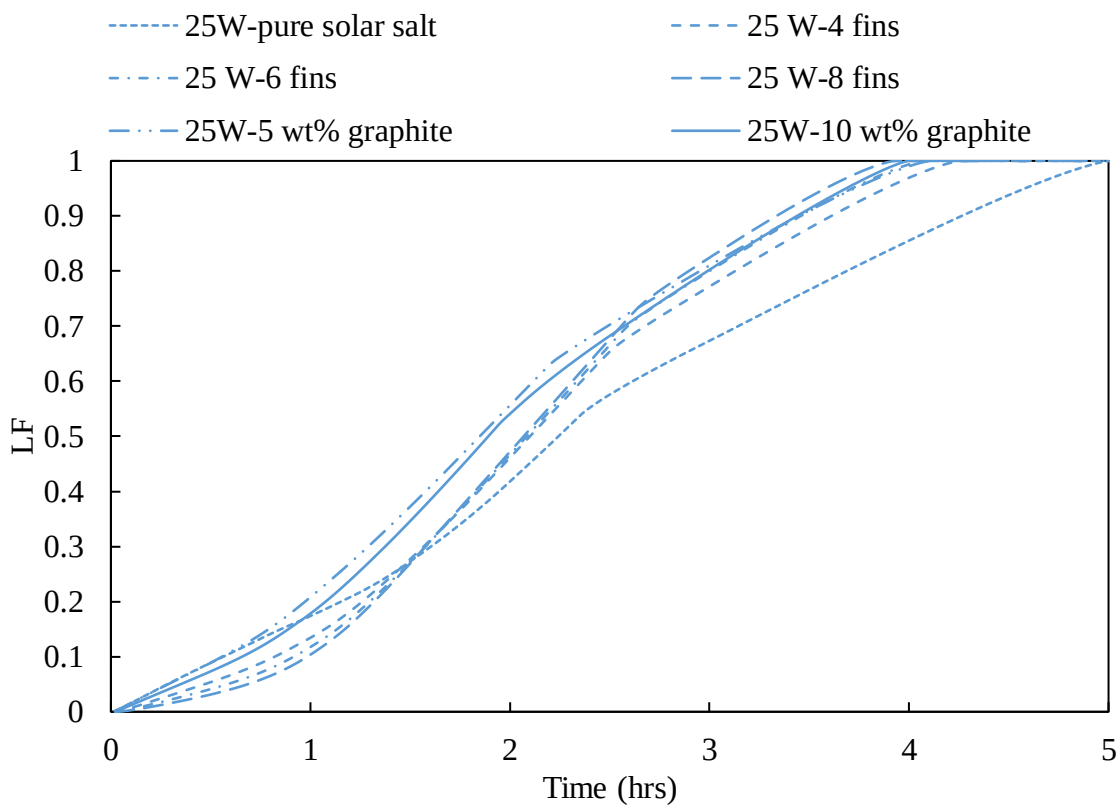

Figure 7-28: LF of PCMs in the TES systems during the charging process.

Figure 7-29 shows the heat accumulated as a function of time in the TES systems using different PCMs and configurations (pure solar salt, mixtures with graphite, use of fins). About 300 kJ of heat were accumulated in the TES systems during the charging time. Pure solar salt provides a slightly higher value of the accumulated heat compared to the using fins and graphite mixtures because of the higher value of latent heat and specific heat capacity. Using fins decreases the amount of PCM in the container by about 0.1 to 0.3 kg. The TES systems with graphite mixtures have a lower latent heat than solar salt, see Table 3-2 and Table 7-4, which reduces accumulated energy. During the charging process, the amount of accumulated heat in systems with graphite mixtures or fins grows faster due to intensification of the heat transfer through the PCM. The heat accumulating rate reduces for all the cases after the melting of the PCM in the upper half container is

completed and the conduction heat transfer becomes the dominant heat transfer mechanism in the bottom part of the container. Increasing the fins number from 4 to 8 could accelerate energy accumulation by 39 %. Also, it was found that using fins is more efficient in the acceleration of energy accumulation compared to using the graphite mixtures.

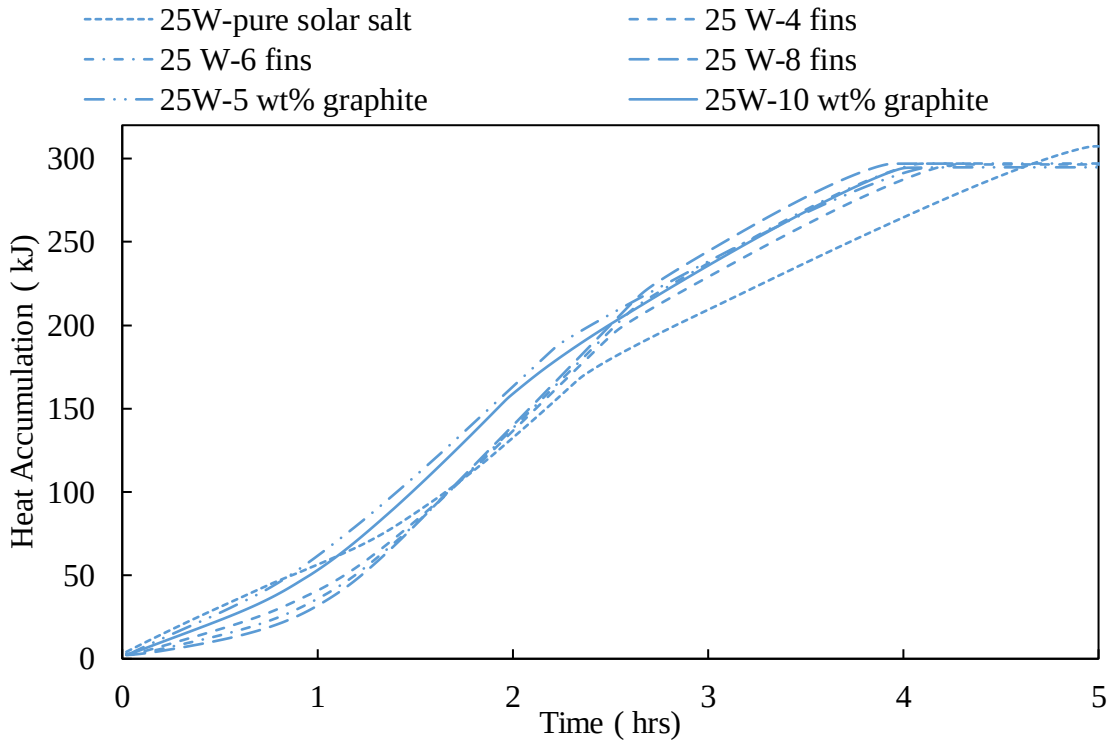

Figure 7-29: Heat accumulated in the TES systems during the charging process.

Figure 7-30 and Figure 7-31 show the HTC (heat transfer coefficient) and the Nu number values for the TES systems with different PCMs and configurations. Conventionally, it is expected that a higher HTC leads to a higher Nu number. But in the solar salt systems, due to a sharp increase in the conductivity several times (due to heat transfer intensification methods), a higher HTC may result in low Nu numbers. It can be seen that the values of HTC and Nu number are increasing during the melting process of PCMs due to the increasing effect of natural convection during the melting process. However,

these values then start to decrease after melting in the upper half of the PCM container is completed and melting in the bottom part of the container is dominated by thermal conduction heat transfer. Values increase slightly after the PCM is fully melted and become constant (mode of the sensible heating). It was found that solar salt with graphite provides higher values of HTC and lower values of Nu number due to the higher thermal conductivity of the mixture. The rise in the number of fins enhances the HTC due to heat transfer intensification through the TES systems up to a certain limit when the fins slow down the circulation of the molten PCM due to the reduced space between fins, which leads to a reduction in the HTC.

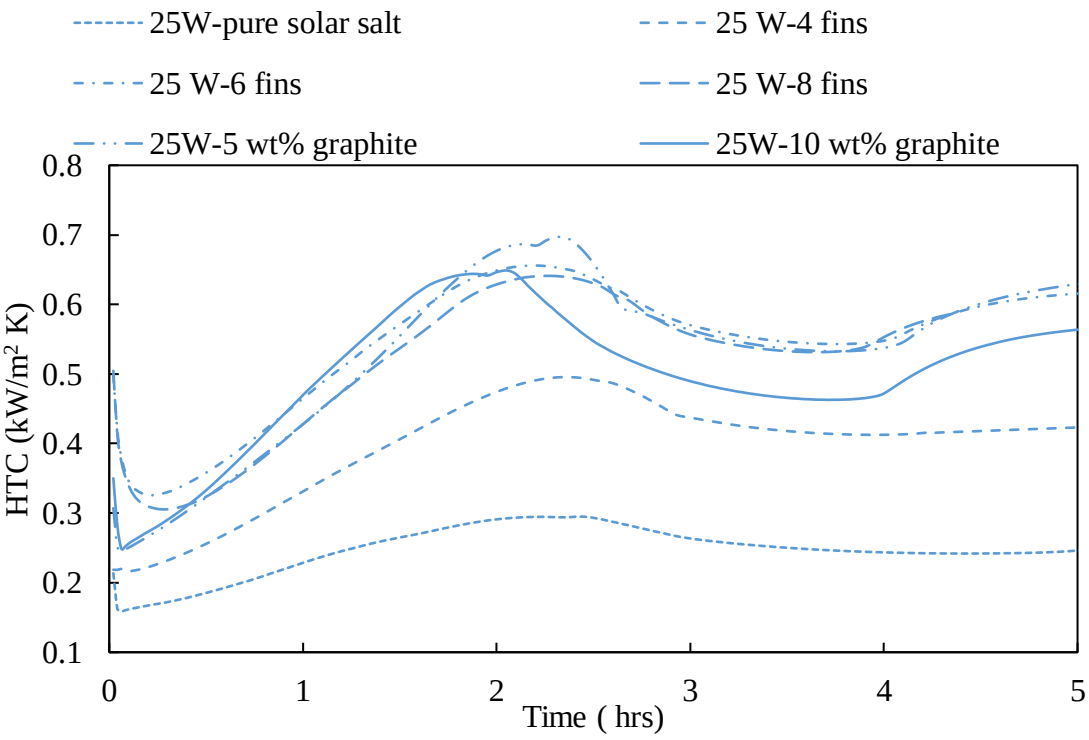

Figure 7-30: HTC for the TES systems during the charging process.

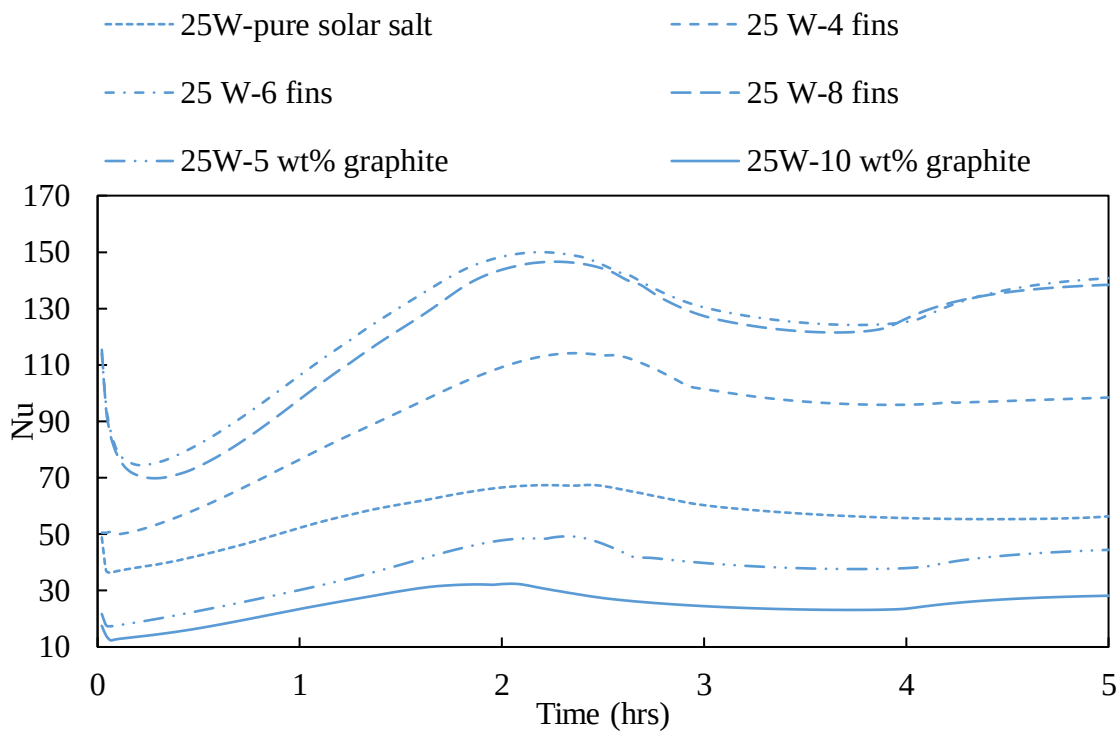

Figure 7-31: Nu number for the TES systems during the charging process.

Figure 7-32 shows the melting time variation in TES with different PCMs and configurations. It can be seen that increasing the number of fins and the percentage of graphite decrease the melting time of the PCM. Using 8 fins has resulted in a shorter melting time in comparison to the solar salt mixture with 10 wt% graphite. Using 6 fins provides a shorter melting time compared to that for solar salt with 5 wt% graphite. This is attributed to the increase of the surface to volume ratio in the system, which intensifies the heat transfer through the PCM by conduction heat transfer. The solar salt with graphite mixture improves the thermal conductivity of solar salt. As a result, using 8 fins and solar salt with 10 wt% graphite shorten the melting time by 21.6 % and 20.4 %, respectively, compared to pure solar salt only case.

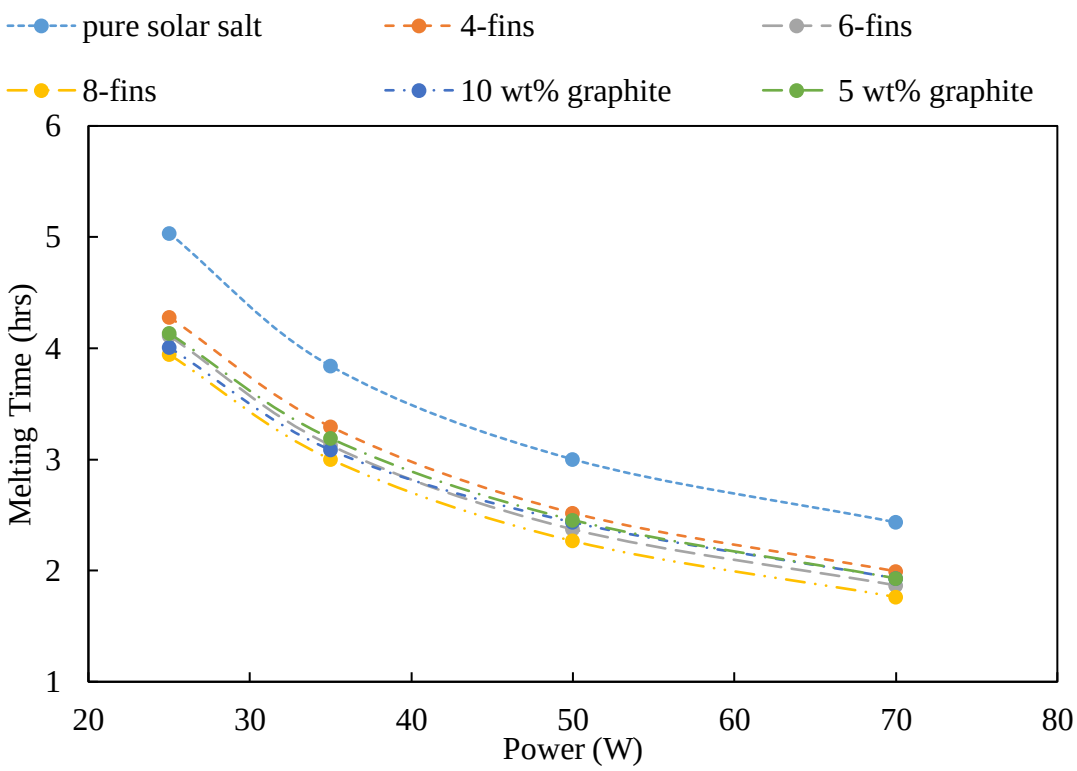

Figure 7-32: Melting times in the TES systems versus power input during the TES charging process.

Figure 7-33 shows the variation of the average temperature of PCMs during the discharging process, which starts at a temperature of about 270 ºC and ends at a temperature of around 160 ºC. The process begins with sensible heat reduction (cooling of the liquid PCM) between 270 ºC and 247 ºC, with the temperature decreasing linearly. As the phase transition starts, a sudden drop in the average temperature can be noticed. Using the average temperature as a method to determine the overall solidification time can be misleading as the PCM melts at different rates in various locations across the container. It was observed that in solar salt temperature decreasing rate is greater in the TES with fins than in TES with graphite mixture PCMs. Figure 7-34 shows that the average temperature and LF of solar salt with a discharging power of 25 W, which indicates full solidification to take place in 5 hours, whilst the average temperature curves

the full solidification time of 4 hours. The reason is that the temperature difference in various locations of the TES systems can be significant.

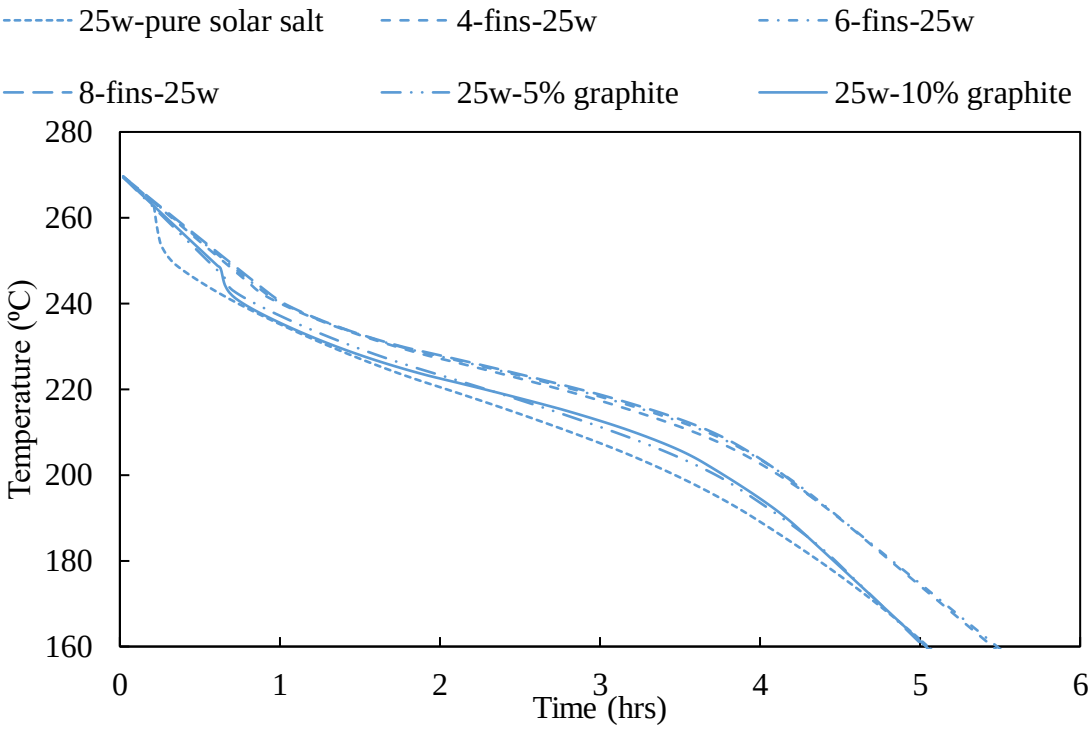

Figure 7-33: Average temperature of the TES systems during the discharging process.

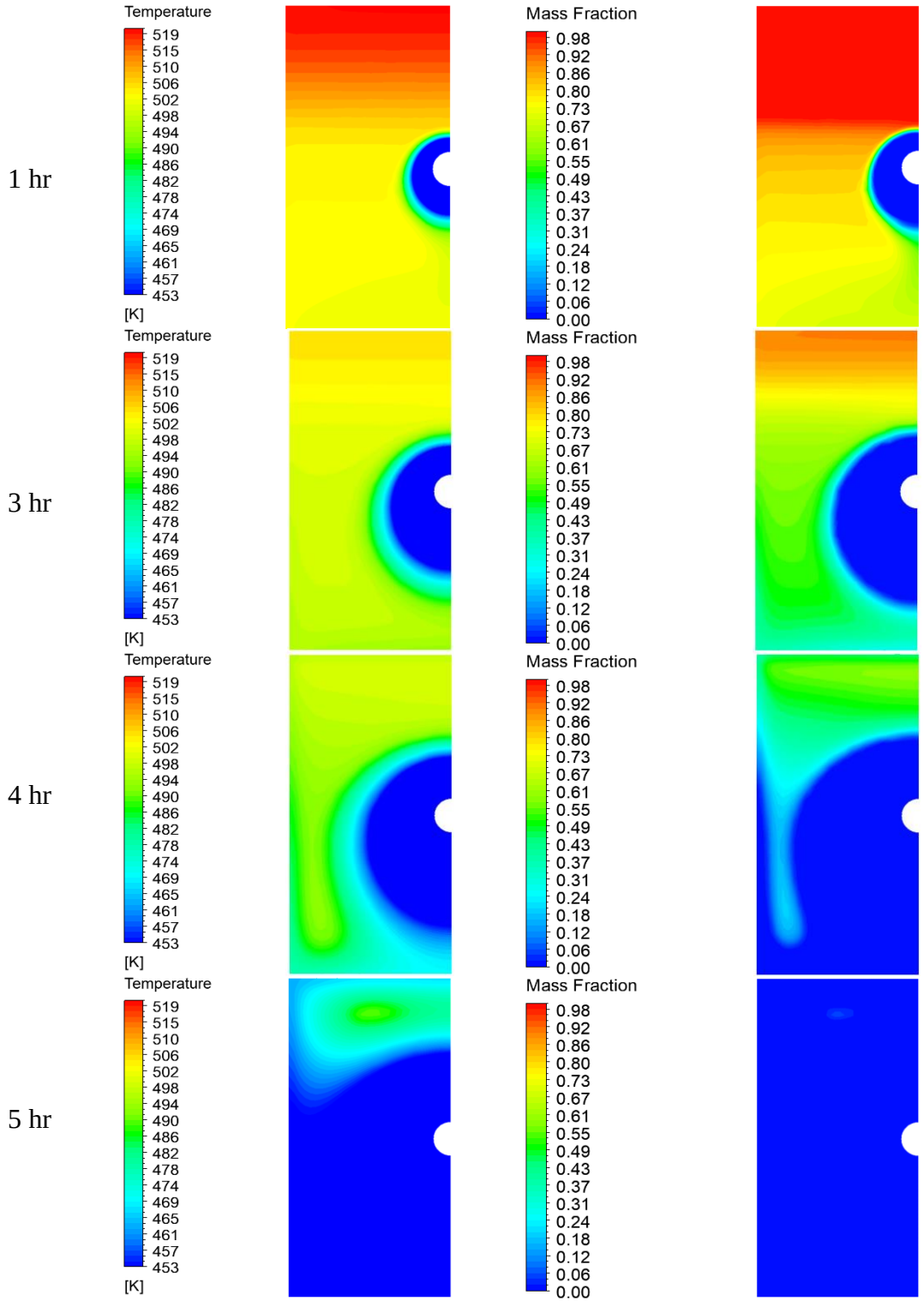

Figure 7-34: TES systems with the finned containers with the discharging power of 25 W

(a) Temperature contours (b) Melting fraction

Figure 7-35 shows a variation of the LF of PCMs in TES systems with different PCMs and configurations. It can be seen that during the discharging process, solidification starts after the initial cooling of the liquid PCM in sensible heat reduction mode. When the temperature decreases below the solidification temperature of PCM (about 247 ºC), the solidification process begins. The higher discharging power leads to a shorter solidification time. The pure PCM solidifies slower due to its low thermal conductivity. As the solidification process advances, pure solar salt solidification rate decreases, while for other configurations it increases. This is due to the low thermal conductivity of pure salt in comparison to the graphite mixtures and the existence of fins. The solidification time for the TES with 8 fins is the same as for the TES with 10 wt% graphite mixture. The use of a 5 wt% graphite mixture provides a shorter solidification time by 2% compared to the TES with 6 fins. The solidification time is decreased by 35% when TES with 8 fins or 10 wt% graphite mixture is used (compared to the TES with pure solar salt).

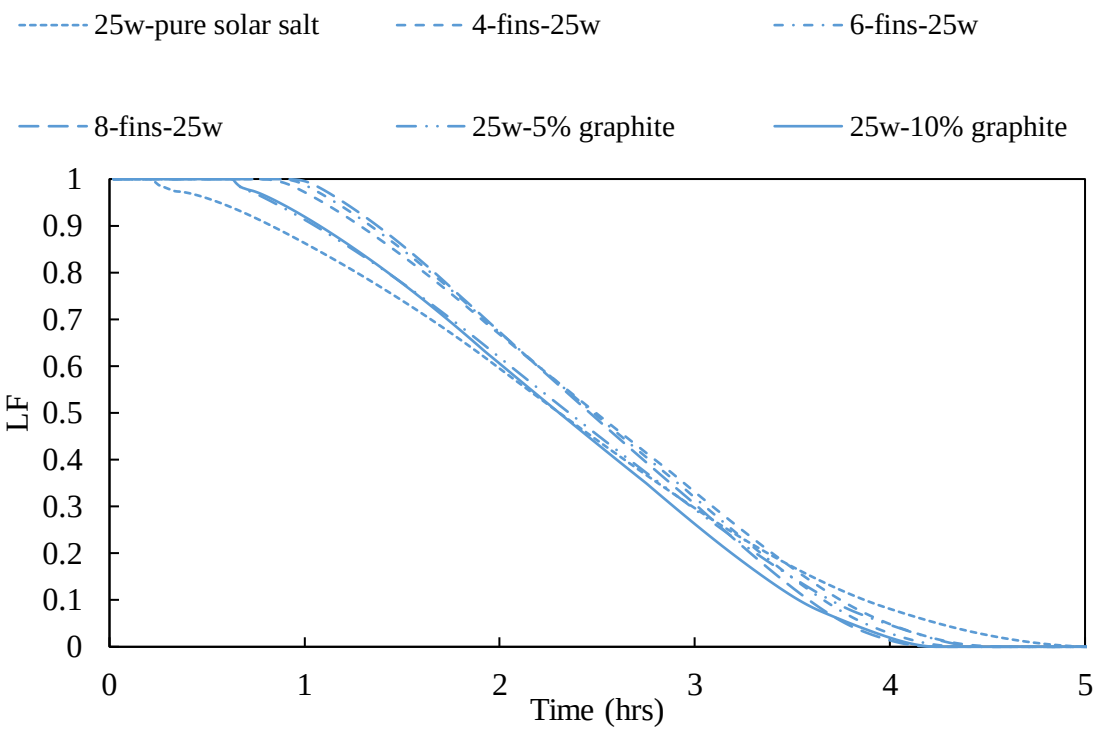

Figure 7-35: LF variation in TES systems during the discharging process.

Figure 7-36 shows the reduction of the stored energy during the discharging process in the TES systems with different PCMs and configurations. Pure solar salt provides higher initial accumulated energy due to the weight and the latent heat in comparison to the fins and graphite mixture, respectively. The discharge of energy takes place first like a sensible heat reduction, so the temperature of the liquid PCM reduces to the melting temperature of about 247 ºC. This is followed by the solidification process and then sensible heat reduction due to the cooling of the solid PCM. Using a higher concentration of graphite or number of fins accelerates the heat discharging process.

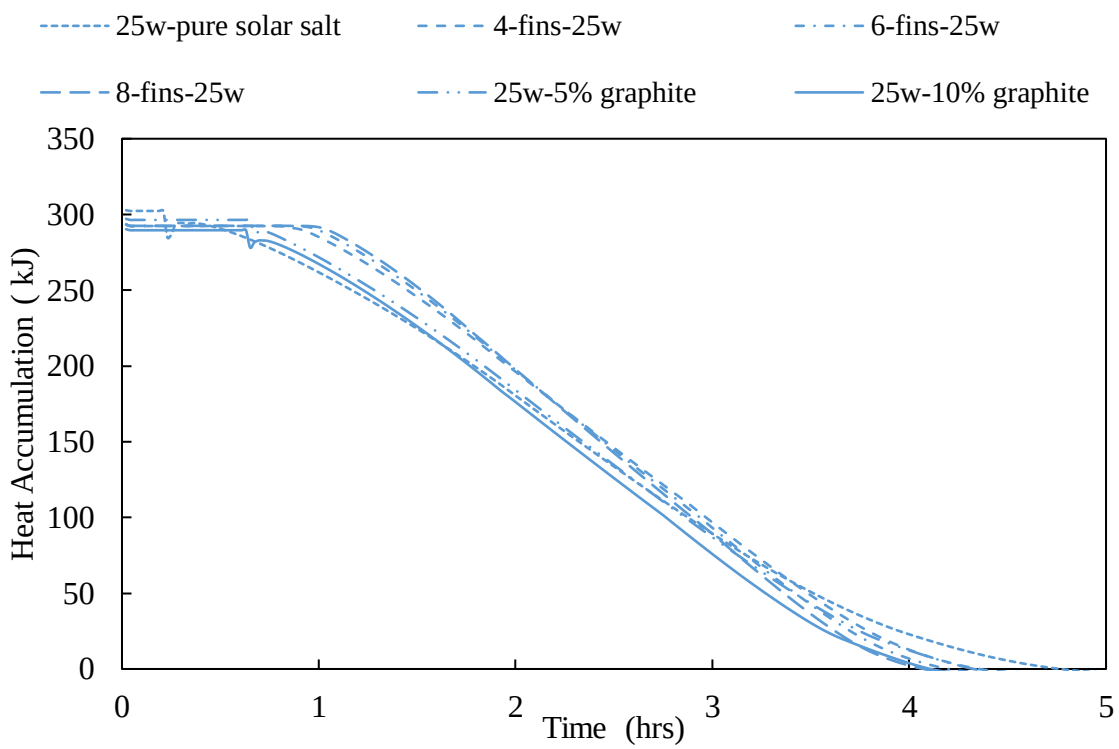

Figure 7-36: Discharging of the accumulated energy in the TES systems.

Figure 7-37 and Figure 7-38 present the HTC and Nu numbers for the TES systems during the discharging process. It can be seen that the HTC and Nu numbers decrease as the discharging process advances due to the cooling of the liquid PCMs. When the temperature of the PCM reaches the solidification temperature, a sudden increase in the HTC and Nu values can be seen. This can be explained by a large amount of heat released during the solidification process. As the discharging process continues, the values of HTC and Nu number decrease significantly due to the solidification process dominated by conduction heat transfer. The HTC and Nu number stabilize as the temperature gradient also becomes constant.

Increasing the number of fins from 4 to 8 and increasing the concentration of graphite both increase the HTC and Nu number due to the intensification of heat transfer through the PCM.

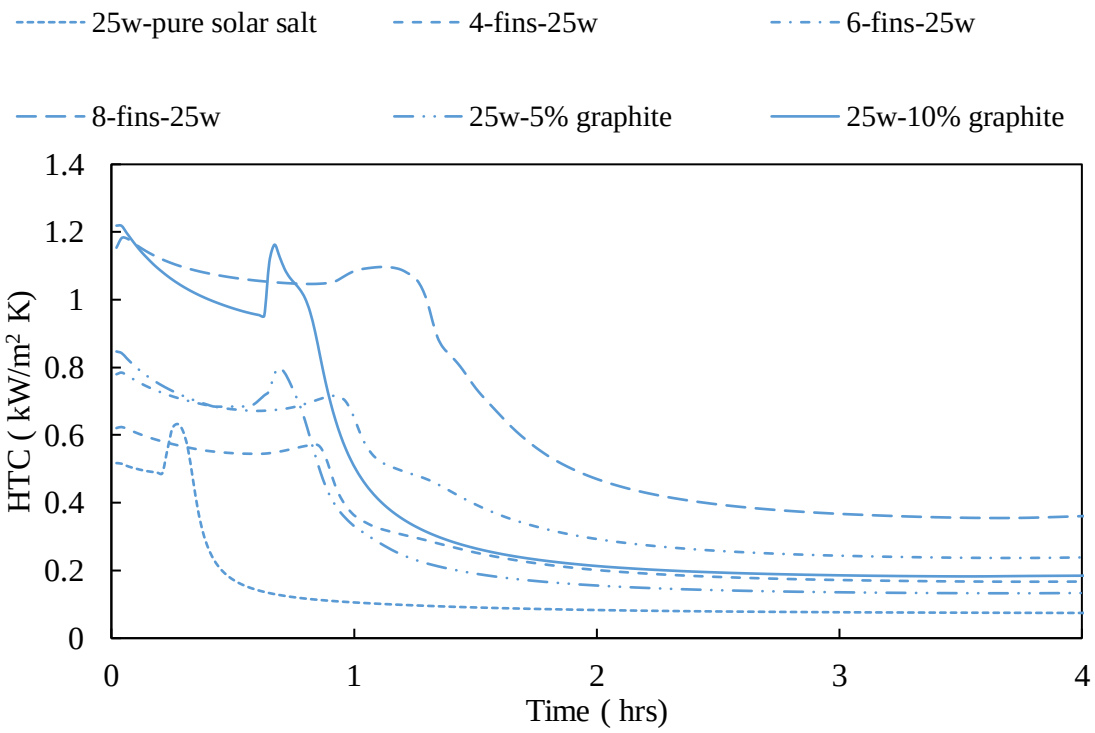

Figure 7-37: HTC variation in the TES systems during the discharging process.

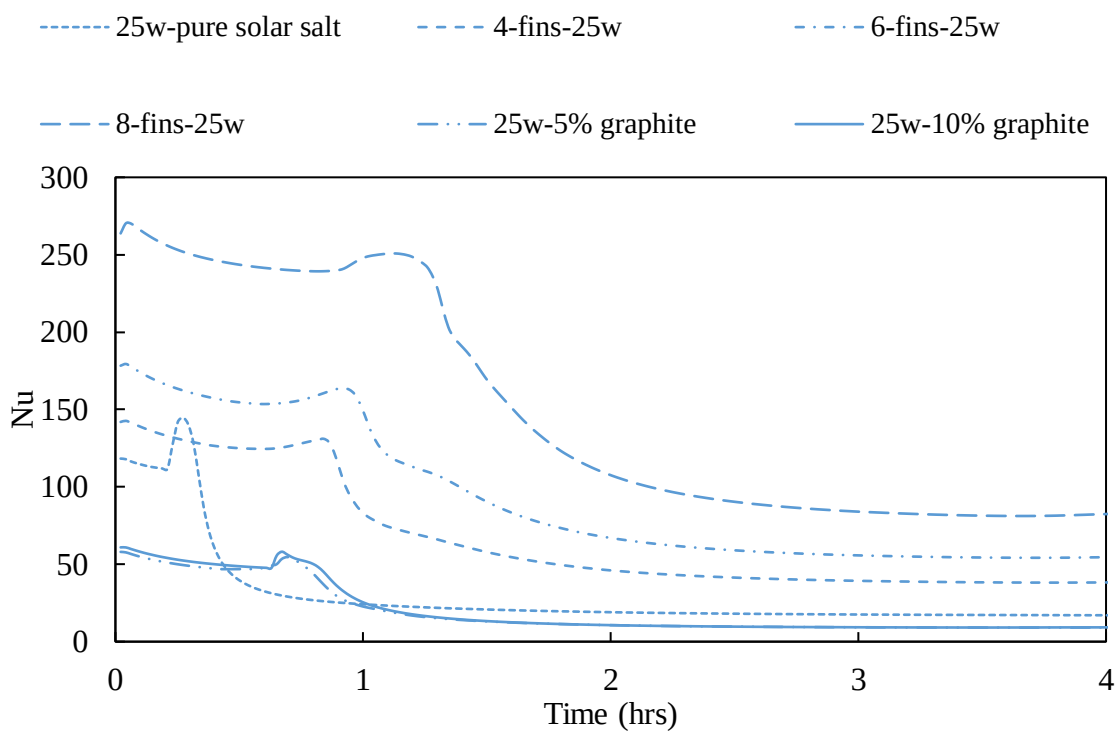

Figure 7-38: Nu number variation in the TES systems during the discharging process.

Figure 7-39 shows the solidification time in the TES systems with different PCMs and configurations. The solidification time decrease with the use of a higher concentration of graphite in the PCM mixture or more fins in the container which increases the thermal conductivity in the system and decreases the specific heat of the mixture. The TES system with 6 fins provides a shorter time of discharge than that for the TES system with the 5wt% graphite mixture. The TES system with 8 fins provides the same discharging time as the system which uses the 10 wt% graphite mixture. The solidification time in the system with 8 fins and 10 wt% graphite mixture is reduced by about 37 % in comparison to the TES system with pure solar salt.

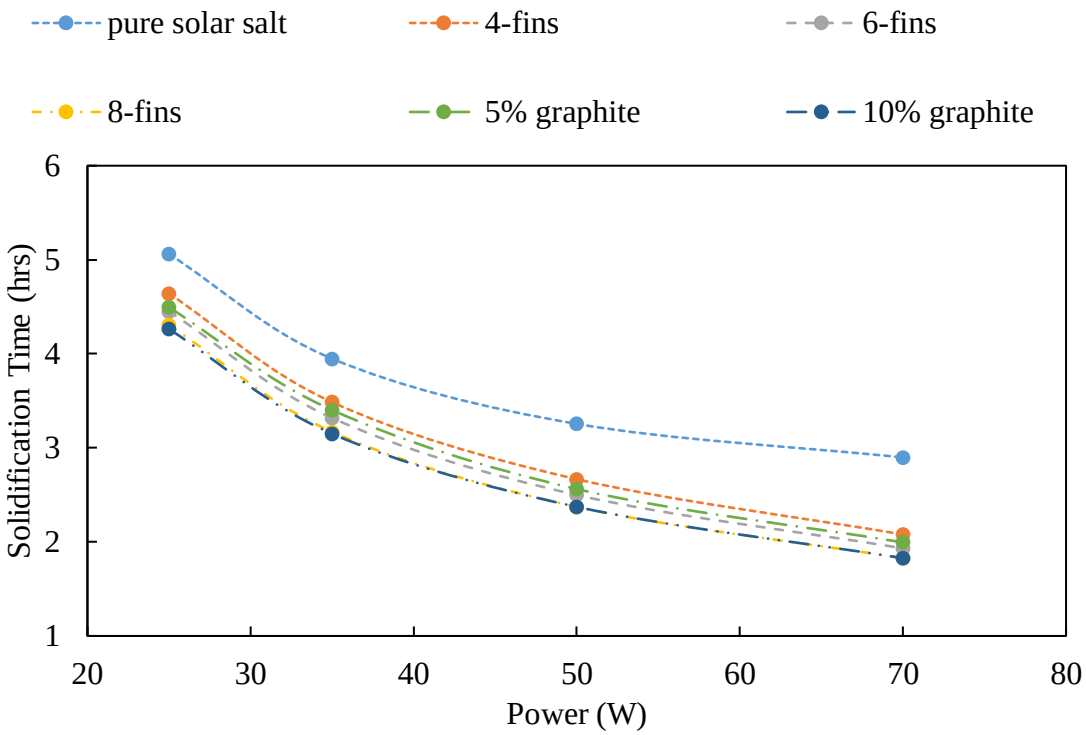

Figure 7-39: Solidification time in the TES systems during the discharging process.

7.4.2 TES system with the metal alloy

The charging process of the TES system with the metal alloy was started at the temperature of 136 °C and finished at the temperature of 160 °C. Figure 7-40 shows the variation of the average temperature of the metal alloy in the TES system for different power inputs. The gradual increase in the average temperature occurs in the first stage of the heating process between 136 and 138 °C due to the high thermal conductivity of the solid PCM. As the heat charging process advances, the average temperature increases at different rates. The temperature stabilizes when the melting temperature of about 142 °C is achieved. Then a rapid temperature increase can be observed between 142 and 156 °C due to the heating of the liquid PCM. The average temperature in the TES system does not provide an accurate estimation of the melting time because of the significant

temperature difference in various locations. As the phase change process is completed, the sharp increase in the average temperature can be observed due to the high thermal conductivity of the PCM. The melting time decreases from 4.7 hours to 1.8 hours with an increase in the input power value from 25 to 70 W.

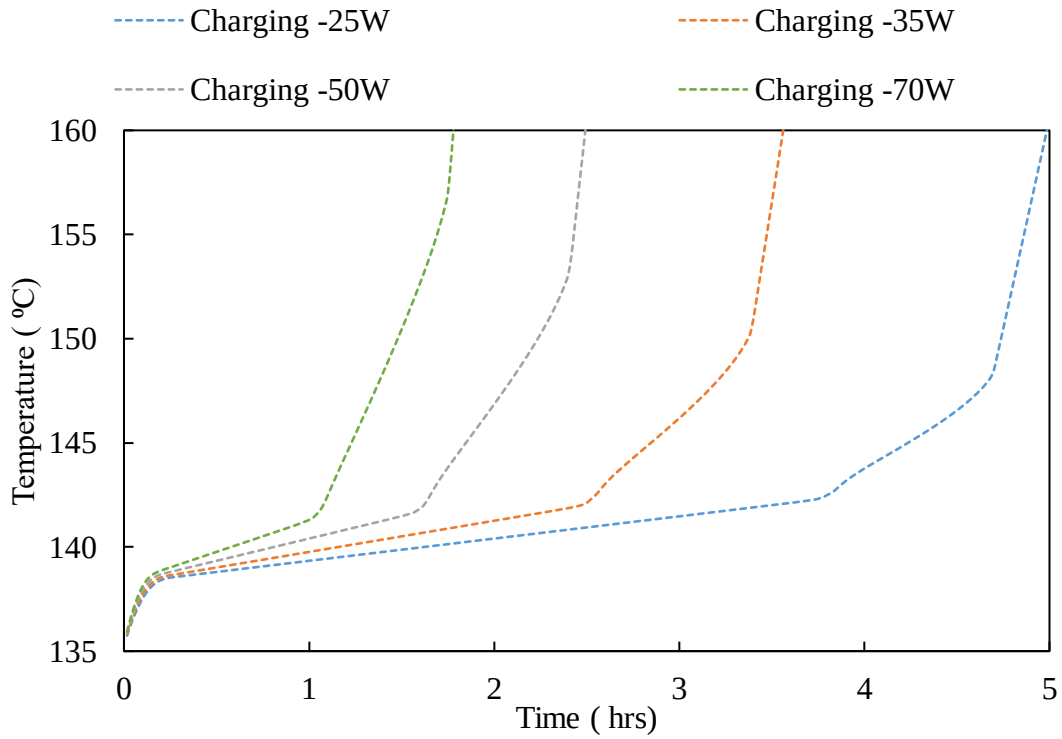

Figure 7-40: The average temperature in the TES systems with metal alloy during the charging process.

Figure 7-41 shows the LF variation of the metal alloy during the charging process using the different power inputs. The melting in the metal alloy can be seen as an almost linear process of increasing the LF and this is a result of its high thermal conductivity and rapid phase change process. The melting time decreases from 4.7 to 1.8 hours when the power is increased from 25 to 70 W respectively.

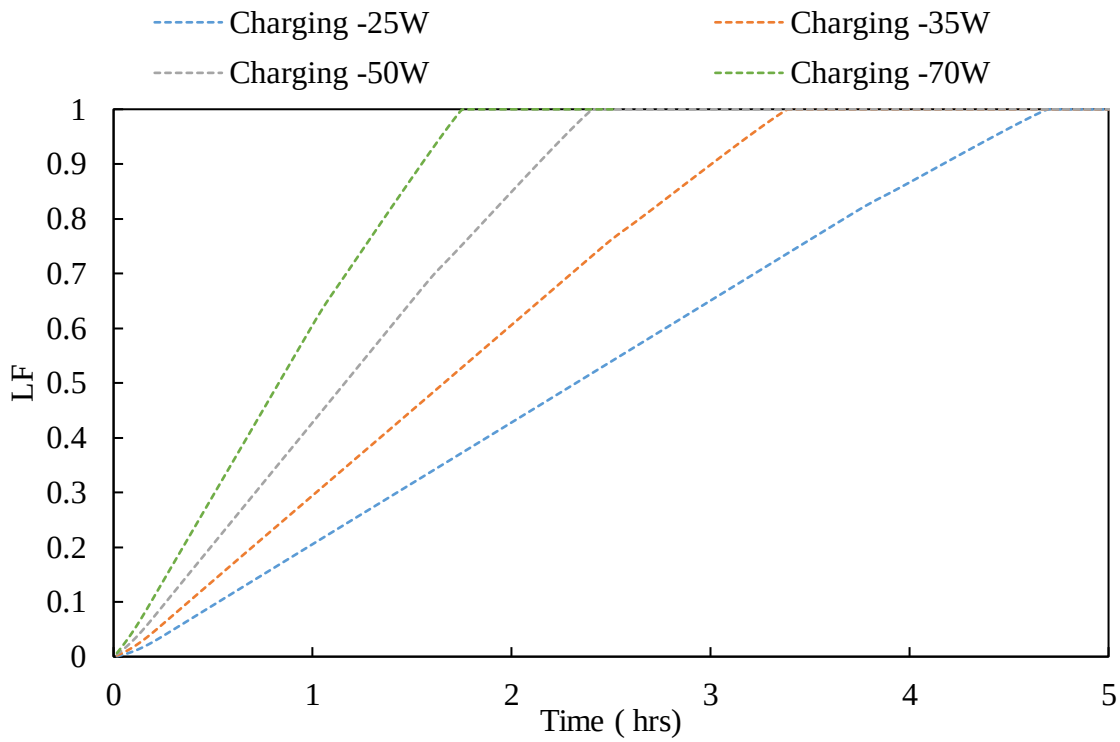

Figure 7-41: Variation of the LF of the PCMs during the charging process.

Figure 7-42 shows the accumulated energy in the TES system with the metal alloy during the charging process with different power inputs. The accumulated energy also increases linearly. The TES system could accumulate 500 kJ of energy (the mass of the PCM is 11 kg). The higher is power input the greater is rate of heat accumulation in the system.

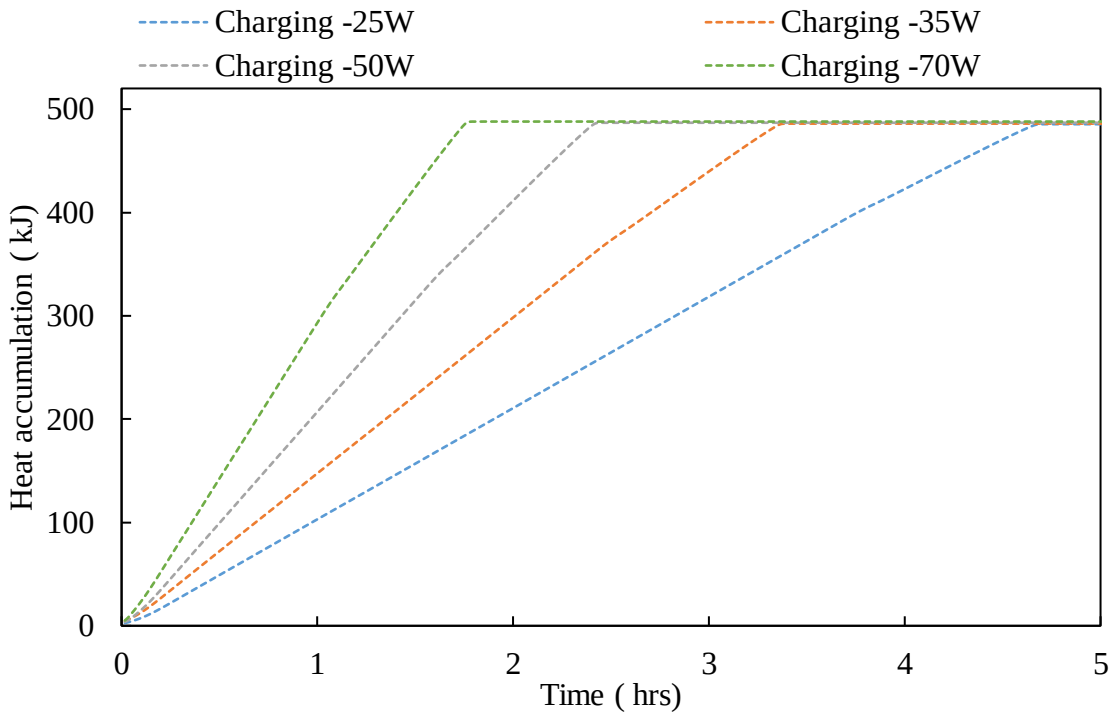

Figure 7-42: Accumulated Energy in the TES systems during the charging process.

Figure 7-43 and Figure 7-44 show the variation of the HTC and Nu numbers in the TES with the metal alloy for different power inputs. The values of HTC and Nu number decrease at the earlier stage due dominance of the conduction heat transfer mechanism. When the temperature reaches the melting temperature their values increase during the charging process due to the development of convective flows in the upper part of the container. Values decrease after melting in the upper parts is completed conduction heat transfer is dominant in the lower part of the container. When the melting process is fully completed the HTC and Nu number values increase and stabilise due to the sensible heating mode.

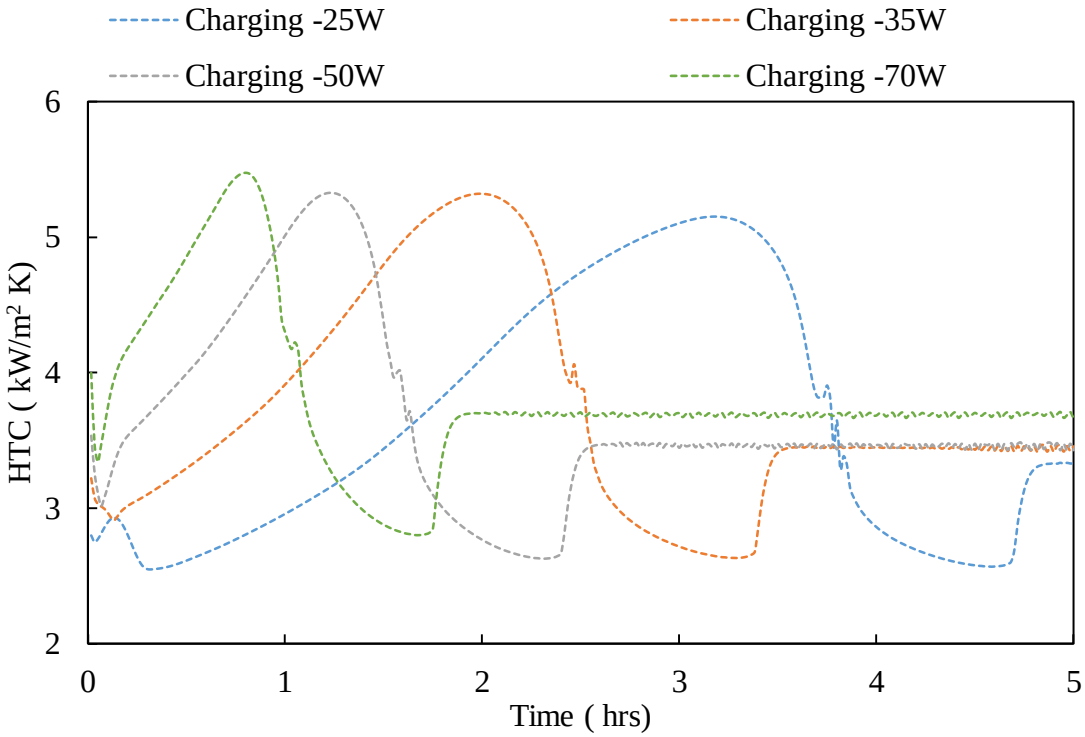

Figure 7-43: HTC variation in the TES systems during the charging process.

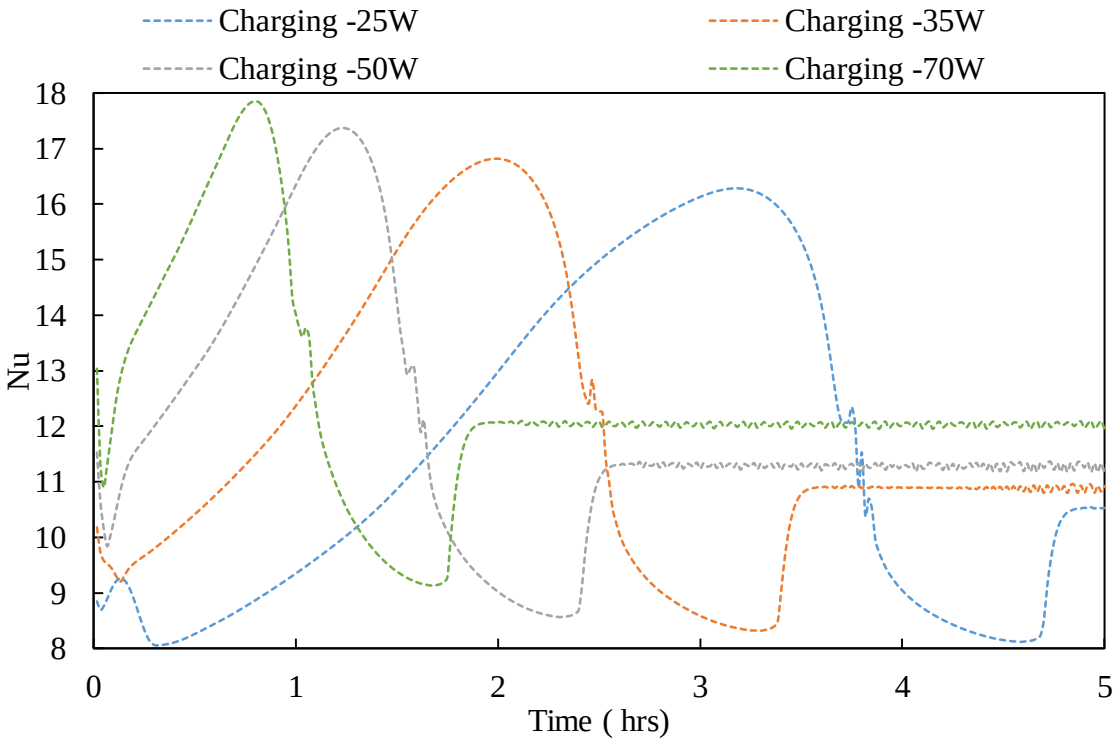

Figure 7-44: Nu number variations in the TES during the charging process.

Figure 7-45 shows the variation in the average temperature in the TES system with metal alloy during the heat discharging process in the temperature range of 150 and 120 ^{o}C. The temperature decreases rapidly in the sensible heat mode due to the high thermal conductivity of the molten PCM. When the temperature of the PCM reaches the solidification temperature level of 131.2 ^{o}C, the average temperature drop rate decreases due to the phase change process (from liquid to solid). As the discharging process advances, the average temperature reaches the solidification temperature of 126 ^{o}C. A sharp reduction in temperature is then noticed due to the dominance of the conduction heat transfer in the solid PCM. The heat discharging time reduces with discharging power increase: from 5 to 1.8 hours for 25 and 70 W, respectively.

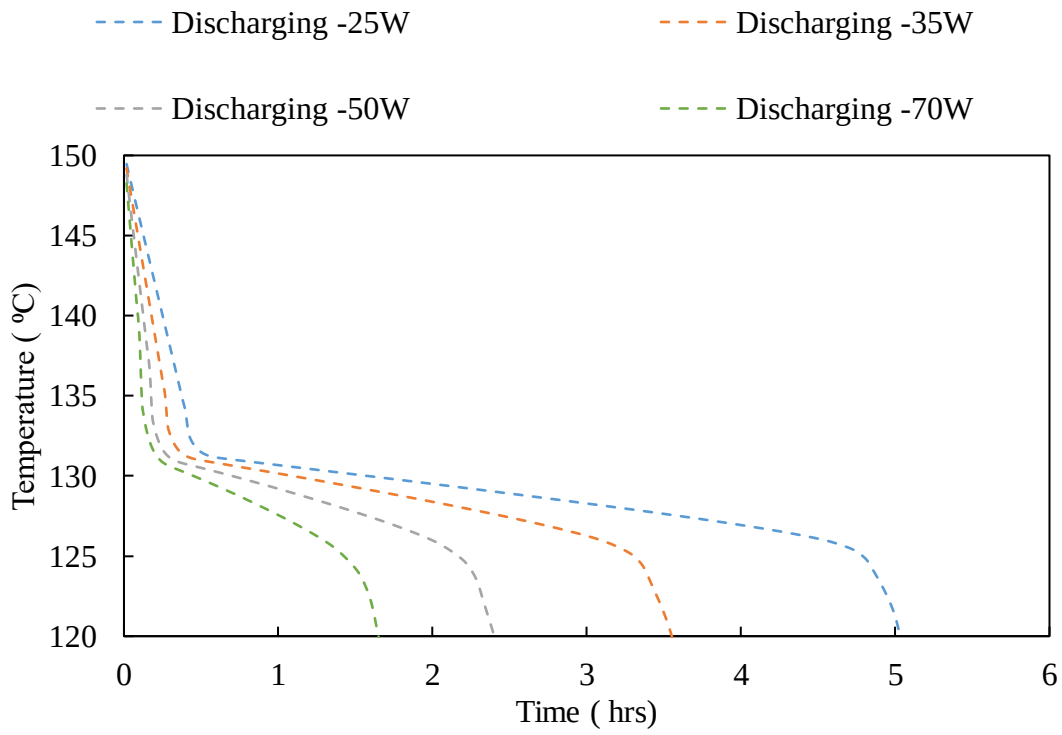

Figure 7-45: The average temperature variation in the TES system during the heat discharging process.

Figure 7-46 shows the LF of the metal alloy during the discharging process with different discharging powers. The solidification process starts after the liquid is cooled down to the solidification temperature. A linear behaviour can be observed for the solidification process due to the high thermal conductivity of the PCM. Increasing the discharging power decreases the solidification time from 5 to 1.8 hours. The LF diagram describes the solidification process more accurately than the average temperature diagram due to local temperature variations inside the TES system.

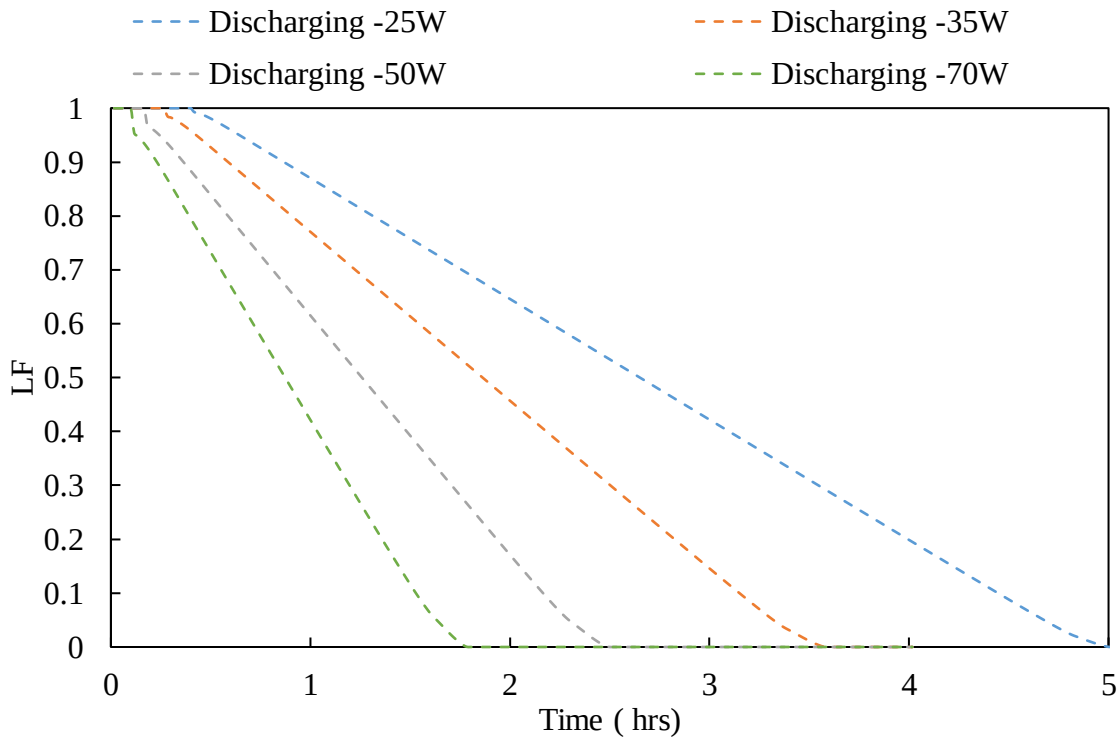

Figure 7-46: LF variation during the discharging process.

Figure 7-47 shows the reduction in the accumulated energy during the discharging process. The energy is discharged slowly in the first stage, as the liquid PCM is being cooled down. When the temperature reaches the solidification temperature, the discharging rate of energy increases as a result of the phase change process from solid to

liquid. The discharging rate also exhibits a linear behaviour due to the high thermal conductivity of the PCM.

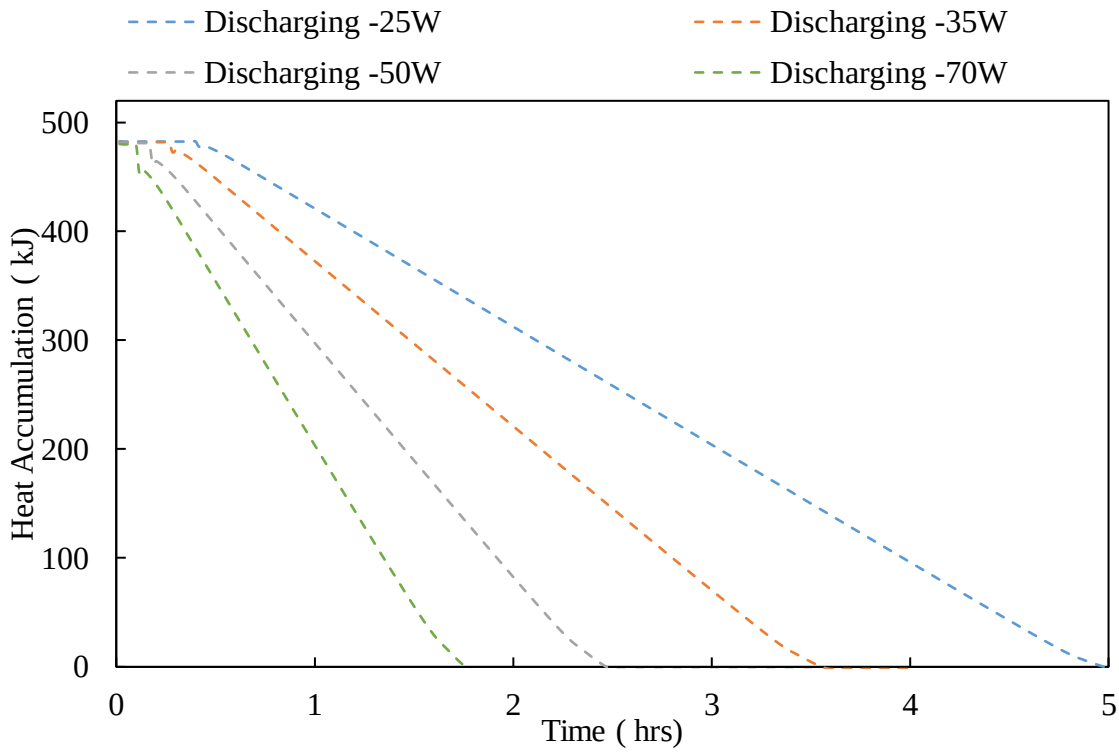

Figure 7-47: Discharging the accumulated energy in the TES system.

Figure 7-48 shows the melting and solidification times of the TES system with metal alloy for different power values. The melting and solidification times have the same trend with a difference in the magnitude of about 5 %. The high thermal conductivity of the metal alloy is the reason for this phenomenon, which yields a uniform temperature throughout the PCM. Increasing the charging and discharging powers from 25 to 70 W decreases the melting and solidification times by around 3 hours.

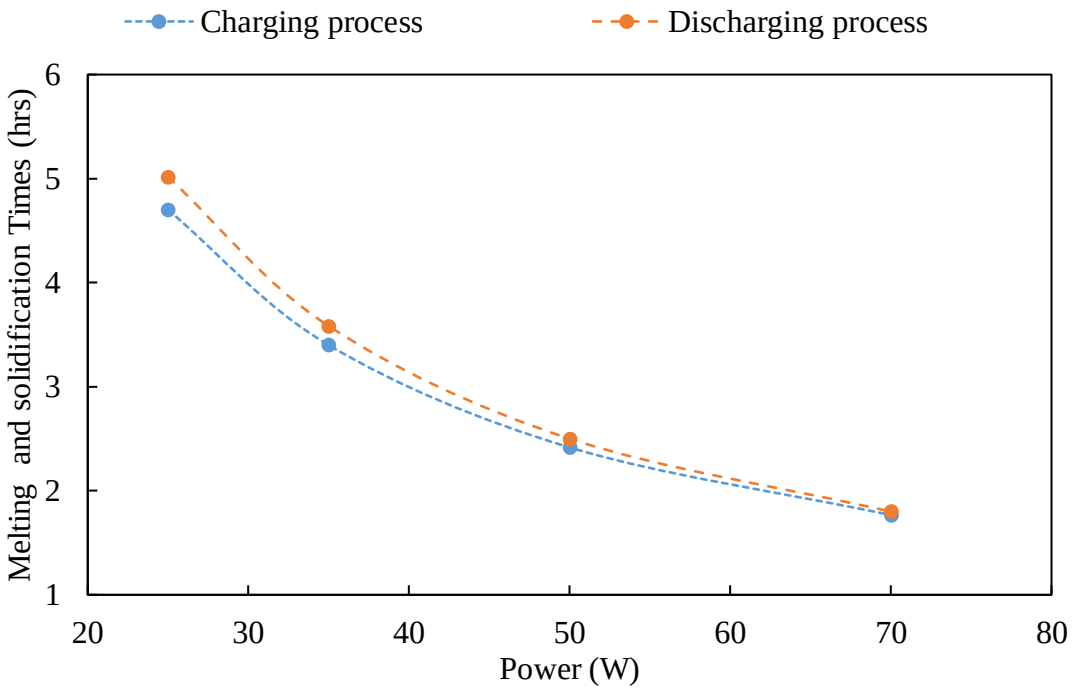

Figure 7-48: Melting and solidification times in the TES system versus power input/output.

The results for the liquid fraction and Nusselt number for the TES system with the metal PCM are presented in the form of dimensionless parameters in Appendix B.

7.4.3 Deriving dimensionless correlations for predicting LF and Nu number

Dimensionless correlations are derived using the numerical modelling results to predict the LF and Nu number in the TES during melting and solidification processes.

Figure 7-49 shows the variation of the LF in the melting process of solar salt in comparison to [204]. In [204], a sphere with different diameters was used with the RT27 (Rubitherm GmbH) as a PCM that has a melting temperature of 24.5-26.5 ^{o}C. The liquid fraction of solar salt was observed to have the same values until 50% of the PCM. However, the rise in the liquid fraction of solar salt begins to slow down as the melting

developes from the centre of the container due to convection heat transfer, which is not an influencing factor on the sphere (melting from spherical surface).

Figure 7-50 and Figure 7-51 compare the LF of the TES system with solar salt against data in [7, 205-209] during the charging process and the liquid fraction of the TES system with solar salt against data in [210-215] during discharging time, respectively. These comparisons were carried out using the heating/cooling applied from the centre of the container. The liquid fraction in the TES system with solar salt during the charging and discharging processes have a close tendency to other cases, which can be used to predict the LF of different TES systems with various PCMs. However, the results for solar salt cannot be used to predict the LF for the metals due to the high thermal conductivity of the metals. Therefore, another comparison was carried out to predict the LF of metals using the numerical results of the TES system with the metal alloy.

Figure 7-52 shows a comparison of numerical results for the charging process with a power input of 25 W against literature data (flat plates) in [70, 216, 217]. It can be seen that the current dimensionless analysis carried out for the LF of the metal alloy is capable to predict the LF of other metal alloys. Figure 7-53 shows the solidification process of the metal alloy against different cases from the literature [108, 218, 219] to generate dimensionless correlations for the LF and Nu number.

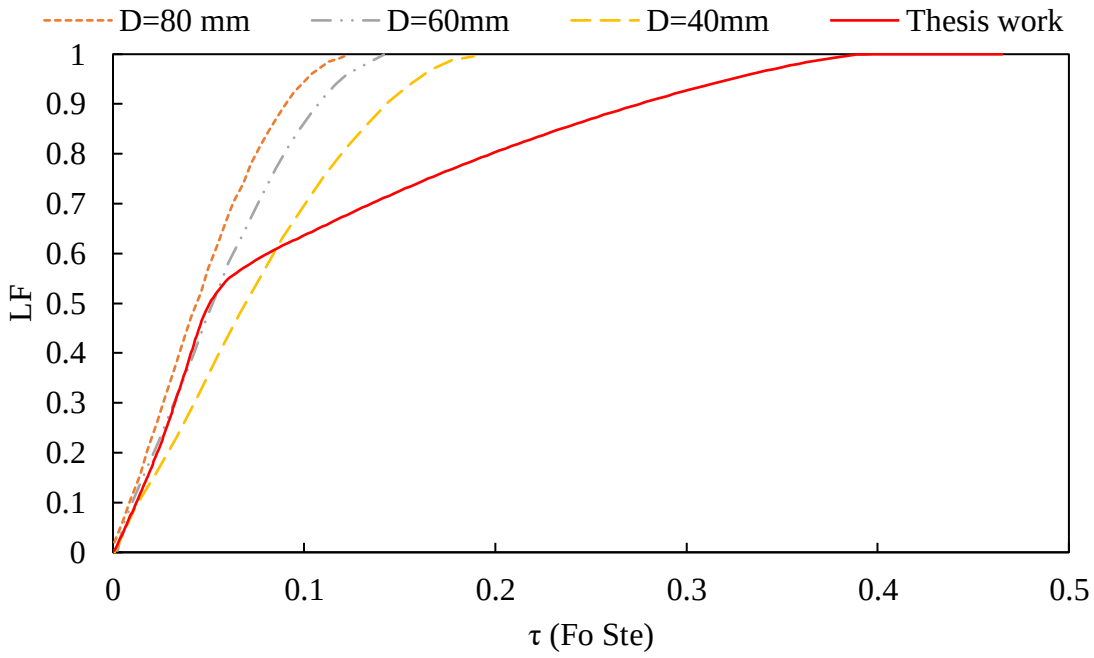

Figure 7-49: Comparison of the variations of the LF of solar salt during the charging process with data in the literature.

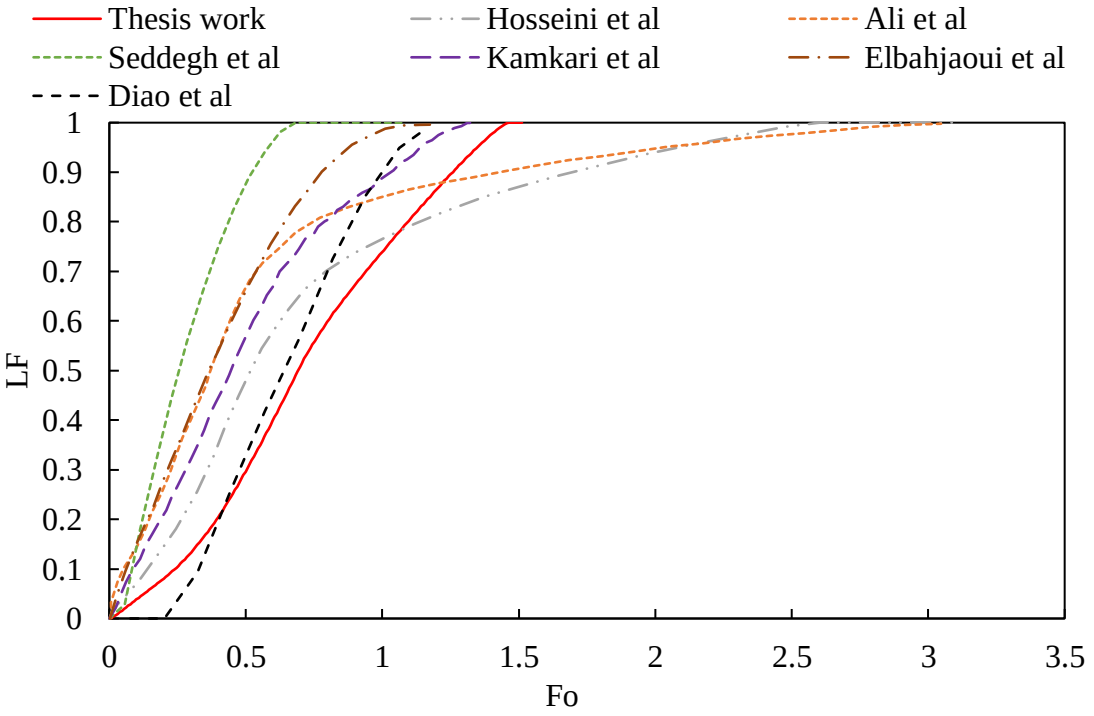

Figure 7-50: Comparison of variations of the LF of solar salt with 10 wt% graphite during the charging process with data in the literature.

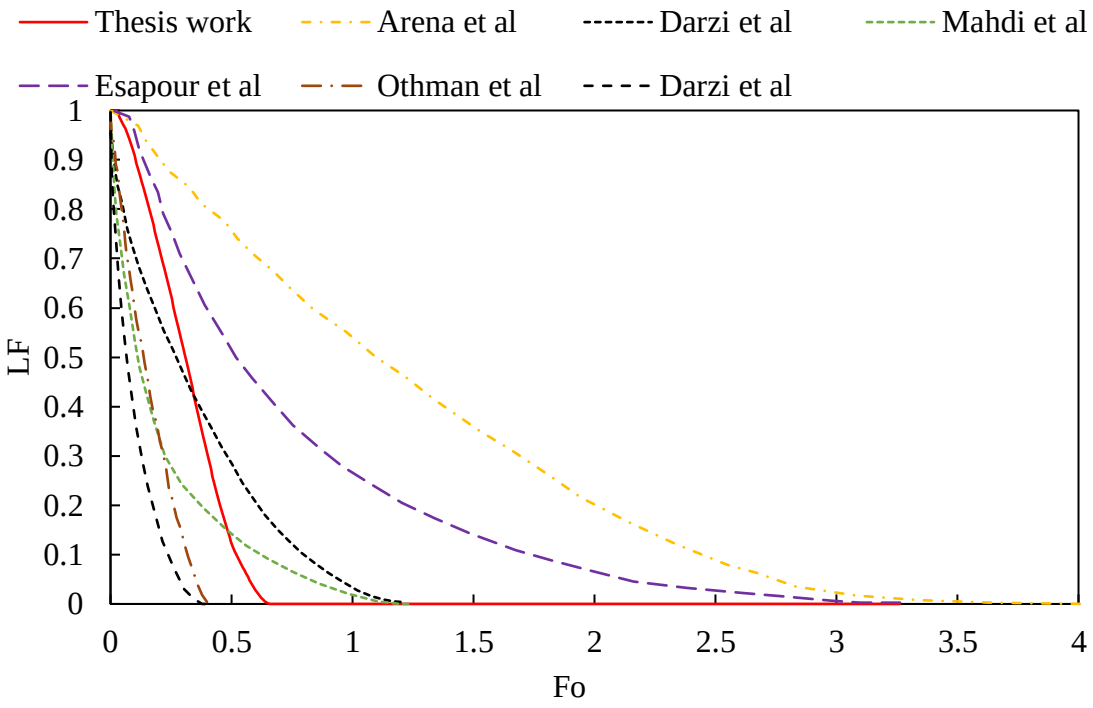

Figure 7-51: Comparison of variations of the LF during the discharging process for solar salt with 10 wt% graphite with data in the literature.

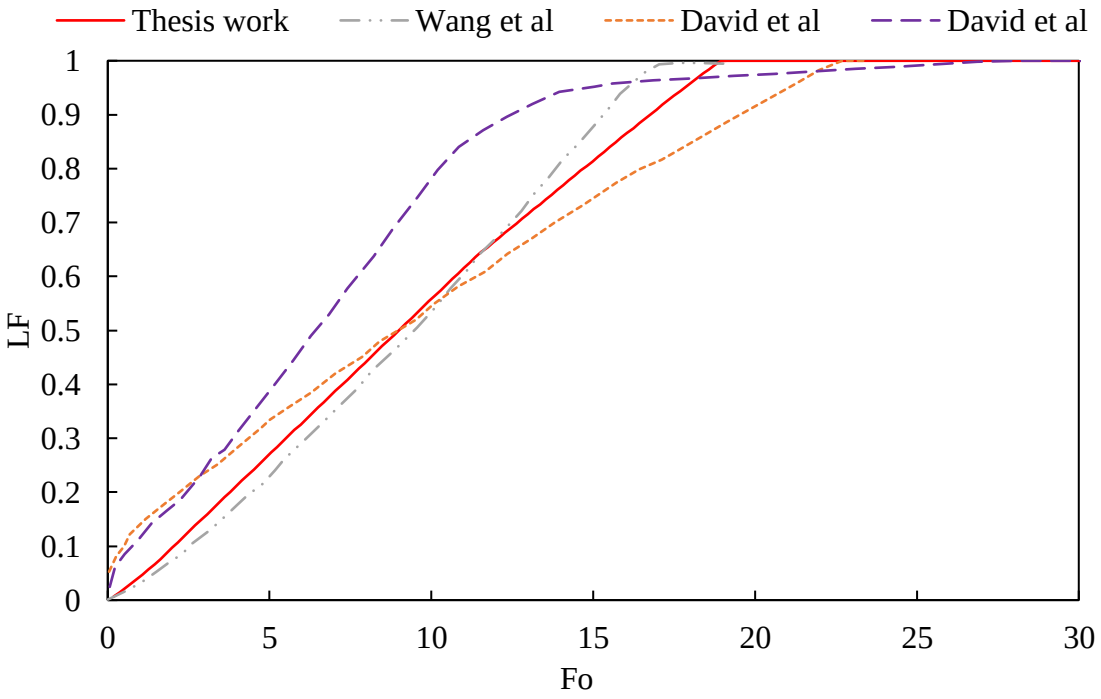

Figure 7-52: Comparison of variations in the LF during the charging process for the metal alloy with data in the literature.

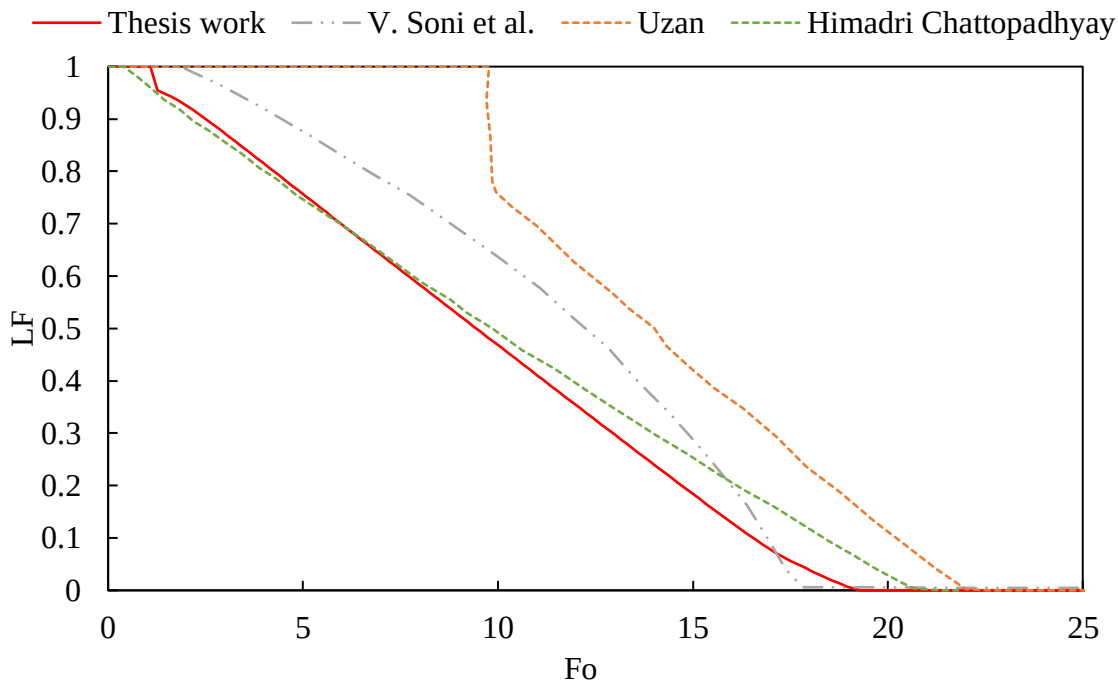

Figure 7-53: Comparison of LF during the discharging process of the metal alloy with data in the literature.

The current dimensionless analysis is capable to predict the variation of the LF in other cases described in the literature. However, it was evident that metals have different behaviour than OPCM due to their high thermal conductivity, and such cases should be treated separately.

The curve fitting toolbox in Matlab R2017a was used to derive the dimensionless correlations. The forms of the correlations are used as they usually deployed in the literature, where the thickness of the fins is 1.5mm.

The variation of the LF for solar salt during the charging process can be expressed as:

$$LF = 1 - exp(-231.4/C_1 \cdot Fo^{2.279} \cdot Ste^{0.3}) \quad (7\text{-}2)$$

For the case of pure solar salt, solar salt with graphite and the use of a certain number of fins in the container (NF) C_1 is a constant:

$$C_1 = 1, or \left({k_{solar\ salt\ with\ graphite}}/{k_{solar\ salt}}\right)^{2.15}, or\ {1}/{\sqrt[4]{NF}} \tag{7-3}$$

For pure solar salt, the Nu number is expressed as:

$$Nu = 122.1 \cdot Fo^{0.151} \cdot Ste^{-0.3437} \tag{7-4}$$

Nu number for the TES with fins and graphite mixture, as expressed by:

$$Nu = 174.127 \cdot C_2 \cdot Fo^{0.2287} \cdot Ste^{-0.3773} \tag{7-5}$$

Here C_2 is a constant:

$$C_2 = \left({k_{pure\ salt}}/{k_{pure\ salt\ with\ graphite}}\right), or\ \sqrt[3]{NF/3} \tag{7-6}$$

The previous correlations are valid for the following Fo and Ste number ranges:

$$0.0015 \leq Fo \leq 1 \tag{7-7}$$

$$0.004 \leq Ste \leq 1.2 \tag{7-8}$$

The LF and Nu number for the TES with solar salt during the discharging process can be expressed as:

$$LF = \exp(-231.4 \cdot C_3 \cdot Fo^{2.279} \cdot Ste^{0.3}) \tag{7-9}$$

For the case of pure solar salt, solar salt with graphite and the use of a certain number of fins in the container (NF) C_3 is a constant:

$$C_3 = 0.55, \left(\frac{\sqrt[3]{percentage\ of\ graphite}}{2} / (\ 5 + \left(\left(\frac{k_{mixture}}{k_{pure\ salt}}\right)\right)^2\right), \tag{7-10}$$

$$0.8 \cdot \sqrt[3]{{Number\ of\ fins}/{2}}$$

For the TES with pure solar salt, solar salt with graphite and with fins, respectively.

$$Nu = C_4 \cdot 74.89 \cdot Fo^{-0.06034} \cdot Ste^{-0.8235} \tag{7-11}$$

Here, C_4 is a constant:

$$C_4 = 1, \left(\left({k_{pure\ salt}}/{k_{mixture}} \right) \right), (\sqrt[3]{NF} - 0.1 \cdot NF) \quad (7\text{-}12)$$

These correlations are valid for the following Fo and Ste ranges:

$$0.001 \leq Fo \leq 1.5 \quad (7\text{-}13)$$

$$0.14 \leq Ste \leq 1.2 \quad (7\text{-}14)$$

The LF and Nu number for the TES with the metal alloy during the charging process can be expressed as:

$$LF = 0.04868 \cdot Fo \cdot Ste^{-0.05} \quad (7\text{-}15)$$

$$Nu = 0.8984 \cdot Fo^{0.1439} \cdot Ste^{-0.833} \quad (7\text{-}16)$$

These correlations are valid for the following Fo and Ste ranges:

$$0.18 \leq Fo \leq 40 \quad (7\text{-}17)$$

$$0.004 \leq Ste \leq 0.16 \quad (7\text{-}18)$$

The LF and Nu number for the TES with the metal alloy during the discharging process can be expressed as:

$$LF = 1 - 0.52 \cdot Fo \cdot Ste \quad (7\text{-}19)$$

$$Nu = 4.5 + 0.06253 \cdot (Fo \cdot Ste)^{-1.259} \quad (7\text{-}20)$$

These correlations are valid for the following Fo and Ste ranges:

$$0.0018 \leq Fo \leq 40 \quad (7\text{-}21)$$

$$0.002 \leq Ste \leq 0.08 \quad (7\text{-}22)$$

Figure 7-54 to Figure 7-67 show a comparison between the numerical results and the predicted results obtained for the variations of the LF and Nu number during charging and discharging processes versus dimensionless time.

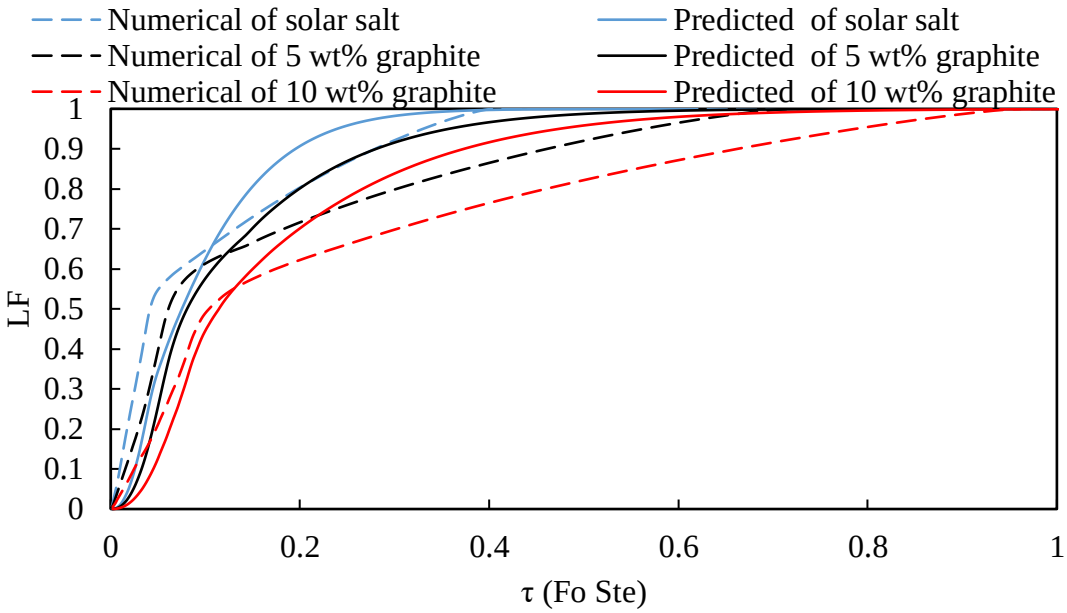

Figure 7-54: Comparison between the numerical and predicted results for the LF versus dimensionless time during the charging process (TES with solar salt and mixtures with graphite).

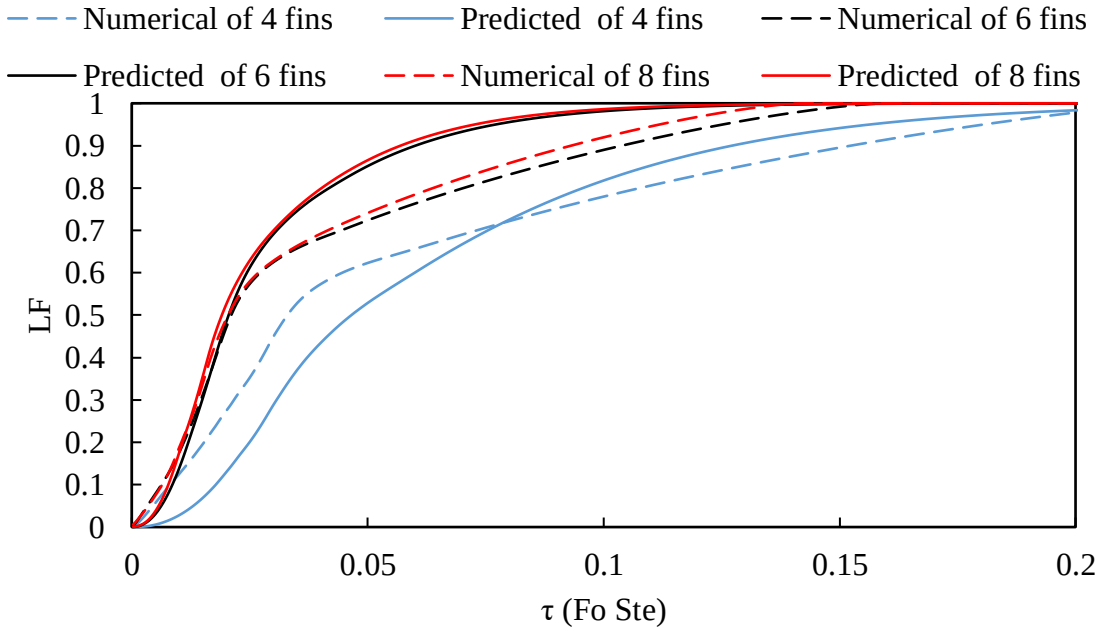

Figure 7-55: Comparison between the numerical and predicted results for LF versus dimensionless time during the charging process (TES with solar salt and fins).

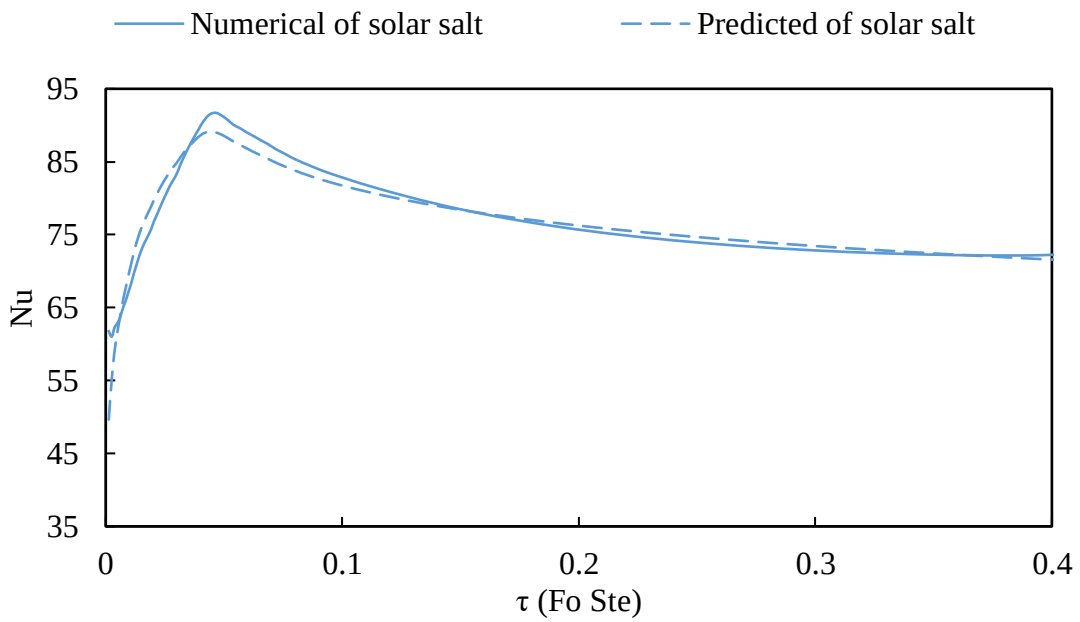

Figure 7-56: Comparison between the numerical and predicted results for Nu number versus dimensionless time during the charging process (TES with solar salt).

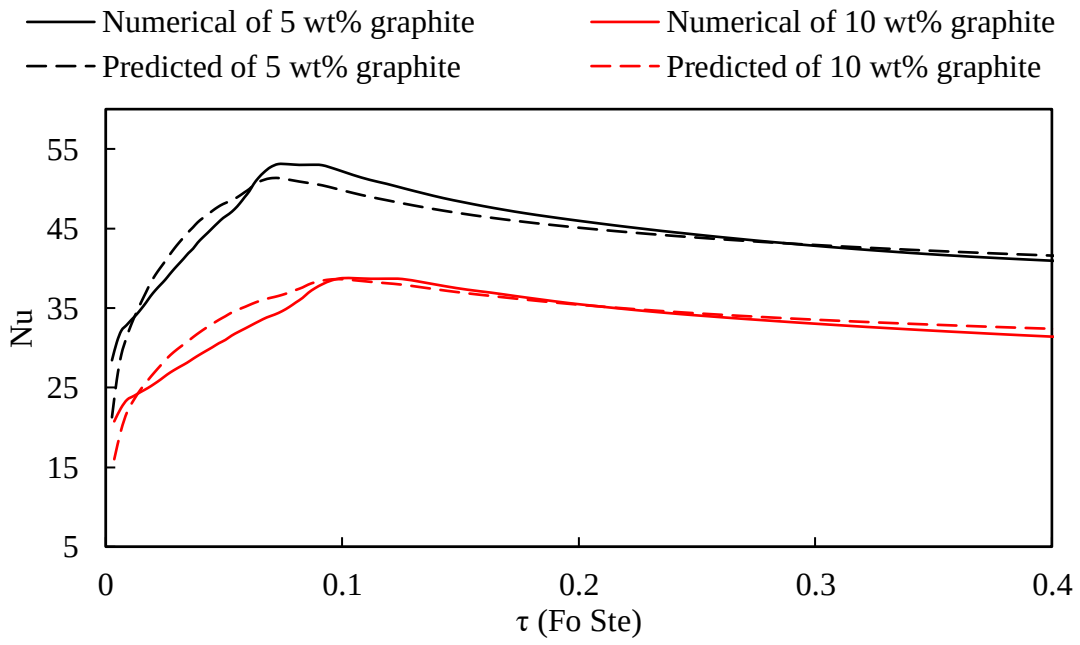

Figure 7-57: Comparison between the numerical and predicted results for Nu number versus dimensionless time during the charging process (TES with solar salt and mixtures with graphite).

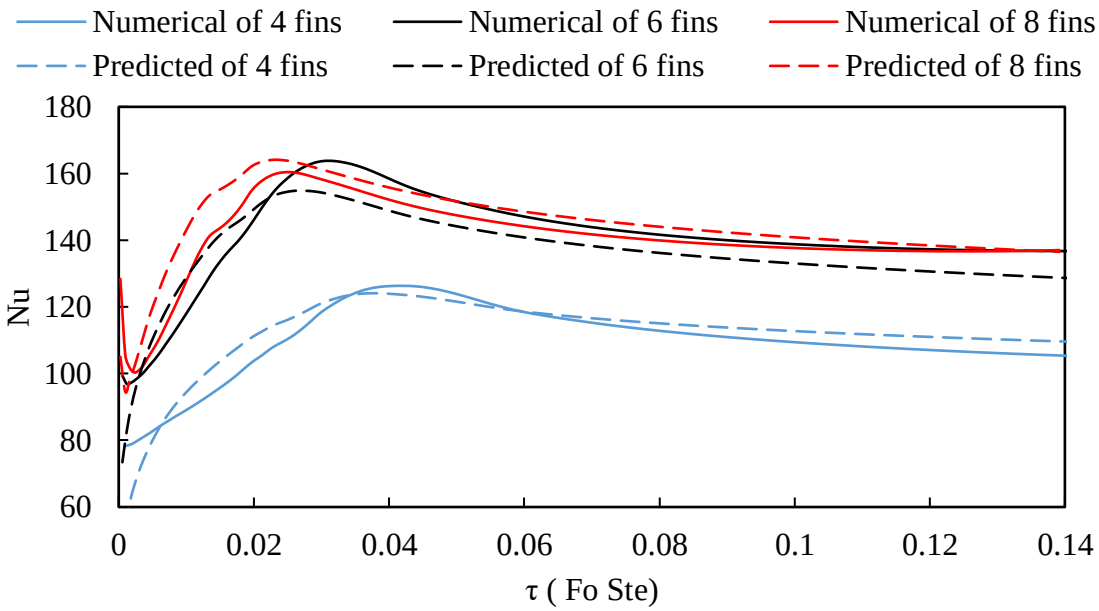

Figure 7-58: Comparison between the numerical and predicted results for the Nu number versus dimensionless time during the charging process (TES with solar salt and fins).

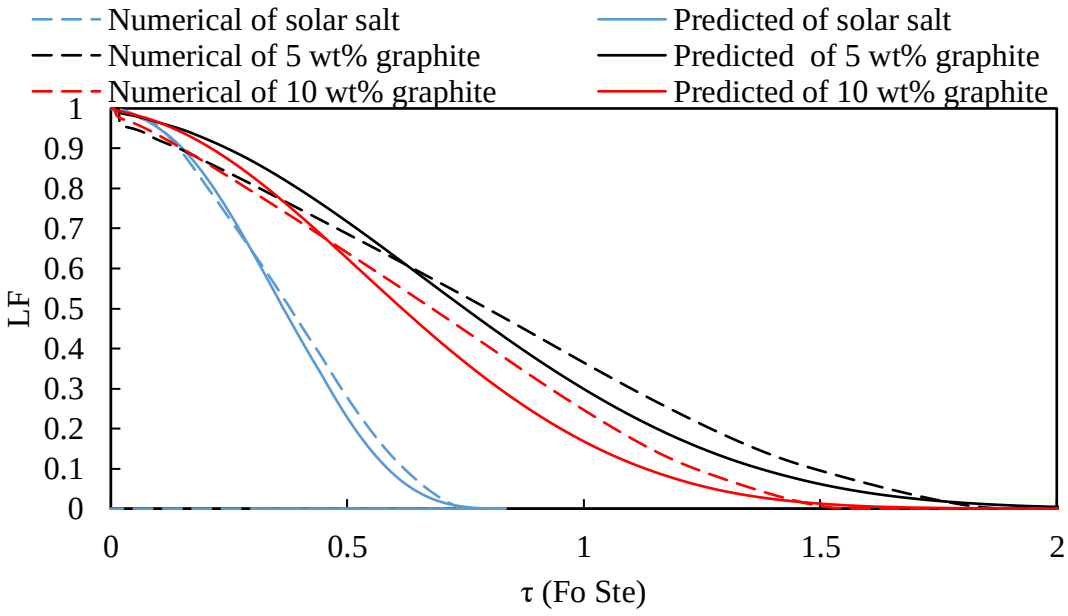

Figure 7-59: Comparison between the numerical and predicted results for the LF versus dimensionless time during the discharging process (TES with solar salt and mixtures with graphite).

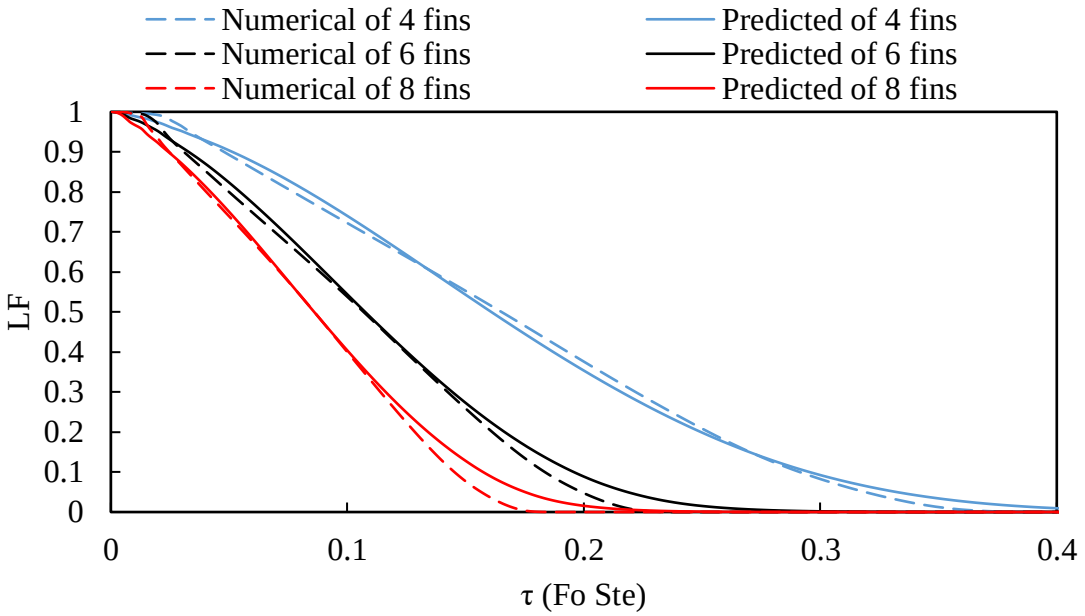

Figure 7-60: Comparison between the numerical and predicted results for the LF versus dimensionless time during the discharging process (TES with solar salt and fins).

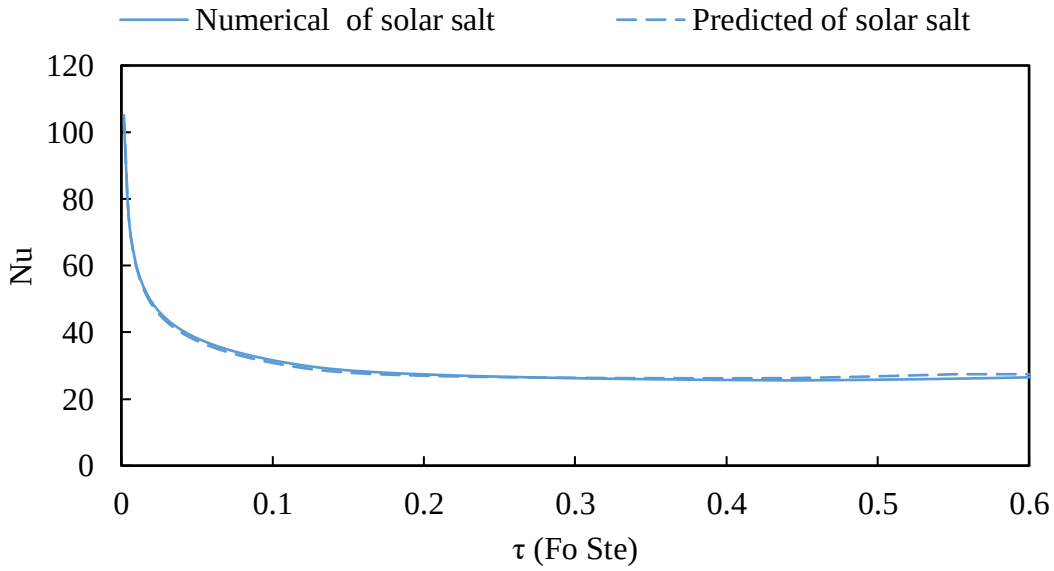

Figure 7-61: Comparison between the numerical and predicted results for the Nu number versus dimensionless time during the discharging process (TES with solar salt).

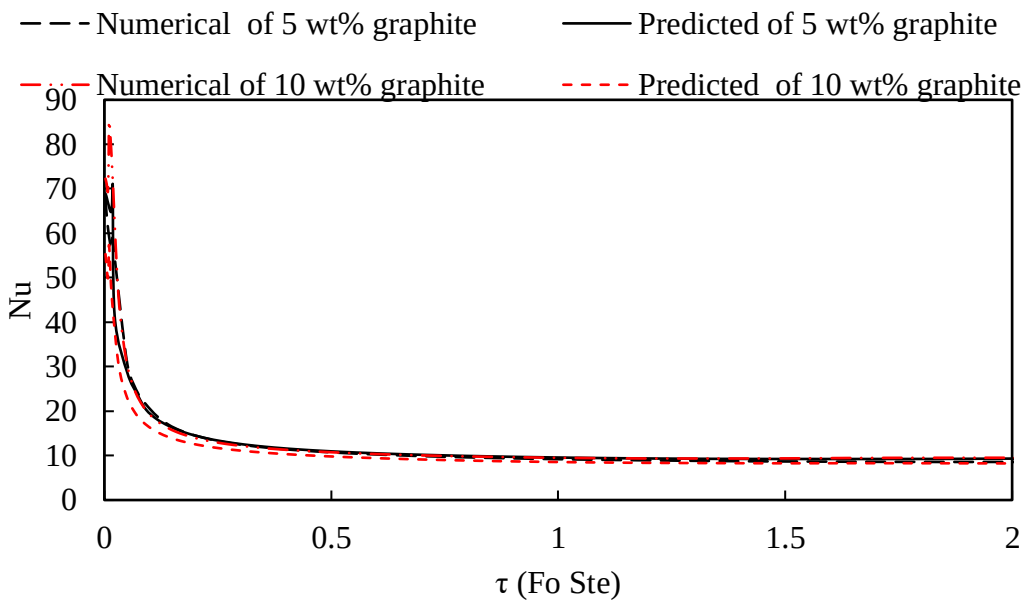

Figure 7-62: Comparison between the numerical and predicted results for the Nu number versus dimensionless time during the discharging process (TES with solar salt mixtures with graphite).

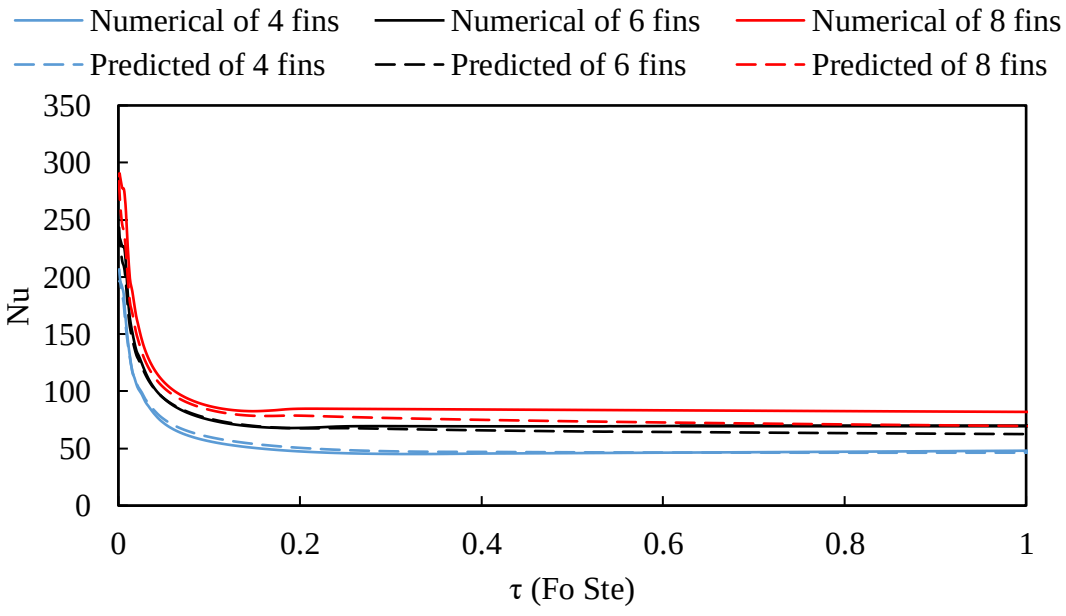

Figure 7-63: Comparison between the numerical and predicted results for the Nu number versus dimensionless time during the discharging process (TES with solar salt and fins).

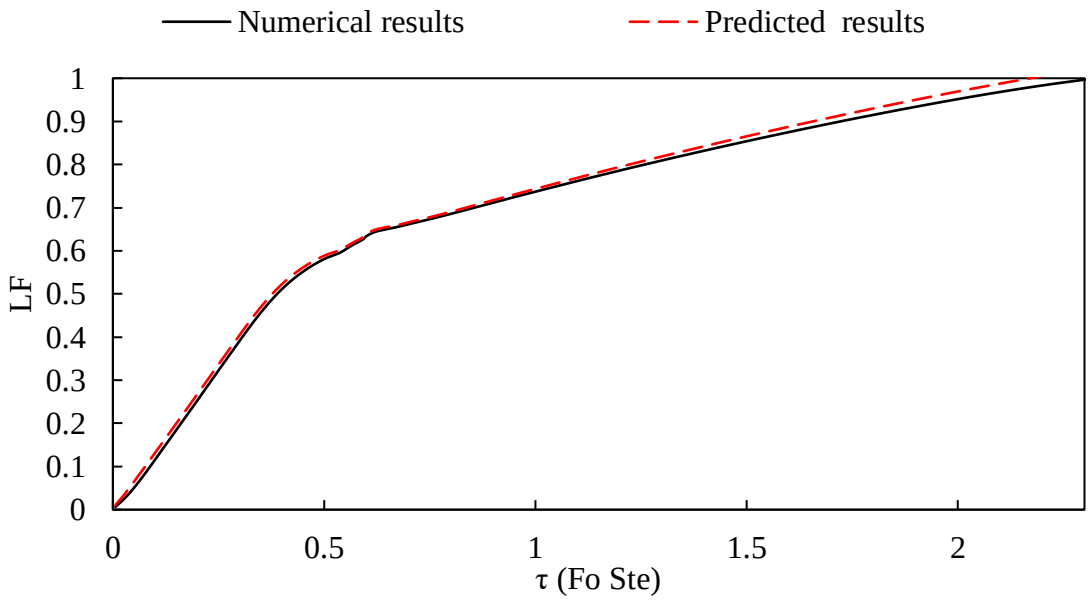

Figure 7-64: Comparison between the numerical and predicted results for the LF versus dimensionless time during the charging process (TES with the metal alloy).

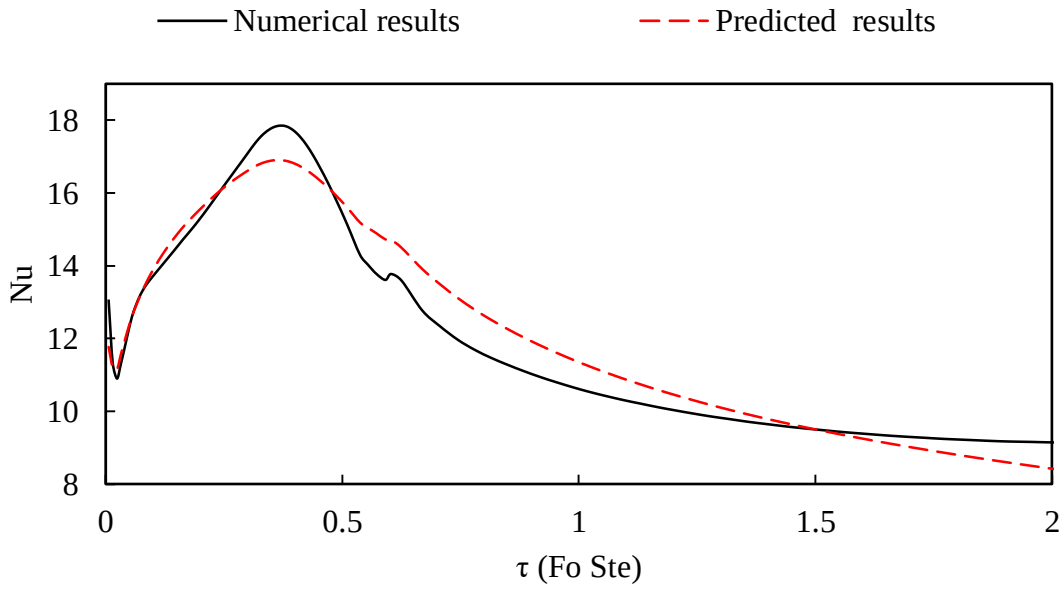

Figure 7-65: Comparison between the numerical and predicted results for the Nu number versus dimensionless time during the charging process (TES with the metal alloy).

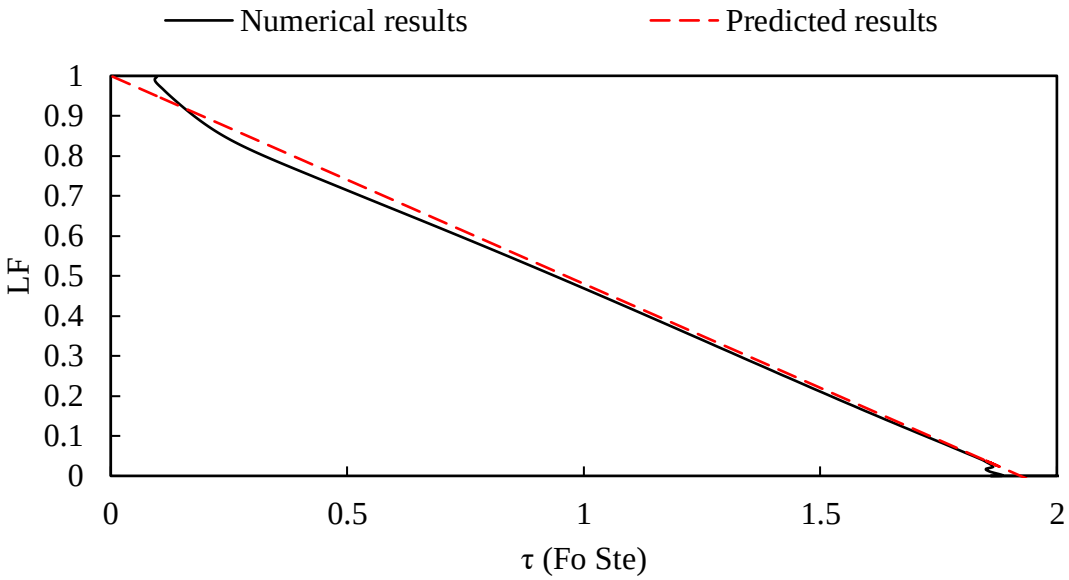

Figure 7-66: Comparison between the numerical and predicted results for the LF versus dimensionless time during the discharging process (TES with the metal alloy).

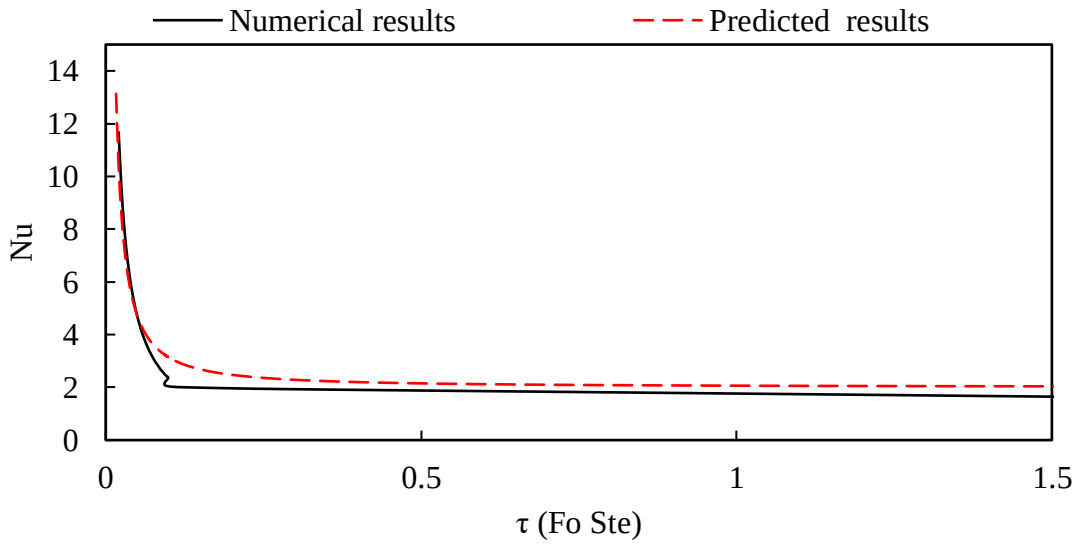

Figure 7-67: Comparison between the numerical and predicted results for the Nu number versus dimensionless time during the discharging process (TES with the metal alloy).

It can be seen that the derived correlations accurately predict the variations in the LF and Nu number in different TES systems with PCMs (solar salt and metal alloy) during charging and discharging processes. The maximum difference between the numerical results and predicted results was found to be 15%, which was evaluated using the following equation:

$$Accuracy = (Num_{results} - Pre_{results})/(Num_{results}) \times 100\ \% \qquad (7\text{-}23)$$

Here, Num and Pre are numerical and predicted results, respectively.

7.5 Conclusions

Numerical investigations were conducted and theoretical results on temperature variations in TES systems were compared with experimental results, thereby demonstrating the capability of numerical models to predict TES system performance within acceptable accuracy.

Numerical investigations were carried out to compare different TES systems with solar salt with the addition of graphite and in a container with fins as well as with the metal alloy. These investigations were performed for various charging/discharging power inputs and results were compared to data published in the existing literature. The comparison demonstrates that the modelling used in this work provides results close to those published and the obtained theoretical data was used to derive dimensionless correlations for predicting the LF and Nu number for TES systems with solar salt with the addition of graphite and in a container with fins as well as with the metal alloy.

Chapter 8 Conclusions and Future Work

8.1 Conclusions

The literature review was conducted on TES systems for medium- and low-temperature applications. The main challenges in the design of TES systems were related to the low thermal conductivity of PCMs and their cost, therefore, different thermal conductivity improvement techniques in TES systems were analysed, including the deployment of fins in the TES containers and using PCM additives. The use of low purity metal alloys was also considered as a promising strategy to reduce the overall cost of TES systems based on metal alloys as PCMs. Solar salt and Bi-Sn were selected as PCMs in this research due to their superior thermal properties and melting temperatures in the medium- and low-temperature ranges. For heat transfer intensification of solar salt, the use of fins and the addition of graphite were examined. For the metal alloys, the low purity metals of Bi and Sn were adopted to produce the alloy with a reduced cost.

Experimental investigations were performed to quantify the thermal properties of PCMs, including the melting and solidification points, latent heat and thermal conductivity. These were then used in the study of the thermal performance of TES systems. The TES systems tested were: with pure solar salt and a conventional container; with pure solar salt and fins; with pure solar salt and with 10 wt% of graphite; with the metal alloy. All experimental investigations were conducted using around 3 kg of solar salt (in TES systems with different configurations) and 11 kg of the metal alloy.

In addition, numerical investigations were carried out to validate the numerical models with the experimental results.

The validated models were used to carry out modelling of a wide range of TES systems with solar salt, its mixtures with graphite, and the metal alloy. These results were checked against published results, showing good agreement. The obtained numerical data from this stage was then used to derive dimensionless correlations to predict the LF and Nu number in the studied TES systems for use in the design process.

8.1.1 Heat transfer intensifications techniques tested

Graphite was found to considerably improve the thermal conductivity of solar salt in the TES system and concentrations at the levels of 5 and 10 wt% were required to produce these improvements. Increasing the percentage of graphite increases the thermal conductivity of pure solar salt from 0.318 W/m K to 1.062 W/m K and 1.455 W/m K for 5 wt% and 10 wt% of graphite, respectively. Increasing the percentage of graphite decreases the melting time of solar salt from 5 hours to 4.13 hours and 4 hours for 5 wt% and 10 wt% of graphite, respectively, when the input power is 25 W. However, increasing the graphite percentage decreases the latent heat of fusion and specific heat of the graphite mixtures, which reduces the amount of accumulated heat.

Increasing the number of fins in the container from 4 to 8 improves the thermal performance of the TES system with pure solar salt by decreasing the melting time from 4.28 to 3.9 hours when the input power is 25 W. However, it also reduces the amount of accumulated heat because of a reduction in the amount of solar salt in the TES system by up to 5.7%. It was found that using 6 and 8 fins speed up the melting process by 1% compared to using 5 wt% and 10 wt% of graphite. The solidification time of solar salt

decreases with an increase of the percentage of graphite in the mixture, from 5 to 4.5 hours and 4.3 hours using 5 wt% and 10 wt% graphite, respectively, at the discharging power of 25 W. In addition, the discharging time decreases from 4.6 to 4.3 hours with an increase in the number of fins from 4 to 8. The discharging rate in TES systems with the mixture with 5 wt% graphite is greater than in the TES with 6 fins by 3%. The TES system with 8 fins has the same solidification time as that with the mixture with 10 wt% graphite.

8.1.2 Metal alloy

The TES system with the metal alloy produces a much faster response at the low input power, which makes it the ideal candidate for low-temperature applications. It was shown that the melting and solidification times in such TES systems were approximately the same due to the high thermal conductivity of the metal alloy. The metal alloy TES system can accumulate 40% more energy in comparison to the solar salt TES system of the same size due to the high density of the metal alloy. Therefore, the metal alloy TES system can be considered as competitive against the solar salt TES system.

8.1.3 Numerical techniques

The use of the laminar flow model was found to be sufficient to predict the behaviour of TES systems of different configurations with solar salt and additives due to the low Rayleigh number (as also claimed in the literature). On the other hand, the conduction of the experimental work was necessary to assist the development of the numerical model for the TES systems with the metal alloy (due to the lack of experimental data). The turbulence SST-transition model was found to accurately predict the phase change

process in the TES system with the metal alloy, in which the low freestream turbulent environment was observed around the heat source (Pr number equal to 0.0139).

8.1.4 Dimensionless correlations

Good agreement was observed between the results using the derived correlations for the LF in TES systems with solar salt and metal alloy and those in the literature. The LF and Nu number in TES systems can be accurately predicted for TES systems with different configurations (conventional container and using different number of fins) and PCMs (solar salt and its mixtures with graphite). The derived correlations for LF and Nu number can also predict the behaviour of the TES systems with the metal alloy. The generated dimensionless correlations could be successfully used to design TES systems.

8.2 Future work

The findings in the current research indicate some interesting areas to investigate in future research and development work.

8.2.1 Heat transfer intensification techniques

Different additives could be used to improve the thermal properties of solar salt including Al_2O_3, ZnO, and CuO. Applying each additive with different percentages may yield substantial improvements beyond those achieved in this research using graphite. Therefore, it would be beneficial to expand the range of additives to enhance the thermal properties of solar salt.

Stainless steel fins were used in this work and shown to yield certain improvements in the thermal performance of TES systems. Different fin materials, such as aluminium, low

carbon steel, and copper, were not investigated. Other materials with higher thermal conductivity should be investigated in detail in the future.

Moreover, the combination of intensification techniques, such as the use of additives and fins and their configurations, could be investigated in future work

8.2.2 Metal alloy

Investigating various low purity metal alloys for application in TES systems for high- and medium-temperature applications should be carried out. As metals have very high thermal conductivity, the design of TES systems is simplified. The metal alloys can accumulate a greater amount of thermal energy in comparison to solar salt due to their high density (for the same size of TES systems).

8.2.3 Dimensionless correlations

The dimensionless correlations to predict the LF and Nu number in TES systems were derived for TES systems with different configurations and PCMs (the metal alloy, solar salt and its mixtures with graphite as an additive). It is desirable to expand these correlations to cover various types of metal alloys and other PCM materials with different types of additives.

References

[1] M. Kenisarin and K. Mahkamov, "Solar energy storage using phase change materials," *Renewable & Sustainable Energy Reviews,* vol. 11, pp. 1913–1965, 2007.

[2] S. D. Sharma, H. Kitano, and K. Sagara, "Phase change materials for low temperature solar thermal applications," *Res. Rep. Fac. Eng. Mie Univ,* vol. 29, no. 1, pp. 31-64, 2004.

[3] T. Kousksou, A. Jamil, T. El Rhafiki, and Y. Zeraouli, "Paraffin wax mixtures as phase change materials," *Solar Energy Materials and Solar Cells*, vol. 94, no. 12, pp. 2158-2165, 2010.

[4] Y. Yuan, N. Zhang, W. Tao, X. Cao, and Y. He, "Fatty acids as phase change materials: a review," *Renewable and Sustainable Energy Reviews*, vol. 29, pp. 482-498, 2014.

[5] N. Das, Y. Takata, M. Kohno, and S. Harish, "Melting of graphene based phase change nanocomposites in vertical latent heat thermal energy storage unit," *Applied Thermal Engineering*, vol. 107, pp. 101-113, 2016.

[6] R. Elbahjaoui, H. E. Qarnia, and M. E. Ganaoui, "Melting of nanoparticle-enhanced phase change material inside an enclosure heated by laminar heat transfer fluid flow," *The European Physical Journal Applied Physics*, vol. 74, no. 2, 2016.

[7] M. J. Hosseini, A. A. Ranjbar, K. Sedighi, and M. Rahimi, "A combined experimental and computational study on the melting behavior of a medium temperature phase change storage material inside shell and tube heat exchanger," *International Communications in Heat and Mass Transfer*, vol. 39, no. 9, pp. 1416-1424, 2012.

[8] Z. N. Meng and P. Zhang, "Experimental and numerical investigation of a tube-in-tank latent thermal energy storage unit using composite PCM," *Applied Energy*, vol. 190, pp. 524-539, 2017.

[9] J. M. Mahdi and E. C. Nsofor, "Solidification enhancement in a triplex-tube latent heat energy storage system using nanoparticles-metal foam combination," *Energy,* vol. 126, pp. 501-512, 2017.

[10] B. Buonomo, D. Ercole, O. Manca, and S. Nardini, "Numerical investigation on thermal behaviors of two-dimensional latent thermal energy storage with PCM and aluminum foam," *Journal of Physics: Conference Series,* vol. 796, p. 012031, 2017.

[11] R. Elbahjaoui and H. El Qarnia, "Transient behavior analysis of the melting of nanoparticle-enhanced phase change material inside a rectangular latent heat storage unit," *Applied Thermal Engineering,* vol. 112, pp. 720-738, 2017.

[12] S. Seddegh, X. Wang, and A. D. Henderson, "A comparative study of thermal behaviour of a horizontal and vertical shell-and-tube energy storage using phase change materials," *Applied Thermal Engineering,* vol. 93, pp. 348-358, 2016.

[13] M. Kenisarin and K. Mahkamov, "Salt hydrates as latent heat storage materials: Thermophysical properties and costs," *Solar Energy Materials and Solar Cells,* vol. 145, pp. 255-286, 2016.

[14] P. D. J. Myers, T. E. Alam, R. Kamal, D. Y. Goswami, and E. Stefanakos, "Nitrate salts doped with CuO nanoparticles for thermal energy storage with improved heat transfer," *Applied Energy,* vol. 165, pp. 225-233, 2016.

[15] K. Pielichowska and K. Pielichowski, "Phase change materials for thermal energy storage," *Progress in materials science,* vol. 65, pp. 67-123, 2014.

[16] M. Lachheb, A. Adili, F. Albouchi, F. Mzali, and S. B. Nasrallah, "Thermal properties improvement of lithium nitrate/graphite composite phase change materials," *Applied Thermal Engineering,* vol. 102, pp. 922-931, 2016.

[17] V. M. B. Nunes, C. S. Queirós, M. J. V. Lourenço, F. J. V. Santos, and N. d. C. A. Castro, "Molten salts as engineering fluids – A review: Part I. Molten alkali nitrates," *Applied Energy,* vol. 183, pp. 603-611, 2016.

[18] C. McCulley and S. Vyazovkin, "Crystallization of ionic salts for calibration of differential scanning calorimeters," *Thermochimica Acta,* vol. 640, pp. 62-65, 2016.

[19] R. W. Carling, "Heat capacities of $NaNO_3$ and KNO_3 from 350 to 800 K," *Thermochimica Acta,* vol. 60, no. 3, pp. 265-275, 1983.

[20] B. K. Purohit and V. S. Sistla, "Crystallization of inorganic salt hydrates in polymeric foam for thermal energy storage application," *Journal of Energy Storage,* vol. 12, pp. 196-201, 2017.

[21] J. M. Mahdi and E. C. Nsofor, "Solidification of a PCM with nanoparticles in triplex-tube thermal energy storage system," *Applied Thermal Engineering,* vol. 108, pp. 596-604, 2016.

[22] Y. Liu and Y. Yang, "Use of nano-α-Al_2O_3 to improve binary eutectic hydrated salt as phase change material," *Solar Energy Materials and Solar Cells,* vol. 160, pp. 18-25, 2017.

[23] C. Y. Zhao, Y. Ji, and Z. Xu, "Investigation of the $Ca(NO_3)_2$–$NaNO_3$ mixture for latent heat storage," *Solar Energy Materials and Solar Cells,* vol. 140, pp. 281-288, 2015.

[24] D. Zhou and P. Eames, "Thermal characterisation of binary sodium/lithium nitrate salts for latent heat storage at medium temperatures," *Solar Energy Materials and Solar Cells,* vol. 157, pp. 1019-1025, 2016.

[25] D. Zhou and P. Eames, "A study of a eutectic salt of lithium nitrate and sodium chloride (87–13%) for latent heat storage," *Solar Energy Materials and Solar Cells,* vol. 167, pp. 157-161, 2017.

[26] X. Chen, C. Wang, Y. Wu, B. Liu, and C. Ma, "Characteristics of the mixed convection heat transfer of molten salts in horizontal square tubes," *Solar Energy,* vol. 147, pp. 248-256, 2017.

[27] J. Lu, T. Yu, J. Ding, and Y. Yuan, "Thermal storage performance of molten salt thermocline system with packed phase change bed," *Energy Conversion and Management,* vol. 102, pp. 267-274, 2015.

[28] Y.-t. Wu, Y. Li, Y.-w. Lu, H.-f. Wang, and C.-f. Ma, "Novel low melting point binary nitrates for thermal energy storage applications," *Solar Energy Materials and Solar Cells,* vol. 164, pp. 114-121, 2017.

[29] Á. G. Fernández and J. C. Gomez-Vidal, "Thermophysical properties of low cost lithium nitrate salts produced in northern Chile for thermal energy storage," *Renewable Energy,* vol. 101, pp. 120-125, 2017.

[30] Y. Y. Chen and C. Y. Zhao, "Thermophysical properties of $Ca(NO_3)_2$ -$NaNO_3$ -KNO_3 mixtures for heat transfer and thermal storage," *Solar Energy,* vol. 146, pp. 172-179, 2017.

[31] Y. Jin, J. Cheng, X. An, T. Su, P. Zhang, and Z. Li, "Accurate viscosity measurement of nitrates/nitrites salts for concentrated solar power," *Solar Energy,* vol. 137, pp. 385-392, 2016.

[32] W. M. Madgin and H. V. A. Briscoe, "CCCXLIV.—The melting-point (solidus) curve for mixtures of potassium nitrate and sodium nitrate," *Journal of the Chemical Society, Transactions,* vol. 127, pp. 2914-2916, 1925.

[33] C. Martin, T. Bauer, and H. Müller-Steinhagen, "An experimental study of a non-eutectic mixture of KNO_3 and $NaNO_3$ with a melting range for thermal energy storage," *Applied Thermal Engineering,* vol. 56, no. 1-2, pp. 159-166, 2013.

[34] C. Kramer and C. J. Wilson, "The phase diagram of $NaNO_3$—KNO_3," *Thermochimica Acta,* vol. 42, no. 3, pp. 253-264, 1980.

[35] E. W. Gabisa and A. Aman, "Characterization and experimental investigation of $NaNO_3$: KNO_3 as solar thermal energy storage for potential cooking application," *Journal of Solar Energy,* vol. 2016, 2016.

[36] R. Serrano-López, J. Fradera, and S. Cuesta-López, "Molten salts database for energy applications," *Chemical Engineering and Processing: Process Intensification,* vol. 73, pp. 87-102, 2013.

[37] A. B. Zavoico, "Solar power tower design basis document, revision 0; Topical," Sandia National Labs.2001.

[38] D. A. Nissen, "Thermophysical properties of the equimolar mixture sodium nitrate-potassium nitrate from 300 to 600. degree. C," *Journal of Chemical and Engineering Data,* vol. 27, no. 3, pp. 269-273, 1982.

[39] R. DiGuilio and A. Teja, "A rough hard-sphere model for the thermal conductivity of molten salts," *International journal of thermophysics,* vol. 13, no. 5, pp. 855-871, 1992.

[40] N. Boerema, G. Morrison, R. Taylor, and G. Rosengarten, "Liquid sodium versus Hitec as a heat transfer fluid in solar thermal central receiver systems," *Solar Energy,* vol. 86, no. 9, pp. 2293-2305, 2012.

[41] G. J. Janz, C. B. Allen, N. Bansal, R. Murphy, and R. Tomkins, "Physical properties data compilations relevant to energy storage. II. Molten salts: data on single and multi-component salt systems," National standard reference data system1979.

[42] J. E. Pacheco *et al., Results of molten salt panel and component experiments for solar central receivers: cold fill, freeze/ thaw, thermal cycling and shock, and instrumentation tests*. 1995.

[43] Y. Luo, X. Du, A. Awad, and D. Wen, "Thermal energy storage enhancement of a binary molten salt via in-situ produced nanoparticles," *International Journal of Heat and Mass Transfer,* vol. 104, pp. 658-664, 2017.

[44] Y.-t. Wu, Y. Li, N. Ren, and C.-f. Ma, "Improving the thermal properties of $NaNO_3$ -KNO_3 for concentrating solar power by adding additives," *Solar Energy Materials and Solar Cells,* vol. 160, pp. 263-268, 2017.

[45] M. Chieruzzi, G. F. Cerritelli, A. Miliozzi, J. M. Kenny, and L. Torre, "Heat capacity of nanofluids for solar energy storage produced by dispersing oxide nanoparticles in nitrate salt mixture directly at high temperature," *Solar Energy Materials and Solar Cells,* vol. 167, pp. 60-69, 2017.

[46] P. Gimenez-Gavarrell and S. Fereres, "An experimental study of the effect of SiO_2 nanoparticles on the phase change characteristics of KNO_3-$NaNO_3$ mixtures for thermal energy storage," presented at the ASME 2015 International Mechanical Engineering Congress and Exposition, Houston, Texas, USA, 2015.

[47] Z. Acem, J. Lopez, and E. Palomo Del Barrio, "KNO_3/$NaNO_3$ – Graphite materials for thermal energy storage at high temperature: Part I. – Elaboration methods and thermal properties," *Applied Thermal Engineering,* vol. 30, no. 13, pp. 1580-1585, 2010.

[48] J. Xiao, J. Huang, P. Zhu, C. Wang, and X. Li, "Preparation, characterization and thermal properties of binary nitrate salts/expanded graphite as composite phase change material," *Thermochimica Acta,* vol. 587, pp. 52-58, 2014.

[49] J. Lopez, Z. Acem, and E. Palomo Del Barrio, "KNO_3/$NaNO_3$ – Graphite materials for thermal energy storage at high temperature: Part II. – Phase transition properties," *Applied Thermal Engineering,* vol. 30, no. 13, pp. 1586-1593, 2010.

[50] S. Pincemin, R. Olives, X. Py, and M. Christ, "Highly conductive composites made of phase change materials and graphite for thermal storage," *Solar Energy Materials & Solar Cells,* vol. 92, no. 6, pp. 603–613, 2008.

[51] W.-D. Steinmann and R. Tamme, "Latent heat storage for solar steam systems," *Journal of solar energy engineering,* vol. 130, no. 1, 2007.

[52] Q. Yu, Y. Lu, C. Zhang, Y. Wu, and B. Sunden, "Research on thermal properties of novel silica nanoparticle/binary nitrate/expanded graphite composite heat storage blocks," *Solar Energy Materials and Solar Cells,* vol. 201, 2019.

[53] C. W. Foong, J. E. Hustad, J. Løvseth, and O. J. Nydal, "Numerical study of a high temperature latent heat storage (200-300 ^{0}C) using eutectic nitrate salt of sodium nitrate and potassium nitrate," in *COMSOL Conference*, Paris, 2010.

[54] M. D. Muhammad and O. Badr, "Performance of a finned, latent-heat storage system for high temperature applications," *Applied Thermal Engineering,* vol. 116, pp. 799-810, 2017.

[55] J. Vogel, J. Felbinger, and M. Johnson, "Natural convection in high temperature flat plate latent heat thermal energy storage systems," *Applied Energy,* vol. 184, pp. 184-196, 2016.

[56] D. Laing, T. Bauer, W. Steinmann, and D. Lehmann, "Advanced high temperature latent heat storage system–design and test results," in *The 11th International Conference on Thermal Energy Storage–Effstock*, Sweden, 2009.

[57] M. Augspurger, K. K. Choi, and H. S. Udaykumar, "Optimizing fin design for a PCM-based thermal storage device using dynamic Kriging," *International Journal of Heat and Mass Transfer,* vol. 121, pp. 290-308, 2018.

[58] A. H. Tesfay, F. Y. Hagos, K. G. Yohannes, O. J. Nydal, and M. B. Kahsay, "Preparing side charging of PCM storage: theoretical and experimental investigation," *IOP Conference Series: Materials Science and Engineering,* vol. 100, 2015.

[59] C. Guo and W. Zhang, "Numerical simulation and parametric study on new type of high temperature latent heat thermal energy storage system," *Energy Conversion and Management,* vol. 49, no. 5, pp. 919-927, 2008.

[60] S. A. Mohamed *et al.*, "A review on current status and challenges of inorganic phase change materials for thermal energy storage systems," *Renewable and Sustainable Energy Reviews,* vol. 70, pp. 1072–1089, 2017.

[61] X.-H. Yang, S.-C. Tan, and J. Liu, "Numerical investigation of the phase change process of low melting point metal," *International Journal of Heat and Mass Transfer,* vol. 100, pp. 899-907, 2016.

[62] F. Ma and P. Zhang, "Investigation on the performance of a high-temperature packed bed latent heat thermal energy storage system using Al-Si alloy," *Energy Conversion and Management,* vol. 150, pp. 500-514, 2017.

[63] T. Bouhal, S. ED-Din fertahi, T. Kousksou, and A. Jamil, "CFD thermal energy storage enhancement of PCM filling a cylindrical cavity equipped with submerged heating sources," *Journal of Energy Storage,* vol. 18, pp. 360-370, 2018.

[64] X.-H. Yang, S.-C. Tan, Z.-Z. He, Y.-X. Zhou, and J. Liu, "Evaluation and optimization of low melting point metal PCM heat sink against ultra-high thermal shock," *Applied Thermal Engineering,* vol. 119, pp. 34-41, 2017.

[65] P. Blanco-Rodríguez *et al.,* "Experiments on alab scale TES unit using eutectic metal alloy as PCM," *Energy Procedia,* vol. 69, pp. 769-778, 2015.

[66] D. Gonzalez-Nino *et al.,* "Experimental evaluation of metallic phase change materials for thermal transient mitigation," *International Journal of Heat and Mass Transfer,* vol. 116, pp. 512-519, 2018.

[67] X.-H. Yang, S.-C. Tan, Y.-J. Ding, L. Wang, J. Liu, and Y.-X. Zhou, "Experimental and numerical investigation of low melting point metal based PCM heat sink with internal fins," *International Communications in Heat and Mass Transfer,* vol. 87, pp. 118-124, 2017.

[68] D. Gonzalez-Nino, L. M. Boteler, N. R. Jankowski, D. Ibitayo, and P. O. Quintero, "Voiding effects on the thermal response of metallic phase change materials under pulsed power loading," presented at the Proceedings of the ASME 2017 International Technical Conference and Exhibition on Packaging and Integration of Electronic and Photonic Microsystems InterPACK2017, San Francisco, California, USA, 2017.

[69] O. Ben-David, A. Levy, B. Mikhailovich, and A. Azulay, "3D numerical and experimental study of gallium melting in a rectangular container," *International Journal of Heat and Mass Transfer,* vol. 67, pp. 260-271, 2013.

[70] O. Ben-David, A. Levy, B. Mikhailovich, and A. Azulay, "Impact of rotating permanent magnets on gallium melting in an orthogonal container," *International Journal of Heat and Mass Transfer,* vol. 81, pp. 373-382, 2015.

[71] L.-W. Fan, Y.-Y. Wu, Y.-Q. Xiao, Y. Zeng, Y.-L. Zhang, and Z.-T. Yu, "Transient performance of a thermal energy storage-based heat sink using a liquid metal as

the phase change material," *Applied Thermal Engineering,* vol. 109, pp. 746-750, 2016.

[72] T. Kousksou, M. Mahdaoui, M. Hlimi, R. El Alaiji, and T. El Rhafiki, "Latent energy storage: Melting process around heating cylinders," *Case Studies in Thermal Engineering,* vol. 8, pp. 128-140, 2016.

[73] N. Lorenzin and A. Abánades, "A review on the application of liquid metals as heat transfer fluid in concentrated solar power technologies," *International Journal of Hydrogen Energy,* vol. 41, no. 17, pp. 6990-6995, 2016.

[74] S. P. Singh, B. K. Barman, and P. Kumar, "Cu-Bi alloys with high volume fraction of Bi: A material potentially suitable for thermal surge protection and energy storage," *Materials Science and Engineering: A,* vol. 677, pp. 140-152, 2016.

[75] P. Aigang, W. Junbiao, and Z. Xianjie, "Prediction of Melting Temperature and Latent Heat for Low-melting Metal PCMs," *Rare Metal Materials and Engineering,* vol. 45, no. 4, pp. 874-880, 2016.

[76] H. Ge, H. Li, S. Mei, and J. Liu, "Low melting point liquid metal as a new class of phase change material: An emerging frontier in energy area," *Renewable and Sustainable Energy Reviews,* vol. 21, pp. 331-346, 2013.

[77] A. M. Shamseldin *et al.*, "A review on current status and challenges of inorganic phase change materials for thermal energy storage systems," *Renewable and Sustainable Energy Reviews,* vol. 70, pp. 1072–1089, 2017.

[78] H. Li and J. Liu, "Revolutionizing heat transport enhancement with liquid metals: Proposal of a new industry of water-free heat exchangers," *Frontiers in Energy,* journal article vol. 5, no. 1, pp. 20-42, March 01 2011.

[79] A. G. Wee, R. L. Schneider, and S. A. Aquilino, "Use of low fusing alloy in dentistry," *The Journal of Prosthetic Dentistry,* vol. 80, no. 5, pp. 540-545, 1998.

[80] K. Zhou, Z. Tang, Y. Lu, T. Wang, H. Wang, and T. Li, "Composition, microstructure, phase constitution and fundamental physicochemical properties of low-melting-point multi-component eutectic alloys," *Journal of Materials Science & Technology,* vol. 33, no. 2, pp. 131-154, 2017.

[81] L. Wang and J. Liu, "Liquid metal material genome: Initiation of a new research track towards discovery of advanced energy materials," *Frontiers in Energy,* vol. 7, no. 3, pp. 317-332, 2013.

[82] R. Raud, R. Jacob, F. Bruno, G. Will, and T. A. Steinberg, "A critical review of eutectic salt property prediction for latent heat energy storage systems," *Renewable and Sustainable Energy Reviews,* vol. 70, pp. 936-944, 2017.

[83] B. Ding, X. Zhu, H. Wang, X.-Y. He, and Y. Tan, "Experimental study on phase change heat transfer characteristics of alloys," *International Journal of Heat and Mass Transfer,* vol. 105, pp. 261-269, 2017.

[84] J. Nieto-Maestre, I. Iparraguirre-Torres, Z. A. Velasco, I. Kaltzakorta, and M. M. Zubieta, "Novel metallic alloys as phase change materials for heat storage in direct steam generation applications," presented at the AIP Conference Proceedings, 2016.

[85] R. Boussaa *et al.*, "Macrosegregations in Sn-3 wt%Pb alloy solidification: Experimental and 3D numerical simulation investigations," *International Journal of Heat and Mass Transfer,* vol. 100, pp. 680-690, 2016.

[86] Z. Wang, Z. Sun, X. Wang, H. Zhang, and S. Jiang, "Effects of element addition on liquid phase separation of Bi-Ga immiscible alloy: Characterization by electrical resistivity and coordination tendency," *Materials & Design,* vol. 114, pp. 111-115, 2017.

[87] M. I. I. Ramli, M. A. A. M. Salleh, R. M. Said, and N. Saud, "Thermal and mechanical properties of Sn-Cu-Ni-XSiC composite solder," in *AIP Conference Proceedings*, 2017, vol. 1835, p. 020027.

[88] S. Amares, M. N. E. Efzan, and T. C. Yap, "Characterizations of physical properties of Sn-Bi solder alloy," *Advanced Materials Research,* vol. 845, pp. 261-265, 2013.

[89] X. Hu, Y. Li, Y. Liu, and Z. Min, "Developments of high strength Bi-containing Sn0.7Cu lead-free solder alloys prepared by directional solidification," *Journal of Alloys and Compounds,* vol. 625, pp. 241-250, 2015.

[90] C. L. Chuang, L. C. Tsao, H. K. Lin, and L. P. Feng, "Effects of small amount of active Ti element additions on microstructure and property of Sn3.5Ag0.5Cu solder," *Materials Science and Engineering: A,* vol. 558, pp. 478-484, 2012.

[91] A. A. El-Daly and A. M. El-Taher, "Evolution of thermal property and creep resistance of Ni and Zn-doped Sn–2.0Ag–0.5Cu lead-free solders," *Materials & Design,* vol. 51, pp. 789-796, 2013.

[92] H. Okamoto, "Al-Ni (Aluminum-Nickel)," *Journal of Phase Equilibria and Diffusion*, vol. 25, no. 4, 2004.

[93] Z. Mei, f. Hua, and J. Glazer, "Low temperature soldering," in *The IEEE/CPMT International Electronics Manufacturing Technology (IEMT) Symposium* 1997, pp. 463-476.

[94] H. R. Kotadia, P. D. Howes, and S. H. Mannan, "A review: On the development of low melting temperature Pb-free solders," *Microelectronics Reliability*, vol. 54, no. 6-7, pp. 1253-1273, 2014.

[95] Y. Plevachuk, V. Sklyarchuk, G. Gerbeth, S. Eckert, and R. Novakovic, "Surface tension and density of liquid Bi–Pb, Bi–Sn and Bi–Pb–Sn eutectic alloys," *Surface Science,* vol. 605, no. 11-12, pp. 1034-1042, 2011.

[96] R. M. Shalaby, "Effect of silver and indium addition on mechanical properties and indentation creep behavior of rapidly solidified Bi–Sn based lead-free solder alloys," *Materials Science and Engineering: A,* vol. 560, pp. 86-95, 2013.

[97] F. Yang, L. Zhang, Z.-q. Liu, S.-j. Zhong, J. Ma, and L. Bao, "Properties and microstructures of Sn-Bi-X lead-free solders," *Advances in Materials Science and Engineering,* vol. 2016, pp. 1-15, 2016.

[98] s.-w. Chen, c.-c. Lin, and c.-m. Chen, "Determination of the melting and solidification characteristics of solders using differential scanning calorimetry," *Metallurgical and Materials Transactions A,* vol. 29, no. 7, pp. 1965–1972, 1998.

[99] Z. Mei and J. W. Morris, "Characterization of eutectic Sn-Bi solder joints," *Journal ot Electronic Materials,* vol. 21, no. 6, pp. 599-607, 1992.

[100] M. Mhadhbi, *Phase change materials and their applications*. BoD–Books on Demand, 2018.

[101] A. Dinker, M. Agarwal, and G. D. Agarwal, "Heat storage materials, geometry and applications: A review," *Journal of the Energy Institute,* vol. 90, no. 1, pp. 1-11, 2017.

[102] E. Tumilowicz, C. L. Chan, P. Li, and B. Xu, "An enthalpy formulation for thermocline with encapsulated PCM thermal storage and benchmark solution using the method of characteristics," *International Journal of Heat and Mass Transfer,* vol. 79, pp. 362-377, 2014.

[103] K. Nithyanandam and R. Pitchumani, "Optimization of an encapsulated phase change material thermal energy storage system," *Solar Energy,* vol. 107, pp. 770-788, 2014.

[104] A. d. Gracia and L. F. Cabeza, "Numerical simulation of a PCM packed bed system: A review," *Renewable and Sustainable Energy Reviews,* vol. 69, pp. 1055-1053, 2017.

[105] K. A. R. Ismail and J. R. Stuginsky, "A parametric study on possible fixed bed models for pcm and sensible heat storage," *Applied Thermal Engineering,* vol. 19, no. 7, pp. 757-788, 1999.

[106] G. Manfrida, R. Secchi, and K. Stańczyk, "Modelling and simulation of phase change material latent heat storages applied to a solar-powered organic rankine cycle," *Applied Energy,* vol. 179, pp. 378-388, 2016.

[107] J. P. Bédécarrats, J. Castaing-Lasvignottes, F. Strub, and J. P. Dumas, "Study of a phase change energy storage using spherical capsules. Part II: Numerical modelling," *Energy Conversion and Management,* vol. 50, no. 10, pp. 2537-2546, 2009.

[108] A. Y. Uzan, Y. Kozak, Y. Korin, I. Harary, H. Mehling, and G. Ziskind, "A novel multi-dimensional model for solidification process with supercooling," *International Journal of Heat and Mass Transfer,* vol. 106, pp. 91-102, 2017.

[109] A. Esen and S. Kutluay, "A numerical solution of the Stefan problem with a Neumann-type boundary condition by enthalpy method," *Applied Mathematics and Computation,* vol. 148, no. 2, pp. 321-329, 2004.

[110] S. S. Chandel and T. Agarwal, "Review of cooling techniques using phase change materials for enhancing efficiency of photovoltaic power systems," *Renewable and Sustainable Energy Reviews,* vol. 73, pp. 1342-1351, 2017.

[111] J. Borderon, J. Virgone, and R. Cantin, "Modeling and simulation of a phase change material system for improving summer comfort in domestic residence," *Applied Energy,* vol. 140, pp. 288-296, 2015.

[112] Q. Zhang, Y. Huo, and Z. Rao, "Numerical study on solid–liquid phase change in paraffin as phase change material for battery thermal management," *Science Bulletin,* vol. 61, no. 5, pp. 391-400, 2016.

[113] M. Kenisarin and K. Mahkamov, "Passive thermal control in residential buildings using phase change materials," *Renewable and Sustainable Energy Reviews,* vol. 55, pp. 371-398, 2016.

[114] G. Alva, Y. Lin, L. Liu, and G. Fang, "Synthesis, characterization and applications of microencapsulated phase change materials in thermal energy storage: A review," *Energy and Buildings,* vol. 144, pp. 276-294, 2017.

[115] R. K. Sharma, P. Ganesan, V. V. Tyagi, H. S. C. Metselaar, and S. C. Sandaran, "Developments in organic solid–liquid phase change materials and their applications in thermal energy storage," *Energy Conversion and Management,* vol. 95, pp. 193–228, 2015.

[116] Y. E. Milián, A. Gutiérrez, M. Grágeda, and S. Ushak, "A review on encapsulation techniques for inorganic phase change materials and the influence on their thermophysical properties," *Renewable and Sustainable Energy Reviews,* vol. 73, pp. 983-999, 2017.

[117] M. M. A. Khan, R. Saidur, and F. A. Al-Sulaiman, "A review for phase change materials (PCMs) in solar absorption refrigeration systems," *Renewable and Sustainable Energy Reviews,* vol. 76, pp. 105-137, 2017.

[118] Z. Khan, Z. Khan, and A. Ghafoor, "A review of performance enhancement of PCM based latent heat storage system within the context of materials, thermal stability and compatibility," *Energy Conversion and Management,* vol. 115, pp. 132-158, 2016.

[119] T. Khadiran, M. Z. Hussein, Z. Zainal, and R. Rusli, "Advanced energy storage materials for building applications and their thermal performance characterization: A review," *Renewable and Sustainable Energy Reviews,* vol. 57, pp. 916-928, 2016.

[120] J. P. d. Cunha and P. Eames, "Thermal energy storage for low and medium temperature applications using phase change materials – A review," *Applied Energy,* vol. 177, pp. 227–238, 2016.

[121] M. Kuta, D. Matuszewska, and T. M. Wójcik, "Reasonableness of phase change materials use for air conditioning – a short review," *E3S Web of Conferences,* vol. 14, p. 01033, 2017.

[122] S. E. Kalnæs and B. P. Jelle, "Phase change materials and products for building applications: A state-of-the-art review and future research opportunities," *Energy and Buildings,* vol. 94, pp. 150-176, 2015.

[123] N. Soares, A. R. Gaspar, P. Santos, and J. J. Costa, "Experimental evaluation of the heat transfer through small PCM-based thermal energy storage units for building applications," *Energy and Buildings,* vol. 116, pp. 18-34, 2016.

[124] M. A. Wahid, S. E. Hosseini, H. M. Hussen, H. J. Akeiber, S. N. Saud, and A. T. Mohammad, "An overview of phase change materials for construction architecture thermal management in hot and dry climate region," *Applied Thermal Engineering,* vol. 112, pp. 1240-1259, 2017.

[125] T. Nomura and T. Akiyama, "High-temperature latent heat storage technology to utilize exergy of solar heat and industrial exhaust heat," *International Journal of Energy Research,* vol. 41, no. 2, pp. 240-251, 2017.

[126] Y. Zheng *et al.,* "Experimental and computational study of thermal energy storage with encapsulated $NaNO_3$ for high temperature applications," *Solar Energy,* vol. 115, pp. 180-194, 2015.

[127] Z. Fan, I. C. A. Ferreira, and A. H. Mosaffa, "Numerical modelling of high temperature latent heat thermal storage for solar application combining with double-effect H_2O/LiBr absorption refrigeration system," *Solar Energy,* vol. 110, pp. 398-409, 2014.

[128] S. S. M. Tehrani, R. A. Taylor, P. Saberi, and G. Diarce, "Design and feasibility of high temperature shell and tube latent heat thermal energy storage system for solar thermal power plants," *Renewable Energy,* vol. 96, pp. 120-136, 2016.

[129] C. E. Andraka, A. M. Kruizenga, B. A. Hernandez-Sanchez, and E. N. Coker, "Metallic phase change material thermal storage for dish stirling," *Energy Procedia,* vol. 69, pp. 726-736, 2015.

[130] K. Bhagat and S. K. Saha, "Numerical analysis of latent heat thermal energy storage using encapsulated phase change material for solar thermal power plant," *Renewable Energy,* vol. 95, pp. 323-336, 2016.

[131] S. Kaguei, B. Shiozawa, and N. Wakao, "Dispersion-concentric model for packed bed heat transfer," *Chemical Engineering Science,* vol. 32, no. 5, pp. 507-513, 1976.

[132] H. Peng, H. Dong, and X. Ling, "Thermal investigation of PCM-based high temperature thermal energy storage in packed bed," *Energy Conversion and Management,* vol. 81, pp. 420-427, 2014.

[133] L. F. Cabeza *et al.*, "Immersion corrosion tests on metal-salt hydrate pairs used for latent heat storage in the 32 to 36°C temperature range" *material and corrosion,* vol. 53, pp. 902-907, 2002.

[134] L. F. Cabeza *et al.*, "Immersion corrosion tests on metal-salt hydrate pairs used for latent heat storage in the 32 to 36°C temperature range," *Material and Corrosion,* vol. 52, pp. 748-754, 2001.

[135] L. F. Cabeza, J. Roca, M. Nogués, H. Mehling, and S. Hiebler, "Immersion corrosion tests on metal-salt hydrate pairs used for latent heat storage in the 48 to 58°C temperature range," *Materials and Corrosion,* vol. 53, pp. 902-907, 2002.

[136] A. J. Farrell, B. Norton, and D. M. Kennedy, "Corrosive effects of salt hydrate phase change materials used with aluminium and copper," *Journal of Materials Processing Technology*, vol. 175, no. 1-3, pp. 198-205, 2006.

[137] P. Moreno *et al.*, "Corrosion of metal and metal alloy containers in contact with phase change materials (PCM) for potential heating and cooling applications," *Applied Energy*, vol. 125, pp. 238-245, 2014.

[138] A. Vasu *et al.*, "Corrosion effect of phase change materials in solar thermal energy storage application," *Renewable and Sustainable Energy Reviews*, vol. 76, pp. 19-33, 2017.

[139] A. Solé, L. Miró, C. Barreneche, I. Martorell, and L. F. Cabeza, "Corrosion of metals and salt hydrates used for thermochemical energy storage," *Renewable Energy,* vol. 75, pp. 519-523, 2015.

[140] F. C. Porosini, "Salt hydrates used for latent heat storage: Corrosion of metals and reliability of thermal performance," *Solar Energy,* vol. 41, no. 2, pp. 193-197, 1988.

[141] E. Oró, L. Miró, C. Barreneche, I. Martorell, M. M. Farid, and L. F. Cabeza, "Corrosion of metal and polymer containers for use in PCM cold storage," *Applied Energy,* vol. 109, pp. 449-453, 2013.

[142] A. Abhat, "Low temperature latent heat thermal energy storage: Heat storage materials," *Solar Energy,* vol. 30, no. 4, pp. 313-332, 1983.

[143] V. Danielik, P. Šoška, and K. Felgerová, "Corrosive effects of nitrate-containing phase change materials used with copper," *Acta Chimica Slovaca,* vol. 9, no. 2, pp. 75-83, 2016.

[144] V. Danielik, P. Šoška, K. Felgerová, and M. Zemanová, "The corrosion of carbon steel in nitrate hydrates used as phase change materials," *Materials and Corrosion,* vol. 68, no. 4, pp. 416-422, 2017.

[145] S. Ushak, P. Marín, Y. Galazutdinova, L. F. Cabeza, M. M. Farid, and M. Grágeda, "Compatibility of materials for macroencapsulation of inorganic phase change materials: Experimental corrosion study," *Applied Thermal Engineering,* vol. 107, pp. 410-419, 2016.

[146] N. Yoneda and S. Takanashi, "Eutectic mixtures for solar heat storage," *Solar Energy,* vol. 21, no. 1, pp. 61-63, 1978.

[147] M. Kenisarin, "Short-term storage of solar energy. 1. Low temperature phase-change materials," *Geliotekhnika,* vol. 29, no. 2, pp. 46-64, 1993.

[148] K. Nagano, K. Ogawa, T. Mochida, K. Hayashi, and H. Ogoshi, "Performance of heat charge/discharge of magnesium nitrate hexahydrate and magnesium chloride hexahydrate mixture to a single vertical tube for a latent heat storage system," *Applied Thermal Engineering,* vol. 24, no. 2-3, pp. 209-220, 2004.

[149] L. F. Cabeza, J. Roca, M. Nogueés, H. Mehling, and S. Hiebler, "Long term immersion corrosion tests on metal-PCM pairs used for latent heat storage in the 24 to 29°C temperature range," *Materials and Corrosion,* vol. 56, no. 1, pp. 33-39, 2005.

[150] E. Oró, A. d. Gracia, A. Castell, M. M. Farid, and L. F. Cabeza, "Review on phase change materials (PCMs) for cold thermal energy storage applications," *Applied Energy,* vol. 99, pp. 513–533, 2012.

[151] A. Shukla, D. Buddhi, and R. L. Sawhney, "Thermal cycling test of few selected inorganic and organic phase change materials," *Renewable Energy,* vol. 33, no. 12, pp. 2606-2614, 2008.

[152] G. R. Dheep and A. Sreekumar, "Influence of accelerated thermal charging and discharging cycles on thermo-physical properties of organic phase change materials for solar thermal energy storage applications," *Energy Conversion and Management,* vol. 105, pp. 13-19, 2015.

[153] M. Iten, S. Liu, A. Shukla, and P. D. Silva, "Investigating the impact of Cp -T values determined by DSC on the PCM-CFD model," *Applied Thermal Engineering,* vol. 117, pp. 65-75, 2017.

[154] M. K. Rathod and J. Banerjee, "Thermal stability of phase change materials used in latent heat energy storage systems: A review," *Renewable and Sustainable Energy Reviews,* vol. 18, pp. 246-258, 2013.

[155] C. Alkan, K. Kaya, and A. Sarı, "Preparation, thermal properties and thermal reliability of form-stable paraffin/polypropylene composite for thermal energy storage," *Journal of Polymers and the Environment,* vol. 17, pp. 254-258, 2009.

[156] M. Hadjieva, S. Kanev, and J. Argirov, "Thermophysical properties of some paraffins applicable to thermal energy storage," *Solar Energy Materials and Solar Cells,* vol. 27, pp. 181-187, 1992.

[157] S. D. Sharma, D. Buddhi, and R. L. Sawhney, "Accelerated thermal cycle test of latent heat-storage materials," *Solar Energy,* vol. 66, no. 6, pp. 483-490, 1999.

[158] A. Sharma, S. D. Sharma, and D. Buddhi, "Accelerated thermal cycle test of acetamide, stearic acid and paraffin wax for solar thermal latent heat storage applications," *Energy Conversion and Management,* vol. 43, no. 14, pp. 1923-1930, 2002.

[159] H. Kimura and J. Kai, "Phase change stability of $CaCl_2 \cdot 6H_2O$," *Solar Energy,* vol. 33, no. 6, pp. 557-563, 1984.

[160] H. Feilchenfeld and S. Sarig, "Calcium chloride hexahydrate: A phase-changing material for energy storage," *Industrial & Engineering Chemistry Product Research and Development,* vol. 24, no. 1, pp. 130-133, 1985.

[161] V. V. Tyagi and D. Buddhi, "Thermal cycle testing of calcium chloride hexahydrate as a possible PCM for latent heat storage," *Solar Energy Materials and Solar Cells,* vol. 92, no. 8, pp. 891-899, 2008.

[162] A. A. El-Sebaii, S. Al-Amir, F. M. Al-Marzouki, A. S. Faidah, A. A. Al-Ghamdi, and S. Al-Heniti, "Fast thermal cycling of acetanilide and magnesium chloride hexahydrate for indoor solar cooking," *Energy Conversion and Management,* vol. 50, no. 12, pp. 3104-3111, 2009.

[163] A. A. El-Sebaii, S. Al-Heniti, F. Al-Agel, A. A. Al-Ghamdi, and F. Al-Marzouki, "One thousand thermal cycles of magnesium chloride hexahydrate as a promising

PCM for indoor solar cooking," *Energy Conversion and Management,* vol. 52, no. 4, pp. 1771-1777, 2011.

[164] H. E. S. Fath, "Technical assessment of solar thermal energy storage technologies," *Renewable Energy,* vol. 14, no. 1-4, pp. 35-40, 1998.

[165] T. Wada, R. Yamamoto, and Y. Matsuo, "Heat storage capacity of sodium acetate trihydrate during thermal cycling," *Solar Energy,* vol. 33, no. 3-4, pp. 373-375, 1984.

[166] H. Kimura and J. Kai, "Phase change stability of sodium acetate trihydrate and its mixtures," *Solar Energy,* vol. 35, no. 6, pp. 527-534, 1985.

[167] H. Kimura and J. Kai, "Feasibility of trichlorofluoromethane (CCl3F, R11) heptadecahydrate as a heat storage material," *Energy Conversion and Management,* vol. 25, no. 2, pp. 179-186, 1985.

[168] A. Sharma, V. V. Tyagi, C. R. Chen, and D. Buddhi, "Review on thermal energy storage with phase change materials and applications," *Renewable and Sustainable Energy Reviews,* vol. 13, no. 2, pp. 318-345, 2009.

[169] H. Mehling and L. F. Cabeza, "Phase change materials and their basic properties," in *Thermal energy storage for sustainable energy consumption: Fundamentals, case studies and design*, H. Ö. Paksoy, Ed. Dordrecht: Springer Netherlands, 2007, pp. 257-277.

[170] S. Marks, "An investigation of the thermal energy storage capacity of glauber's salt with respect to thermal cycling," *Solar Energy,* vol. 25, pp. 255-258, 1980.

[171] H. Mehling and L. F. Cabeza, *Heat and cold storage with PCM*. Springer, 2008.

[172] B. Zalba, J. M. Marín , L. F. Cabeza, and H. Mehling, "Review on thermal energy storage with phase change: materials, heat transfer analysis and applications," *Applied Thermal Engineering,* vol. 23, no. 3, pp. 251-283, 2003.

[173] PCM Energy P. Ltd. (2018). *Phase change material manufacturers.* Available: http://www.pcmenergy.com/

[174] RUBITHERM Phase Change Material. (2018). *Rubitherm® Technologies GmbH is an expert in PCM technology and develops together with you specific product solutions*. Available: https://www.rubitherm.eu/en//index.html

[175] Climator Sweden AB. (2018). *Each ClimSel product has a unique phase change process and specific thermodynamic properties that make them suitable for*

customer applications in different temperature ranges. Available: http://climator.com/

[176] PCM products. (2018). *Phase change materials: Thermal management solutions*. Available: http://www.pcmproducts.net/

[177] Microtek Laboratories. (2018). *Microtek offers PCM blends that can be used in multiple applications. Since pure PCM above its melt point is a free flowing liquid, it does require a containment system.* Available: http://www.microteklabs.com/index.html

[178] PureTemp. (2018). *PureTemp phase change materials*. Available: http://www.puretemp.com/

[179] M. Kenisarin and K. Mahkamov, "Salt hydrates as latent heat storage materials:Thermophysical properties and costs," *Solar Energy Materials and Solar Cells,* vol. 145, pp. 255-286, 2016.

[180] M. M. Kenisarin, "High-temperature phase change materials for thermal energy storage," *Renewable and Sustainable Energy Reviews,* vol. 14, no. 3, pp. 955-970, 2010.

[181] Magnametals. (2019). *Magnametals are now the largest and lowest cost supplier of gallium, ferrofluid, magnetic field viewer film, pyrolytic graphite and bismuth in small quantities, to individuals, universities, schools and businesses, all over the world based in the UK.* . Available: https://magnametals.co.uk/

[182] A. Abhat, "Thermal performance of a finned heat-pipe latent heat store," *International journal of ambient energy,* vol. 5, no. 4, pp. 193-206, 1984.

[183] A. M.-A. C. Supplier. (4/4/2019). *ACS material is a high-tech enterprise involved in advanced nanomaterials development and production*. Available: https://www.acsmaterial.com/media/catalog/product/t/d/tds-pyrolytic_graphite_powder.pdf

[184] A. elements. (4/4/2019). Available: https://www.americanelements.com/pyrolytic-graphite-7782-42-5

[185] A. Einstein, "A new determination of molecular dimensions," *Ann. Phys.*, vol. 19, pp. 289-306, 1906.

[186] Y. Plevachuk, V. Sklyarchuk, G. Gerbeth, and S. Eckert, "Thermophysical properties of liquid tin–bismuth alloys," *International Journal of Materials Research* vol. 101, no. 7, 2010.

[187] A. Dobosz and T. Gancarz, "Reference data for the density, viscosity, and surface tension of liquid Al–Zn, Ag–Sn, Bi–Sn, Cu–Sn, and Sn–Zn eutectic alloys," *Journal of Physical and Chemical Reference Data,* vol. 47, no. 1, 2018.

[188] Y. I. Dutchak, V. P. Osipenko, and P. V. Panasyuk, "Thermal conductivity of Sn-Bi alloys in the solid and liquid states," *Soviet Physics Journal,* vol. 11, no. 10, pp. 145-147, 1968.

[189] R. J. Hooper *et al.*, "Prediction and characterization of heat-affected zone formation in tin-bismuth alloys due to nickel-aluminum multilayer foil reaction," *Journal of Applied Physics,* vol. 117, no. 24, 2015.

[190] (2018). Available: http://www.thermopedia.com/es/content/595/

[191] S.-C. Costa *et al.*, "Experimental and numerical study on melting of solar salt in a finned metallic container," in *ASME 2018 International Mechanical Engineering Congress and Exposition*, Pittsburgh, PA, USA, 2018: American Society of Mechanical Engineers.

[192] Available: https://uk.rs-online.com/web/p/thermal-adhesives/1609024/

[193] S. J. Kline and F. A. Mcclintock, "Describing uncertainties in single sample experiments," *Mechanical Engineering,* vol. 75, no. 1, pp. 3-8, 1953.

[194] K. Kitamura, F. Kami-iwa, and T. Misumib, "Heat transfer and fluid flow of natural convection around large horizontal cylinders," *International Journal of Heat and Mass Transfer,* vol. 42, pp. 4093-4106, 1999.

[195] H. K. Versteeg and W. Malalasekera, *An introduction to computational fluid dynamics: the finite volume method*. Pearson education, 2007.

[196] G. Nardini and M. Paroncini, "Heat transfer experiment on natural convection in a square cavity with discrete sources," *Heat and Mass Transfer,* vol. 48, no. 11, pp. 1855-1865, 2012.

[197] ANSYS, "Fluent theory guide 15.0," *ANSYS, Canonsburg, PA,* 2013.

[198] D. C. Wilcox, *Turbulence modeling for CFD*. DCW industries La Canada, CA, 1998.

[199] F. R. Menter, "Two-equation eddy-viscosity turbulence models for engineering applications," *AIAA journal,* vol. 32, no. 8, pp. 1598-1605, 1994.

[200] M. N. Özişik, H. R. Orlande, M. J. Colaço, and R. M. Cotta, *Finite difference methods in heat transfer*. Boca Raton: CRC press, 2017.

[201] V. R. Voller and C. Prakash, "A fixed grid numerical modelling methodology for convection-diffusion mushy region phase-change problems," *International Journal of Heat and Mass Transfer,* vol. 30, no. 8, pp. 1709-1719, 1987.

[202] A. Khalifa, L. Tan, A. Date, and A. Akbarzadeh, "Performance of suspended finned heat pipes in high-temperature latent heat thermal energy storage," *Applied Thermal Engineering,* vol. 81, pp. 242-252, 2015.

[203] N. S. Bondareva and M. A. Sheremet, "Flow and heat transfer evolution of PCM due to natural convection melting in a square cavity with a local heater," *International Journal of Mechanical Sciences,* vol. 134, pp. 610-619, 2017.

[204] E. Assis, L. Katsman, G. Ziskind, and R. Letan, "Numerical and experimental study of melting in a spherical shell," *International Journal of Heat and Mass Transfer,* vol. 50, no. 9-10, pp. 1790-1804, 2007.

[205] Y. H. Diao, L. Liang, Y. H. Zhao, Z. Y. Wang, and F. W. Bai, "Numerical investigation of the thermal performance enhancement of latent heat thermal energy storage using longitudinal rectangular fins and flat micro-heat pipe arrays," *Applied Energy,* vol. 233-234, pp. 894-905, 2019.

[206] B. Kamkari and D. Groulx, "Experimental investigation of melting behaviour of phase change material in finned rectangular enclosures under different inclination angles," *Experimental Thermal and Fluid Science,* vol. 97, pp. 94-108, 2018.

[207] R. Elbahjaoui, H. El Qarnia, and M. El Ganaoui, "Numerical study of the melting of nano-PCM in a rectangular storage unit heated by upward heat transfer fluid," *Energy Procedia,* vol. 139, pp. 86-91, 2017.

[208] A. R. Darzi, M. Farhadi, and K. Sedighi, "Numerical study of melting inside concentric and eccentric horizontal annulus," *Applied Mathematical Modelling,* vol. 36, no. 9, pp. 4080-4086, 2012.

[209] S. Seddegh, X. Wang, M. M. Joybari, and F. Haghighat, "Investigation of the effect of geometric and operating parameters on thermal behavior of vertical shell-and-tube latent heat energy storage systems," *Energy,* vol. 137, pp. 69-82, 2017.

[210] A. A. Rabienataj Darzi, M. Jourabian, and M. Farhadi, "Melting and solidification of PCM enhanced by radial conductive fins and nanoparticles in cylindrical annulus," *Energy Conversion and Management,* vol. 118, pp. 253-263, 2016.

[211] M. Esapour, A. Hamzehnezhad, A. A. Rabienataj Darzi, and M. Jourabian, "Melting and solidification of PCM embedded in porous metal foam in horizontal

multi-tube heat storage system," *Energy Conversion and Management,* vol. 171, pp. 398-410, 2018.

[212] J. M. Mahdi and E. C. Nsofor, "Solidification enhancement of PCM in a triplex-tube thermal energy storage system with nanoparticles and fins," *Applied Energy,* vol. 211, pp. 975-986, 2018.

[213] B. Othman and S. Chakib, "Study of the solidification process of a phase change material contained in a heat exchanger with the presence of a porous medium," *Mechanics,* vol. 22, no. 5, 2016.

[214] A. A. Rabinataj Darzi, H. Hassanzadeh Afrouzi, M. Khaki, and M. Abbasi, "Unconstrained melting and solidification inside rectangular enclosure," *Journal of Fundamental and Applied Sciences,* vol. 7, no. 3, 2015.

[215] S. Arena, G. Cau, and C. Palomba, "CFD simulation of melting and solidification of PCM in thermal energy storage systems of different geometry," *Journal of Physics: Conference Series,* vol. 655, 2015.

[216] O. Ben-David, A. Levy, B. Mikhailovich, M. Avnaim, and A. Azulay, "Impact of traveling permanent magnets on low temperature metal melting in a cuboid," *International Journal of Heat and Mass Transfer,* vol. 99, pp. 882-894, 2016.

[217] G. Wang, C. Xu, G. Wei, and X. Du, "Numerical study of a novel dual-PCM thermal energy storage structure filled with inorganic salts and metal alloy as the PCMs," *Energy Procedia,* vol. 158, pp. 4423-4428, 2019.

[218] V. Soni, A. Kumar, and V. K. Jain, "A novel solidification model considering undercooling effect for metal based low temperature latent thermal energy management," *Journal of Energy Storage,* vol. 21, pp. 528-542, 2019.

[219] H. Chattopadhyay, "Estimation of solidification time in investment casting process," *The International Journal of Advanced Manufacturing Technology,* vol. 55, no. 1-4, pp. 35-38, 2010.

Appendix A: Validation of the Numerical results versus Experimental results

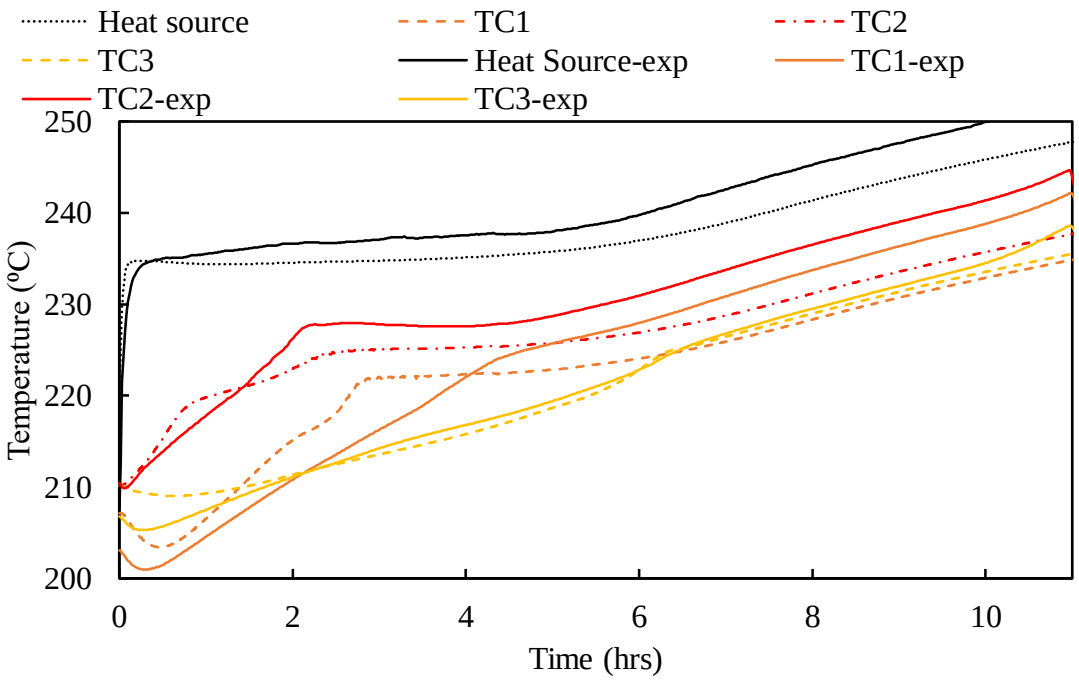

Figure A- 1: Temperature distribution and variation in the TES system with pure solar salt during the charging process with power input of 25 W (part-1).

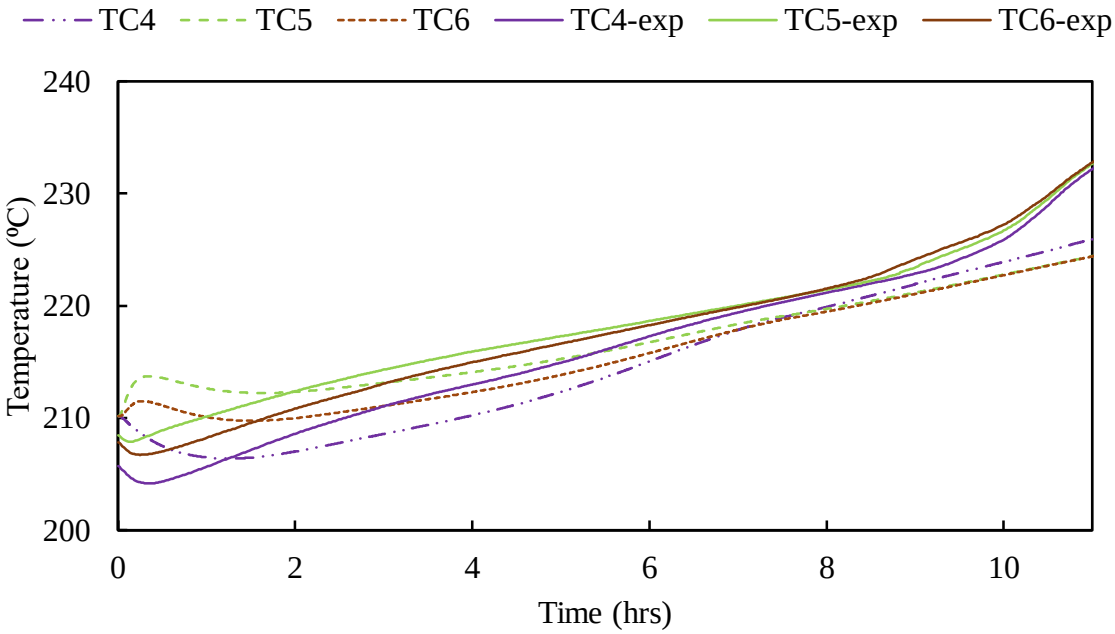

Figure A- 2: Temperature distribution and variation in the TES system with pure solar salt during the charging process with power input of 25 W (part-2).

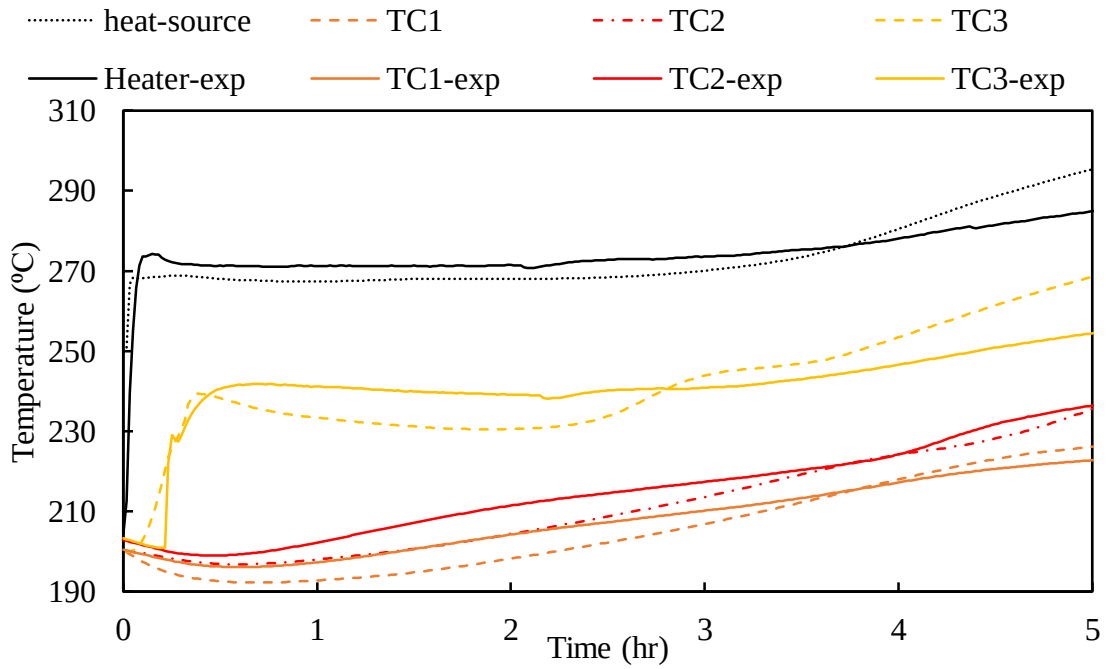

Figure A- 3: Temperature distribution and variation in the TES system with pure solar salt during the charging process with the power input of 35 W (part-1).

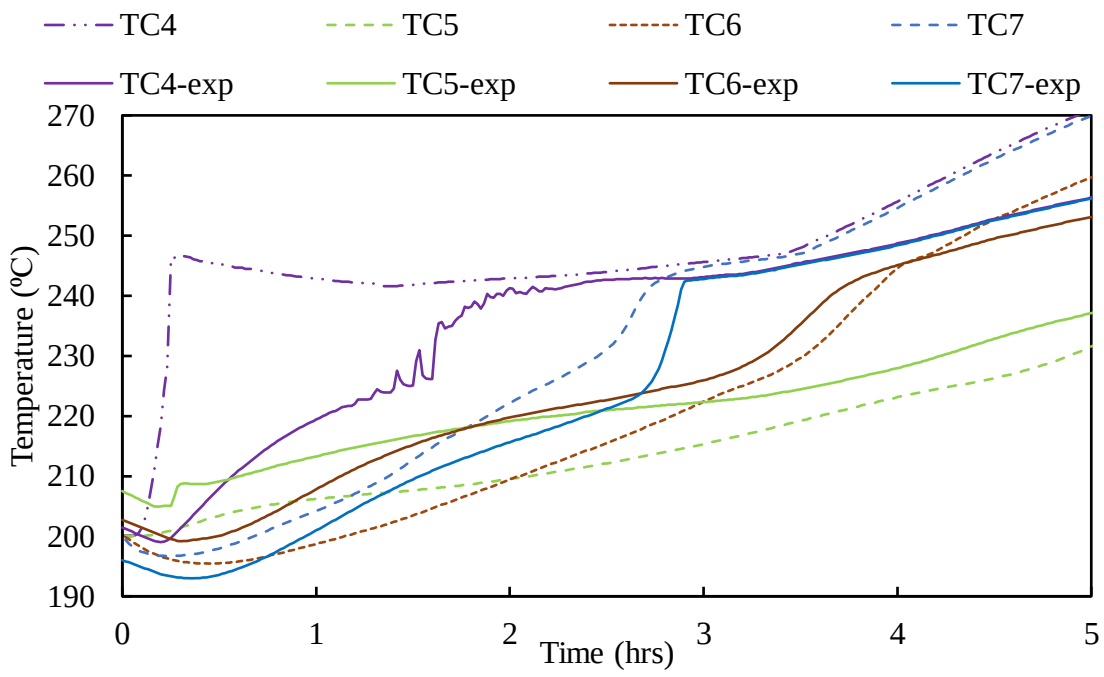

Figure A- 4: Temperature distribution and variation in the TES system with pure solar salt during the charging process with power input of 35 W (part-2).

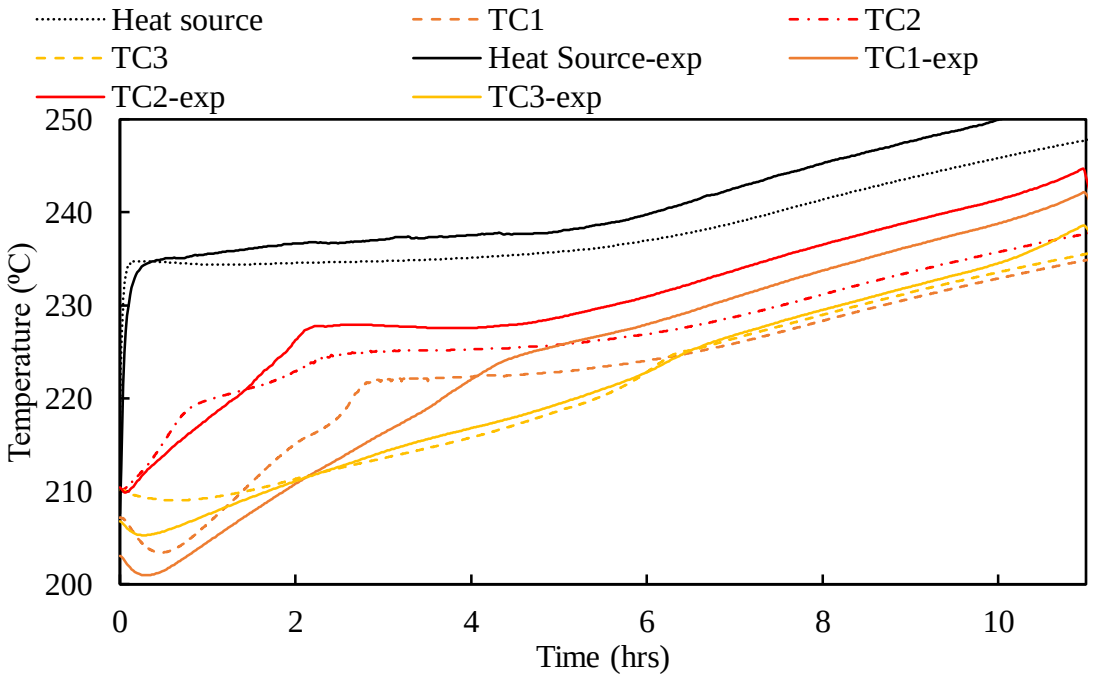

Figure A- 5: Temperature distribution and variation in the TES system with solar salt stainless steel fins during the charging process with the power input of 25 W (part-1).

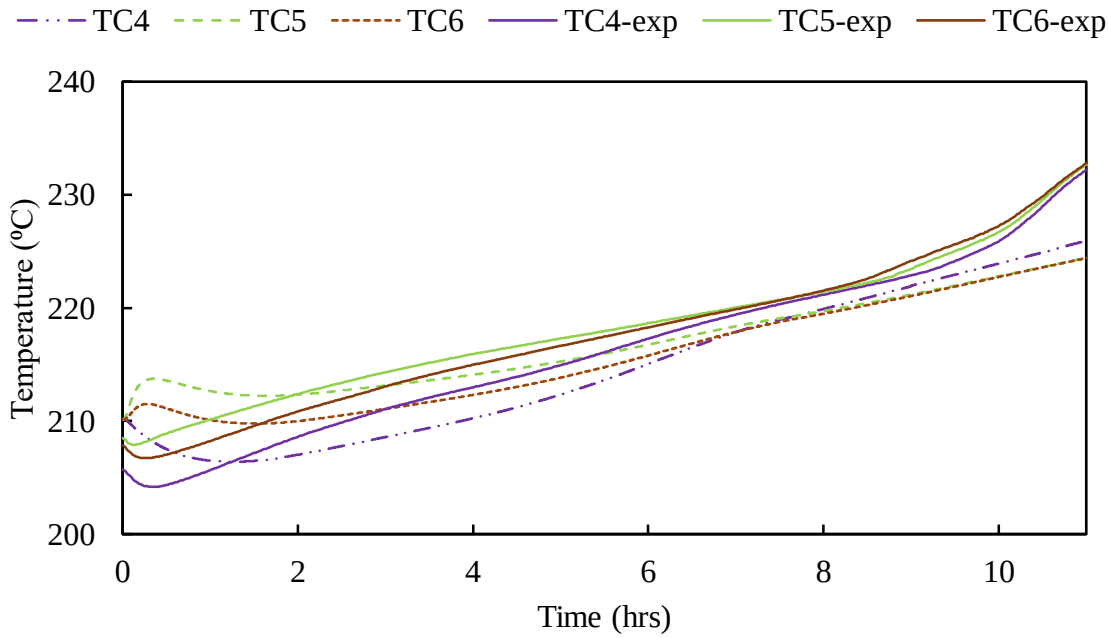

Figure A- 6: Temperature distribution and variation in the TES system with solar salt stainless steel fins during the charging process with the power input of 25 W (part-2).

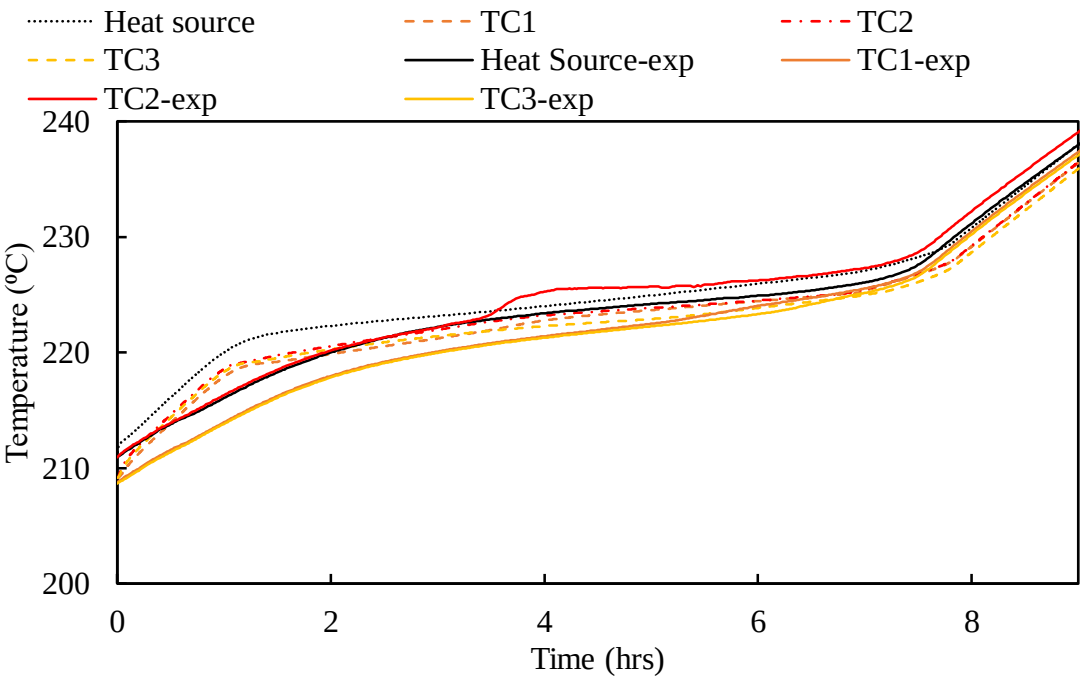

Figure A- 7: Temperature distribution and variation in the TES system with solar salt aluminium fins during the charging process with the power input of 25 W (part-1).

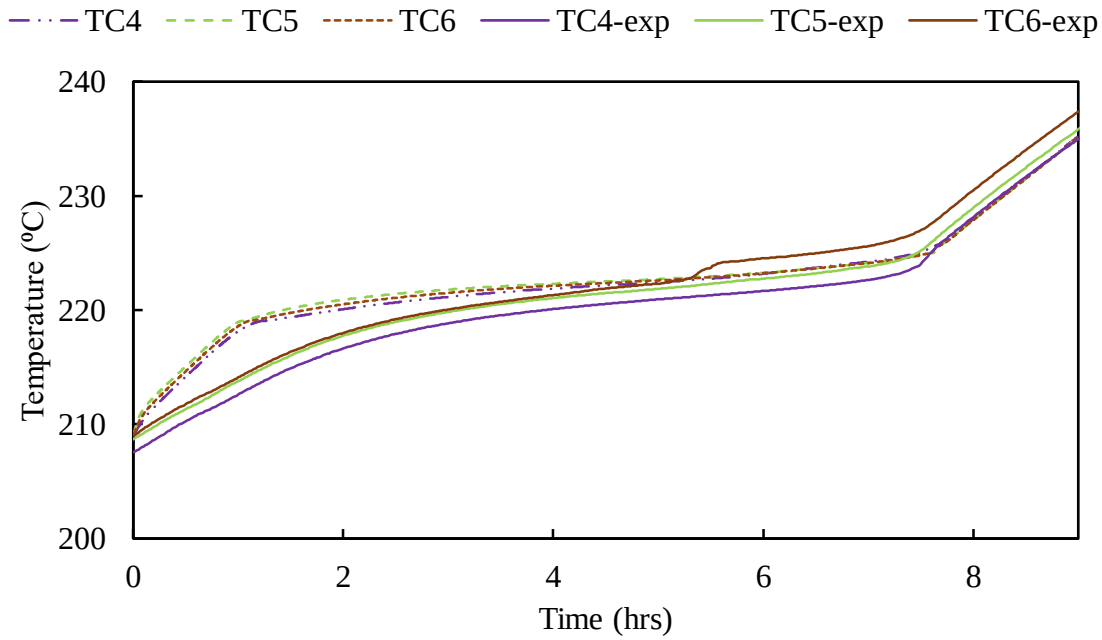

Figure A- 8: Temperature distribution and variation in the TES system with solar salt aluminium fins during the charging process with the power input of 25 W (part-2).

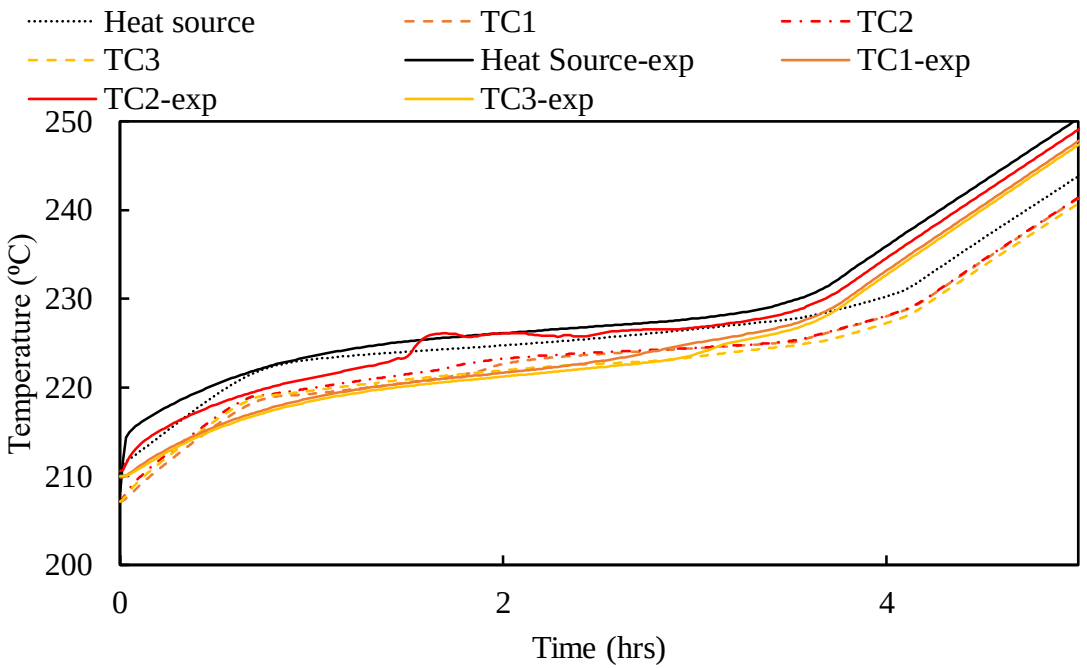

Figure A- 9: Temperature distribution and variation in the TES system with solar salt aluminium fins during the charging process with the power input of 35 W (part-1).

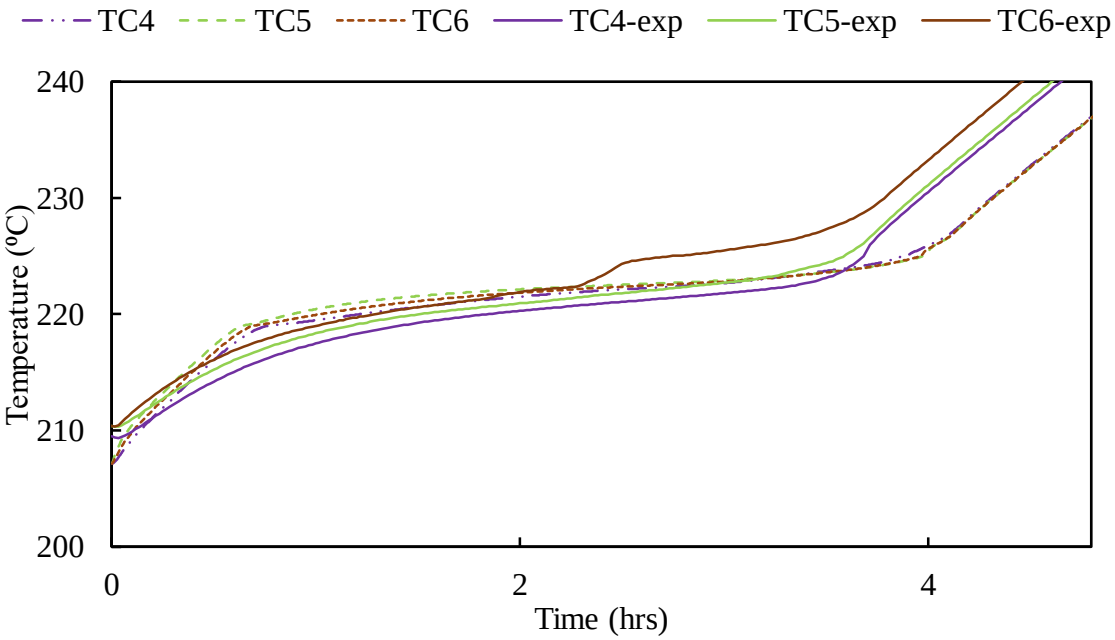

Figure A- 10: Temperature distribution and variation in the TES system with solar salt aluminium fins during the charging process with the power input of 35 W (part-2).

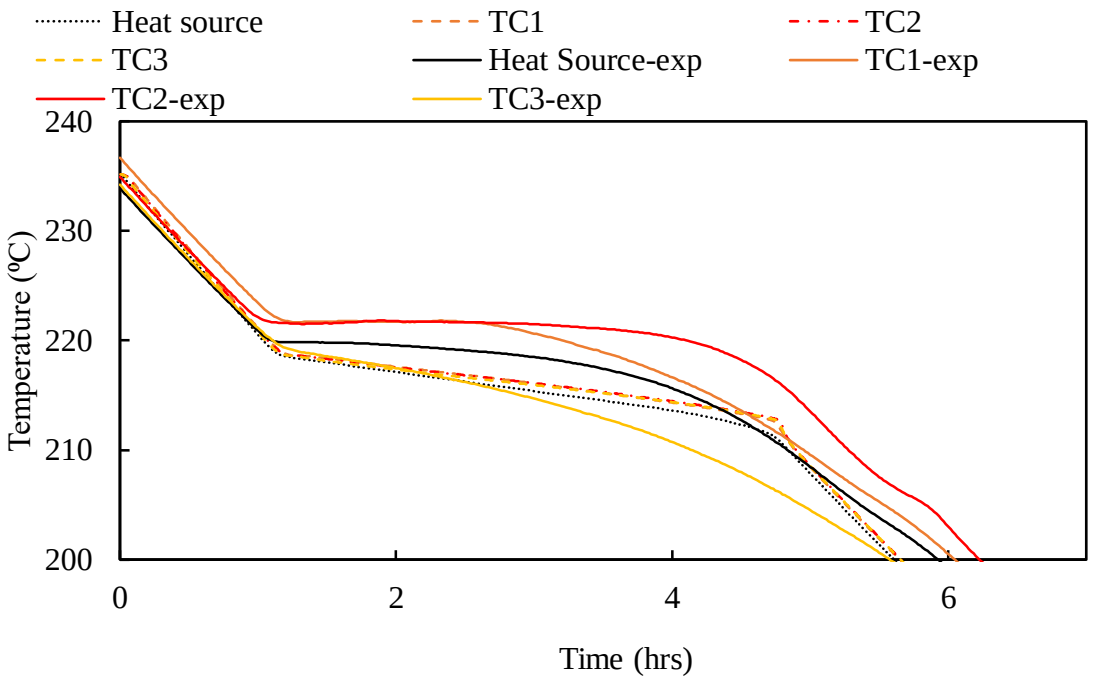

Figure A- 11: Temperature distribution and variation in the TES system with pure solar salt and aluminium container during the discharging process (part-1).

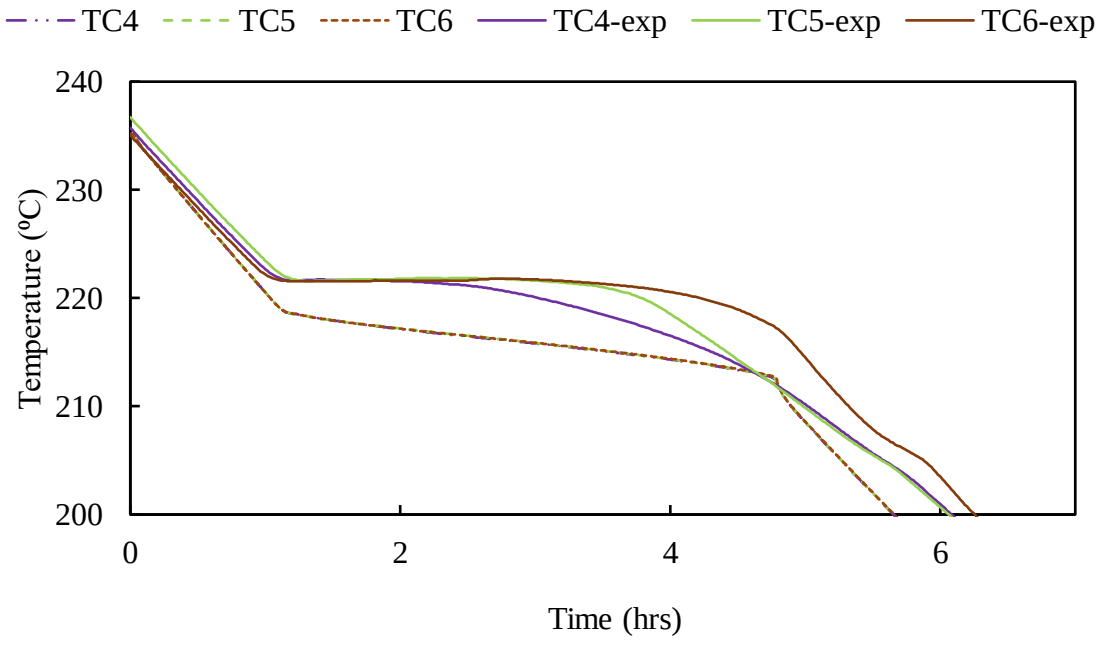

Figure A- 12: Temperature distribution and variation in the TES system with pure solar salt and aluminium container during the discharging process (part-2).

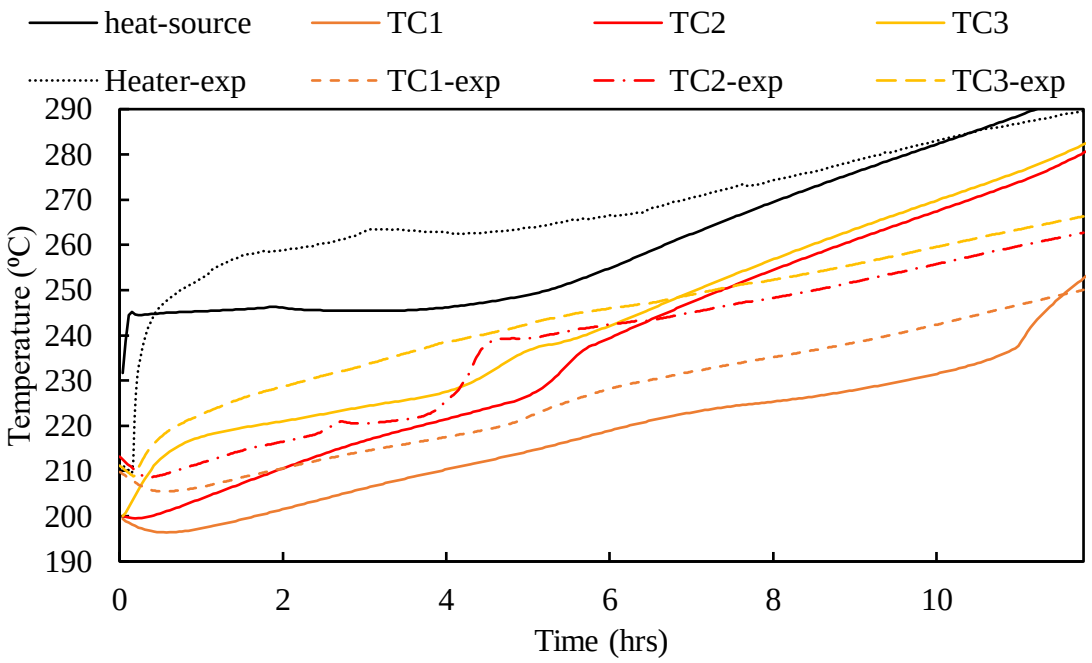

Figure A- 13: Temperature distribution and variation in the TES system with solar salt and 10 wt% graphite during the charging process with the power input of 25 W (part-1).

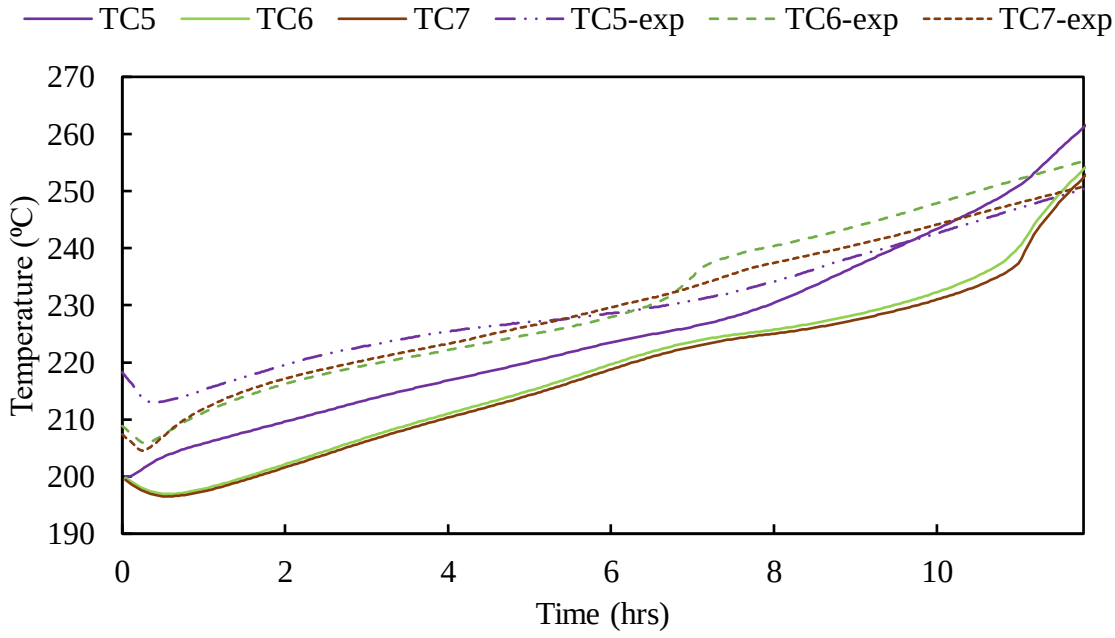

Figure A- 14: Temperature distribution and variation in the TES system with solar salt and 10 wt% graphite during the charging process with the power input of 25 W (part-2).

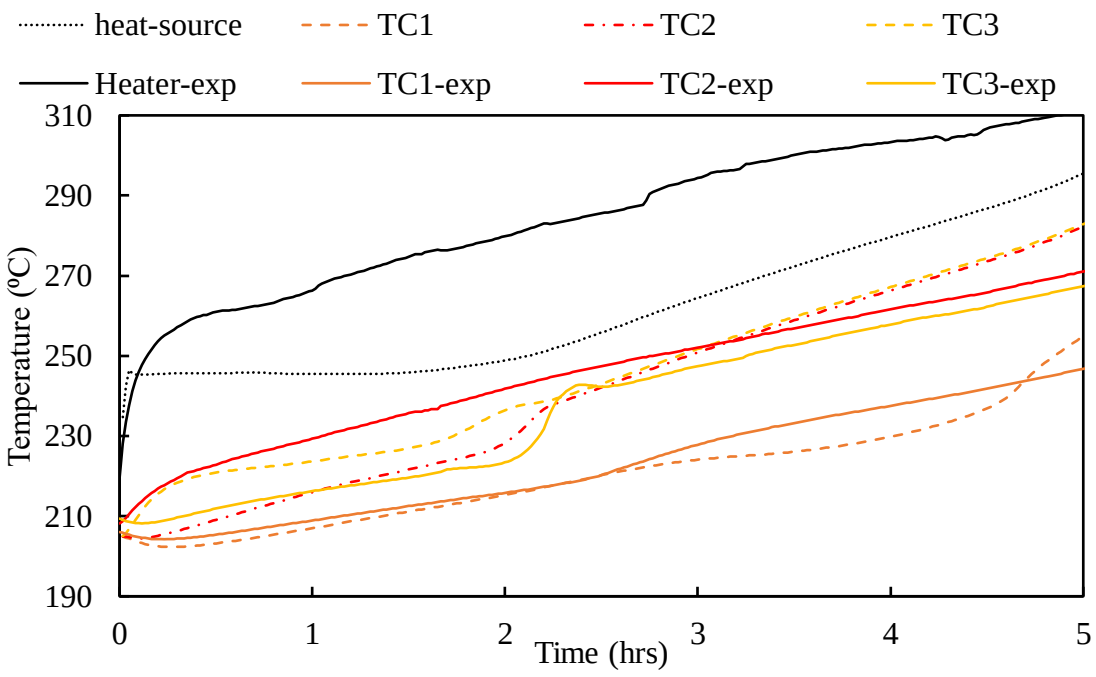

Figure A- 15: Temperature distribution and variation in the TES system with solar salt and 10 wt% graphite during the charging process with the power input of 35 W (part-1).

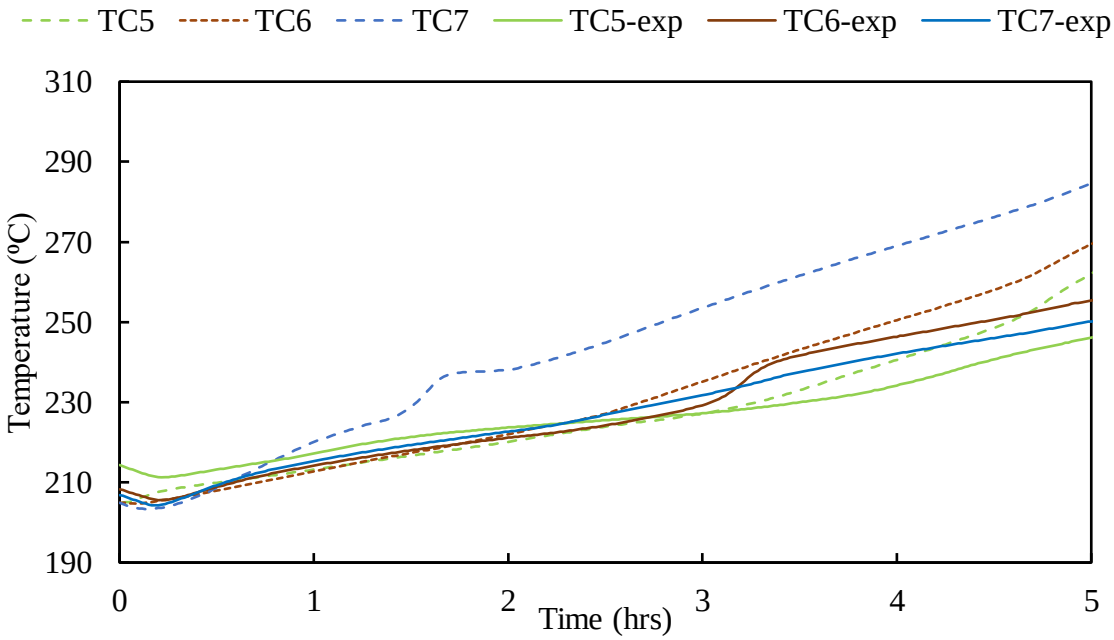

Figure A- 16: Temperature distribution and variation in the TES system with solar salt and 10 wt% graphite during the charging process with the power input of 35 W (part-2).

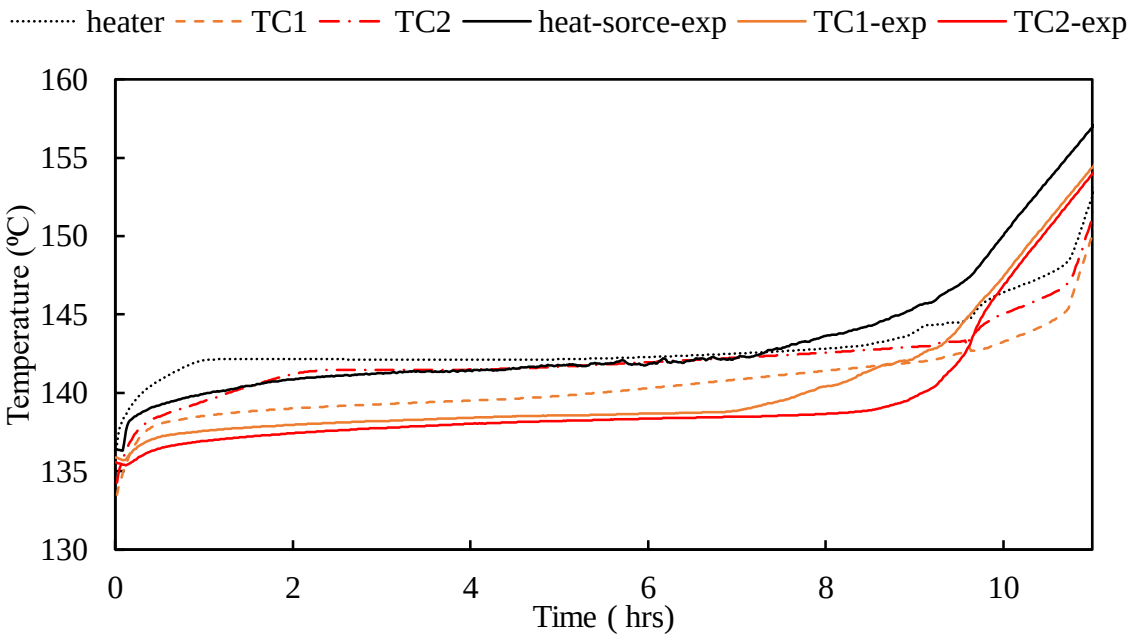

Figure A- 17: Temperature distribution and variation in the TES system with metal alloy during the charging process with the power input of 18 W (part-1).

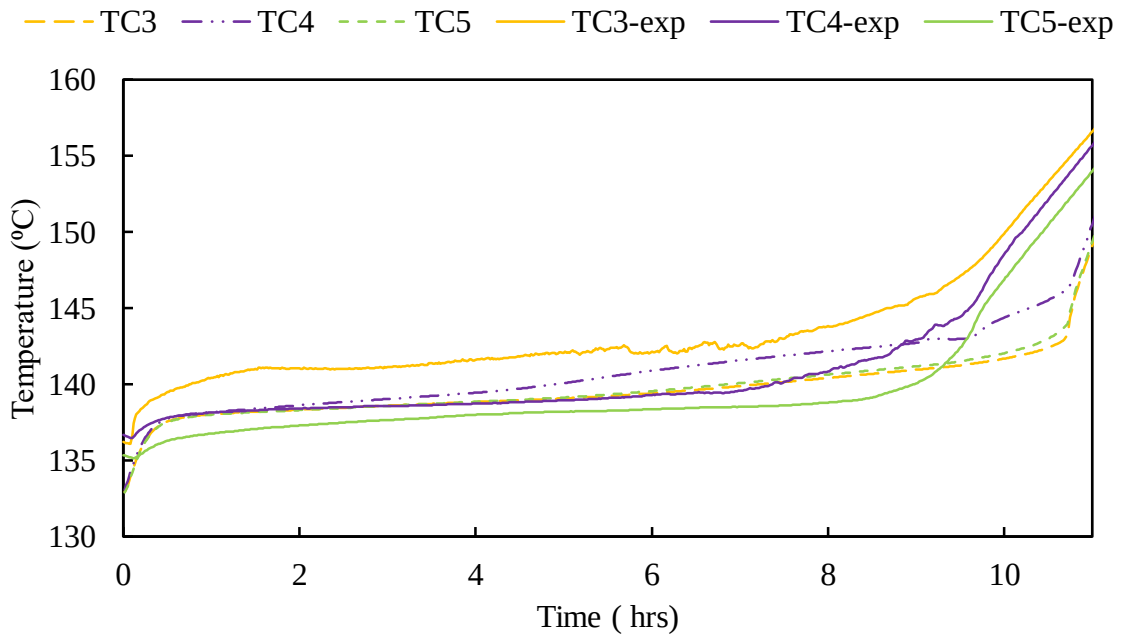

Figure A- 18: Temperature distribution and variation in the TES system with metal alloy during the charging process with the power input of 18 W (part-2).

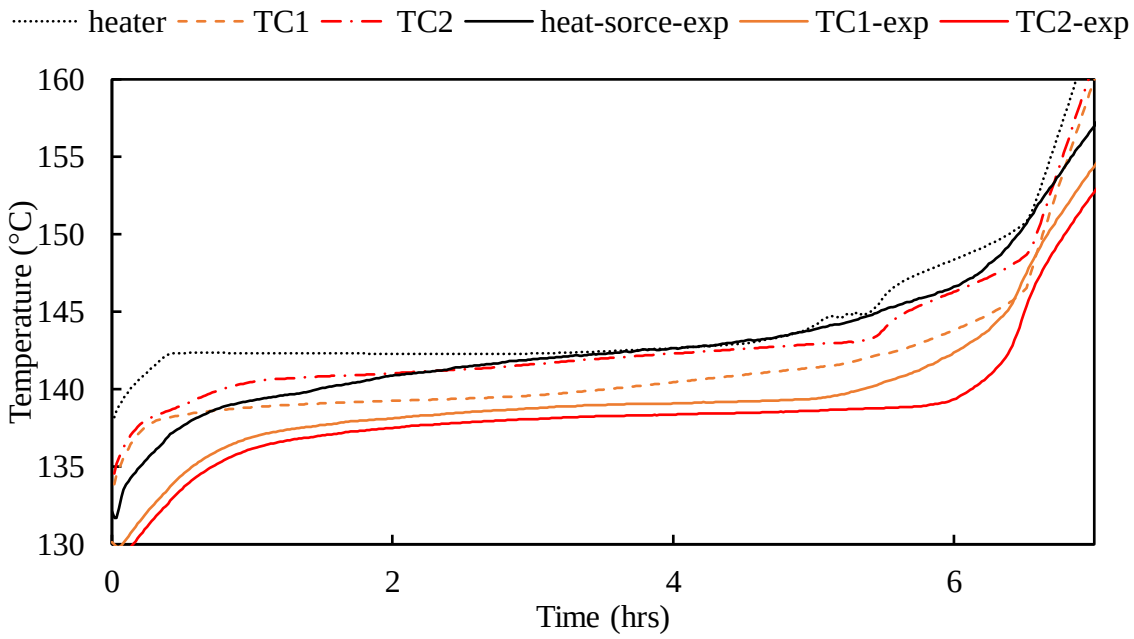

Figure A- 19: Temperature distribution and variation in the TES system with metal alloy during the charging process with the power input of 25 W (part-1).

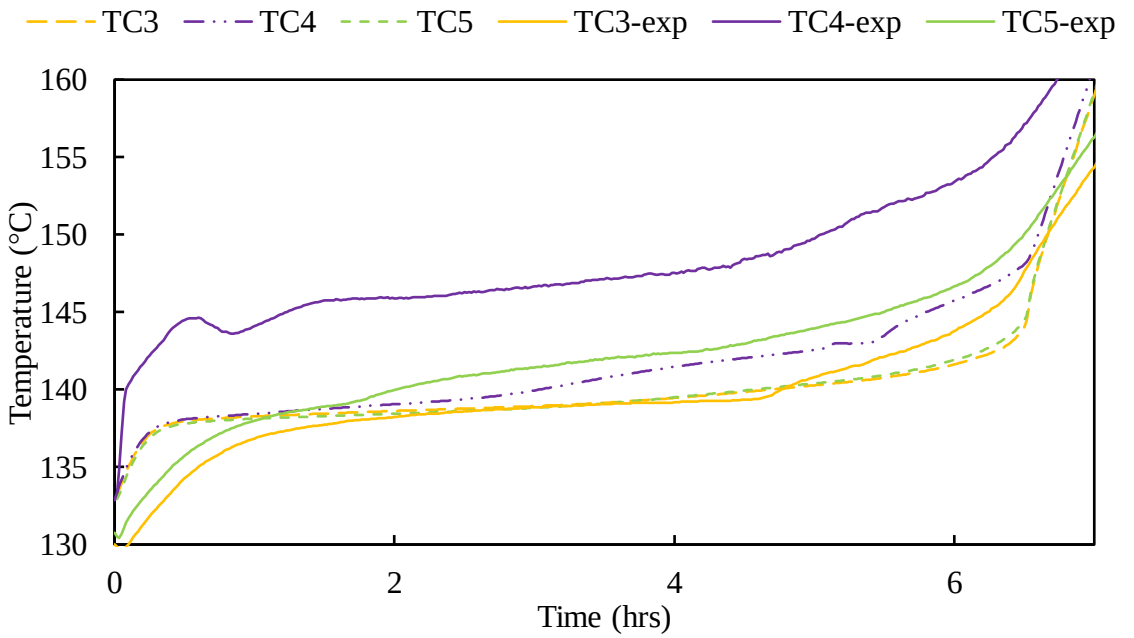

Figure A- 20: Temperature distribution and variation in the TES system with metal alloy during the charging process with the power input of 25 W (part-2).

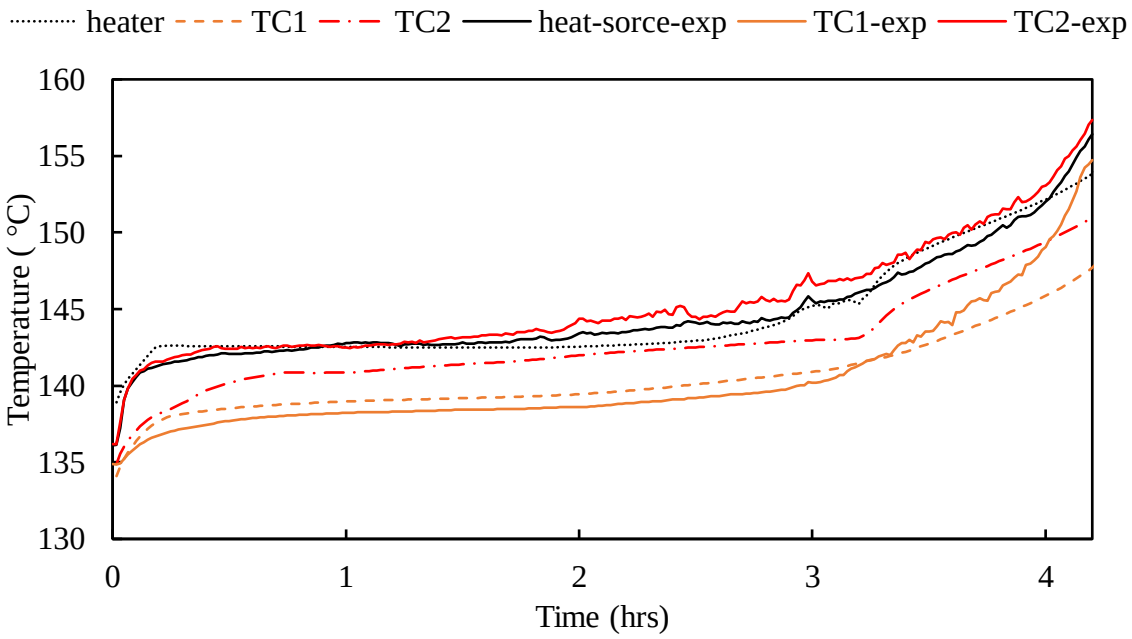

Figure A- 21: Temperature distribution and variation in the TES system with metal alloy during the charging process with the power input of 35 W (part-1).

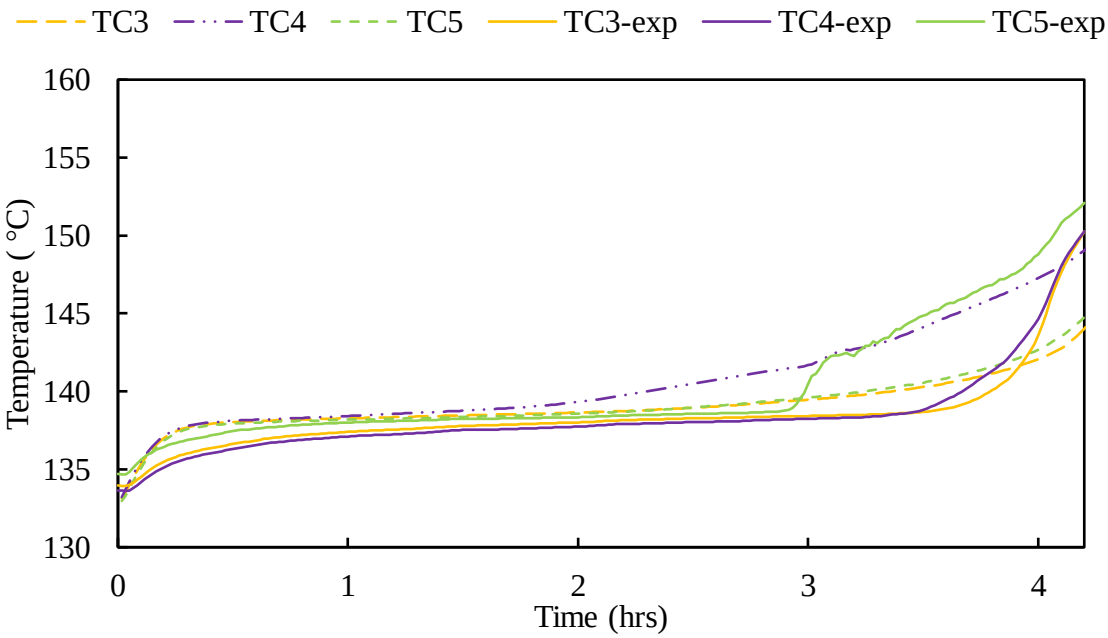

Figure A- 22: Temperature distribution and variation in the TES system with metal alloy during the charging process with the power input of 35 W (part-2).

Appendix B: Numerical results for TES system using PCMs with different power inputs and dimensionless numbers

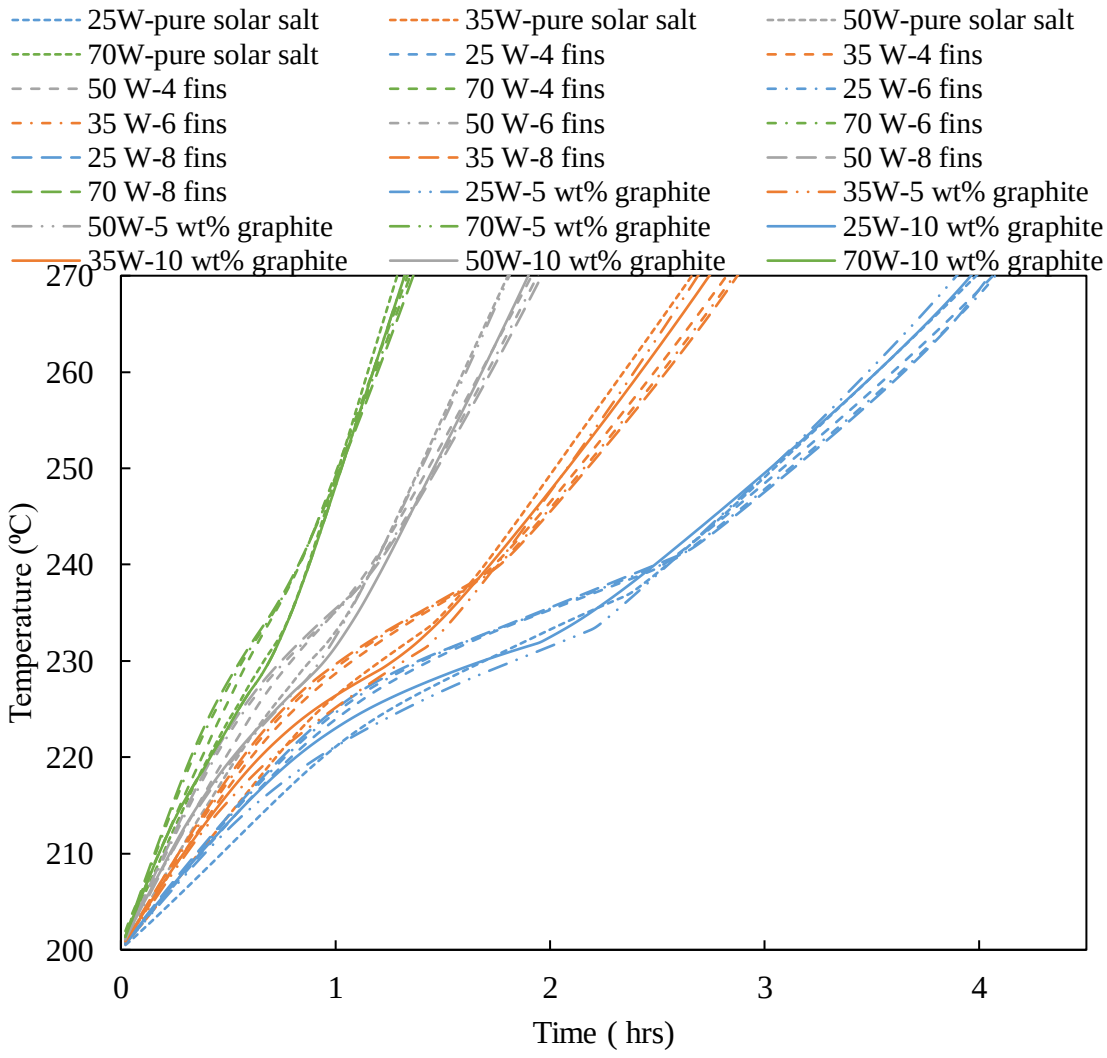

Figure B- 1: Average temperature of TES systems using solar salt with different configurations during the energy charging process.

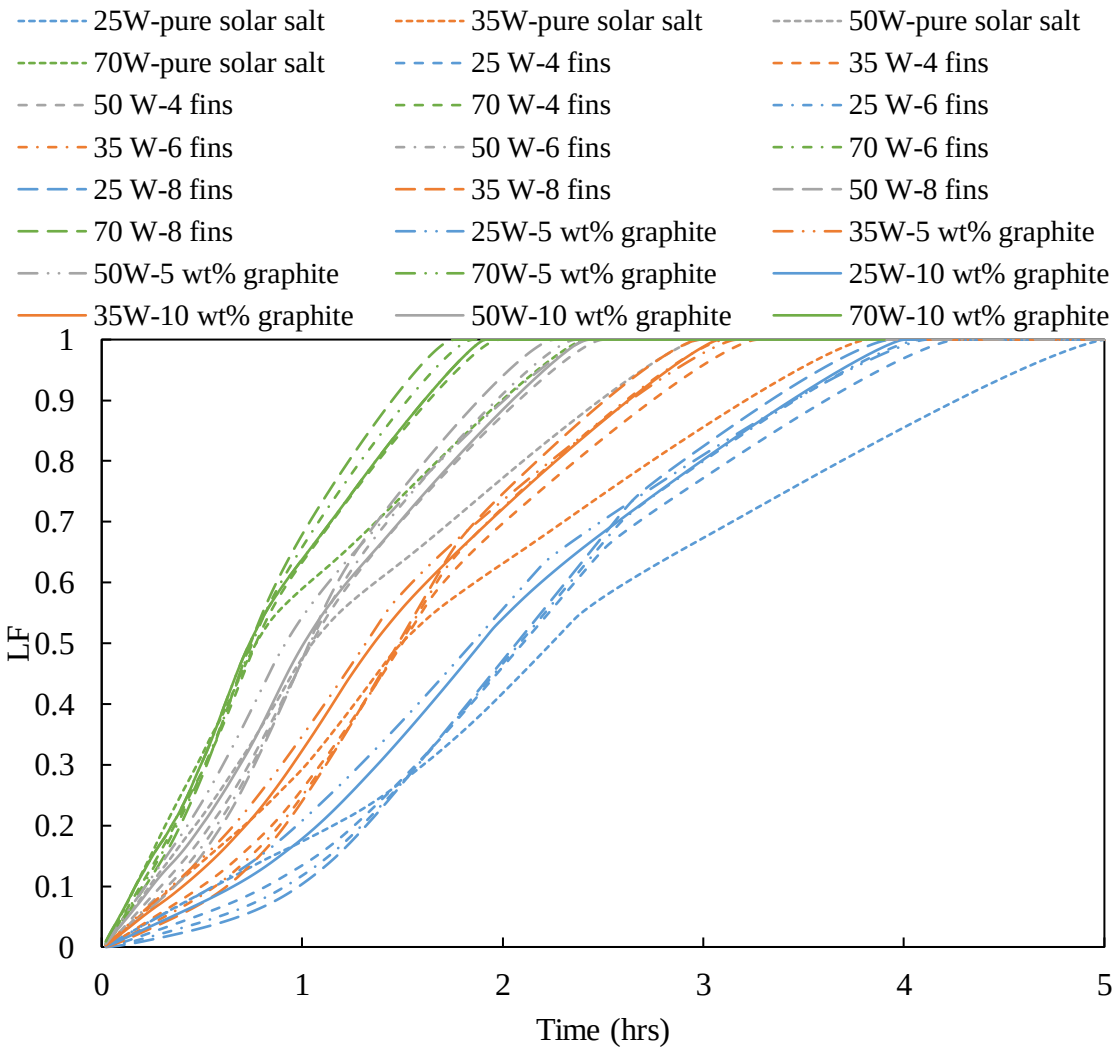

Figure B- 2: LF of PCMs in the TES systems using solar salt with different configurations during the energy charging process.

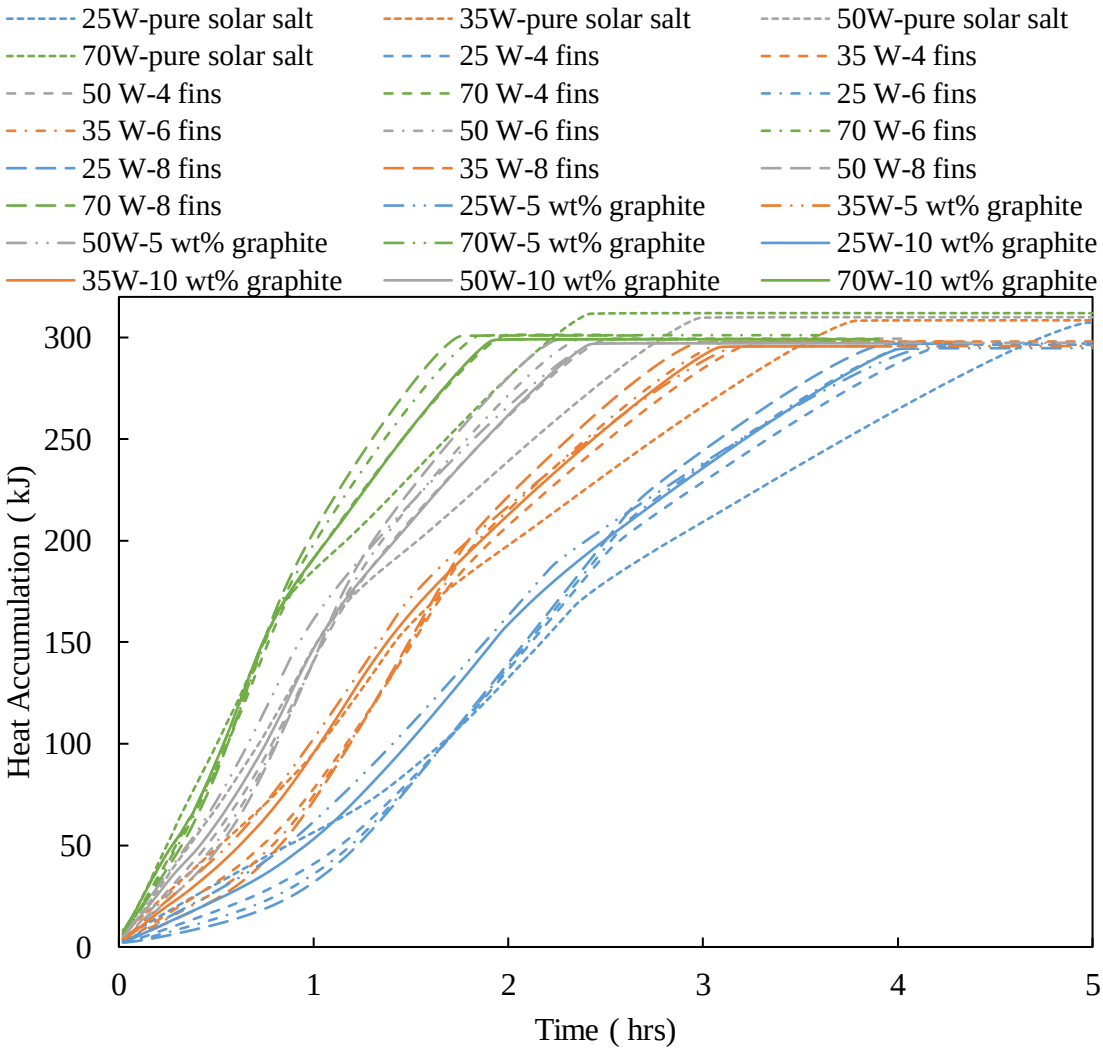

Figure B- 3: Heat accumulated in the TES systems using solar salt with different configurations during the charging process.

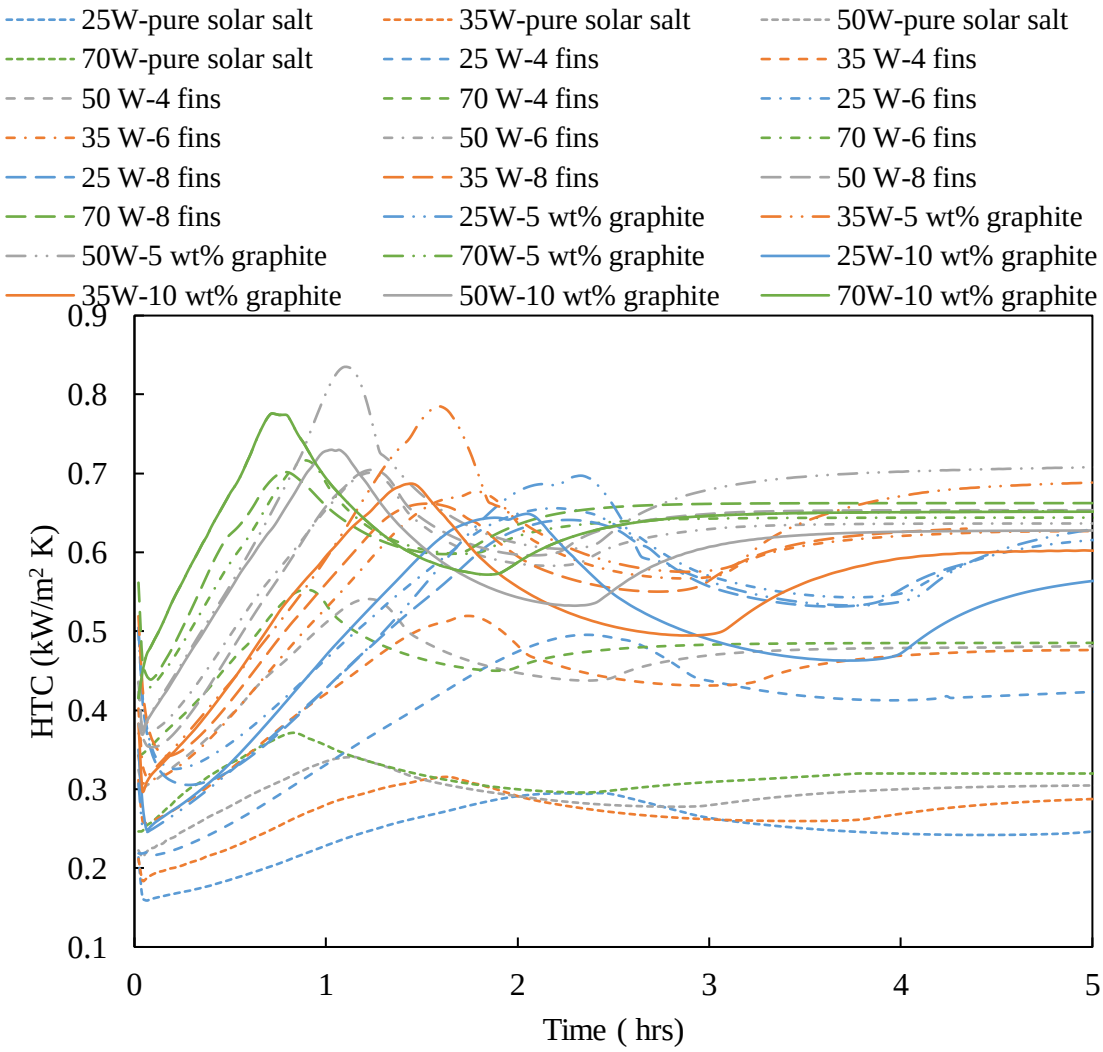

Figure B- 4: HTC for the TES systems using solar salt with different configurations during the charging process.

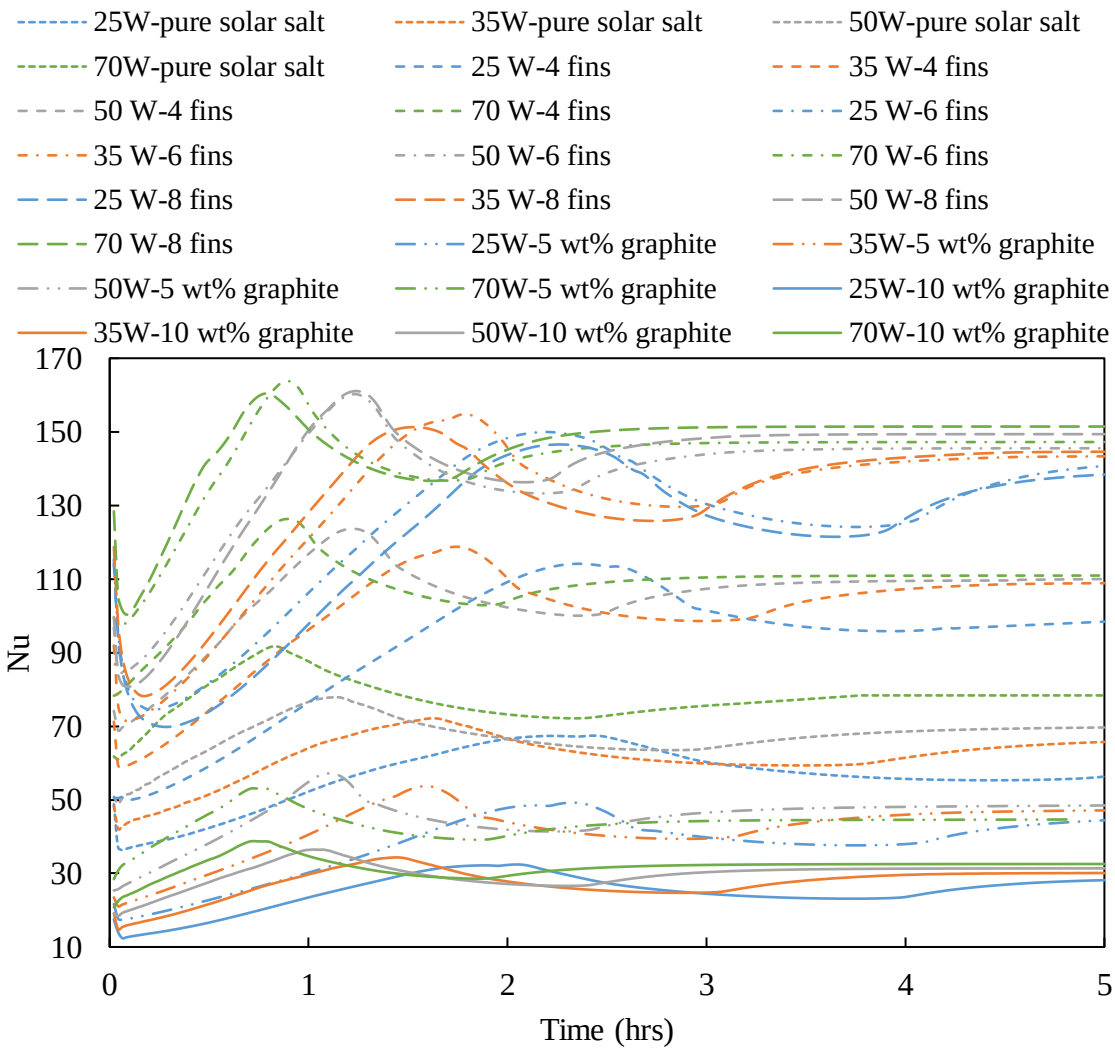

Figure B- 5: Nu number for the TES systems using solar salt with different configurations during the charging process.

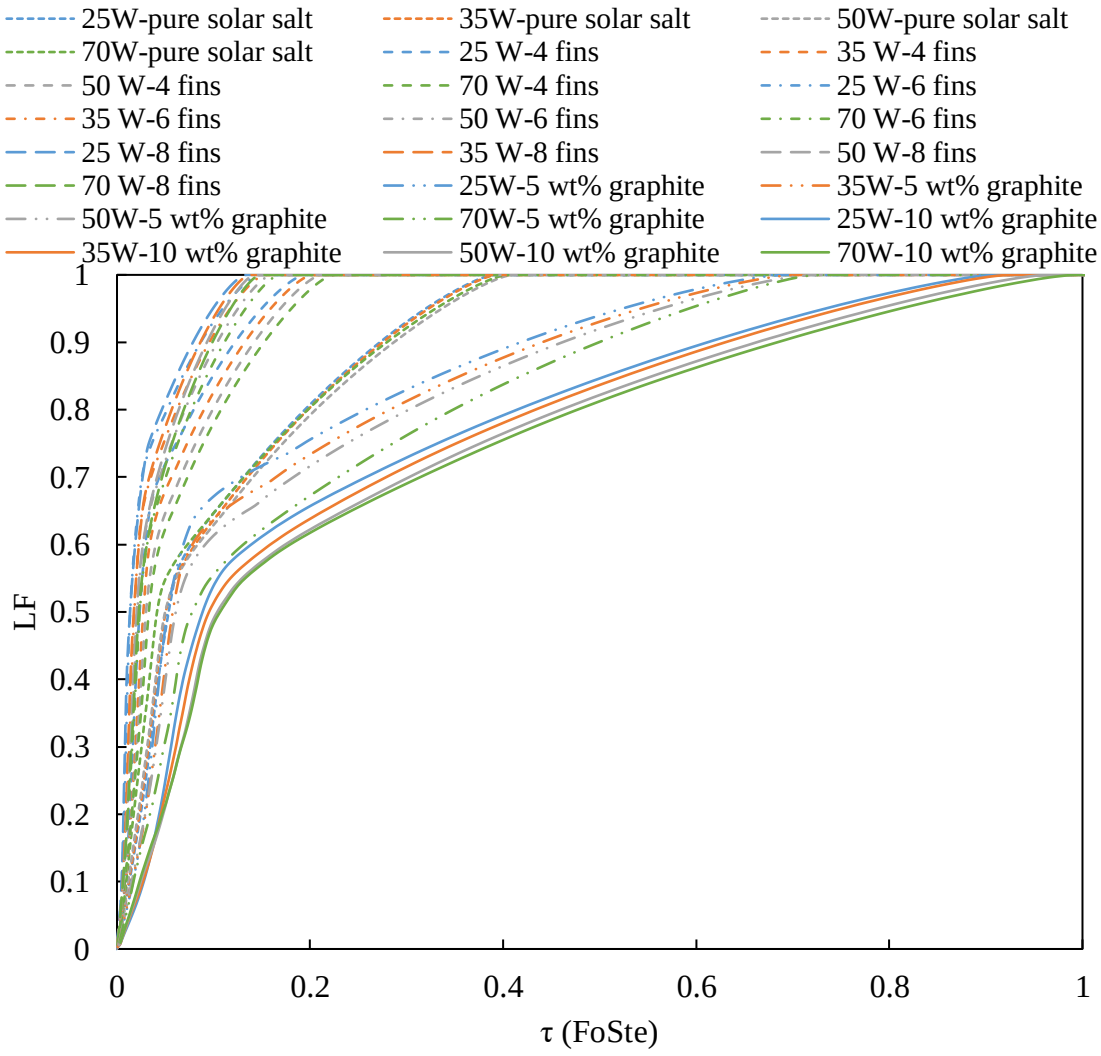

Figure B- 6: LF versus dimensionless time using for TES systems using solar salt with different configurations during the charging process.

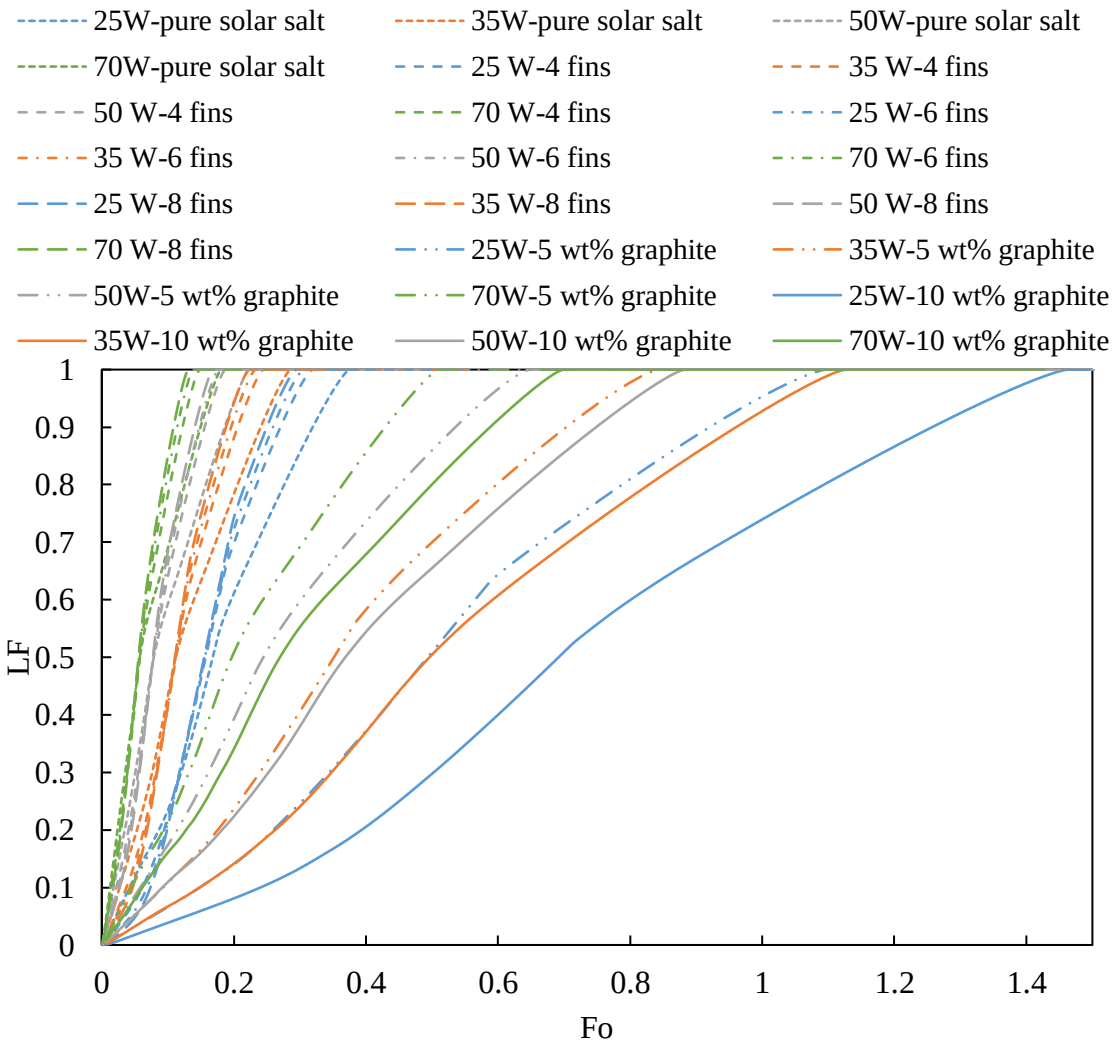

Figure B- 7: LF versus Fourier number for TES systems using solar salt with different configurations during the charging process.

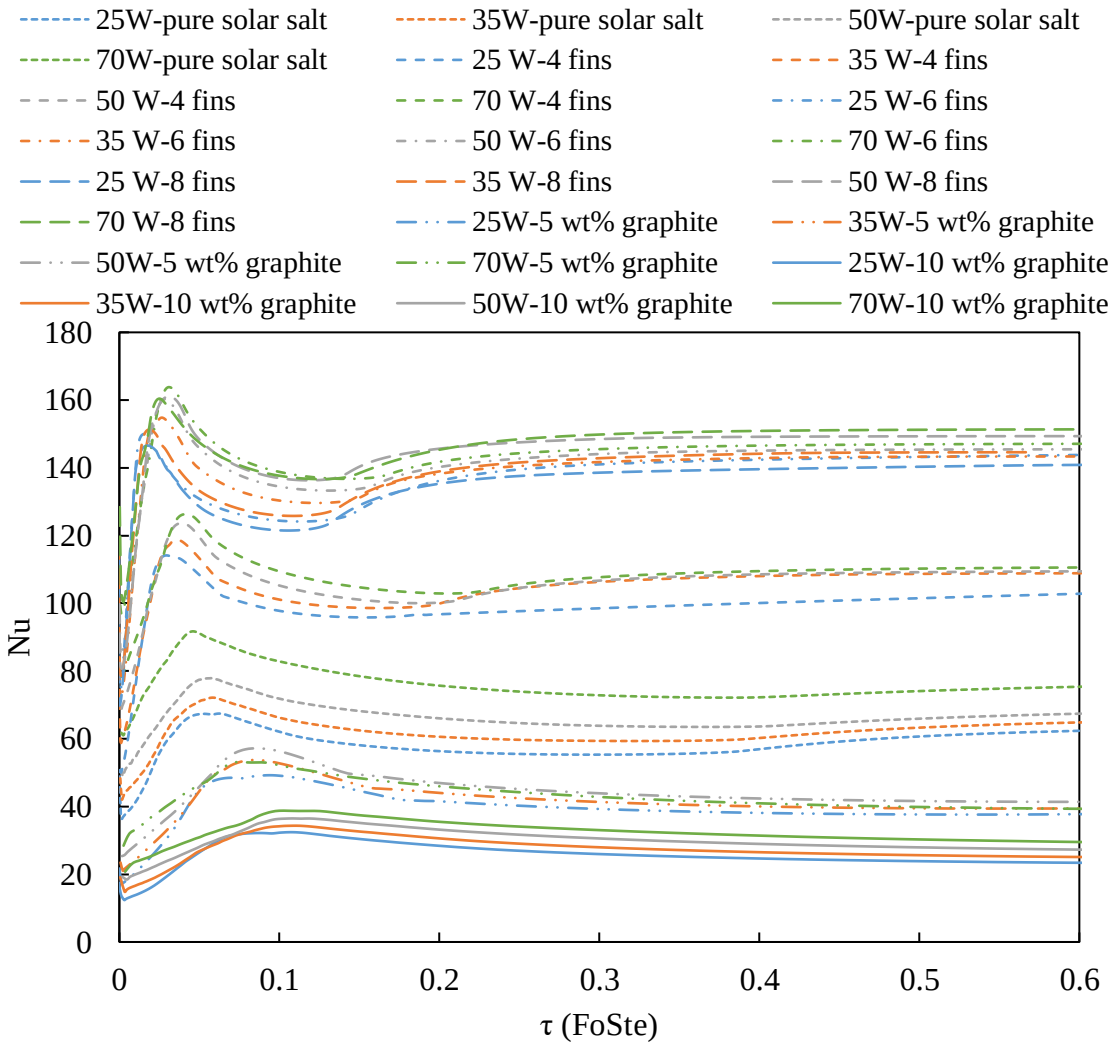

Figure B- 8: Nu number versus dimensionless time for TES systems using solar salt with different configurations during the charging process.

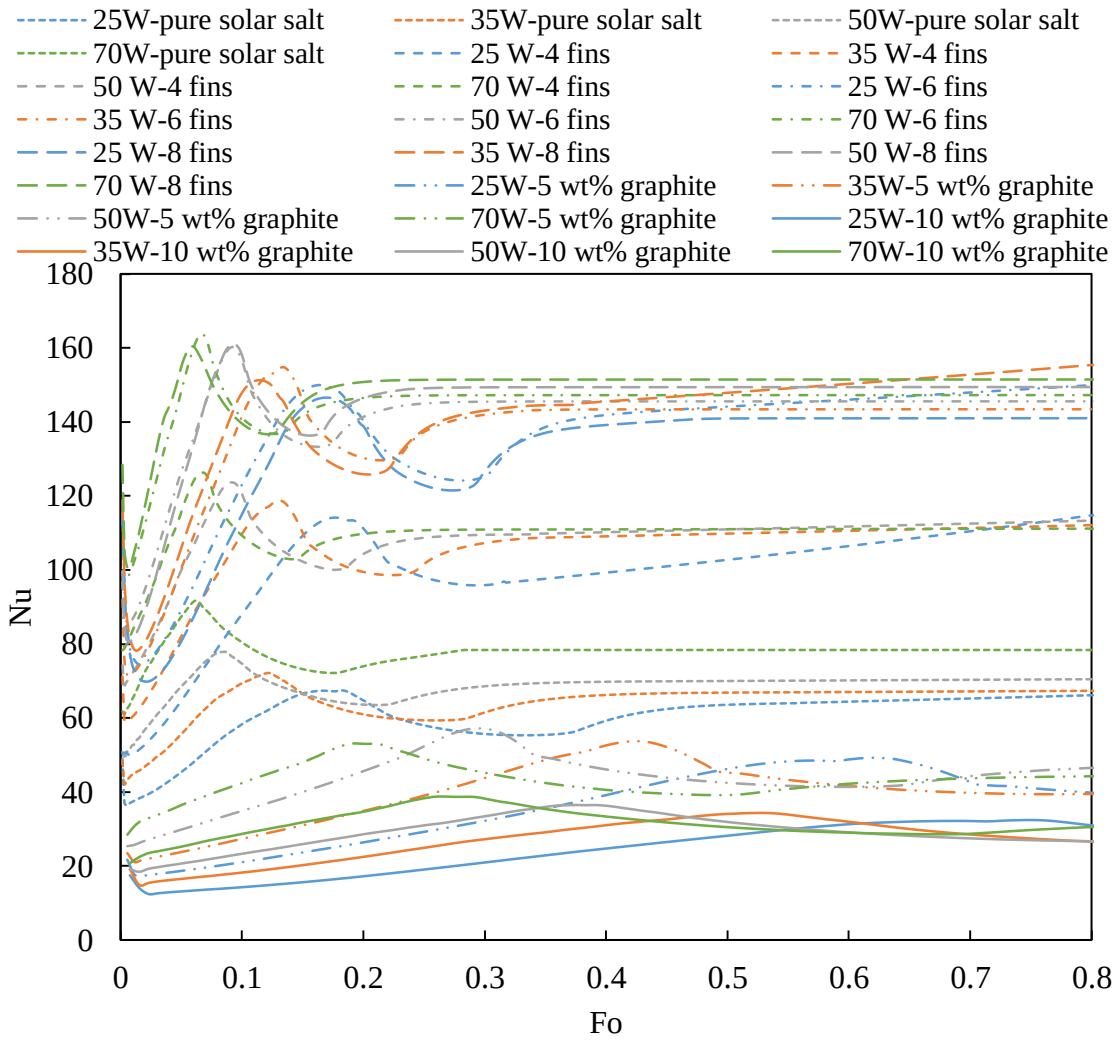

Figure B- 9: Nu number versus Fourier number for TES systems using solar salt with different configurations during the charging process.

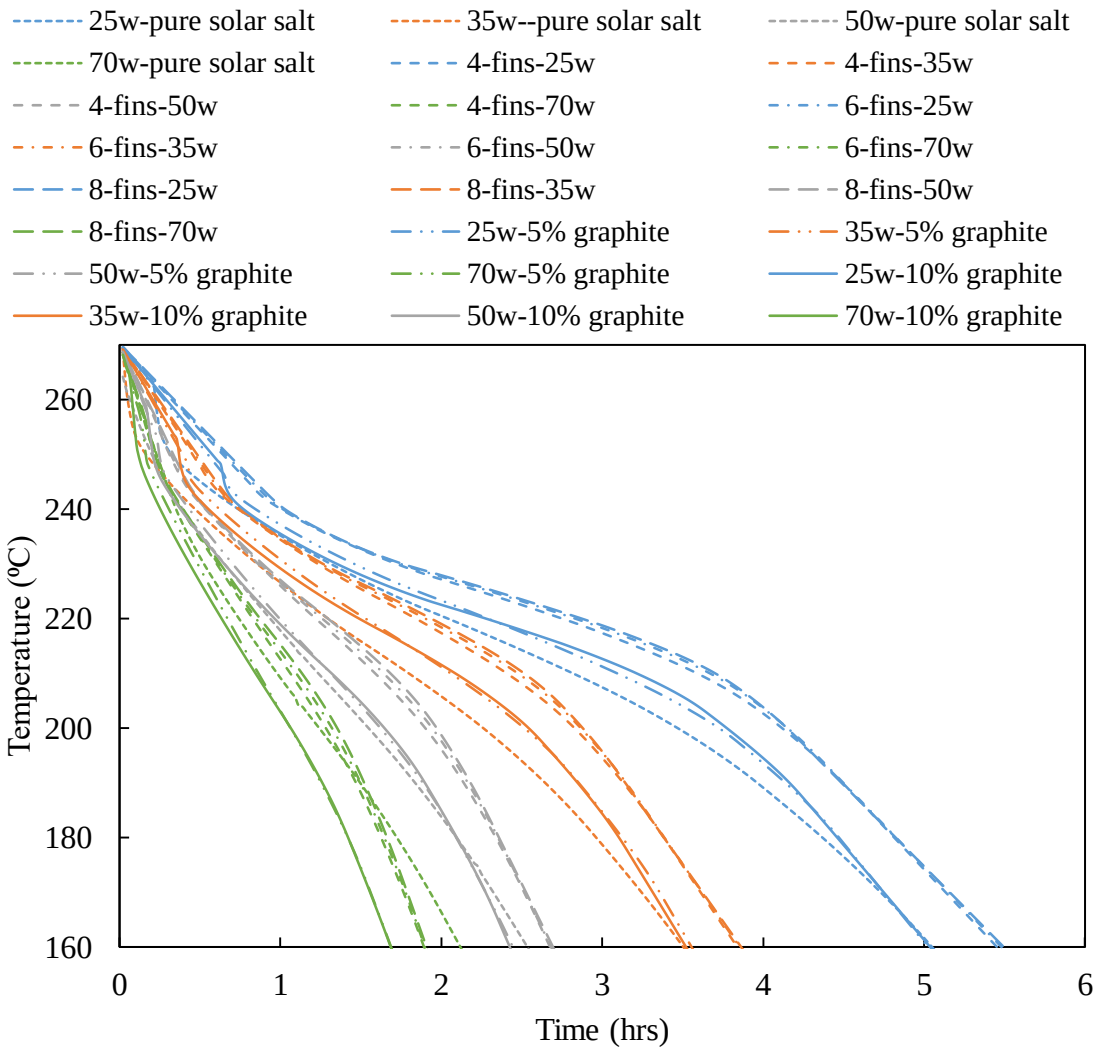

Figure B- 10: Average temperature of the TES systems using solar salt with different configurations during the discharging process

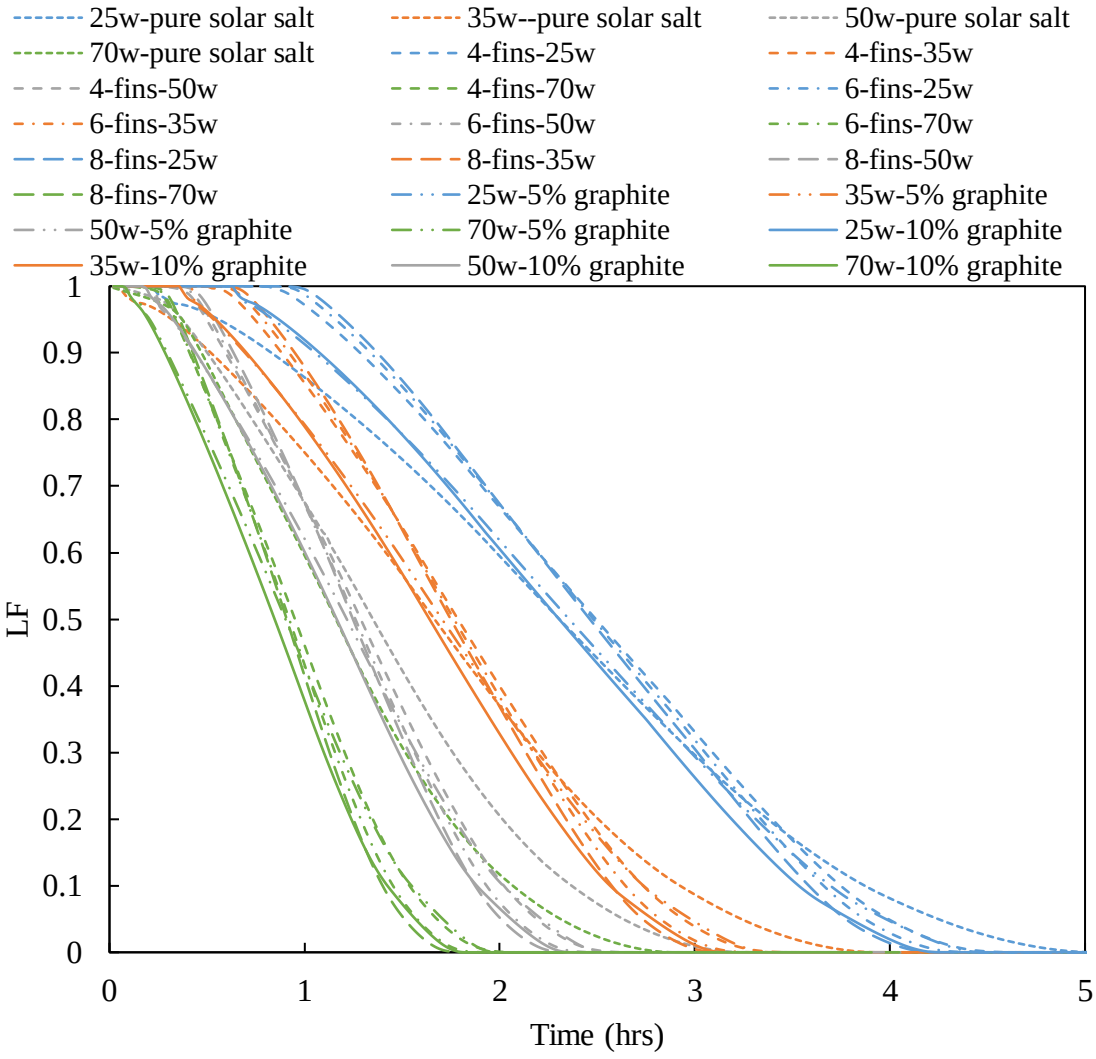

Figure B- 11: LF variation in the TES systems using solar salt with different configurations during the discharging process.

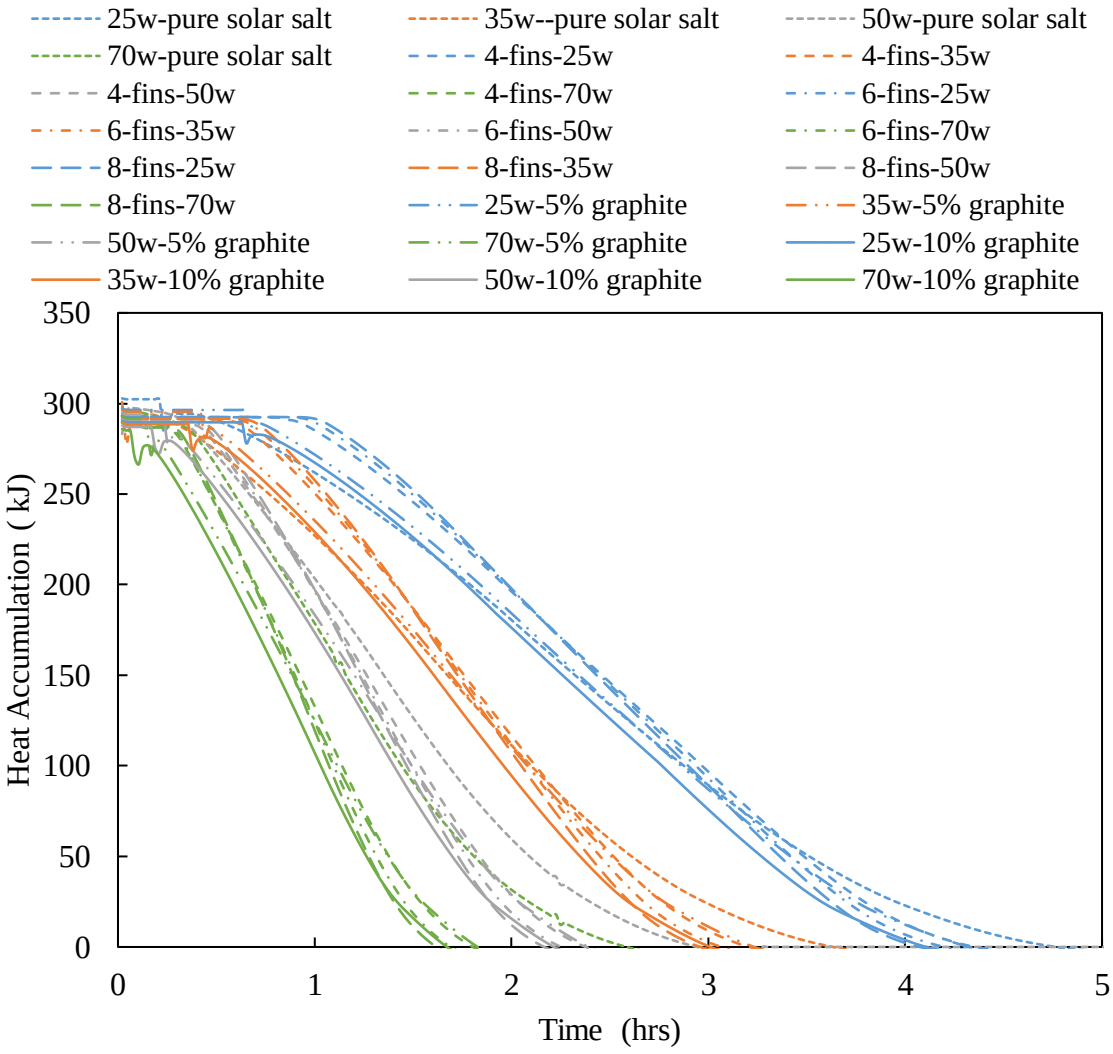

Figure B- 12: Discharging of the accumulated energy in the TES systems using solar salt with different configurations during the discharging process.

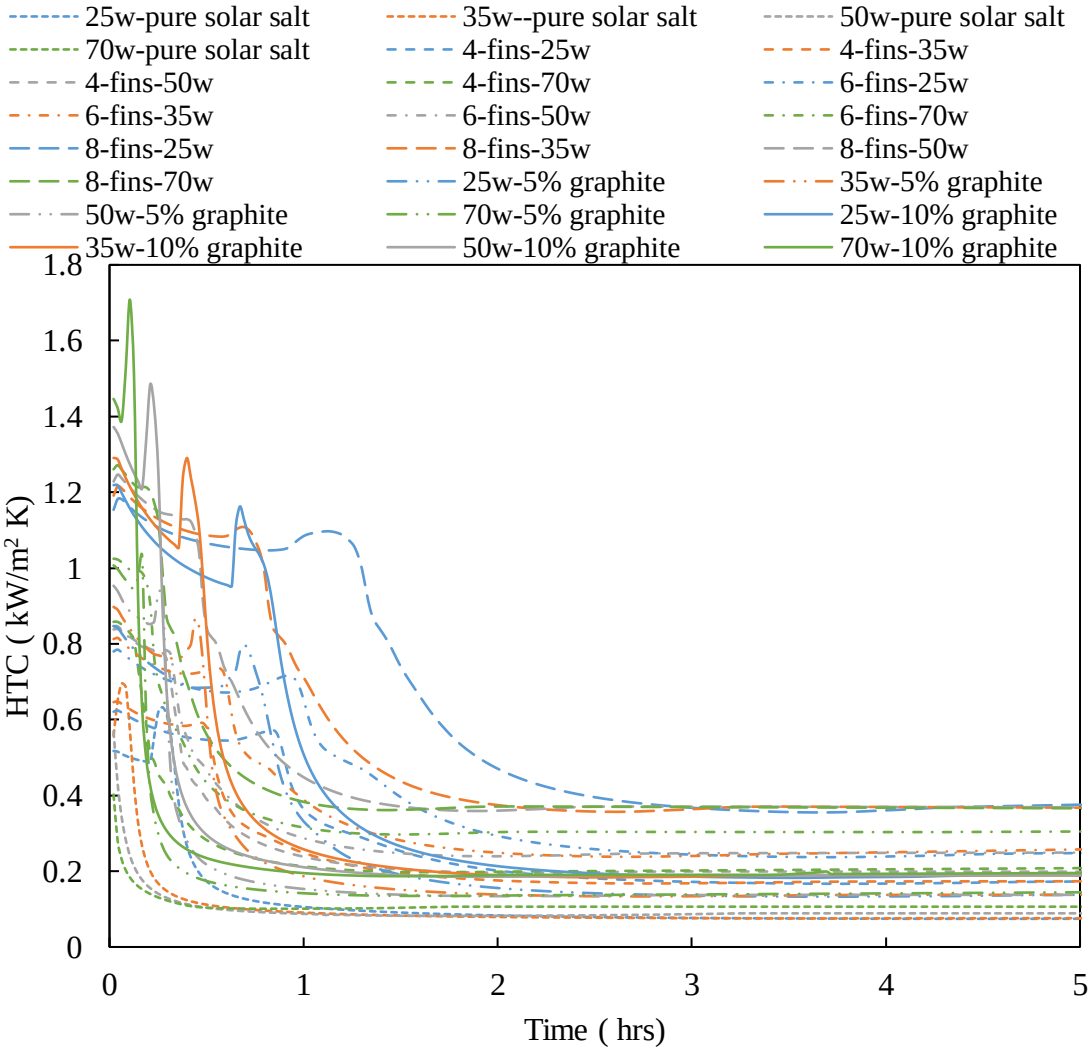

Figure B- 13: HTC variation in the TES systems using solar salt with different configurations during the discharging process.

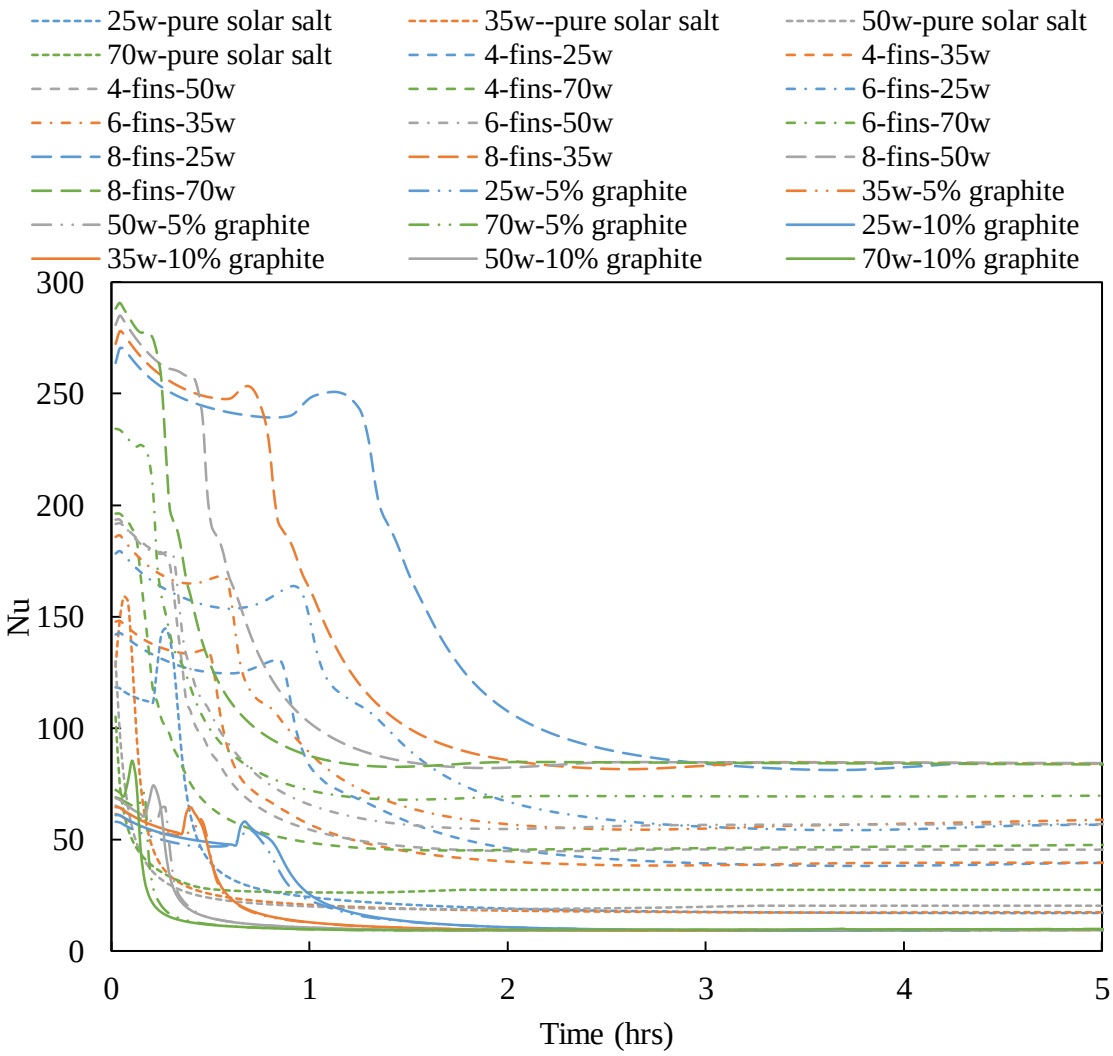

Figure B- 14: Nu number variation in the TES systems using solar salt with different configurations during the discharging process.

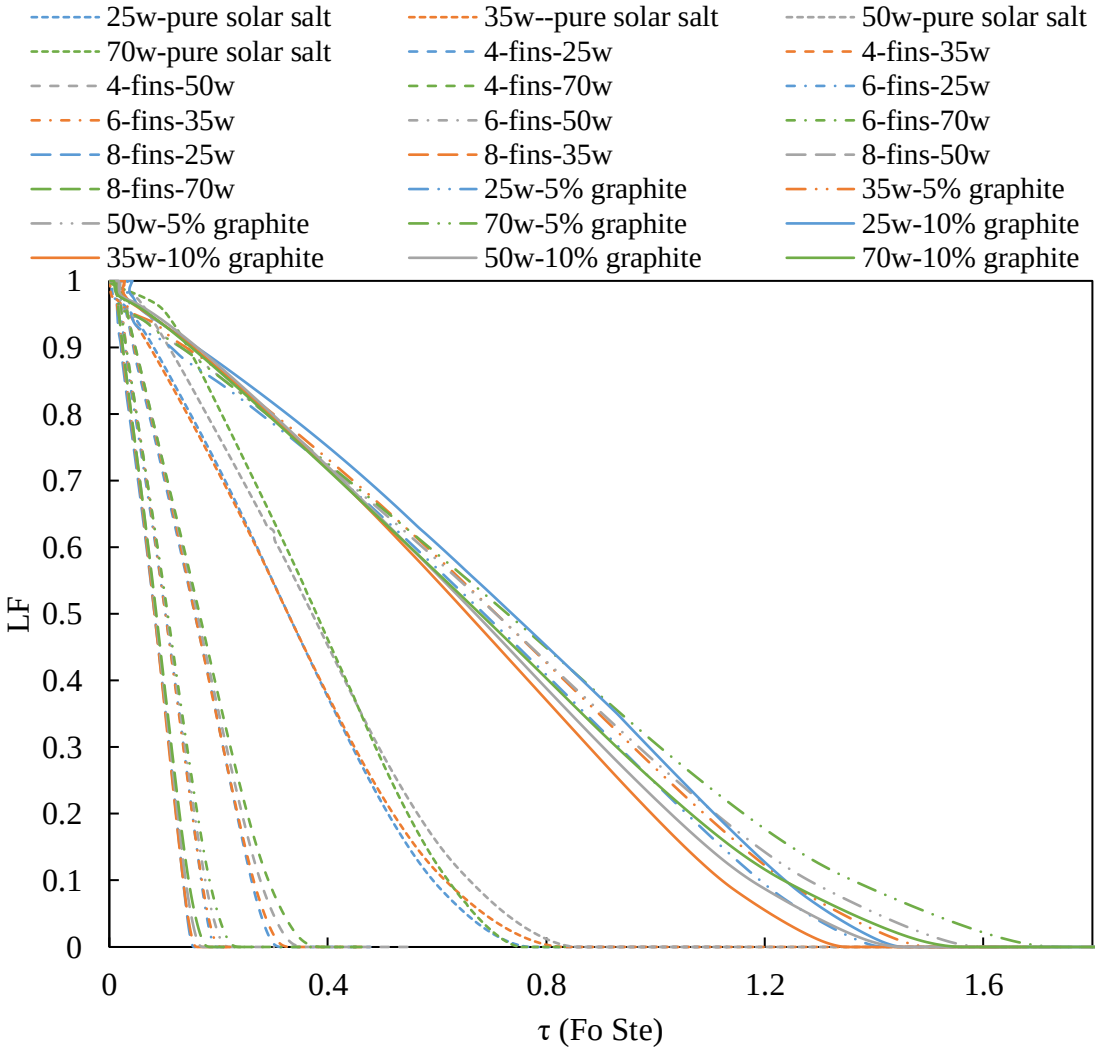

Figure B- 15: LF versus dimensionless time in the TES systems using solar salt with different configurations during the discharging process.

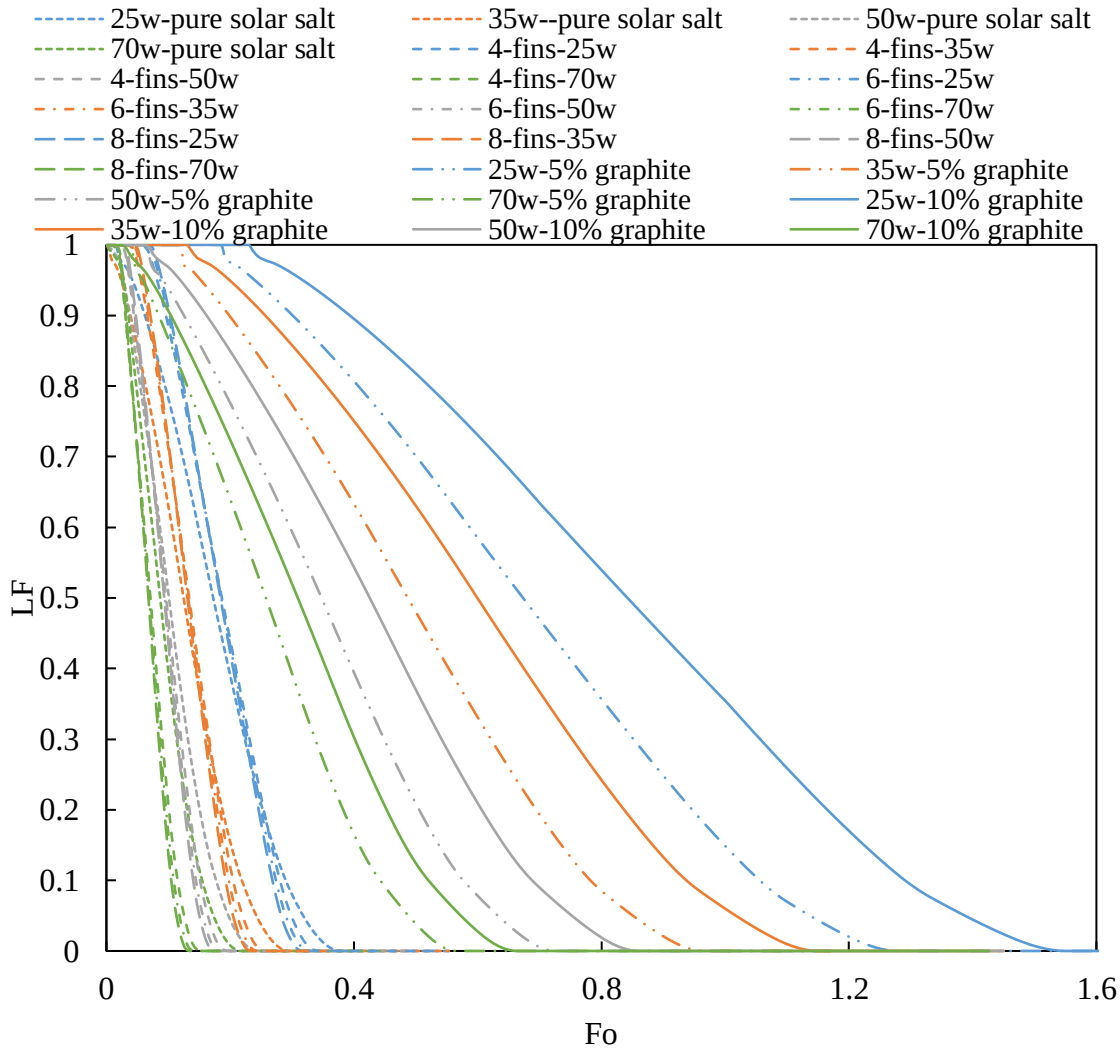

Figure B- 16: LF versus Fourier number in the TES systems using solar salt with different configurations during the discharging process.

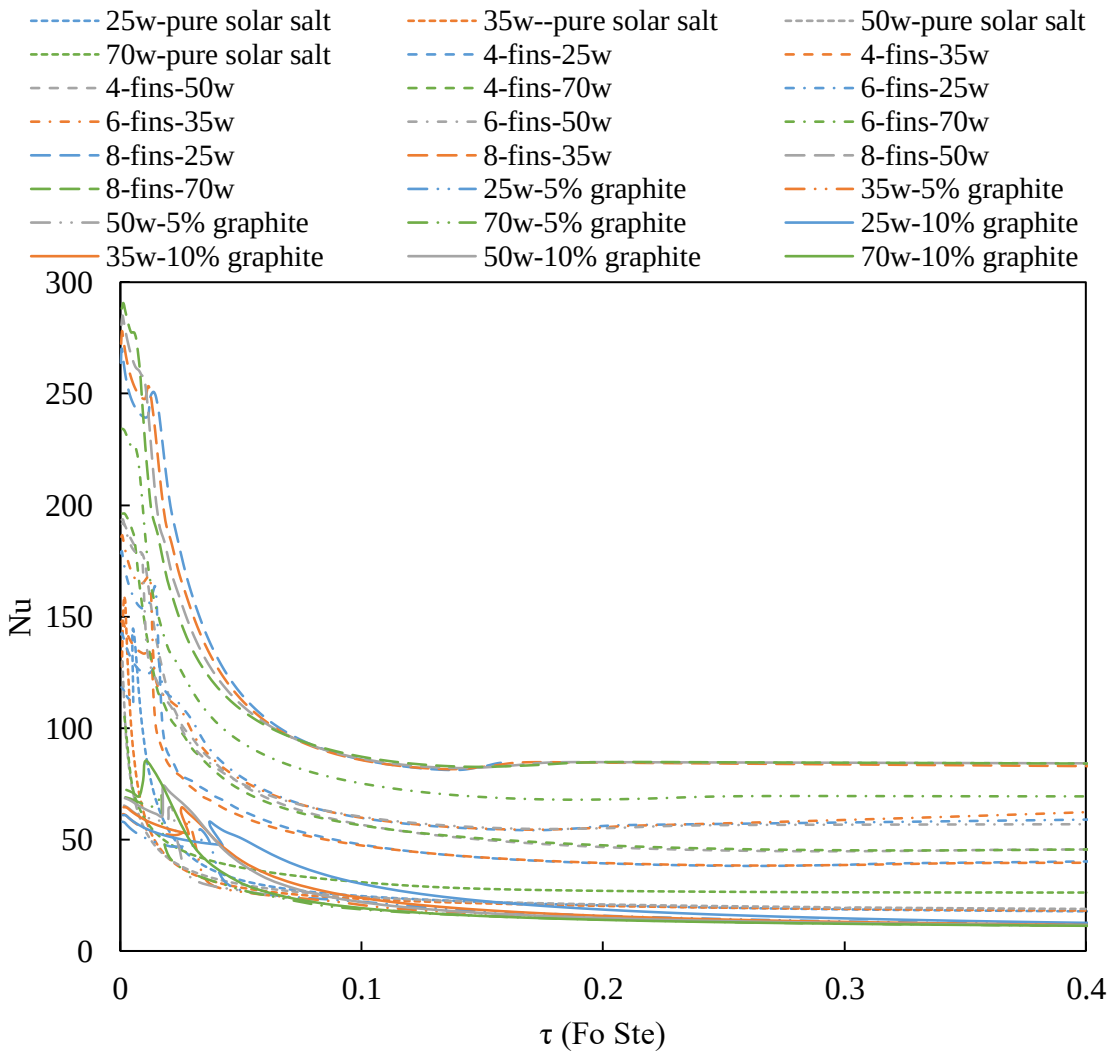

Figure B- 17: Nu number versus dimensionless time in the TES systems using solar salt with different configurations during the discharging process.

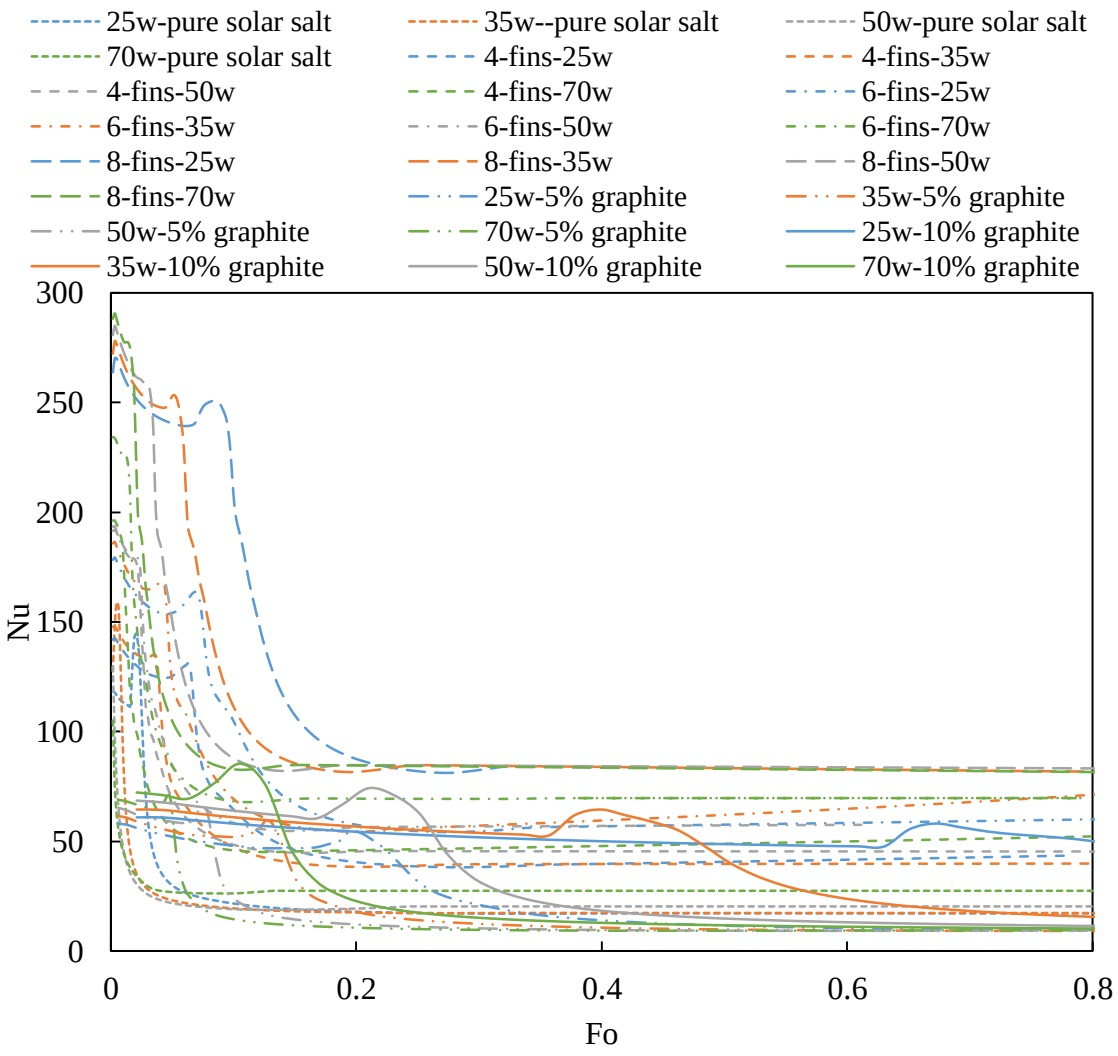

Figure B- 18: Nu number versus Fourier number in the TES systems using solar salt with different configurations during the discharging process.

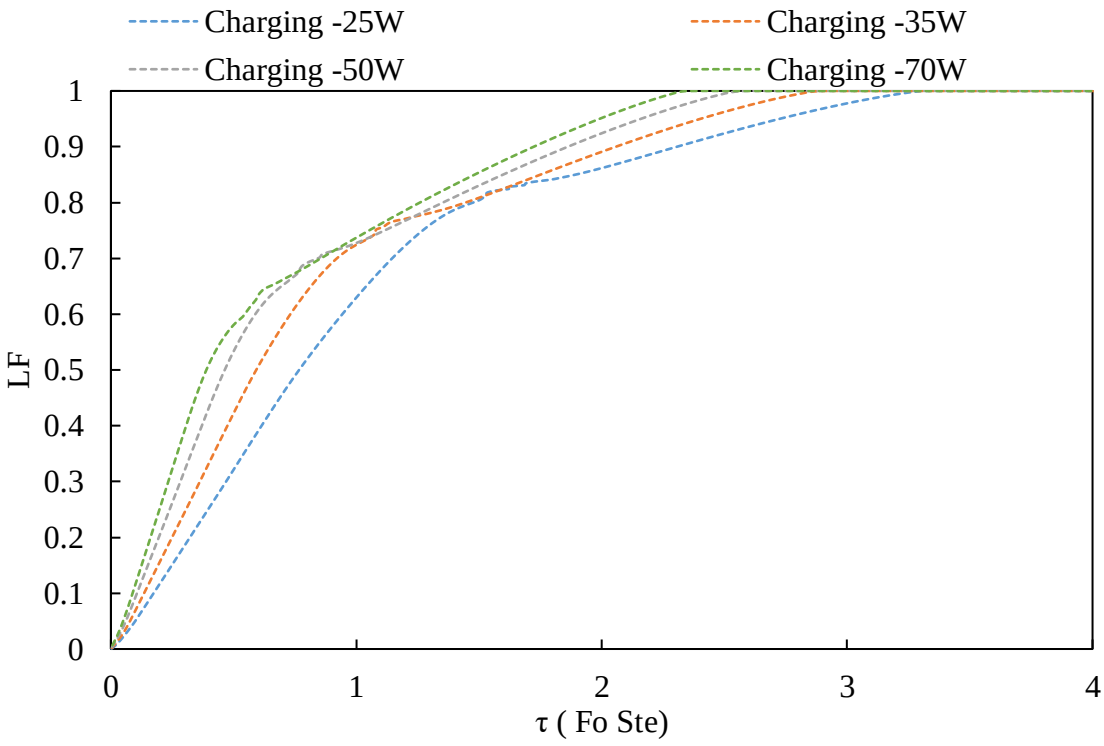

Figure B- 19: LF versus dimensionless time in the TES system using metal PCM during charging process.

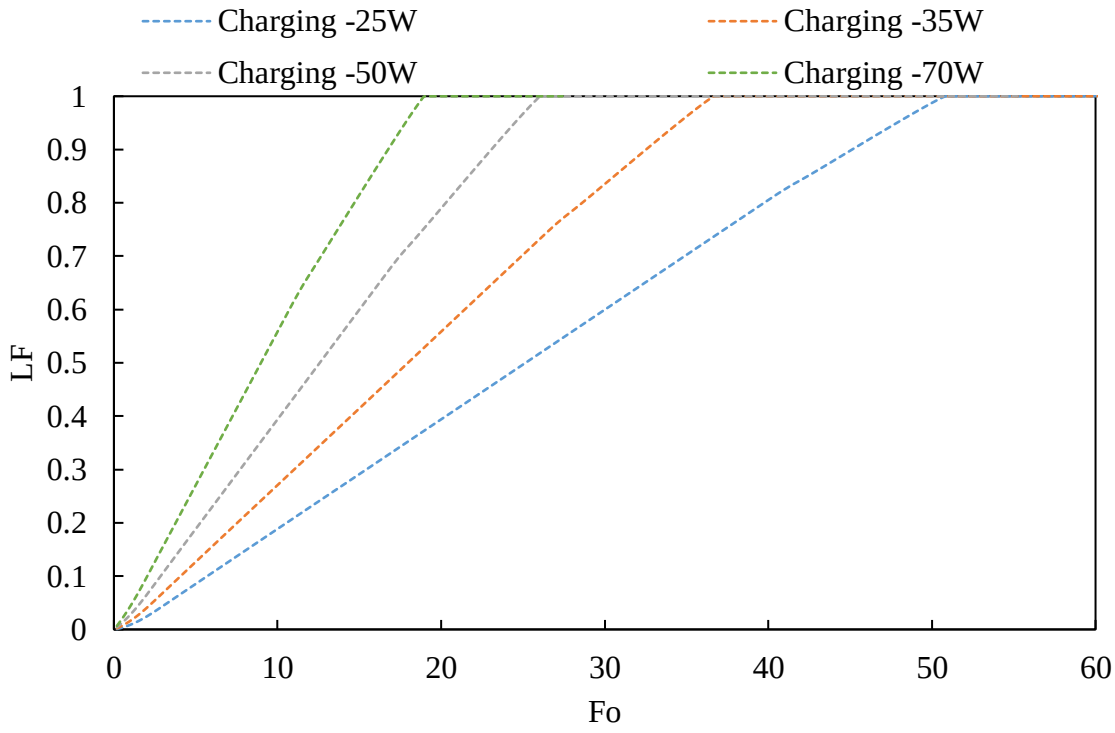

Figure B- 20: LF versus Fourier number in the TES system using metal PCM during the charging process.

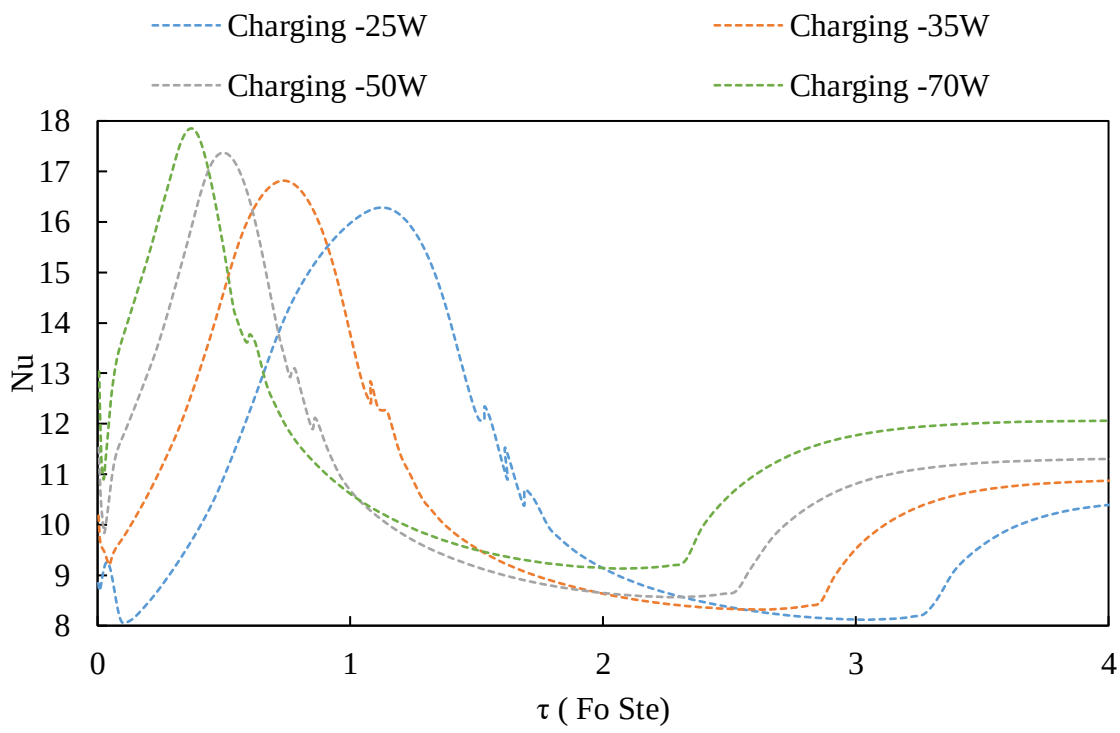

Figure B- 21: Nu number versus dimensionless time in the TES system using metal PCM during charging process.

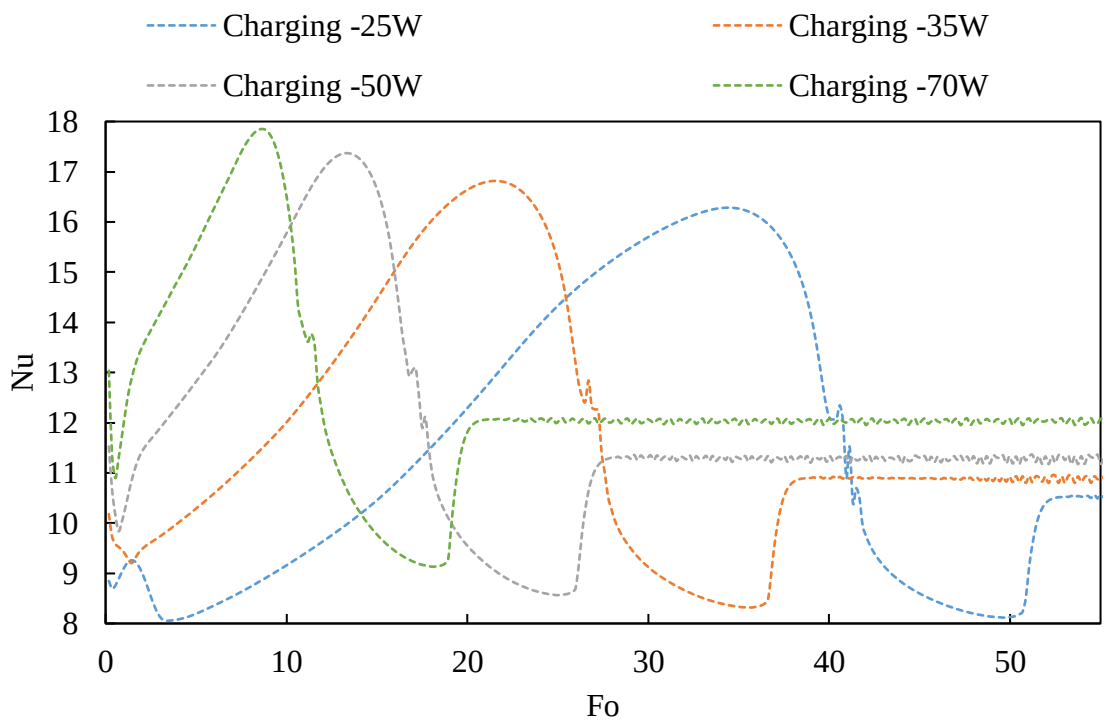

Figure B- 22: Nu number versus Fourier number in the TES system using metal PCM during charging process.

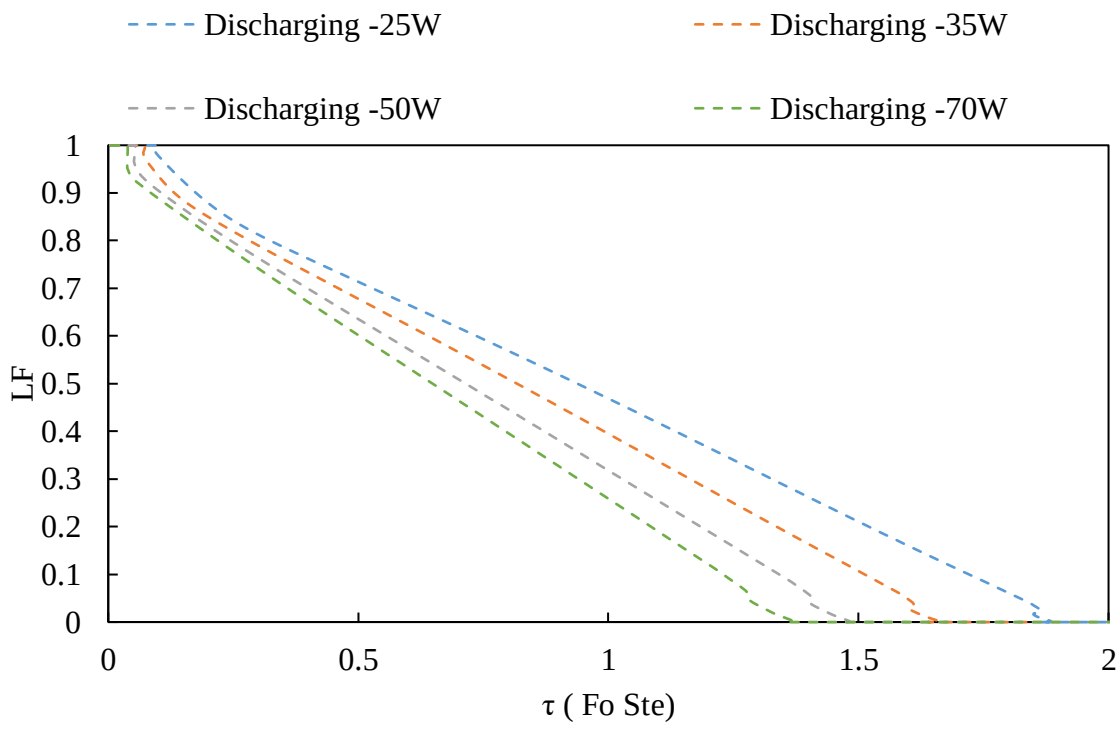

Figure B- 23: LF versus dimensionless time in the TES system using metal PCM during discharging process.

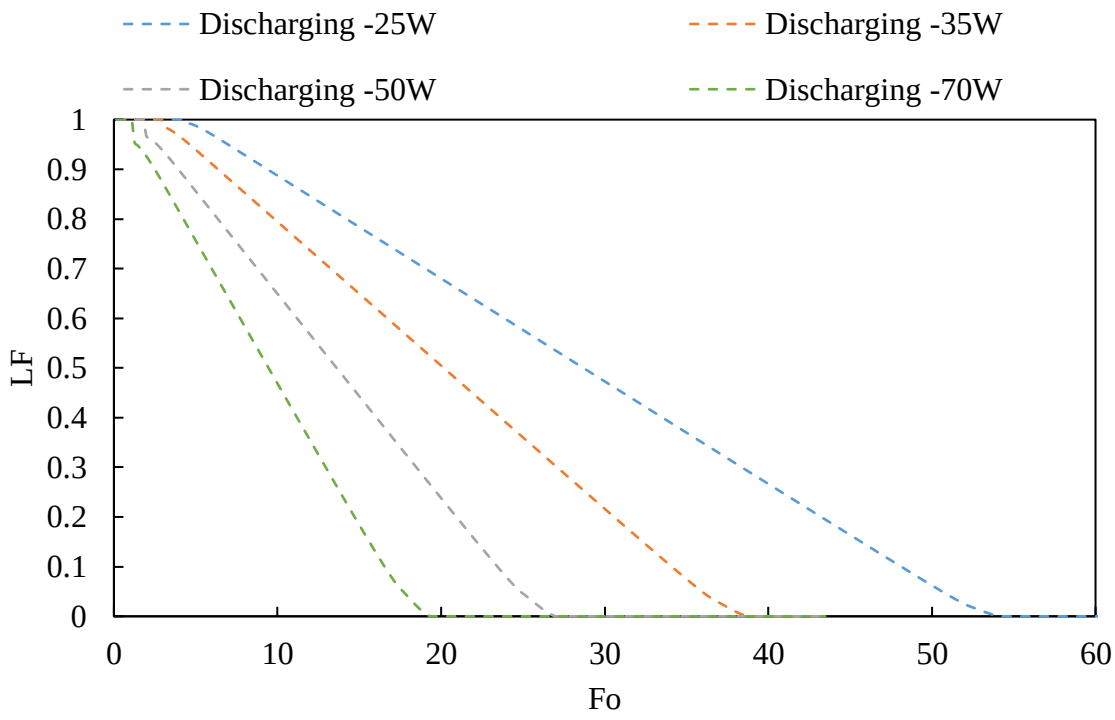

Figure B- 24: LF versus Fourier number in the TES system using metal PCM during discharging process.

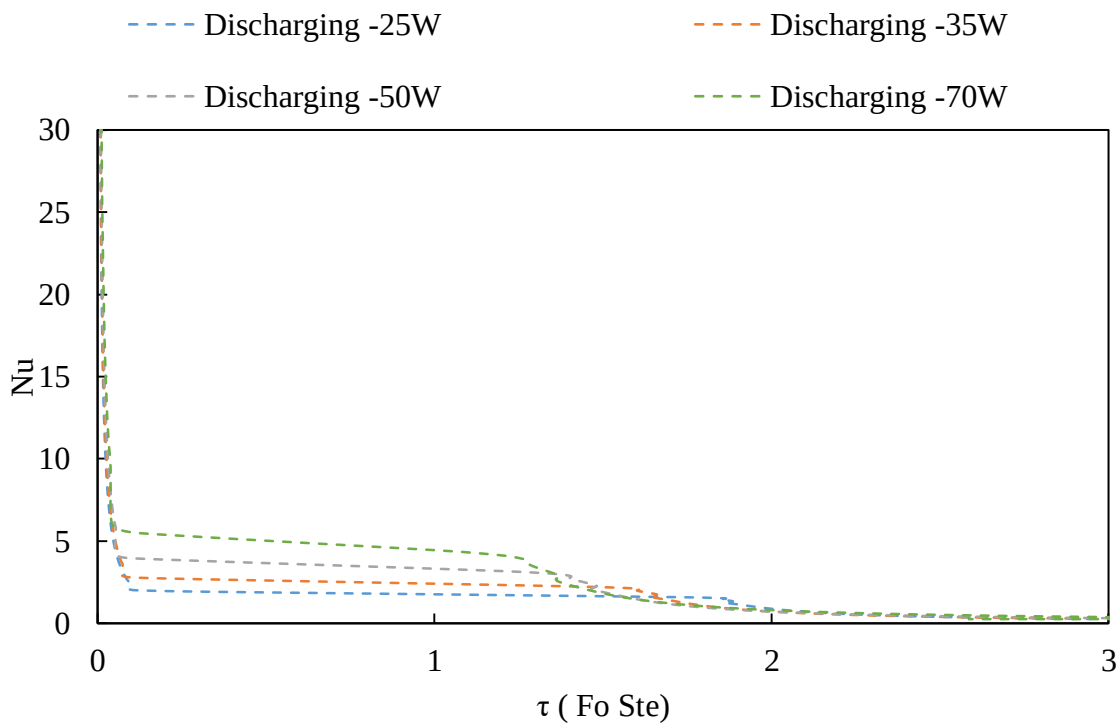

Figure B- 25: Nu number versus dimensionless time in the TES system using metal PCM during discharging process.

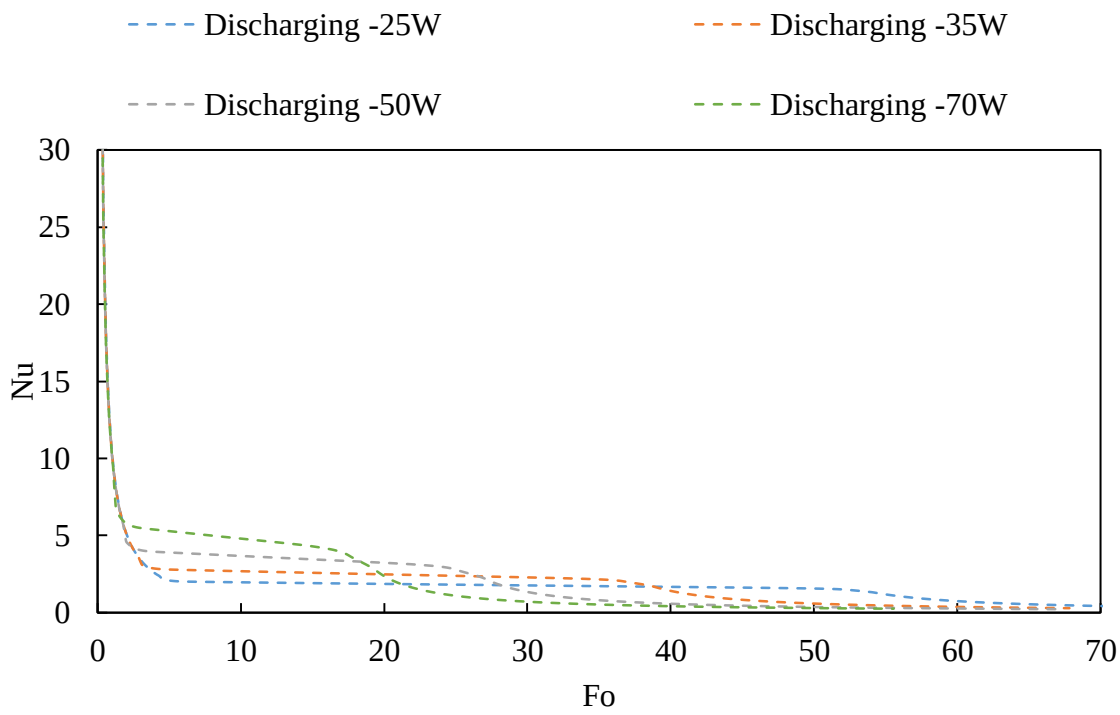

Figure B- 26: Nu number versus Fourier number during the discharging process.